



UNIVERSITAT^{DE}
BARCELONA

Advances in semiconducting nanowires for gas sensing: synthesis, device testing, integration and electronic nose fabrication

Guillem Domènech Gil



Aquesta tesi doctoral està subjecta a la llicència **Reconeixement 4.0. Espanya de Creative Commons.**

Esta tesis doctoral está sujeta a la licencia **Reconocimiento 4.0. España de Creative Commons.**

This doctoral thesis is licensed under the **Creative Commons Attribution 4.0. Spain License.**



UNIVERSITAT DE
BARCELONA

Advances in semiconducting nanowires for gas sensing: synthesis, device testing, integration and electronic nose fabrication

Guillem Domènech Gil

Director: Albert Romano Rodríguez

Departament d'Enginyeria Electrònica i Biomèdica
Institut de Nanociència i Nanotecnologia (IN²UB)

Advances in semiconducting nanowires for gas sensing: synthesis, device testing, integration and electronic nose fabrication

Memòria presentada per optar al grau de doctor
per la Universitat de Barcelona
Programa de doctorat en Nanociències

Autor

Guillem Domènech Gil

Director i tutor

Albert Romano Rodríguez

Departament d'Enginyeria Electrònica i Biomèdica
Institut de Nanociència i Nanotecnologia (IN²UB)



UNIVERSITAT DE
BARCELONA

Acknowledgements

First of all, I would like to thank my Ph.D. supervisor, Prof. Albert Romano Rodríguez for giving me the opportunity to participate in a research project for the first time, providing guidance and support during the work developed for more than 4 years, and for opening the path to new and exciting projects focused on nanoscience, always with enthusiasm and critical, but constructive, spirit.

I am also very grateful to have had the occasion of sharing parts of my research with Dr. Sven Barth and Dr. Paolo Pellegrino, who helped me to increase the quality of the work done during this thesis. I want to thank their support, their free transfer of knowledge and their ability in showing me key points for my research and career path, aspects that sometimes are missed among the scientific community.

I would also like to thank Dra. Isabel Gràcia and Dr. Carles Cané for providing the microhotplates and micromembranes, always with the best predisposition and open to new proposals.

I want to give thanks to the colleagues from the department who helped and supported me many times, giving a special mention to Jordi Samà, which whom I started my laboratory experience. Thanks also to my friends and labmates, Aïda Varea, Cristian Fàbrega, Olga Casals, Joan Daniel Prades, Xana Rodríguez, Omar Olmedo, Anna Batlle, Peter Pfeiffer, Montse Manadé, Xavi Arrese, Elena Aymerich, Alex Cabal, John Jaiber, Ismael Benito, Ismael Gabaldón, Christian Driau, Gerard Sánchez, Ferran, Carles and Qoumaruddin. I have spent many good times with them, inside and outside the laboratory, laughs and, of course, debates about science and, also, about completely different topics, what made my daily work easier and softer. I would also like to express my gratitude to Catalina, Julià, Lluís López, Adrià, Javi, Dani, Juan, Giovanni, Martí, Oriol Blàzquez, Mauricio Moreno, Romen Rodríguez and Sergi Hernández, who also helped me during these years when it was necessary and have spent many good times.

I would like to thank the moments shared with Irmina Peiró, Elena Aymerich, Paula Pirker, Aleksandra Adamczyk, Lily Walter and Alex Rodríguez, from who I also learned. It was really nice to help them in their works and get close to science together.

Sincere thanks to Alba, who stayed a long part of the thesis by my side, having lots of debates about chemistry that helped me considerably.

I have also to thank the strong support and encouraging that I received from Acadèmia Informa't, Concepció, Núria, Jordi and all the teachers and students that shared these years and lectures with me.

Of course, this would not have been possible without spending time with my friends from outside the faculty. I thank them all the time they spent listening to explanations about my research, that was very amusing (for me), and for being there when it is necessary, to have a beer or to take a break. Thank you, Jordi, Rubi, Gerard, Laura, Bernat, Marta, Júlia, Charlie, Sabier, Enric, Silvia, Mar, Cayu, Andreu and Alicia May, I always have fun with you.

Finally, I would like to express my gratitude to my family, that with a lot of patience, always listen to me. Specially, to my parents, that are incredible referents each one, and to my brother from who I learn every day, overtaking our differences.

This work has been partially funded by the Spanish Ministry of Economy and Competitiveness, through projects TEC2013-48147-C6-1R (TEMIN-AIR) and TEC2016-79898-C6 (AEI/FEDER, EU).

Table of contents

| | |
|---|------------|
| 1. Introduction | 5 |
| 1.1 Solid-state gas sensors | 6 |
| 1.2 Gas solid interactions | 12 |
| 1.2.1 Physisorption and chemisorption | 12 |
| 1.2.2 Adsorption isotherms | 16 |
| 1.2.3 Chemoresistive gas sensors | 20 |
| 1.2.4 Two-probe measurements with individual nanowires | 23 |
| 1.3 Chemical vapor deposition | 24 |
| 1.3.1 Vapor-liquid-solid mechanisms | 24 |
| 1.3.2 Chemical vapor deposition..... | 27 |
| 1.3.3 Carbothermal reduction..... | 31 |
| 1.4 Integration methodologies | 34 |
| 1.4.1 Microhotplates and micromembranes | 34 |
| 1.4.2 Focused electron-ion beam induced deposition techniques | 35 |
| 1.4.3 Electron lithography | 37 |
| 1.4.4 Dielectrophoresis..... | 39 |
| 1.4.5 Site-selective growth..... | 41 |
| 1.5 References..... | 43 |
| 2. Objectives | 51 |
| 3. Individual semiconducting metal oxide nanowires for gas sensing | 55 |
| 3.1 Gas sensor based on individual indium oxide nanowire..... | 57 |
| 3.2 Gas sensor based on individual gallium oxide nanowire..... | 69 |
| 4. Advanced integration methodologies for nanowire-based gas sensors..... | 105 |
| 4.1 Dielectrophoretic alignment of individual tungsten oxide nanowires for gas sensing | 107 |
| 4.2 Gas sensor based on individual tin oxide nanowire contacted by Electron Beam Lithography..... | 125 |
| 5. Electronic-nose based on semiconducting nanowires | 137 |

| | |
|---|------------|
| 5.1 Site-selective growth and In-situ integration of different nanowire material for Electronic-nose applications | 139 |
| 6. Conclusions and future work | 163 |
| 6.1 General conclusions | 163 |
| 6.2 Specific conclusions | 164 |
| 6.3 Future work..... | 167 |
| 7. Resum en català | 171 |
| 8. List of publications and conference contributions..... | 177 |



*“If I have an apple and you have an apple
and we exchange them, then both still have one apple.*

*If I have an idea and you have an idea
and we exchange them, then both will have two ideas.”*

George Bernard Shaw

1. Introduction

In the last two decades nanotechnology has given rise to a scientific and technical revolution, contributing with novel research paths and applications, which has generated huge interests among the scientific community and industry. As a consequence, around the world, there have been important investments in this field with the aim of leveraging new products and commercial opportunities. In fact, nanotechnology has been declared to be the technology of the twenty-first century and only time will tell if this statement will turn out to be true.

Nanotechnology is the technology suitable to provide tools to manipulate matter at the nanometer scale, meaning 1 to 100 nm at least in one of the material dimensions. Not only the scale is important, as miniaturization along Moore’s law curve is nowadays a routine in the microelectronic industry, but also to exploit the new properties arising from nanoscale effects [1,2]. Nanotechnology is now understood as a broad-base multidisciplinary field forecasted to reach mass use by 2020 and to revolutionize many aspects of human life [2]. Nowadays, new instrumentation and methods have allowed femtosecond measurements with atomic precision [3], single-phonon spectroscopy [4] and sub-nanometer resolution morphological measurements [5], single-atom [6] and single-molecule characterizations [7], simulations of large assemblies of atoms or crystalline structures [8]; the discovery and development of important new phenomena such as plasmonics [9], negative index refraction in IR/visible wavelength radiation [10], precision measurements of the Casimir forces [11], teleportation of information between atoms [12] which could enable quantum computing, biointeractions at the nanoscale [13] or fabrication of graphene [14], among others. Therefore, even being a technology under development that still lacks some required tools and with misconceptions in some

fundamental areas, since its invention all the mentioned achievements point out the potentiality of nanotechnology.

Parallel to this fact, the concern about toxic and harmful gases for human health has been increasing during the last two centuries. This is due to our life style, in which large amounts of gases are propagated either in open air or in indoor environments. This is especially true in the last decades. The presence of toxic gases and pollutants is the first environmental cause of premature death in European Union, with 400.000 premature deaths per year [15,16]. Since the fabrication of the first device intended to sense flammable gases in coal mines in 1816 [17], the fire-damp, warning the lack of oxygen and the excess of methane, an enormous variety of gas sensors have been developed [18], driven by the ever-growing concern of the citizens about such effects.

Gas sensors are transduction devices that transform chemical and/or physical information effects of the presence of a certain gas into an electrical signal, whose value can be measured. In this way, the concentration of gaseous species in the vicinity of the sensors can be surveyed and, if the gases are harmful, the sensor can help preventing dangerous situations by allowing the control of the gas emitting sources.

The gas sensor market was valued at 1.67 billion € in 2017 and it is estimated to grow significantly from 2025 [19]. Gas sensors are adopted for several applications, such as medical, industrial, petrochemical, automotive manufacturing industries, food process, building and domestic appliances or quality control [19].

1.1 Solid-state gas sensors

Solid-state gas sensors are devices based on the change of the physical and/or chemical properties of their sensing materials when exposed to different gas atmospheres. Depending on the sensing material, these properties can be tuned to a certain extent, adapting the fabricated gas sensors to different needs. In this sense, nanotechnology contributes with numerous tools to study in depth the prevailing materials used in gas sensing, unwrapping novel effects occurring in nanostructured materials.

The tremendous variety of solid-state gas sensors available nowadays can be sorted in groups as a function of the transduction mechanism taking place at the sensing material.

This gives rise to optical, mass-sensitive, calorimetric or conductometric gas sensors, among others, which will be briefly described in this section. A section specially devoted to the evolution, advantages, drawbacks and general trends of semiconducting metal oxide-based (MOX) gas sensors, a type of conductometric gas sensors, is presented in this work, as prototypes of MOX-based gas sensor are developed, fabricated and characterized in this thesis.

Optical gas sensors transform the interactions between the gas and the sensing material into changes in the electromagnetic radiation propagation [20]. This effect can be directly related with physical or chemical changes of the target molecule or, for analytes that do not produce optical changes, of a label marker [21]. In general, this kind of sensor presents high selectivity towards particular gaseous compounds, allowing to detect a specific gas in these mixtures. However, they lack portability due to fragile optical components, difficulties in miniaturization and are quite expensive [18]. *Figure 1 a)* shows a schematic diagram of one of this type of devices, namely a surface plasmon resonance-based sensor.

Mass-sensitive gas sensors are based on the mass changes occurring at the material's sensing surface during the interaction with gaseous species. Examples of sensors using this basic principle are microcantilevers [22,23], shown in *Figure 1 b)*, surface acoustic wave [24] or quartz crystal microbalance sensors [25]. In general, these sensors present fast and high responses to the surrounding gases, but their behavior depends considerably on temperature and humidity, apart from needing complex electronic circuits to operate.

Calorimetric gas sensors are based on the temperature variation produced by a gas on certain materials, which will be later measured as resistance variation. In this case, the detecting elements consist of small “pellets” of catalyst-loaded ceramics whose resistance

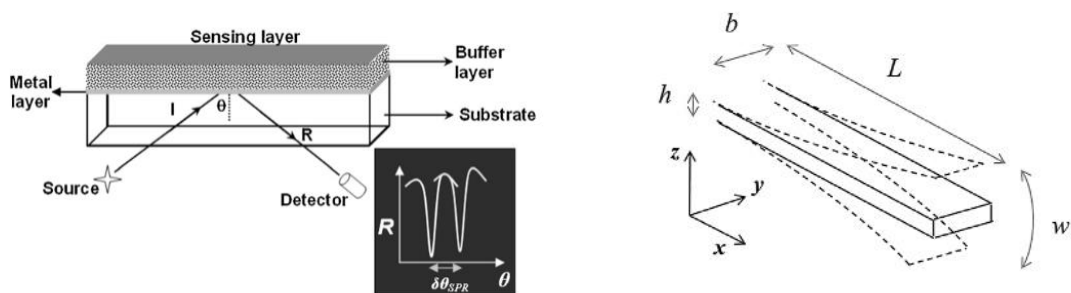


Figure 1: (a) Schematic diagram of surface plasmon resonance-based sensor (reprinted from Ref. [21]) and (b) schematic representation of microcantilever and the transverse deflection (reprinted from Ref. [23]).

changes according to the surrounding gas species [26]. The term pellistor is used to designate this type of sensors, combining the words pellet and resistor.

Among the conductometric gas sensors, one of the most extended sensing materials are the semiconducting MOX. These materials are used to transduce the chemical reactions occurring at their surface with the surrounding gas, such as reduction, oxidation, adsorption or other surface reactions between adsorbed species, into reversible and measurable electrical resistance variation, which are used to extract the concentration of the different gases present in the ambient near the sensor.

The first written evidence regarding the idea of using the changes in conductivity/resistivity of a MOX under the presence of gases dates back to 1959 in a work by Mollwo and Heiland [27], who studied the conductivity changes of ZnO when kept under vacuum at temperatures up to 600 °C and, simultaneously, exposed to oxygen and hydrogen. The first practical gas sensor based on a semiconductor MOX was proposed in Japan in 1962 by Seiyama [28], and shortly afterwards by Taguchi [29], using as sensing element films of ZnO and SnO₂, respectively. Taguchi founded Figaro Engineer Inc. in 1967, which is a worldwide company that still supplies gas sensors based on MOX all around the globe. During the next few years, the use of SnO₂-based gas sensors started to spread in Japan, while other types of metal oxides were simultaneously investigated [30], as shown in *Table 1*. Seiyama and co-workers studied the selectivity and sensitivity of MOXs, as well as their modifications using noble metals [31], gaining a large amount of information on the behavior of different metal oxide materials, which has strongly impacted the sensor fabrication field. However, the understanding of the sensing mechanisms and kinetics are still incomplete, due to complicated crossed effects, such as surface defects, surface adsorption properties, metal-semiconductor junctions or MOX particle size influence.

| Year | Material | Gas detected | Researcher |
|-------------|---|---|-----------------------|
| 1962 | ZnO (thin film) | H ₂ , Alcohol | Seiyama, et. al. [28] |
| | SnO ₂ | Combustible gas | Taguchi [29] |
| 1963 | SnO ₂ + Pd, Pt, Ag. | Combustible gas | Taguchi [32] |
| 1966 | ZnO, SnO ₂ | Reducing gas | Seiyama, et. al. [33] |
| | SnO ₂ + Al ₂ O ₃ | Combustible gas | Taguchi [34] |
| 1967 | WO ₃ + Pt | H ₂ , N ₂ H ₄ , WH ₃ , H ₂ S | Shaver [35] |

| | | | |
|-------------|---|-----------------------------------|-----------------------|
| | In ₂ O ₃ + Pt | H ₂ , Hydrocarbon | Loh [36] |
| 1969 | SnO ₂ + SiO ₂ | Combustible gas | Taguchi [37] |
| 1971 | ZnO + Pt + Ga ₂ O ₃ | CH ₄ , NH ₃ | Bott, et. al. [38] |
| 1972 | SnO ₂ + Pd | Propane | Seiyama, et. al. [39] |

Table 1: summary of key solid-state gas sensor publications during the decade 1962-1972.

To understand the behavior of MOX as gas sensors, detailed studies measuring simultaneously the resistance change of the sensing material and the gas species adsorption are essential. For this purpose, two different set-ups are generally used: under clean, dry and ultrahigh-vacuum conditions or/and at pressures and temperatures mimicking real ambient conditions [40]. The experimental methodology was established in the course of more than 50 years [41], with a first systematic approach formulated in 1985 in a series of papers entitled “Development of chemical sensors: empirical art or systematic approach?” collected in a book [40]. Up to that moment, several techniques were already applied to investigate the gas adsorption, such as electron paramagnetic resonance (EPR) for investigations of oxygen adsorption [42] or infrared spectroscopy (IR) for CO adsorption studies [43]. The mentioned systematic approach pushed forward the basic understanding of the chemical reactions occurring at the surface of the sensing material and the corresponding conduction mechanisms. An example of this is the exhaustive study of SnO₂ surface reactions when exposed to acetic acid, methane and CO, published in 1989 [44]. By the end of the 90s, different spectroscopic methodologies were applied for sensors operating under ideal or under in situ real operation conditions. As shown in *Figure 2*. This fact led, in the early 2000, to the definition of in situ and operando spectroscopic techniques [45]:

- In situ spectroscopy: *spectroscopic characterization of sensing material under operation conditions or conditions relevant to operation; herein, the sensing performance of this material may be not characterized or may be characterized in a separate experiment.*
- Operando spectroscopy: *spectroscopic characterization of an active sensing element in real time and under operating conditions with the simultaneous read-out of the sensor activity and monitoring of gas composition.*

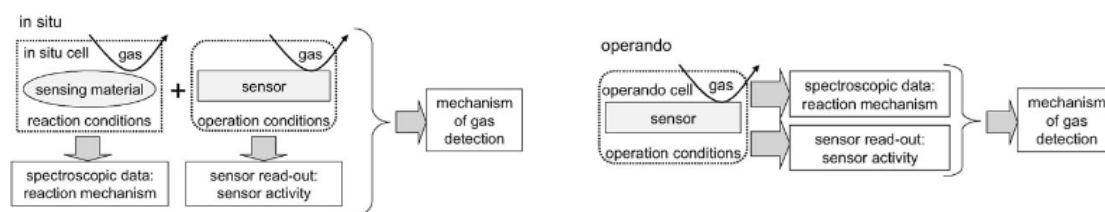


Figure 2: Scheme of a) in situ and b) operando spectroscopy (reprinted from Ref. [45]).

The operando spectroscopy couples the electrical and spectroscopic techniques with the aim of correlating the sensor activity with the gas composition of its surroundings. If these techniques are applied under real ambient conditions, then the study can elucidate and predict how a sensing material will behave when exposed to a non-controlled ambient that combines gases or gas mixtures whose interaction are already known.

With the appearance of nanomaterials, a new scenario was presented, with morphologies giving rise to a much larger surface-to-volume ratio compared to thin film materials, which is expected to give rise to an increase of the sensor sensitivity. The use of nanoparticles (NP) of metal oxides was the first choice and extensive work was carried out in the 90s and early 2000s to fabricate high crystalline quality and nanometre-sized NPs for their use in gas sensors. However, the difficulty in fulfilling both requirements simultaneously, as improving crystalline quality required high temperature treatments, which resulted to increase in nanomaterial size, limited this improvement path.

Nanowires (NWs) were considered for gas nanosensor fabrication at a later point, as their surface-to-volume ratio is lower than that of NPs, but with higher crystallinity and stability at elevated temperatures. The first proposal of a MOX gas sensor containing nanowires (NWs) as a sensing element was published by Kolmakov et al. in 2003 in California [46] using SnO₂ NWs to detect CO and O₂. One year later, a study on ZnO NWs working as ethanol sensors [47] was presented in China. The amount of chemical reactions that are continuously taking place at the surface of the sensing material are directly related with the total available surface adsorption sites. Nowadays, NWs are being incorporated as active material in many different gas sensing approaches, and with several surface treatments, with the aim of enhancing their intrinsic properties, as for example individual NWs [48] and/or decorated with novel metal nanoparticles [49] or using other MOX, such as WO₃ [50], TiO₂, CeO₂, Ga₂O₃ [51], etc.. These possibilities were the starting point for the fabrication of gas sensors developed in this PhD thesis dissertation.

Working with MOX as sensing material has several advantages, such as simplicity in device configuration (especially for chemoresistors) and relatively high reliability, low cost of fabrication, robustness, long operating time and reasonable baseline drift, even in the presence of corrosive gases or when aging occurs, as well as the fact that the sensors respond to a wide variety of gases. However, the sensors generally lack selectivity, require the development of practical integration methodologies, use considerable electrical power to operate and require long stabilization times [40].

The electronic-nose configuration (e-nose) appeared to solve the lack of selectivity of the gas sensors, employing them as an olfactory system in a smell assessment instrument, mimicking the human nose but trying to overcome its natural limitations, like non-quantified results, tiring or subjectivity [52]. To promote this technology, MOX-based gas sensors became ideal candidates in areas such as food and automobile industry or indoor and environmental air monitoring. An e-nose is, according to the accepted definition, *a device that comprises an array of heterogeneous gas sensors and a pattern recognition system* [53]. The heterogeneity can arise either from a combination of different types of sensors, different materials or the same material operating at different conditions, generally, at different temperatures. Nowadays, several e-noses are commercially available in the market (i-Pen, PEN2, QCS, Artinose, FF2, Prometheus, Aromascan A32S, Cyranose 320, etc. [52]), mainly based on metal oxide semiconducting materials, for generic purposes and suitable for a broad range of applications. The e-nose field is still unripe, but with time it could become the strategy to overcome the selectivity problem of most of the gas sensors, being able to discriminate among different gases in a complex atmosphere.

To fabricate MOX-based gas sensors, the general procedure includes the synthesis of the MOX sensing material on a specific substrate, followed by the transfer and integration of this material in the final architecture of the sensing device. The implementation of this procedure occurs with different difficulties due to the various technological steps required. To reduce the fabrication steps, the site-selective growth and in-situ integration of the sensing material in the final device has been proposed in some recent works of our research group [54]. This strategy joins the material fabrication and the integration in the final device and, consequently, reduces the technological steps involved in the whole process, increasing its robustness and decreasing the expected cost per unit, shading some light to the lack of practical methodologies for material integration.

From all this it is clear that a breakthrough could be achieved in the new generation of MOX-based gas sensor prototypes by combining the different mentioned strategies in a single system: using NWs to enhance the sensitivity of the sensors, simplifying the fabrication, increasing the robustness and reducing the cost by employing the site-selective growth and in-situ integration of NWs and increasing the selectivity via the e-nose configuration.

1.2 Gas solid interactions

The basic processes occurring at the surface of MOX sensing materials, involving chemical and physical reactions that are later transduced into an electrical signal and used to monitor the presence of different gas species around the sensor, are described in this section. The first part presents the different types of categorized adsorption situations that can take place between a gas atom or molecule and the surface of a solid material. Next, a general description of the adsorption processes occurring is presented and discussed. Finally, the events that lead to the conductance variations measured in gas sensing are described.

1.2.1 Physisorption and chemisorption

The adsorption process is the first step of the gas sensing mechanism. By definition, adsorption is an increase in the concentration of a dissolved substance at the interface between condensed and gaseous phases due to the effect of surface forces. To study the adhesion of a gas molecules (adsorbate) on a solid surface (adsorbent), the Hertz-Knudsen equation can be used as a mathematical description of the flux of molecules (ϕ_i) reaching a surface [55]:

$$\phi_i = \frac{p}{(2\pi mk_B T)^{1/2}} \quad (1)$$

where p denotes the pressure, m is the mass of the molecule, k_B , the Boltzmann constant and T , the temperature. This equation shows that the gas molecules adsorption on an adsorbent is a process highly dependent on the temperature, pressure and adsorbate mass. In addition, and not in appearing in *Equation 1* as they show complex dependencies, material [56], structure [57] and surface chemical states [58] are demonstrated to strongly

affect the adsorption. This gives rise to non-linear dependencies of adsorption with these latter parameters, which makes it difficult to understand and model the gas molecule adsorption processes. After being adsorbed, the adsorbate can be desorbed, a process that typically requires energy to occur, because the adsorption brings the adsorbate to a state of lower energy. Desorption is defined as the reverse process to adsorption and can be, for example, thermally promoted. The basic principle of the MOX-based gas sensors is the measurement of an electrical signal as a result of the charge carrier transfer between the MOX and the adsorbed and/or desorbed gas molecules. When a steady state between adsorption and desorption is achieved, the electrical signal to this particular gas mixture is constant.

In general, two types of adsorption situations are considered: physical or chemical, called physisorption and chemisorption, respectively. Usually, the difference between physisorption and chemisorption lies in the forces retaining the adsorbate on the adsorbent, inducing or not a chemical bonding arrangement and a charge transfer. In the case of physisorption, all the gas species in the surroundings of the material tend to be adsorbed as the result of Van der Waal forces: London, Debye and/or Keesom. In general, the process is reversible, non-dissociative, the adsorbate remains unmodified and occurs at temperatures close to the boiling point of the adsorbate [59]. At higher temperatures the chemisorption, occurring with charge transfer between the adsorbate and the surface of the material, dominates. However, it is not clear which is the exact limit of charge transfer or energy involved to distinguish between chemical and physical adsorption [59], which makes the line separating both phenomena a controversial issue. Additionally, there could exist intermediate states, as for example, some authors propose to differentiate between strong and weak chemisorption [59].

It is generally accepted that the physisorption can be described as a combination of potential energies from the long-range attractive polarization potential and the Pauli repulsion for electrons, binding an atom or a molecule to a solid surface [60,61]. Lennard-Jones proposed a simple formula to depict both interactions by a unique potential [62]:

$$V_{phys}(r) = 4\varepsilon \left[\left(\frac{\sigma}{r}\right)^{12} - \left(\frac{\sigma}{r}\right)^6 \right] \quad (2)$$

where ε is the depth of the potential, σ , the distance at which the potential is zero and r , the distance from the surface. Thus, Van der Waals forces induce a long-range

interaction that, independently of the gas specie, attracts the adsorbate to minimize its energy at a distance of $r > 0.3$ nm, involving few hundreds of meV [63]. The small energy involved in this process makes the adsorbate molecules easily mobile on the surface and, thus, can be rapidly desorbed.

In the case of chemisorption, there is a reorganization of the electrons from the adsorbate and from the solid adsorbent. During the adsorption process, the energies involved are of the order of the chemical bonds of the gas molecule, which can lead to the formation of new bonds and breaking of existing ones. The process is dissociative (the molecules break down into smaller molecules or individual atoms), can be localized in a specific site and is irreversible for some molecules [63]. In addition, chemisorption is not as temperature restricted as physisorption. However, its relevant effects for gas sensing purposes are related to a specific range of temperatures. At low temperatures the mechanism barely occurs, being extremely slow in contrast to physisorption, which dominates. In general definitions, the equilibrium distance for chemisorption is usually found to be between 0.1 and 0.3 nm [64] and the energy involved in chemisorption processes are around several eV. Even though there exist some key points that are different for physisorption and chemisorption, there is not a clear barrier that separates them in temperature or pressure.

For chemisorption, the potential energy can be mathematically described using the Lennard-Jones, the Morse or the Buckingham potentials [64]. The Lennard-Jones

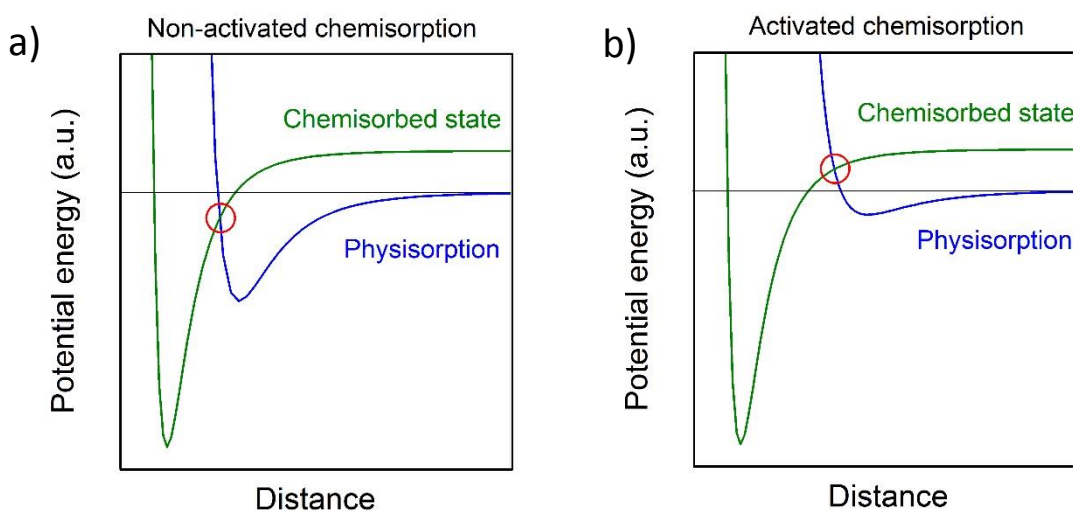


Figure 3: Potential energy in a) a non-activated chemisorption and b) an activated chemisorption process. The activated chemisorption requires additional energy of the adsorbate in order to pass from the physisorbed to the chemisorbed state.

potential is represented as a function of the distance from the surface of the solid material in *Figure 3 a)* and *b)* for a non-activated and an activated process, respectively. The difference between both lies in whether the crossing point of the physisorption and chemisorption potential energies occurs at a positive or negative energy value. When a gas molecule or atom approaches the surface, it first experiences the Van der Waals interaction, like in a physisorption process. As it comes closer to the surface, the chemisorption potential starts to become important.

In a non-activated chemisorption situation, the adsorbate can reach the chemisorbed state almost straightforward, without activation energy. For the activated chemisorption, the meeting point of potentials occurs at positive energies. As a consequence, if the molecule or atom has enough energy when approaching the surface, the gas specie will overcome this energy barrier and adopt its lower energy state, following the chemisorption potential curve.

For chemisorption, the activation energy can be understood to represent the energy necessary for the dissociation of a molecule, which can be described as an Arrhenius-like process [65] and, thus, temperature dependant:

$$k_p = Ae^{-E_p/k_B T} \quad (3)$$

where k_p denotes the reaction rate constant, A is the pre-exponential factor, E_p , the activation energy of the process, k_B , the Boltzmann constant and T , the temperature. *Equation 3* applies both to activated and non-activated processes. Desorption is also a process that requires to overcome an energy barrier to occur. For this reason, the activation energy E_p can be referred to E_{ads} or E_{des} , depending on whether the study is focused on adsorption or desorption.

Summarizing the adsorption and desorption events that can occur when a gas molecule interacts with a clean solid surface could be:

1. The gas molecule is elastically scattered without any loss of energy, giving rise to no adsorption or desorption.
2. The gas molecule is inelastically scattered: being physisorbed, when impinging with low energies, or chemisorbed, for high enough energies.

3. If the gas molecule is physisorbed, it can be later (a) desorbed, being scattered back to the gas phase, (b) diffused to a neighbour site or (c) chemisorbed.
4. If the gas molecule is chemisorbed it can afterwards (a) release chemical energy to the solid and become localized at the adsorption site, (b) lose chemical energy and dissipate the excess of energy by diffusion or (c) be desorbed.

The main differences between physisorption and chemisorption can be summarized as follow:

| <i>Physisorption</i> | <i>Chemisorption</i> |
|---------------------------------|------------------------------------|
| Weak and long-range interaction | Strong and short-range interaction |
| No surface reaction | Surface reactions |
| Non-site specific | Site localized |
| Energy range: meV | Energy range: eV |

Table 2: Comparison between the main characteristics of physisorption and chemisorption.

1.2.2 Adsorption isotherms

The statistical description of the adsorption processes occurring on a solid surface of a monoatomic gas at a constant temperature is a problem described by several models, called *adsorption isotherms*. The study of the different adsorption mechanisms is key to understand the processes occurring at the surface of the studied sensing materials. These adsorption processes can be interpreted using various isotherm models, such as the Langmuir [59], Freundlich [66] or Brunauer, Emmett and Teller (BET) [67] isotherms. The isotherms help to understand the interaction between the solid surface and the gas molecules in a steady state of adsorption, shading light to the dynamics of the system. The adsorption isotherms reveal the amount of gas molecules adsorbed on a solid surface given certain conditions of pressure and temperature.

The Langmuir isotherm is a simple and ideal model that is based on several assumptions:

1. There is only monolayer adsorption
2. There are limited adsorption sites
3. All sites have the same adsorption probability
4. There is no interaction between adsorbed molecules

With these assumptions, the Langmuir isotherm equation can be derived from gas kinetics theory [59], describing the adsorption and desorption ratio in the steady state, as:

$$\theta = \frac{bP_x}{1+bP_x} \quad (4)$$

where P_x is the adsorbate partial pressure, b is a parameter that depends on the adsorbate, the adsorbent and the temperature, and θ is the normalized surface coverage. The latter is the ratio between the adsorbed molecules (N) and the total number of available sites (N^*):

$$\theta = \frac{N}{N^*} \quad (5)$$

In more detail, the parameter b in *Equation 4* is defined as:

$$b = \frac{sk_0}{v\sqrt{2\pi mk_B T}} e^{\left(\frac{Q}{k_B T}\right)} \quad (6)$$

where s is the effective surface area, k_0 is the sticking probability, v , the oscillation frequency of adsorbed molecules, Q , the adsorption heat ($Q = E_{des} - E_{abs}$) and m is the mass of a single molecule. The effective surface area is defined as a geometrical controlling factor for a chemical reaction. It is not uniquely determined for every specific material, but it also depends on the type of chemical reaction, the state of agglomeration and on the compactness of the agglomerates.

This model defines isotherm type I, shown in *Figure 4*, suitable for ultraclean, well-ordered surfaces interacting with small-molecule adsorbates, but oversimplified to

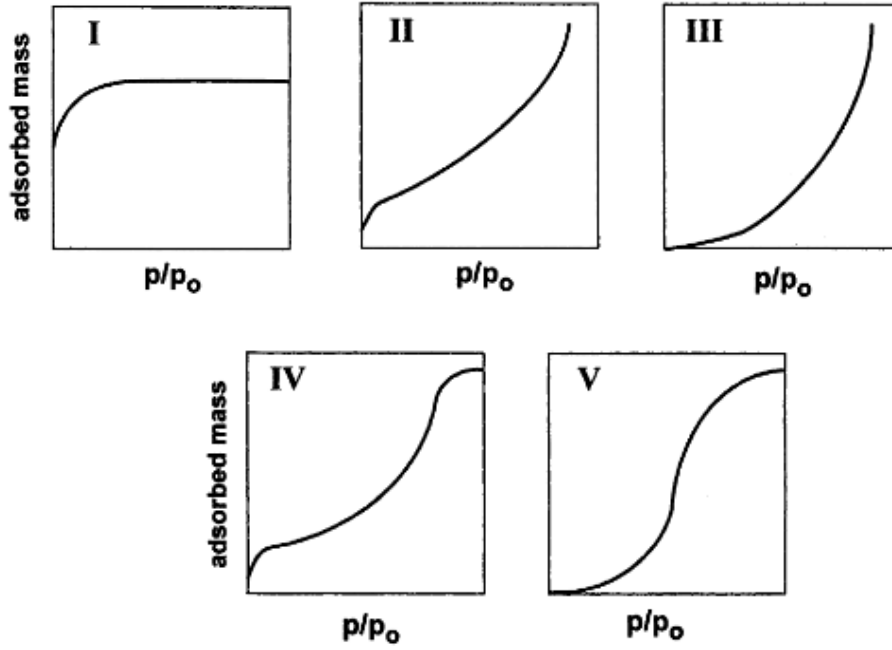


Figure 4: Classification of typical adsorption isotherms (I-V) showing vapor adsorption as a function of relative pressure p/p_0 (reprinted from Ref. [66]).

correctly describe real-world scenarios [67]. From this isotherm, it can be observed that at low pressures the coverage is proportional to the equilibrium pressure of the gas, while at high pressures, it tends asymptotically to 1. Apart from offering a first approach to understand the adsorption process, this model is the basis of most of the adsorption theory. Other adsorption models treat the first adsorbed monolayer as described by the Langmuir model, adding further terms to describe the adsorption of subsequent layers. Furthermore, the surface coverage can be also related to the sensor response in a complicated manner [69]:

$$S \propto \theta(P, T) \quad (7)$$

The BET isotherms establish different relations between the equilibrium and saturation pressures, p and p_0 respectively, and the adsorbate surface coverage, extending the Langmuir theory to multilayer adsorption. Such surface coverage can be determined from following relation [67,69]:

$$\theta(P, T) = \frac{p/p_0}{1-p/p_0} \frac{b_{BET}(T)}{[1+p/p_0(b_{BET}(T)-1)]} \quad (8)$$

where $b_{BET}(T)$ stands for the BET constant:

$$b_{BET}(T) = \exp\left[\frac{\varepsilon_1 - \varepsilon_{lf}}{k_B T}\right] \quad (9)$$

and where ε_1 and ε_{lf} are two energy parameters that measure the strength of adsorption of the first monolayer at the surface and in each following monolayer of adsorbate, respectively. Multilayer adsorption can occur when $\varepsilon_1 > \varepsilon_{lf}$. Isotherm type II and III can be modeled using the BET equation. The difference in the shape between these two isotherms results from the differences in the strength of the adsorbate-adsorbent interaction [67]. Isotherms types IV and V are characteristic of adsorption processes on mesoporous solids via multilayer adsorption, followed by capillary condensation. They can be described using a combination of the BET model and a second model that accounts for capillary condensation in small pores or capillaries [67] or with special treatments on BET theory [70]. Isotherm type IV is an intermediate case between I and III, where the adsorbed number of molecules per site is finite. Isotherm type V is similar to type II and the difference comes from the processes followed at low pressures after adsorption: in the isotherm type V case multianchorage occurs and, while for isotherm type II, a dimerization process takes place. Type V is typically obtained in carbon-based materials interacting with water vapor [71,72].

To model even more realistic situations, in addition to the postulates of the Langmuir model, the assumption of molecule dissociation can be made. This approach, the so-called dissociative Langmuir model, is satisfactorily used to describe the adsorption process of dissociated oxygen atoms at MOX surfaces [73]. The model assumes that the gas molecule is formed by m atoms and that it dissociates into n parts as a result of the adsorption. Assuming only a dissociation into 2 parts (order 2), the formula for the surface coverage results in:

$$\theta = \frac{(bP_x)^{1/2}}{1+(bP_x)^{1/2}} \quad (10)$$

This equation can be used for the theoretical study of semiconductor gas sensors. Via numerical simulations, the response of the sensor towards individual gas species can be quantitatively modeled, studying the effects of parameters such as the operating temperature or the doping level on the sensor response. It is worth to mention that the Freundlich isotherm [74], proposed as an empirical relation before the appearance of the

Langmuir model, can also be used for semiconducting gas sensors, and is formulated as follows:

$$\theta = aP_x^{1/n} \quad (11)$$

where n is a constant value always < 1 . The particularity of the Freundlich model is that it assumes an exponential decay in the heat of adsorption with increasing coverage that the Langmuir model does not account for [67], which results in a better fitting to a real-world scenario.

1.2.3 Chemoresistive gas sensors

This section is devoted to the mechanisms that, after the adsorption of a gas atom or molecule at the surface of a solid semiconducting MOX, produce the variations in the sensor signal due to charge transfer between the gas species and the sensing material.

When a gas molecule is adsorbed at the surface of a solid, electrons can be captured by this molecule or electrons from the molecule can be transferred to the solid [75,76]. This is possible if the lowest unoccupied orbital of the molecule is located below the Fermi level of the solid (acceptor levels) or if the highest occupied orbital from the adsorbate is above the Fermi level of the solid (donor levels). When one of these two situations occur, a net charge is fixed at the surface of the solid, giving rise to an electric

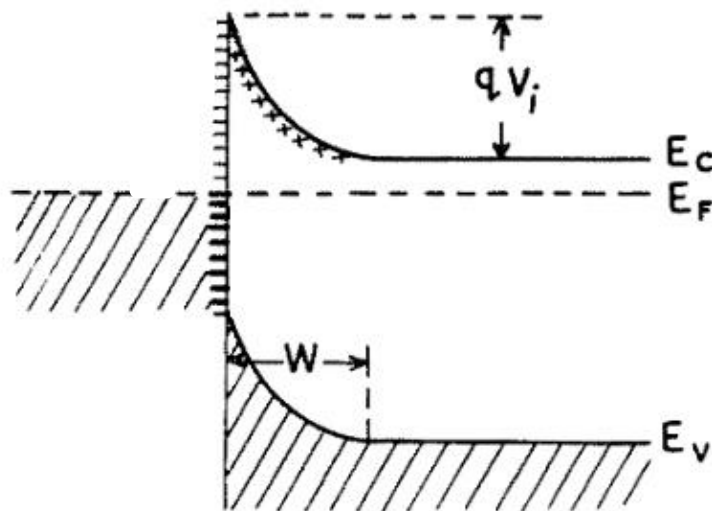


Figure 5: Energy band diagram of an n-type metal oxide semiconductor, where an adsorbate at the surface creates an acceptor level, which produces an upward band bending (adapted from Ref. [79]).

field inside the semiconductors, that causes energy band bending in the material. For example, if the semiconductor donates one electron to the adsorbed molecule, this gives rise to the accumulation of negative charge at the surface, as shown in *Figure 5*, and produces an upward bending of the band diagram close to the surface. Assuming a n-type semiconductor with a Fermi level within the bandgap and close to the conduction band, the band bending produces a reduction of the majority charge carrier density (electrons) and close to the surface and gives rise to an electron depletion layer, which contains fixed positive charge that compensates the negative surface charge at the surface. The change in the density of charge carriers at the depletion layer produces conductivity variations in the semiconductor, leading to a resistance change, in this example, a reduction. The conductivity variation can be described as:

$$\Delta\sigma = e[\mu_n \int n(z) - n_{bulk} dz + \mu_p \int p(z) - p_{bulk} dz] \quad (12)$$

where n states for the density of electrons, p , for that of holes and μ_n and μ_p are the electron and hole mobilities, respectively.

Combining the chemical adsorption formalism and the semiconductor physics calculations, the so-called power law for the resistance of a semiconducting gas sensors is proposed:

$$R = aP^n \quad (13)$$

where a is a constant and the value of n depends on the morphology, the bulk properties of the sensing material and the dissociation mechanism. The relation described in *Equation 13* is supported by experiments [77]. Regarding the geometry of the sensing material, it is worth mentioning that it acquires special relevance, since, theoretically, the full depletion of the semiconductor metal oxide could be reached. This fact is expected to greatly enhance the response of the sensors. From these observations, it is evident that the surface-to-volume ratio and geometry of the sensing material are important factors influencing the conductivity and, consequently, the response of the sensor.

Regarding the crystallinity of the sensing material, polycrystalline materials present different behavior than their monocrystalline counterparts, for which only the surface is supposed to be contributing to the gas sensing properties. The presence of grain boundaries in polycrystalline materials produces multiple Schottky barriers and, according to the previous reasoning, different space charge region depletions are induced

between the individual grains, thus, contributing to the change in the resistance of the material and modifying the effect of the adsorbed gas molecules in an uncontrolled manner. Furthermore, it is expected that the diffusion of the adsorbed molecules along the surface of a polycrystalline material is slower than in a monocrystalline material and, therefore, the response time of the final devices is generally longer. At the junction of the semiconductor and the metal electrodes, commonly used to contact the sensing materials, also a Schottky barrier may be found. When gas adsorption takes place, the height of this barrier may be modified, producing resistance variations in the sensing device. A sketch of these processes is depicted in *Figure 6*.

The response of the sensors towards the different adsorbing species is defined in this work as the relative change in the sensor's resistance, irrespective from oxidizing or reducing gases or p- or n-type semiconductors, as:

$$S = \text{Response (\%)} = \frac{|R_{air} - R_{gas}|}{R_{air}} \quad (14)$$

The sensor's response time (τ_{resp}) is here defined as the time span between 10 and 90 % of the steady state resistance after the exposure of a certain constant gaseous concentration. In a similar way, the recovery time (τ_{rec}) is the time span between the gas

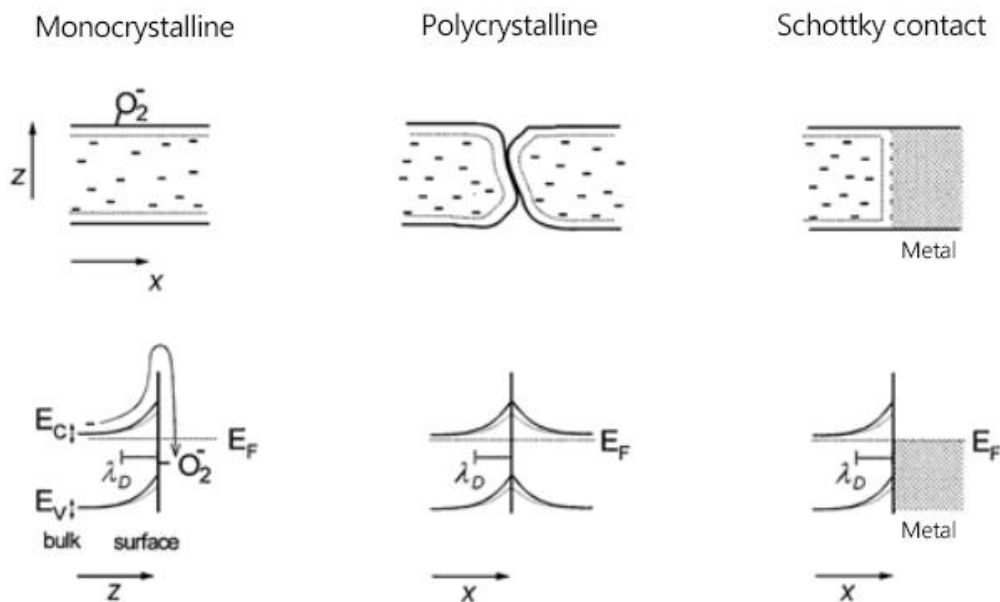


Figure 6: Energy band diagrams of three different scenarios where the adsorption of gas leads to band bending, affecting the conductivity of the semiconductor material: monocrystalline, polycrystalline material, which is represented by a grain boundary, and a Schottky contact, formed by the junction of a metal and a semiconductor (adapted from Ref. [76]).

stimulus is interrupted and the resistance changes from the 10 to the 90 % of the interval between the steady state and the base resistances.

1.2.4 Two-probe measurements with individual nanowires

For a precise determination of the free charge carriers in the semiconducting material, the use of four electrical contacts to the material is the preferred configuration, as it allows performing four-probe measurements, which allows minimizing the contact resistance between the metal and the semiconductor. However, to simplify the electrical circuits required for the device readout and to decrease the time and cost of fabrication, two contacts are generally used. Using this configuration, in direct current measurements, the voltage drop measured when applying a fixed current is the sum of the contributions of the voltage drop at the resistance corresponding to the NW (R_{NW}) and that corresponding to the contacts or the Schottky interface (R_{SI}). The overall resistance measure, R , is given by:

$$R = R_{NW} + R_{SI} \quad (15)$$

It is important to know which is the relative contribution of each of these 2 terms, because it is difficult to discriminate which is the one that changes most in the presence of gas in the sensor's environment. It is well-known that a Schottky barrier is fabricated when depositing Pt contacts to a MOX NW, due to the difference in the metal work function and the electron affinity of the semiconducting NW [78-80]. A Schottky barrier acts as a potential barrier at the interface between both materials. This effect can be observed as a nonlinear behavior in the current-voltage (I-V) characteristics when measuring at room temperature and can be explained interpreting the system as a two back-to-back Schottky barriers connected in series at the ends of the NW [78]. In the present work, however, the experimental conditions are such that the contribution of the Schottky barrier in the total resistance is low and, thus, we will be measuring mostly the contribution of the NWs.

1.3 Chemical vapor deposition

1.3.1 Vapor-liquid-solid mechanisms

Whiskers, the first name that the NWs received when they were first reported, were observed in natural ores in 1500s. The concept of growth is commonly used to describe the formation of whiskers or NWs. This concept was adopted in 1600s because the silver whiskers from the rocks seemed to grow like grass [81]. In the 1950s, intensive research in the Bell Telephone Laboratories led to the growth of whiskers of several materials including B, B₄C, Al₂O₃, SiC, and Si₃N₄ [81]. The main objective of these studies was a reinforcement additive to be introduced in metals and plastics.

In the mid 1960's, Wagner and Ellis from the Bell Laboratories, first proposed the vapor-liquid-solid (VLS) mechanism in a series of publications [82-84] focused on silicon whiskers growth. These publications elucidated how the whiskers growth proceeded, stating, among other things, that: (a) an impurity is essential for whisker growth and (b) a small globule is present at the tip of the whisker during the growth [82]. Nowadays, the "impurity" is commonly known as catalyst in the NW literature (possibly a misleading term in this context) and the globule is used as the logical demonstration of the occurrence of the VLS mechanism.

In the VLS mechanism it is proposed, as initial scenario, that the catalyst forms a liquid alloy droplet with the substrates, while the material that will later form the whisker

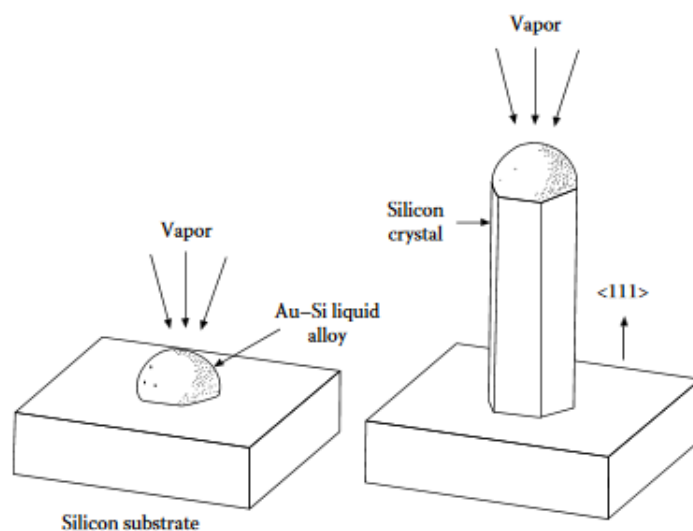


Figure 7: Schematic illustration of the VLS mechanism as proposed by R.S. Wagner (reprinted from Ref. [82]).

is in the gas phase. This situation transforms the catalyst into the preferred deposition site for the vapor phase material on the substrate, as shown in *Figure 7* from ref. [83]. The next step occurs at the vapor-liquid interface, where material from the vapor phase is transferred directly into the liquid droplet. This ends up causing the supersaturation of the liquid alloy droplet and the precipitation of material at the liquid-solid interface [83]. At the correct temperature and pressure, this produces a precipitation in solid form whose growth is guided by the catalyst.

It is clear that the catalyst plays a key role in the VLS mechanism and there is a list of criteria that should be considered at the moment of its choice [85]:

1. It must form an alloy or liquid solution with the crystalline material that is attempted to be grown.
2. The distribution coefficient of the catalyst, defined as $K_d = C_s/C_l$, must be less than 1 (where C_s and C_l are the solubilities in the solid and liquid phases, respectively).
3. The equilibrium vapor pressure of the catalyst around the liquid alloy must be small, since evaporation would otherwise change the droplet volume, leading to changes in whisker size during the process.
4. The catalyst must be inert to the byproducts of the chemical reactions that generates the vapor source.
5. The interfacial energies of vapor-solid, vapor-liquid, and liquid-solid systems and the resulting wetting characteristics determine the shape of the growing crystal. A large contact angle is necessary for the formation of whiskers.
6. In growing whiskers of compound materials, the catalyst can be the excess of one of the materials to be grown.
7. The choice of the catalyst and the growth temperature must avoid the formation of an intermediate solid phase constituted by the catalyst and one of the vapor phase materials.
8. To obtain unidirectional growth, the solid-liquid interface must have well-defined crystallographic features.

The importance of the catalyst arises also from the fact that the droplet beads control the diameter and morphology of the grown material. Wagner suggested that there

is a minimum diameter determined by the stability of a liquid droplet in its own vapor [85]:

$$r_{min} = \frac{2\sigma_{LV}V_L}{RT\ln\sigma} \quad (16)$$

where r_{min} is referred to the minimum critical radius of a whisker, σ_{LV} , the liquid-vapor interfacial energy, V_L , the liquid molar volume, R , is the ideal gas constant, T , the temperature, \ln is the napierian logarithm and σ the degree of saturation, given by:

$$\sigma = \frac{P - P_{eq}}{P_{eq}} \quad (17)$$

where P and P_{eq} , are the actual and the equilibrium vapor pressures, respectively. These expressions, that can be used as a general guideline, link the growth conditions and intrinsic properties of the studied materials to the final whisker morphology. Wagner, and later Givargizov, gave large evidence that the growth temperature determines the growth rate, diameter and stability of the whiskers. In the studies of Givargizov one can find the fitting of his data to growth rate, that gave rise to the following expression [86]:

$$V = b \frac{(\Delta\mu)^2}{kT} \quad (18)$$

where V is the growth rate, $\Delta\mu$ is the effective chemical potential and b is a constant. Apart from the growth rate, the temperature also affects the stability of the whiskers [85,86]. The instability during the growth leads to defects in the whisker, such as branches or kinks. These instabilities can be attributed to high temperature gradients or unstable temperatures and may be amplified by high concentrations of the source vapor [85].

The pioneering contributions on whiskers research mentioned in this section, which mainly focused on silicon, lead the trend to the NW investigation. Once it was understood that thin films induce uniform catalyst diameters and that much thinner films yield nanosized structures, Westwater et al., in 1995, published the first discussion about whiskers at the nanoscale [87], using a 5 nm thick Au film. Since then, a fruitful period of NW publications emerged, giving rise to studies of NW growth of a broad variety of inorganic materials. In this thesis, NWs of In_2O_3 , Ga_2O_3 , SnO_2 and Ge have been grown by means of VLS for their application in gas sensor and e-nose prototypes.

1.3.2 Chemical vapor deposition

VLS may be carried out by different techniques, such as chemical vapor deposition (CVD), laser ablation (LA) or molecular beam epitaxy (MBE). The most spread technique is CVD, where the precursor material is introduced in gas phase or evaporates from a solid powder or liquid solution, decomposing at a controlled temperature and pressure [85,86]. It is hard to achieve a proper control by this technique due to the high variability of deposition parameters and wide ranges of gas partial pressures and temperatures that may be covered. However, these drawbacks can be overcome with a meticulous tracking of the experimental conditions and by keeping fixed certain parameters in each performed experiment. Moreover, the CVD technique is considerably cheaper and simpler in comparison to other techniques reported to promote the VLS process [85].

The properties of the NWs grown via VLS are largely dependent on their size, morphology, defects, etc.. These features can be controlled by a rational design and careful tuning of the growing conditions of the CVD process. Therefore, it is important to understand the general aspects and parameters influencing a CVD growth, that can be listed as:

1. *Precursor*: the reactant that will be converted into the desired product is involved in three reactions: thermal decomposition, chemical transport and chemical synthesis [88]. The amount, purity and composition of the precursor material influences the morphology, growth rate, optical properties and gas sensing behavior of the grown material [89,90].
2. *Temperature*: this parameter can affect several features of the CVD system, such as the chemical reactions of precursors in gas phase, the growth rate, the diameter and the crystalline quality of the grown NWs [91,92]. This suggests that the temperature can be used to tune the uniformity, morphology, composition and crystallinity of the grown material. With the use of relatively high temperatures, high crystalline quality NWs can be obtained [90-92].
3. *Substrate*: this is the support for deposition or growth in a CVD process. In addition, the substrates themselves can be used as catalyst for the growth process,

e.g., for the Si whiskers or NW growth reported in [83,93] or the catalytic active nickel substrates used for carbon nanotube growth [93]. More concretely, the crystalline quality and lattice structure of the substrate can affect the growth of the material [88] changing its structural, morphological, optical and electronic properties [93,94]. Besides, the orientation of the substrate can determine the morphology, the growth direction and, depending on the material, the epitaxial relationship of the as-grown material to the substrate [88,94,95]. Finally, the substrate preparation and surface termination are also relevant and impact the final morphology of the synthesized material [95].

4. *Pressure*: most of the CVD systems can be tuned from ambient pressure down to few millitorr, which can change completely the gas flow behavior [88] and the gas phase precursor transport. When growing nanostructured material, in addition to the total pressure inside the CVD reaction system, the growth velocity is influenced by the partial pressures of the precursors in gas phase. In specific regimes, the partial pressure of one of the components can be linearly related to the growth rate of the fabricated material [89], while in other regimes undesired reactions can occur, which will give rise to other growth mechanisms, such as vapor-solid [96].

5. *Catalyst*: this is the material used to promote the local growth inside the CVD system, as in the case of metal-assisted VLS processes for Si NW growth [83,89]. Au is the material of choice in a broad number of experiments due to its availability in different forms (colloids, sputtering targets, evaporation sources). An additional reason to choose this material, for example when fabricating Si NWs using Si substrates, is its binary phase diagram with Si [83,89], shown in *Figure 8*. In comparison to other possible catalyst-precursor combinations, the temperature at which Au-Si form an eutectic group, thus, promoting the VLS mechanism, is lower than with other common metals (Al, Ag, Zn, Ti, Pd...). The Au-Si eutectic group formation temperature decreases about 700 °C and 1050 °C the melting point of pure Au and Si, respectively. Using this material combination, the VLS is promoted at a temperature above at 363 °C (and a composition of about 19 atomic % of Si diluted in Au) [89]. When growing Si NWs, the presence of Si

in the Au drop helps to reach the supersaturation of the liquid alloy droplet and the precipitation of material at the liquid-solid interface. For the growth experiments of In_2O_3 and Ga_2O_3 NWs performed in this thesis, Au is used as catalyst to support the VLS growth, and Si and SiO_2 have been tested as substrates. More dense and longer NWs are grown when SiO_2 is used as substrate, a fact that is also reported in literature [95].

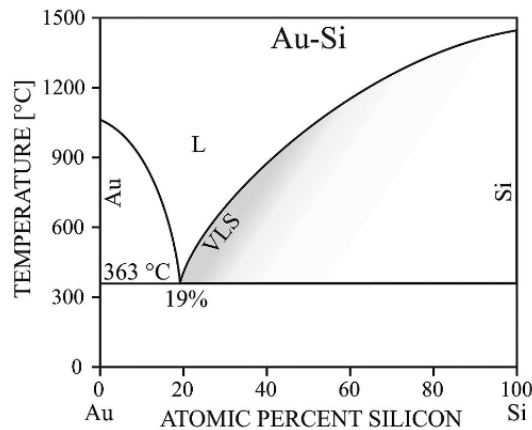


Figure 8: Binary phase diagram of Au-Si (reprinted from Ref. [90]).

A typical CVD setup consists in a horizontal tube furnace connected to a gas injection system, and pressure gauge with or without control, via a mechanical pump. *Figure 9 a)* shows a schematic design of a CVD system. The furnace may have one or more heating zones. The control of more than one zone allows to establish varying temperatures in the different zones, for example, one for the vapor source generation and another for the growth or deposition zone, schematically represented in *Figure 9 b)*. The experiments are typically performed at low pressure (from 1 to 100 Torr), which can help to reduce the oxygen contamination whenever this is critical [85,97]. If the source material needs to be heated so that evaporates, it is placed inside the furnace tube in an alumina crucible. Alumina is the main choice due to its high melting point, good chemical stability, and hardness. These properties allow alumina crucibles to resist perfectly high temperatures and chemical corrosion, to which they are exposed during the growth processes. The tube furnace heats up the precursor material through conduction, radiation and gas convection [85]. Alternatively, the source material can also be heated by Joule effect of the crucible or, if the source material is already in gas phase, the resistive heating can be just applied to heat the tube and substrates.

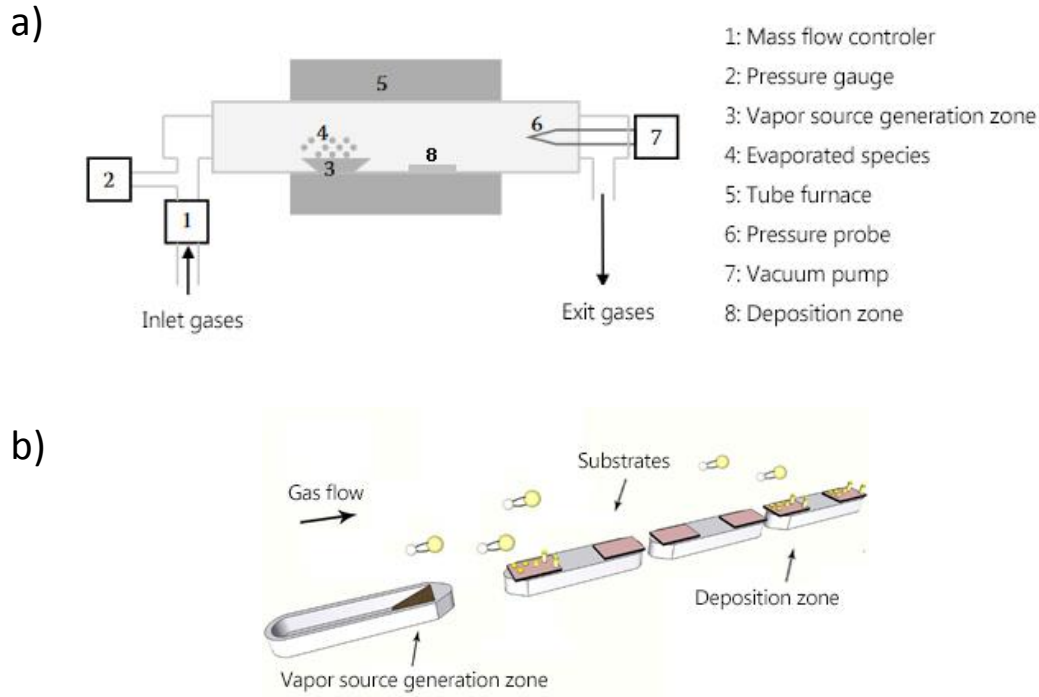


Figure 9: Schematic representation of a) a typical chemical vapor deposition system used for nanowire growth (adapted from Ref. [85]) and b) alumina boats, substrates and precursor layout inside the chemical vapor deposition system (adapted from Ref. [97]).

To achieve controlled NW growth using a CVD system, it is important to purge or even bake the reactor before the beginning of each experiment to remove adsorbed gases from the tube walls and to reduce residual oxygen partial pressure, minimizing the possible contamination. When the precursor is evaporated inside the furnace and already in the gas phase, it is transported along the furnace tube using a carrier gas, typically inert, such as Ar or N₂. To transform the precursor into gas phase several procedures can be followed, such as thermal evaporation or by mixing the solid precursor vapors with other feeding gases to react into the desired final product. The main requirement is to maintain the precursor at temperature and pressure conditions close to its melting, decomposition or sublimation point to produce adequate vapor pressure [54,85,97]. Typically, the substrates are placed downstream, where the temperature is generally lower, and NWs can be collected near the end of the tube furnace [85,97]. Due to the possibility to create this cooler region for deposition, furnace equipped with more than one heating zone are preferred.

1.3.3 Carbothermal reduction

Using a CVD system, substrates coated with a thin layer of catalyst (a suitable metal or MOX precursor), a wide variety of MOX NWs can be grown by adjusting the temperature and pressure conditions of the growth process. The catalyst deposition onto the substrates is done either by sputtering or evaporation of thin layers (<10 nm thick) [85] but can also be achieved by dispersing colloidal nanoparticles. This thesis is focused on the use of solid precursors for the MOX growth.

Solid MOX as precursor material generally requires that it is heated at high temperatures to generate enough vapors and this might be incompatible with the distance and required (lower) temperature needed for achieving the NW growth on the substrates. A way to circumvent this problem consists in mixing graphite with the MOX precursor material to obtain vapors at lower temperatures through the so-called carbothermal reduction [98,99]. Carbothermic reactions involve the reduction of the MOX material using carbon sources as reducing agent. Carbothermal reduction of MOX is one of the oldest technologies of the human history, employed to smelt ores [100], obtaining pure

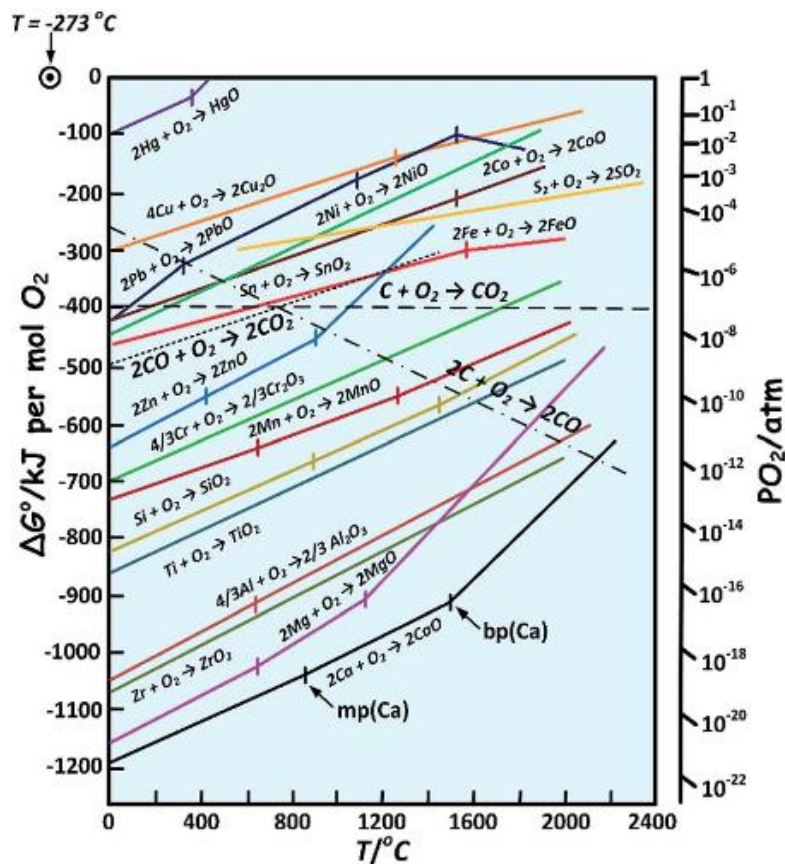
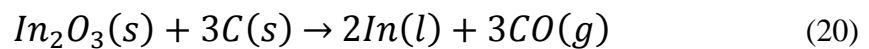
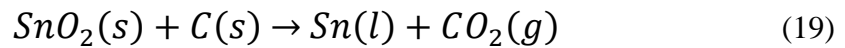


Figure 10: Ellingham diagram for the free energy of the formation of several metal oxides (reprinted from Ref. [99]).

metals like copper, lead, silver, iron, tin and mercury, as well as in some metallurgical processes [100] and to extract oxygen from the lunar regolith [101]. The ability of the metals to participate in carbothermic reactions can be predicted using an Ellingham diagram [98], as shown in *Figure 10*. The diagram presents plots of ΔG (Gibbs free energy variation) for the oxidation of several representative metals and for the oxidation of C to CO, and from CO to CO₂. In a carbothermal reduction two solids (here a metal oxide and carbon) are converted into a new solid (a metal) and a gas (here, CO or CO₂), which takes place when the resulting free energy is negative. In addition to this, to promote the carbothermal reduction, heating is required, otherwise the diffusion of the solids is slow, and the transformation does not take place. In our case, the reduction of the MOX to metal will occur when the resulting ΔG is negative, becoming progressively more feasible at higher temperatures. To clarify the process of carbothermal reduction of graphite when heated, e.g., with SnO₂, which reduces SnO₂ to Sn, the following reactions can be useful [98]:



In *Figure 10* the temperature at which the curves for oxidation of Sn and of C (to CO₂) meet can be read and its value is 629 °C. This indicates that above this temperature, C effectively reduces SnO₂, giving rise to Sn and CO₂. In this temperature range Sn is present in liquid form.

In a similar manner, it is possible to study the reduction capabilities for In₂O₃ and Ga₂O₃ [102] (curves shown in *Figure 11*). For these two compounds, the possible reactions are those indicated in *Equation 20* and the temperatures at which their oxidation curves meet that of C to CO are 760 and 1100 °C, respectively. In the case of In₂O₃, this temperature can be achieved by the employed CVD furnace. However, for the case of Ga₂O₃, the temperature is above the maximum attainable temperature, 1000 °C, which means that the carbothermal reduction method will not be efficient to generate Ga vapors for the growth of the NWs. However, as will be described in the experimental part, NWs have been successfully grown using the carbothermal reduction method.

Another factor that must be considered when growing NWs using graphite to achieve the carbothermal reduction is that the presence of graphite can affect the structure and

composition of the final NW, even promoting the vapor-solid mechanism [104]. Concluding, to grow NWs assisted by carbothermal reduction, the temperature and pressure are critical factors that must be meticulously settled to achieve convenient results.

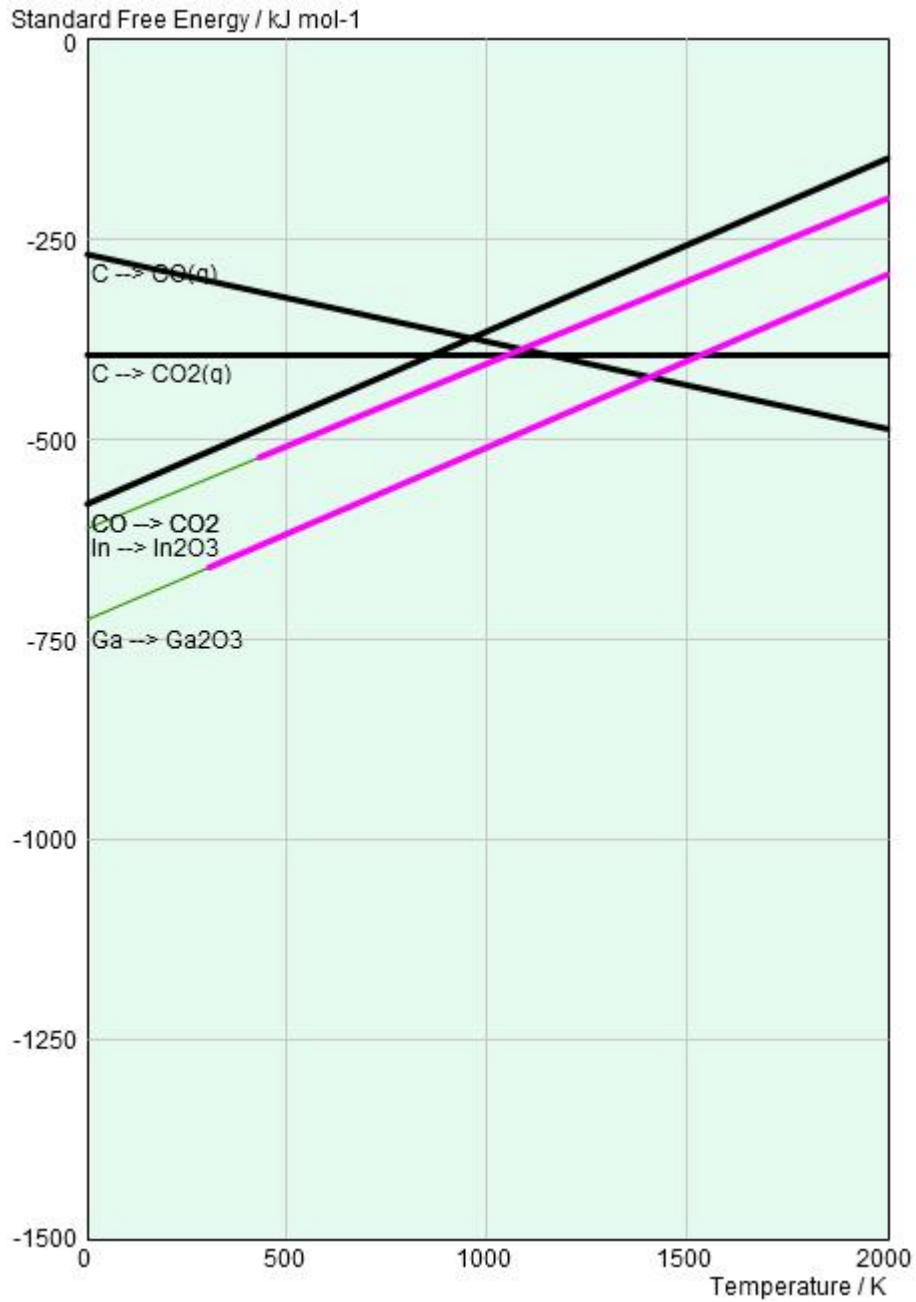


Figure 11: Ellingham diagrams for the free energy of the formation of various metal oxides including a) indium oxide and b) gallium oxide (reprinted from Ref. [103]).

1.4 Integration methodologies

1.4.1 Microhotplates and micromembranes

The substrates used in this thesis to fabricate gas sensors based on NWs, microhotplates (MHP) and micromembranes (MM), are described in this section. MHP and MM are micro-sized thin structures that contain both buried heaters and top electrodes fabricated on silicon wafers. The reduced dimensions of the thermally isolated structures allow to reach temperatures of several hundred degrees °C locally with relatively low power consumptions (in the range of few to tens of mW). Furthermore, the reduced mass of the systems provides a fast-thermal response during both heating and cooling ramps. The main difference between MHP and MM is that the latter are closed microstructures, meaning that the whole border of the MM is attached to the substrate, while MHP are suspended microstructures, i.e., the connection to the substrate is only through a few “arms”. Both MHP and MM used in this thesis have been fabricated at the IMB-CNM (CSIC), using their Clean Room micro and nanofabrication facility. For the fabrication of both MHP and MM, Si_3N_4 and SiO_2 are used due to their low thermal conductivity and low mechanical stress when heated, offering robust and durable structures.

MM are bulk micromachined substrates fabricated on double side polished p-type Si substrates, 300 μm thick. The MM consists of: (a) a layer of 0.3 μm of low pressure chemical vapor deposited Si_3N_4 , deposited on top of the silicon substrate; (b) a meander-shaped micro-heater made from doped polysilicon embedded in the Si_3N_4 layer; (c) a 0.8 μm thick SiO_2 layer, deposited on top of the Si_3N_4 , that acts as electrical isolation to the top; and (d) Ti/Pt electrodes (25 / 150 nm nominal thickness) deposited on top of the SiO_2 layer, providing electrical access to the structures to be measured. The whole thickness of the MM is $\sim 1.1 \mu\text{m}$. The heated area (400 x 400 μm^2) can reach temperatures up to 600 °C with a power consumption of 48 mW under atmospheric pressure in dry air. Each chip contains 4 of these MM.

A MHP, fabricated by surface micromachining, contains: (a) a plasma-enhanced CVD Si_3N_4 layer of 0.3 μm ; (b) a Pt micro-heater embedded in the Si_3N_4 layer; (c) on top of the Si_3N_4 , a 0.8 μm thick SiO_2 is deposited with isolation purposes; and (d) Ti/Pt electrodes (25 / 250 nm nominal thickness) are deposited on top of the SiO_2 layer. The

heated area ($100 \times 100 \mu\text{m}^2$) almost covers the whole MHP and allows to reach temperatures up to $350 \text{ }^\circ\text{C}$ with a power consumption of 6 mW.

1.4.2 Focused electron-ion beam induced deposition techniques

The fabrication of reliable metallic contacts that allow the electrical access to individual NWs, is a complex issue, but possible with the prevailing lithographic techniques. The work developed by the MIND Group of the Departament d'Enginyeries Electrònica i Biomèdica, initiated more than 15 years ago, was pioneer in the field of fabricating reliable nanosized contacts to individual NWs using Dual Beam (DB) systems. The maskless Focused Electron (FEB) and Focused Ion Beam (FIB) Induced Deposition (FEBID and FIBID, respectively) techniques, overviewed in this section, combine in an effective manner the possibility of sample ablation and material deposition in nanosized regions. This is made possible in these DB machines, which combine a Scanning Electron Microscope (SEM) and a Scanning Ion Microscope.

The DB machine is similar to a SEM chamber, where the electron column is placed vertically, while the ion column is tilted 52° with respect to the electron one. The sample holder can be moved in x, y, z, rotated and tilted, granting the possibility to align the sample perpendicular to any of the two beams, at user's convenience. Both electron and ion columns consist of a source of electrons or ions, respectively, that are extracted, accelerated and focused towards the sample by means of electromagnetic or electrostatic lenses, respectively. Typically, the ions used are Ga^+ and can be accelerated at voltages from 1 to 30 kV, while the electrons can be accelerated at voltages from 0.1 to 30 kV.

The metalorganic precursor employed for the deposition of Pt is the trimethylmethylcyclopentadienylplatinum $[(\text{CH}_3)_3(\text{CH}_3\text{C}_5\text{H}_4)\text{Pt}]$ [105]. This precursor allows Pt deposition using FEBID or FIBID, even though, not at the same rate or speed. This is due to the higher efficiency of the ion beam to produce the secondary electrons required for the decomposition of the precursor. In both FEBID or FIBID processes the result is a matrix of C with Pt nanoparticle inclusions of 3 to 10 nm [105]. In the depositions performed in our research group [106], Pt represents less than 27 % in volume of the deposited material, C is always present in concentrations $> 65 \%$ in volume, and Ga is present, when the ion column is used, in a noticeable amount of about 8 %. The resistivity

of the final deposits can be several orders of magnitude higher than the bulk Pt [105,106] due to the high C content. The amount of C content is reported to be higher in the first layers over an insulating surface [105]. This is interpreted to be caused by varying effective substrate, or by a heating effect. At the same time, the use of FIBID reduces the amount of C incorporated onto the deposit [106], and introduces Ga, which is believed to be responsible for the much lower resistivity than with FEBID deposits

Using the ion gun, material from the surface of the bombarded sample will be removed due to the well-known sputtering effect of ions. Apart from milling, the Ga⁺ ions penetrate the sample and are implanted. Both processes take always place when using FIBID techniques or when imaging using the ion beam, even at low acceleration voltages. Thus, a FIBID process always produces damage: removing material and implanting ions in the sample, which damages the crystalline structure of the metal oxides and which can introduce doping. For this reason, FEBID techniques are used to produce the deposition of Pt contacts, avoiding ion implantation when single NWs are contacted in this thesis, but being aware of the much higher resulting resistance.

For the fabrication of metallic contacts to individual NWs, MHP or MM, described in detail in the previous section, are used as substrates. These substrates, with a dispersion of NWs on top, are introduced in the DB system. SEM is used to survey the sample, to find a suitable NW and to produce the contacts between individual NWs and electrodes from the microchip using FEBID, while the FIB is employed only when milling on the sample is necessary.

The steps followed to fabricate contacts to individual NWs can be summarized as follows:

1. Locate a NW suitable for contacting (isolated, minimum 5 μm length and in the proximities of pre-patterned electrodes) using SEM imaging.
2. Prepare the system for FEBID deposition.
3. Deposit two or four contacts connecting the selected NW and the pre-patterned electrodes.

4. If necessary, correct errors by milling using FIB, avoiding exposure of the NWs.

Typically, the parameters used for deposition are an acceleration voltage of 5 kV, a spot size chosen to keep the electron current around 86 pA and dwell times of 5 μ s to achieve deposits of \sim 150 nm width. Using this method, an individual-NW contact fabrication lasts between 2 and 4 hours. In *Figure 12*, a sketch of a Ga₂O₃ NW contacted using FEBID techniques is shown.

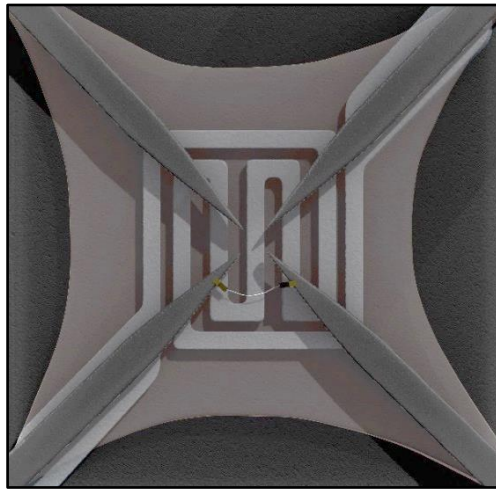


Figure 12: Sketch of a microhotplate with a nanowire electrically contacted to the surface electrodes.

1.4.3 Electron lithography

Electron Beam Lithography (EBL) is, together with DB, one of the most spread techniques in nanofabrication. EBL consists in exposing a thin polymer resist layer with a focused electron beam, modifying the solubility of the exposed polymer, to later dissolve the exposed or non-exposed regions of the polymer, depending on whether the resist is positive or negative tone, respectively [107]. The key objective of EBL is to achieve patterns with high resolution, high density and high reliability. This technique allows to define patterns with critical dimensions below 20 nm, a dimension that strongly depends on each specific EBL system [108]. The first EBL systems were developed adding a pattern generator and a beam blanker to a SEM, as schematically shown in *Figure 13*. The beam blanker is a very fast deflecting system, used to avoid the exposure of the resist in the not-to-be-exposed regions. The modern EBL devices are dedicated

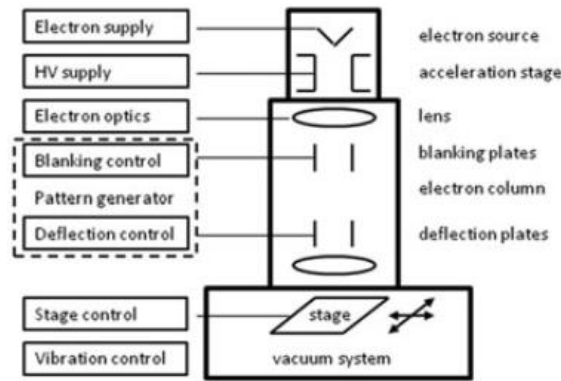


Figure 13: Schematic of an electron beam lithography machine (reprinted from Ref. [107]).

tools incorporating high brightness electron sources for high throughput, high-resolution mechanical stages to be able to expose step-by-step considerably large substrates and high-resolution interferometric stages, that allow very precise positioning of the sample under the beam [107].

The key parameters for EBL writing are the quality of the electron optics, the type of resist, substrate and developer and the process conditions: the electron beam energy and dose, exposure time and aperture size [107]. There exist also other factors that might difficult the writing process, such as proximity effects (delocalization of electrons due to forward and backscattering), collapse of the pattern (caused by swelling and capillary forces) or fluctuations in the sizes of features [107].

The EBL system used in the experimental procedure is a Raith 150-TWO at CNM-CSIC, able to accelerate the electron beam from 10 to 30 kV and with three different apertures of 10, 20 and 30 μm . The larger the aperture, the higher the current that reaches the sample. The system incorporates a Secondary Electron Detector (SED) and an in-lens detector. The working distance used to fabricate the contacts to individual NWs is 10 mm and the vacuum level inside the chamber is, similar to a regular SEM system, about 10^{-6}mbar .

To fabricate metallic contacts to individual NWs using EBL, micromembranes are used as substrates. These substrates, with a dispersion of NWs on top, are first introduced in the EBL system. The steps followed to fabricate contacts to individual NWs can be summarized as follows:

1. Locate several individual NWs suitable for contacting (isolated, minimum 5 μm length and in the proximities of pre-patterned electrodes) using SEM imaging. Locate alignment marks.
2. Design the patterns (writing field size and magnification), beginning from the selected NWs and extending to the electrodes of the MM or MHP.
3. Remove the sample from the EBL machine. Spin-coat the photoresist and soft bake the samples.
4. Introduce the substrates back in to the EBL system, find the alignment marks and expose the resist.
5. Remove the samples and develop the resist.
6. Perform metal deposition and lift-off

The exact details and process conditions of the procedure, developed in the MIND Group of the Departament d'Enginyeries Electrònica i Biomèdica, to fabricate metallic contacts of nanometer size using EBL is explained in detail in one of the papers that support this PhD dissertation [109].

Contacting NWs using EBL techniques, compared to FEBID, is less time consuming due to the possibility to contact several individual NWs in each process, instead of one. At the same time, this method provides a higher throughput and more reproducible results [109].

1.4.4 Dielectrophoresis

Dielectrophoresis (DEP) was first defined in 1951 by Pohl [110] as *the motion of suspensoid particles relative to that of the solvent in which they are contained resulting from polarization forces produced by an inhomogeneous electric field*. This method has gained popularity after the year 2000 [111] due to its contribution in the manipulation of nanostructured material and the literature related to DEP increased considerably. Published papers cover theoretical and technology aspects, with applications focused

towards areas such as biosensors [112], microfluidics [113], nanoassembly [114] or gas sensors [115], among others.

Most publications on DEP force quote a mathematical expression for time-average DEP force of the form [111,116]:

$$F_{DEP-NW} = \frac{1}{2}\pi R^2 l \varepsilon_m \text{Re}\{CM\} \nabla |E_{rms}|^2 \quad (21)$$

$$F_{DEP-SP} = 2\pi \varepsilon_m R^3 CM (\nabla E_{rms}^2) \quad (22)$$

where *Equation 21* is for NWs and *Equation 22* for spherical particles; R is the radius of the spherical particle or of the section of the NW, depending on the formula, l is the particle length, ε_m is the absolute permittivity of the material, Re means the real part, CM is the Clausius-Mossotti (CM) factor, ∇ represents the gradient operator and E_{rms} is the amplitude of the electric field. The CM factor is defined as [111,116]:

$$CM = \frac{\tilde{\varepsilon}_p - \tilde{\varepsilon}_m}{\tilde{\varepsilon}_m} \quad \tilde{\varepsilon}_m = \varepsilon_m - i\sigma/\omega \quad (23)$$

$$CM = \frac{\varepsilon_p - \varepsilon_m}{\varepsilon_p + 2\varepsilon_m} \quad (24)$$

where *Equations 23* and *24* correspond to NWs and spherical particles, respectively; $\tilde{\varepsilon}_m$ is the complex permittivity, $\tilde{\varepsilon}_p$ and $\tilde{\varepsilon}_m$ are the permittivity of the particle and medium, respectively, σ is the conductivity, and ω is the frequency of the AC electric field. These expressions point out that the key factors to control the displacement of suspended particles in a solvent are: (a) the frequency and amplitude of the applied electric field; (b) the electrical properties of the particles and solvent, via the CM factor that directly relates the permittivity and conductivity of the particles and medium with the frequency of the applied electrical field; (c) the particle concentration in the medium; and (d) the electrode geometry.

To fabricate gas sensors based on nanostructured material using DEP, the as-grown material is dispersed in a liquid solution and drop casted on the desired substrates. The points from (a) to (d) may be considered and a fine tuning of the frequency and amplitude of the applied electric field (guided by the study of the CM factor for each specific material) is used to achieve proper material alignments. Another important factor to take into consideration is the concentration and viscosity of the solution. Exploring

different solvents may allow to achieve good alignment results via the proper viscosity of the solution, maintaining the desired particle concentration. It must be mentioned that, when exploring different solvents, also the conductivity of the solution can drastically change, modifying the electric field distribution, inducing deficient DEP alignments. For this reason, a compromise between the conductivity, the permittivity and the viscosity of the medium needs to be studied to find the optimal alignment conditions for each specific solvent. Once these parameters are studied for each particular case and the best options defined, an AC square electric field is applied to the top electrodes of the substrate to achieve the nanostructured material alignment by DEP forces. After the induced alignment, to promote the solvent evaporation, the resulting devices are soft baked at 80 °C for 30 minutes.

This methodology offers a fast, easy and cheap path for the integration of nanostructured material in gas sensing platforms [115,117]. However, the control of the reproducibility and the reliability of the fabricated gas sensors is considerably low compared to other integration methodologies [118].

1.4.5 Site-selective growth

The site-selective growth of inorganic NWs is a novel method, reported for the first time in 2012 in our research group [54], in collaboration with the Institut de Microelectrònica de Barcelona, part of the Consejo Superior de Investigaciones Científicas, and the Technische Universität Wien. In this approach the NWs are grown directly integrated in the final device (MHP or MM) without the need of using further contacting methods such as FEBID, EBL or DEP. It has been demonstrated that it can be applied to integrate webs of NWs of different materials for their use as gas sensors [54,119,120], even in different membranes of the same chip [121]. This strategy is used in this thesis to study a low cost and reliable strategy for the fabrication of e-nose systems in one single chip, presented in Chapter 5.

To promote the NW growth in a specific site of a MHP or MM, a thin film of few nanometers of Au is sputtered on top of the chips to be used as seed for the VLS growth. The precursor material is introduced in gas phase in a small CVD chamber where the chips are located. The integrated heater of these chips, electrically contacted to an external

power source, allows to increase its temperature locally, promoting the growth of nanostructures according to a VLS method only on the hot spots of the device. The NWs grow following the mechanism explained in section 1.3.2, but only in the specific heated locations of the substrates.

The quality of the NWs obtained with this methodology is similar to those fabricated in a common CVD furnace for large area deposition, showing excellent crystallinity. In the midpoint of the locally heated deposition area, the NW coverage is homogeneous and, predominantly, located between the electrodes, which are later used for electrical characterization of the NW webs and to perform the gas sensing experiments. Due to an alloying of the platinum of the electrodes and the sputtered gold, a reduction of the catalytic efficiency for NW growth occurs on top of the electrodes, producing a reduction or, even, the absence of NW growth on them [54].

This methodology offers a simple, scalable and low-cost strategy to fabricate gas sensors based on inorganic NWs, avoiding the additional difficulties that various steps of integration require. As a direct consequence of combining the material growth and integration, the final devices gain robustness, are more easily reproducible and show higher reliability in the gas sensing measurements.

1.5 References

1. M.C. Roco, R.S. Williams, P. Alvisatos; *Nanotechnology research directions: vision for nanotechnology in the next decade*; Kluwer Academic Publications, Dordrecht, Netherlands (2000).
2. M.C. Roco, C.A. Mirkin, M.C. Hersam, *Nanotechnology research directions for societal needs in 2020: summary of international study*; J. Nanopart. Res. 13 (2011) 897-919. doi: 10.1007/s11051-011-0275-5.
3. M. Fischer et al.; *New Limits on the Drift of Fundamental Constants from Laboratory Measurements*; Phys. Rev. Lett. 92 (2004) 230-802. doi: 10.1103/PhysRevLett.92.230802.
4. V.J. Langlais, R.R. Schlittler, H. Tang, A. Gourdon, C. Joachim, J.K. Gimzewski; *Spatially Resolved Tunneling along a Molecular Wire*; Phys. Rev. Lett. 83 (1999) 2809. doi: 10.1103/PhysRevB.67.165326.
5. J.F. Conway, N. Cheng, A. Zlotnick, P.T. Wingfield, S.J. Stahl, A.C. Steven; *Visualization of a 4-helix bundle in the hepatitis B virus capsid by cryo-electron microscopy*; Nature 386 (1997) 91–94. doi: 10.1038/386091a0.
6. X. Zhang, E. Settembre, C. Xu, P.R. Dormitzer, R. Bellamy, S.C. Harrison, N. Grigorieff; *Near-atomic resolution using electron cryomicroscopy and single-particle reconstruction*; Proc. Natl. Acad. Sci. USA 105 (2008) 1867–1872. doi: 10.1073/pnas.0711623105.
7. W. Chiu, M.L. Baker, W. Jiang, M. Dougherty, M.F. Schmid; *Electron cryomicroscopy of biological machines at subnanometer resolution*; Struct. 13 (2005) 363-372. doi: 10.1016/j.str.2004.12.016.
8. A. Stukowski; *Structure identification methods for atomistic simulations of crystalline materials*; Modelling Simul. Mater. Sci. Eng. 20 (2012) 045021. doi: 10.1088/0965-0393/20/4/045021.
9. E. Ozbay; *Plasmonics: merging photonics and electronics at nanoscale dimensions*; Science 311 (2006) 189-193. doi: 10.1126/science.1114849.
10. V.M. Shalaev; *Optical negative-index metamaterials*; Nature Phot. 1 (2007) 41–48. doi:10.1038/nphoton.2006.49.
11. U. Mohideen, A. Roy; *Precision Measurement of the Casimir Force from 0.1 to 0.9 μ m*; Phys. Rev. Lett. 81 (1998) 4549–4552. doi:10.1103/physrevlett.81.4549.
12. M. Riebe, H. Häffner, C.F. Roos, W. Hänsel, J. Benhelm, G.P.T. Lancaster, T.W. Körber, C. Becher, F. Schmidt-Kaler, D. F. V. James, R. Blatt; *Deterministic quantum teleportation with atoms*; Nature 429 (2004) 734–737. doi:10.1038/nature02570.
13. A.E. Nel, L. Mädler, D. Velegol, T. Xia, E.M.V. Hoek, P. Somasundaran, F. Klaessig, V. Castranova, M. Thompson; *Understanding biophysicochemical interactions at the nano-bio interface*; Nature Mat. 8 (2009) 543–557. doi:10.1038/nmat2442.
14. K.S. Novoselov, A.K. Geim, S.V. Morozov, D. Jiang, Y. Zhang, S.V. Dubonos, I.V. Grigorieva, A.A. Firsov; *Electric Field Effect in Atomically Thin Carbon Films*; Science 306 (2004) 666–669. doi:10.1126/science.1102896.
15. M.A. Danzon, R. Van Leeuwen, M. Krzyzanowski, Air Quality Guidelines for Europe, World Health Organization, 2nd ed., Copenhagen, 2000.
16. Cleaner air for all, European commission for the Environment, (n.d.). <http://ec.europa.eu/environment/pubs/pdf/factsheets/air/>.
17. H. Davi; *On the fire-damp of coal mines, and on methods of lighting the mines so as to prevent its explosion*; Phil. Trans. R. Soc. Lond. 106 (1816) 1-22; doi: 10.1098/rstl.1816.0001.
18. S. Lakkis, R. Younes, Y. Alayli, M. Sawan; *Review of recent trends in gas sensing technologies and their miniaturization potential*; Sens. Rev. 34 (2014) 24–35. doi: 10.1108/SR-11-2012-724.
19. *Gas sensor market size, share & trends analysis report by product (CO₂, NO_x, CO, O₂ Sensors), by technology (semiconductor, infrared), by end use (building automation & domestic appliance, industrial), and segment forecasts, 2019 – 2025*; (2018) Report ID: 978-1-68038-083-5.
20. Y. Huang, S.K. Kalyoncu, Q. Zhao, R. Torun, O. Boyraz; *Silicon-on-sapphire waveguides design for mid-IR evanescent field absorption gas sensors*; Opt. Com. 313 (2014) 186–194. doi: 10.1016/j.optcom.2013.10.022.
21. R. Jha, A.K. Sharma; *Design considerations for plasmonic-excitation based optical detection of liquid and gas media in infrared*; Sens. Act. A Phys. 165 (2011) 271-275. doi: 10.1016/j.sna.2010.10.021.

22. J. Zhou, P. Li, S. Zhang, Y. Long, F. Zhou, Y. Huang, M. Bao; *Zeolite-modified microcantilever gas sensor for indoor air quality control*; Sens. Act. B Chem., 94 (2003) 337–342. doi:10.1016/s0925-4005(03)00369-1.
23. M.T. Boudjiet, J. Bertrand, F. Mathieu, L. Nicu, L. Mazonq, T. Leïchlé, I. Dufour; *Geometry optimization of uncoated silicon microcantilever-based gas density sensors*; Sens. Act. B Chem. 208 (2015) 600–607. doi: 10.1016/j.snb.2014.11.067.
24. N. Barié, M. Bücking, U. Stahl, M. Rapp; *Detection of coffee flavour ageing by solid-phase microextraction/surface acoustic wave sensor array technique (SPME/SAW)*; Food Chem. 176 (2015) 212–8. doi: 10.1016/j.foodchem.2014.12.032.
25. D. Compagnone, M. Faieta, D. Pizzoni, C. Di Natale, R. Paolesse, T. Van Caelenberg; *Quartz crystal microbalance gas sensor arrays for the quality control of chocolate*; Sens. Act. B Chem. 207 (2015) 1114–1120. doi: 10.1016/j.snb.2014.10.049.
26. F. Vahidpour, J. Oberländer, M.J. Schöning; *Flexible Calorimetric Gas Sensors for Detection of a Broad Concentration Range of Gaseous Hydrogen Peroxide: A Step Forward to Online Monitoring of Food-Package Sterilization Processes*; Phys. Stat. Sol. A 207 (2018) 1800044. doi: 10.1002/pssa.201800044.
27. G. Heiland, E. Mollwo, F. Stöckmann; *Electronic processes in Zinc Oxide*; Sol. State Phys. 8 (1959) 191–323. doi:10.1016/s0081-1947(08)60481-6.
28. T. Seiyama, A. Kato, K. Fujiishi, M. Nagatani; *A new detector for gaseous components using semiconductive thin films*; Anal. Chem. 34 (1962) 1502–1503. doi:10.1021/ac60191a001.
29. N. Taguchi; Japanese Patent S45–38200 (1962).
30. K. Ihokura, J. Watson; *The stannic oxide gas sensor: principles and applications*; CRC Press (1994) 2 - 4. ISBN: 0-8493-2604-4.
31. W. Gopel, T.A. Jones, M. Kleitz, J. Lundström, T. Seiyama; *Sensors: a comprehensive survey. Vol 2.: Chemical and Biochemical sensors, Part I*; VCH Weinheim (1991) 65 - 70. ISBN: 3-527-26768-9.
32. N. Taguchi; Japanese Patent S47-38840 (1966).
33. T. Seiyama, S. Kagawa; *Study on a detector for gaseous components using semiconductive thin films*; Anal. Chem. 38 (1966) 1069–1073. doi:10.1021/ac60240a031.
34. N. Taguchi; Japanese Patent S50-30480 (1966).
35. P.J. Shaver; *Activated tungsten oxide gas detectors*; Appl. Phys. Lett. 11 (1967) 255–257. doi:10.1063/1.1755123.
36. J.C. Loh; French Patent 1545292 (1967).
37. N. Taguchi; Japanese Patent S50-23317 (1969).
38. B. Bott et al.; British Patent 1 374 575 (1971).
39. T. Seiyama, H. Futada, F. Era, N. Yamazoe; *Gas detection by activated semiconductive sensor*; Denki Kagaku 40 (1972) 244-249.
40. M.A. Carpenter, S. Mathur, A. Kolmakov; *Metal oxide nanomaterials for chemical sensors*; Springer Series (2013) 4 - 7. doi: 10.1007/978-1-4614-5395-6.
41. P.B. Weisz; *Bridges of physics and chemistry across the semiconductor surface*; In: R.H. Kingston; *Semiconductor surface physics*; University of Pennsylvania Press (1956) 247–258. doi: 10.9783/9781512803051.
42. Y. Mizokawa, S. Nakamura; *ESR and electric conductance studies of the fine-powdered SnO₂*; Jap. J. App. Phys. 14 (1975) 779–788. doi:10.1143/jjap.14.779.
43. E.W. Thornton, P.G. Harrison; *Tin oxide surfaces. Part 1. Surface hydroxyl groups and the chemisorption of carbon dioxide and carbon monoxide on tin (IV) oxide*; J. Chem. Soc.71 (1975) 461-472. doi:10.1039/f19757100461.
44. D. Kohl; *Surface processes in the detection of reducing gases with SnO₂-based devices*; Sens. Act. 18 (1898) 71–113. doi:10.1016/0250-6874(89)87026-x.
45. A. Gurlo, R. Riedel; *In situ and operando spectroscopy for assessing mechanisms of gas sensing*; Ang. Chem. Int. Ed. 46 (2007) 3826–3848. doi:10.1002/anie.200602597.
46. A. Kolmakov, Y. Zhang, G. Cheng, M. Moskovits; *Detection of CO and O₂ using tin oxide nanowire sensors*; Adv. Mat. 15 (2003) 997–1000. doi:10.1002/adma.200304889.
47. Q. Wan, Q.H. Li, Y.J. Chen, T.H. Wang, X.L. He, J.P. Li, C.L. Lin; *Fabrication and ethanol sensing characteristics of ZnO nanowire gas sensors*; Appl. Phys. Lett. 84 (2004) 3654–3656. doi:10.1063/1.1738932.
48. F. Hernández-Ramírez, A. Tarancón, O. Casals, J. Arbiol, A. Romano-Rodríguez, J.R. Morante; *High response and stability in CO and humidity measures using a single SnO₂ nanowire*; Sens. and Act. B Chem. 121 (2007) 3-17. doi: 10.1016/j.snb.2006.09.015.

49. A. Kolmakov, D.O. Klenov, Y. Lilach, S. Stemmer, M. Moskovits; *Enhanced gas sensing by individual SnO₂ nanowires and nanobelts functionalized with Pd catalyst particles*; Nano Let. 5 (2005) 667–673. doi:10.1021/nl050082v.
50. J. Polleux, A. Gurlo, N. Barsan, U. Weimar, M. Antonietti, M. Niederberger; *Template-free synthesis and assembly of single-crystalline tungsten oxide nanowires and their gas-sensing properties*; Ang. Chem. Int. Ed. 45 (2006) 261–265. doi:10.1002/anie.200502823.
51. G. Eranna, B.C. Joshi, D.P. Runthala, R.P. Gupta; *Oxide materials for development of integrated gas sensors - a comprehensive review*; Crit. Rev. Sol. State Mat. Sci. 29 (2004) 111–188. doi:10.1080/10408430490888977.
52. A. Loutfi, S. Coradeschi, G.K. Mani, P. Shankar, J.B.B. Rayappan; *Electronic noses for food quality: A review*; J. Food Eng. 144 (2015) 103–111. doi: 10.1016/j.jfoodeng.2014.07.019.
53. J. Gardner, P. Bartlett; *Electronic noses, principles and applications*; Oxford University Press (1999). ISBN: 0198559550.
54. S. Barth, R. Jimenez-Diaz, J. Samà, J.D. Prades, I. Gràcia, J. Santander, C. Cané, A. Romano-Rodriguez; *Localized growth and in situ integration of nanowires for device applications*; Chem. Com. 48 (2012) 4734. doi:10.1039/c2cc30920c.
55. K.W. Kolasinski, *Surface science: Foundations of catalysis and nanoscience*; John Wiley & Sons (2012) 9–49. doi: 10.1002/9781119941798.ch1.
56. G. Korotcenkov; *Semiconductors in gas sensors. Handbook of gas sensor materials*; Springer (2013) 167–195. doi:10.1007/978-1-4614-7165-3_5.
57. G. Korotcenkov; *The role of morphology and crystallographic structure of metal oxides in response of conductometric-type gas sensors*; Mat. Sci. Eng.: R: Reports 61 (2008) 1–39. doi: 10.1016/j.mser.2008.02.001.
58. G. Korotcenkov, B.K. Cho; *Instability of metal oxide-based conductometric gas sensors and approaches to stability improvement (short survey)*; Sens. Act. B: Chem. 156 (2011) 527–538. doi: 10.1016/j.snb.2011.02.024.
59. T. Wolkenstein; *Electronic processes on semiconductor surfaces during chemisorption*; Consultants Bureau (1991) 40 - 51. doi:10.1007/978-1-4615-3656-7.
60. E. Zaremba, W. Kohn; *Van der Waals interaction between an atom and a solid surface*; Phys. Rev. B 13 (1976) 2270–2285. doi:10.1103/physrevb.13.2270.
61. J. Tao, A.M. Rappe; *Physical adsorption: theory of Van der Waals interactions between particles and clean surfaces*; Phys. Rev. Lett. 112 (2014) 106101. doi:10.1103/physrevlett.112.106101.
62. J.E. Lennard-Jones; *Processes of adsorption and diffusion on solid surfaces*; Transactions of the Faraday Society 28 (1932) 333-358. doi:10.1039/tf9322800333.
63. V. Bortolani, N.H. March, M.P. Tosi; *Interaction of atoms and molecules with solid surfaces*; Springer Science + Business Media (1990) 25 - 52. doi:10.1007/978-1-4684-8777-0.
64. M. Muhler, J.M. Thomas, W.J. Thomas; *Principles and practice of heterogeneous catalysis*; Ber. Bun. Phys. Chem. 101 (1997) 1560–1560. doi:10.1002/bbpc.199700023.
65. A.W. Adamson, A.P. Gast; *Physical chemistry of surfaces*; John Wiley & Sons (1997) 685-757. ISBN: 978-0-471-14873-9.
66. D.S. Ballantine, S.J. Martin, A.J. Ricco, G.C. Frye, H. Wohltjen, R.M. White, E.T. Zellers; *Chemical and biological sensors*; Elsevier (1997) 256 – 272. doi: 10.1016/B978-0-12-077460-9.X5000-X.
67. S. Brunauer, P.H. Emmett, E. Teller; *Adsorption of gases in multimolecular layers*; J. Am. Chem. Soc. 60 (1938) 309–319. doi:10.1021/ja01269a023.
68. P. Kim, S. Agnihotri; *Application of water-activated carbon isotherm models to water adsorption isotherms of single-walled carbon nanotubes*; J. Col. Int. Sci. 325 (2008) 64–73. doi: 10.1016/j.jcis.2008.06.002.
69. O. Monereo, J.D. Prades, A. Cirera; *Self-heating effects in large arrangements of randomly oriented carbon nanofibers: Applications to gas sensors*; Sens. Act. B Chem. 211 (2015) 489-497; doi: 10.1016/j.snb.2015.01.095.
70. M. Khalfoui, S. Knani, M.A. Hachicha, A.B. Lamine; *New theoretical expressions for the five adsorption type isotherms classified by BET based on statistical physics treatment*; J. Col. Int. Sci. 263 (2003) 350–356. doi:10.1016/s0021-9797(03)00139-5.
71. E.O. Wiig, A.J. Juhola; *The adsorption of water vapor on activated charcoal*; J. Am. Chem. Soc. 71 (1949) 561–568. doi:10.1021/ja01170a051.
72. G. Marbán, A.B. Fuertes; *Co-adsorption of n-butane/water vapour mixtures on activated carbon fibre-based monoliths*; Carbon 42 (2004) 71–81. doi: 10.1016/j.carbon.2003.09.018.

73. A. Rothschild, Y. Komem; *Numerical computation of chemisorption isotherms for device modeling of semiconductor gas sensors*; *Sens. Act. B: Chem.* 93 (2003) 362–369. doi:10.1016/s0925-4005(03)00212-0.
74. H. Freundlich; *Kapillarchemie, eine Darstellung der Chemie der Kolloide und verwandter Gebiete*; Kolloidchemie, Akad. Verlagsgesellschaft. (1909). doi: 10.1002/bbpc.19090152312.
75. P.T. Moseley; *Solid state gas sensors*; *Meas. Sci. Technol.* 8 (1997) 223–237. doi: 10.1088/0957-0233/8/3/003.
76. N. Barsan, U. Weimar; *Conduction model of metal oxide gas sensors*; *J. Electroceramics* 7 (2001) 143–167. doi:10.1023/a:1014405811371.
77. N. Yamazoe, K. Shimano; *Theory of power laws for semiconductor gas sensors*; *Sens. Act. B: Chem.* 128 (2008) 566–573. doi: 10.1016/j.snb.2007.07.036.
78. F. Hernandez-Ramirez, A. Tarancon, O. Casals, E. Pellicer, J. Rodriguez, A. Romano-Rodríguez, J.R. Morante, S. Barth, S. Mathur; *Electrical properties of individual tin oxide nanowires contacted to platinum electrodes*; *Phys. Rev. B* 76 (2007) 085429. doi:10.1103/physrevb.76.085429.
79. B.L. Sharma; *Metal-semiconductor schottky barrier junctions and their applications*; Plenum Press (1984) 2-8. doi:10.1007/978-1-4684-4655-5.
80. S.M. Sze, K.K. Ng; *Physics of Semiconductor devices*; John Wiley & Sons (2007) 170-173. ISBN: 9780471143239.
81. A.P. Levitt; *Whisker technology*; John Wiley & Sons (1970) 1-13. ISBN: 9780471531500.
82. R.S. Wagner, W.C. Ellis; *Vapor-liquid-solid mechanism of single crystal growth*; *App. Phys. Let.* 4 (1964) 89–90. doi:10.1063/1.1753975.
83. R.S. Wagner, W.C. Ellis; *Vapor-liquid-solid mechanism of crystal growth and its applications to Silicon*; *Trans. Met. Soc. AIME* 233 (1965) 1053-1064. WorldCat ID: 838323356.
84. R.S. Wagner; *Defects in Silicon crystals grown by the VLS technique*; *J. App. Phys.* 38 (1967) 1554-1560. doi:10.1063/1.1709722.
85. M. Meyyappan, M.K. Sunkara; *Inorganic nanowires: applications, properties and characterization*; Taylor & Francis Group (2009) 7-59. ISBN: 9781420067835.
86. E.I. Givargizov; *Fundamental aspects of VLS growth*; *J. Cry. Grow.* 31 (1975) 20-30. doi: 10.1016/0022-0248(75)90105-0.
87. J. Westwater, D.P. Gosain, K. Yamauchi, S. Usui; *Nanoscale silicon whiskers formed by silane/gold reaction at 335 °C*; *Mat. Let.* 24 (1995) 109-112. doi: 10.1016/0167-577X(95)00091-7.
88. Z. Cai, B. Liu, X. Zou, H.-M. Cheng; *Chemical vapor deposition growth and applications of two-dimensional materials and their heterostructures*; *Chem. Rev.* 118 (2018) 6091–6133. doi: 10.1021/acs.chemrev.7b00536.
89. V. Schmidt, J.V. Wittemann, U. Gösele; *Growth, thermodynamics, and electrical properties of silicon nanowires*; *Chem. Rev.* 110 (2010) 361–388. doi: 10.1021/cr900141g.
90. C.W. Pinion, J.D. Christesen, J.F. Cahoon; *Understanding the vapor–liquid–solid mechanism of Si nanowire growth and doping to synthetically encode precise nanoscale morphology*; *J. Mat. Chem. C* 4 (2016) 3890–3897. doi: 10.1039/c5tc03898g.
91. N.D. Cuong, Y.W. Park, S.G. Yoon; *Microstructural and electrical properties of Ga₂O₃ nanowires grown at various temperatures by vapor–liquid–solid technique*; *Sens. Act. B: Chem.* 140 (2009) 240–244. doi: 10.1016/j.snb.2009.04.020.
92. E. Kukovitsky, S. L’vov, N.A. Sainov, V.A. Shustov; *CVD growth of carbon nanotube films on nickel substrates*; *App. Surf. Sci.* 215 (2003) 201-208. doi: 10.1016/S0169-4332(03)00280-0.
93. S. Kumar, C. Tessarek, S. Christiansen, R. Singh; *A comparative study of β-Ga₂O₃ nanowires grown on different substrates using CVD technique*; *J. All. Comp.* 587 (2014) 812–818. doi: 10.1016/j.jallcom.2013.10.165.
94. F. Schuster, S. Weiszer, M. Hetzl, A. Winnerl, J.A. Garrido, M. Stutzmann; *Influence of substrate material, orientation, and surface termination on GaN nanowire growth*; *J. App. Phys.* 116 (2014) 054301. doi: 10.1063/1.4892113.
95. M. Madsen, M. Aagesen, P. Krogstrup, C. Sørensen, J. Nygård; *Influence of the oxide layer for growth of self-assisted InAs nanowires on Si (111)*; *Nano. Res. Let.* 6 (2011) 1-5. doi: 10.1186/1556-276x-6-516.
96. Y. Hao, G. Meng, C. Ye, L. Zhang; *Controlled synthesis of In₂O₃ octahedrons and nanowires*; *Crys. Gro. Des.* 5 (2005) 1617–1621. doi: 10.1021/cg050103z.
97. G. Domènech-Gil, S. Barth, J. Samà, P. Pellegrino, I. Gràcia, C. Cané, A. Romano-Rodríguez; *Gas sensors based on individual indium oxide nanowire*; *Sens. Act. B: Chem.* 238 (2019) 447–454. doi: 10.1016/j.snb.2016.07.084.

98. Y. Shen; *Carbothermal synthesis of metal-functionalized nanostructures for energy and environmental applications*; J. Mat. Chem. A 3 (2015) 13114–13188. doi:10.1039/c5ta01228g.
99. Z. Liu, X. Bi, Z. Gao, W. Liu; *Carbothermal reduction of iron ore in its concentrate-agricultural waste pellets*; Adv. Mat. Sci. Eng. 2018 (2018) 1–6. doi:10.1155/2018/2138268.
100. O. Ostrovski; *The use of natural gas for reduction of metal oxides: constraints and prospects*; Celebrating the Megascala, TMS (2014) 529–536. doi:10.1007/978-3-319-48234-7_52.
101. R. Balasubramaniam, S. Gokoglu, U. Hegde; *The reduction of lunar regolith by carbothermal processing using methane*; Int. J. Min. Proc. 96 (2010) 54–61. doi: 10.1016/j.minpro.2010.06.001.
102. D. R. Stull, H. Prophet; *JANAF Thermochemical Tables*; NSRDS-NBS 37, U.S. Dept of Commerce, National Bureau of Standards, 1971.
103. University of Cambridge, DoITPoMS; *The Interactive Ellingham diagram*; https://www.doitpoms.ac.uk/tlplib/ellingham_diagrams/interactive.php.
104. F.N. Tuzluca, Y.O. Yesilbag, T. Akkus, M. Ertugrul; *Effects of graphite on the synthesis of 1-D single crystal In₂O₃ nanostructures at high temperature*; Mat. Sci. Sem. Proc. 66 (2017) 62–68. doi: 10.1016/j.mssp.2017.04.007.
105. A. Fernández-Pacheco, J.M. Teresa, R. Córdoba, M.R. Ibarra; *Metal-insulator transition in Pt-C nanowires grown by focused-ion-beam-induced deposition*; Phys. Rev. B 79 (2009). doi: 10.1103/physrevb.79.174204.
106. A. Vilà, F. Hernández-Ramírez, J. Rodríguez, O. Casals, A. Romano-Rodríguez, J.R. Morante, M. Abid; *Fabrication of metallic contacts to nanometre-sized materials using a focused ion beam (FIB)*; Mat. Sci. Eng.: C 26 (2006) 1063–1066. doi: 10.1016/j.msec.2005.09.092.
107. M. Stepanova, S. Dew; *Nanofabrication*; Springer-Verlag/Wien (2012) 11–41. doi: 10.1007/978-3-7091-0424-8.
108. A.E. Grigorescu, C.W. Hagen; *Resists for sub-20-nm electron beam lithography with a focus on HSQ: state of the art*; Nanotech. 20 (2009) 292001. doi: 10.1088/0957-4484/20/29/292001.
109. J. Samà, G. Domènech-Gil, I. Gràcia, X. Borrísé, C. Cané, S. Barth, F. Steib, A. Waag, J.D. Prades, A. Romano-Rodríguez; *Electron beam lithography for contacting single nanowires on non-flat suspended substrates*; Sens. Act. B: Chem. 286 (2019) 616–623. doi: 10.1016/j.snb.2019.01.040.
110. H.A. Pohl; *The motion and precipitation of suspensoids in divergent electric fields*; J. App. Phys. 22 (1951) 869–871. doi: 10.1063/1.1700065.
111. R. Pethig; *Dielectrophoresis: status of the theory, technology and applications*; Biomicrofluidics 4 (2010) 022811. doi: 10.1063/1.3456626.
112. N. Abd Rahman, F. Ibrahim, B. Yafouz; *Dielectrophoresis for biomedical sciences applications: a review*; Sensors 17 (2017) 449. doi: 10.3390/s17030449.
113. B. Çetin, D. Li; *Dielectrophoresis in microfluidics technology*; Electroph. 32 (2011) 2410–2427. doi: 10.1002/elps.201100167.
114. C.K.M. Fung, M.Q. H. Zhang, Z. Dong, W.J. Li; *Fabrication of CNT-Based MEMS piezoresistive pressure sensors using DEP nanoassembly*; Proc. Of 5th IEEE Conf. Nanotech. Japan (2005).
115. J. Guilera, C. Fàbrega, O. Casals, F. Hernández-Ramírez, S. Wang, S. Mathur, F. Udrea, A. Luca, S.Z. Ali, A. Romano-Rodríguez, J.D. Prades, J.R. Morante; *Facile integration of ordered nanowires in functional devices*; Sens. Act. B: Chem. 221 (2015) 104–112. doi: 10.1016/j.snb.2015.06.069.
116. H.W. Seo, C.S. Han, S.O. Hwang, J. Park; *Dielectrophoretic assembly and characterization of individually suspended Ag, GaN, SnO₂ and Ga₂O₃ nanowires*; Nanotech. 17 (2006) 3388–3393. doi: 10.1088/0957-4484/17/14/008.
117. O. Chmela, J. Sadílek, G. Domènech-Gil, J. Samà, J. Somer, R. Mohan, A. Romano-Rodríguez, J. Hubálek, S. Vallejos; *Selectively arranged single-wire based nanosensor array systems for gas monitoring*; Nanoscale 00 (2017) 1–11. doi: 10.1039/C8NR01588K.
118. M. Nakano, Z. Ding, J. Suehiro; *Comparison of sensitivity and quantitation between microbead dielectrophoresis-based DNA detection and real-time PCR*; Biosensors 7 (2017) 44. doi: 10.3390/bios7040044.
119. J. Samà, M.S. Seifner, G. Domènech-Gil, J. Santander, C. Calaza, M. Moreno, I. Gràcia, S. Barth, A. Romano-Rodríguez; *Low temperature humidity sensor based on Ge nanowires selectively grown on suspended microhotplates*; Sens. Act. B: Chem. 243 (2017) 669–677. doi: 10.1016/j.snb.2016.12.042.
120. J. Samà, S. Barth, G. Domènech-Gil, J.D. Prades, N. López, O. Casals, I. Gràcia, C. Cané, A. Romano-Rodríguez; *Site-selectively grown SnO₂ NWs networks on micromembranes for efficient ammonia sensing in humid conditions*; Sens. Act. B Chem. 232 (2016) 402–409. doi: 10.1016/j.snb.2016.03.091.

- 121.L. Hrachowina, G. Domènech-Gil, A. Pardo, M.S. Seifner, I. Gràcia, C. Cané, A. Romano-Rodríguez, S. Barth; *Site-specific growth and in situ integration of different nanowire material networks on a single chip: toward a nanowire-based electronic nose for gas detection*; ACS Sensors 3 (2018) 727–734. doi: 10.1021/acssensors.8b00073.



*“Nothing in life is to be feared,
it is only to be understood.
Now it’s time to understand more,
so that we may fear less”
Maria Salomea Skłodowska-Curie*

2. Objectives

The work presented in this dissertation is focused on the fabrication, integration and test of chemoresistive gas sensor devices and systems based on semiconducting nanowires. It represents a step forward in the large experience in the contact fabrication of nanostructured material and their characterization towards different gases for which the research group, in which this work is performed, is well known for more than 15 years. Before the beginning of this PhD work, the NWs used for the research were provided by external laboratories. With the availability of an old CVD furnace, the possibilities to perform the growth in-house started and part of this dissertation is devoted to establishing the conditions for the growth of MOX NWs.

A second direction of research was to deepen into methodologies to integrate the sensing material in the substrates where the gas sensing devices are fabricated, refining them in some cases and proposing new strategies, with the aim of simplifying the integration procedures and increasing the throughput.

The third topic was, to a certain point, a natural extension of the device integration activity when considering one of the major drawbacks of chemoresistors: their lack of selectivity. For this, several nanomaterials were integrated onto the different micromembranes of one single chip, allowing the simultaneous measurements of various gas sensors, constituting a miniaturized electronic nose.

The specific objectives established in this thesis are the following:

- To grow crystalline indium oxide and gallium oxide nanowires via the vapor-liquid-solid mechanism using a chemical vapor deposition furnace and solid precursors.
- To fabricate devices based on individual indium oxide and gallium oxide nanowires, contacted on top of microhotplates using Focused Electron Beam Induced Deposition, and to characterize their gas sensing properties.
- To develop advanced techniques and strategies to achieve the contact fabrication to nanowires on top of microhotplates and micromembranes, and to test their gas sensing properties.
- To fabricate a nano-electronic-nose based on a single chip containing several micromembranes, each with different site-selective grown nanowires, and to study their gas discrimination capabilities.

3

*“What we know is a drop,
what we don’t know is an ocean”*

Isaac Newton

3. Individual semiconducting metal oxide nanowires for gas sensing

Two of the main objectives of this thesis were: (1) to establish the proper set of conditions to successfully grow In_2O_3 and Ga_2O_3 NWs and (2) their evaluation as sensing element of gas nanosensors.

In section 3.1 the growth of In_2O_3 NWs via the VLS mechanism and using *Au* nanodroplets for their promotion, is addressed. The growth of these NWs was found to be strongly dependent on the oxygen concentration in the gas atmosphere, on the temperature and on the pressure inside the tube, promoting the formation of nanorods and/or octahedral microstructures during the growth experiments, the latter formed by the vapor-solid mechanism. The set of conditions that give rise to the successful growth of In_2O_3 NWs employing the CVD furnace were as follows: temperatures of 900 and 720 °C for the precursor and for the substrates, respectively, pressure between 2 and 100 Torr, an oxygen concentration between 0.01 and 0.02 % of carrier gas, which is pure argon gas (5N), at a flux of 100 sccm and 0.25 g of a mixture of pure In_2O_3 (99.99%) nanopowder and graphite in a 4:1 wt proportion as precursor material. The structural and optical characterization of the samples containing exclusively NWs have confirmed that they are monocrystalline, with a cubic lattice, and that their average dimensions are diameter around 150 nm and length about 5 μm . In_2O_3 NWs have been transferred to microhotplates and have been contacted with a Pt-containing material using FEBID, so that chemoresistors based on individual In_2O_3 NWs have been fabricated.

The sensors were characterized at temperatures between 200 to 300 °C, achieved using the embedded heater of the microhotplates, and towards different concentrations of carbon monoxide (CO), nitrogen dioxide (NO₂) and ethanol (EtOH), always diluted in dry synthetic air. The measurements revealed that the sensors present high resistance variation to EtOH, of 47% at 300°C for EtOH at a concentration of 100 ppm, while the effect of NO₂ and CO is below 10% for the whole concentration range measured. Furthermore, the fastest sensors responded in about 4 minutes, which makes these sensors suitable for practical applications.

In section 3.2 the growth conditions and gas sensing characterization of sensors based on single Ga₂O₃ NWs are presented. The growth is performed in the same furnace as explained in section 3.1, but the experimental conditions are different. For Ga₂O₃ NWs the oxygen-concentration in the carrier gas only slightly changes the results, which gives to NWs in almost all conditions. Other differences are that the optimal growth was obtained at temperatures of 950 °C for the precursor and 820 °C for the substrates. In these experiments, to keep the same amount of gallium to carbon ratio, the used precursor was 0.45 g of a mixture of pure Ga₂O₃ (99.99%) nanopowder mixed with graphite in a 2:3 wt proportion. The characterization revealed that the diameter of the NWs was of 50 ± 20 nm, the length was of 12 ± 5 μm and perfectly matched with the monoclinic β-Ga₂O₃ crystalline structure. Very important is that the NWs were surrounded by a carbon shell of about 4 to 10 nm, which is a direct effect of the carbothermal reduction process. Similar to the In₂O₃ NWs, chemoresistors were fabricated using FEBID on top of microhotplates.

The chemoresistors were very selective, with a high resistance variation when exposed to relative humidity diluted in dry synthetic air at room temperature (20 °C), not responding to other gases, like CO, NO₂, EtOH, ... This behavior is completely different to that reported for Ga₂O₃, which normally respond to other gases and at high temperatures. This different response pattern is attributed to the carbon shell around the nanowires. Furthermore, these sensors responded in times as short as 2 minutes, making them very fast. This fact, together with the high selectivity, make these sensors very interesting for real gas sensing applications.

3.1 Gas sensor based on individual indium oxide nanowire



Gas sensors based on individual indium oxide nanowire



Guillem Domènech-Gil^{a,*}, Sven Barth^b, Jordi Samà^a, Paolo Pellegrino^a, Isabel Gràcia^c, Carles Cané^c, Albert Romano-Rodríguez^a

^a Universitat de Barcelona (UB), MIND-Department of Engineering and Institute of Nanoscience and Nanotechnology (IN2UB), c/Martí i Franquès 1, E-08028 Barcelona, Spain

^b Vienna University of Technology (TUW), Institute of Materials Chemistry, Am Getreidemarkt 9/BC/02, A-1060 Vienna, Austria

^c Consejo Superior de Investigaciones Científicas (CSIC), Institut de Microelectrònica de Barcelona (IMB-CNM), Campus UAB, E-08193, Bellaterra, Spain

ARTICLE INFO

Article history:

Received 8 January 2016

Received in revised form 1 July 2016

Accepted 17 July 2016

Available online 18 July 2016

Keywords:

Indium oxide

Nanowires

Gas nanosensor

Chemoresistor

ABSTRACT

Indium oxide nanostructures have been prepared by carbothermal reduction method. From them, nanowires have been structurally and optically characterized using X-ray diffraction, scanning and transmission electron microscopy and photoluminescence. The indium oxide nanowires have been removed from the substrate and contacted by Focused Electron- and Focused Ion-Beam Induced Deposition techniques to interdigitates on suspended microhotplates, which allow heating up to 300 °C with a low power consumption of only 8 mW. The gas response of the tested devices towards ethanol, carbon monoxide and nitrogen dioxide diluted in dry synthetic air at different concentrations and temperatures has been carried out showing a selectivity towards ethanol with responses up to 50% at temperatures between 200 and 300 °C, while only small response to high concentrations of carbon monoxide and nitrogen dioxide is observed.

© 2016 Published by Elsevier B.V.

1. Introduction

Indium oxide (In_2O_3) is a transparent n-type semiconductor with a direct band-gap of about 3.6 eV [1]. Among several different applications, In_2O_3 thin films have been widely used as gas sensor for detecting toxic gases in air [2–4]. The use of nanostructured In_2O_3 for sensing gases like NO_2 , O_3 or CO, has been reported in literature proving the potential for sensing applications [5–7]. Using nanowires (NWs) as main active components of a sensing system, due to the increased surface to volume ratio of the material combined with their high crystallinity, is expected to give rise to a corresponding enhancement of the sensing properties. A further benefit of such morphology is its considerably lower power consumption as compared to their bulk counterpart, attainable by an adequate device layout, allowing to match the limits required in mobile gas sensing applications [5,6]. Chemical Vapour Deposition (CVD) is extensively employed in the synthesis of In_2O_3 NWs due to the feasibility of growing monocrystalline structures. The NW morphology of the metal oxide semiconducting materials has been demonstrated to present high sensitivities, up to parts per billions (ppb), towards gases like CO or H_2 [5,7–13] as a function of

their surface features. However, the selectivity still is an issue, as for most semiconducting metal oxides. Other In_2O_3 morphologies can also be synthesized, such as nanorods or nanooctahedra [14–19] but, due to the difficulty of assembling them individually onto substrates with electrodes for fabricating sensing devices, they remain almost unexplored, while they might present equally interesting properties for gas sensing applications.

Several methods for the synthesis of In_2O_3 nanostructures have been proposed in literature, which can be divided in two broad categories, namely the solution-based techniques and the vapour-phase processes. Liquid- or solution-based techniques include approaches such as electrodeposition [20], which provides a rapid synthesis method for polycrystalline NW growth. Vapour-phase techniques comprehends methods such as molecular beam epitaxy [21], laser ablation [22] as well as CVD [23], among others, which allow the growth of monocrystalline NWs. A drawback related to this latter is the long time needed for the deposition when compared to the electrodeposition technique, due to the high temperatures required for heating up and cooling of the whole quartz tube. A CVD-like process which is less time-consuming and more energy-efficient is based on the growth of monocrystalline NWs on top of microhotplates, using a small heater incorporated in the microstructure, which allows to achieve the temperature required for the precursor decomposition with only few mW [24,25]. However, this approach allows the growth of a NWs network, and does

* Corresponding author.

E-mail address: guillemdom@gmail.com (G. Domènech-Gil).

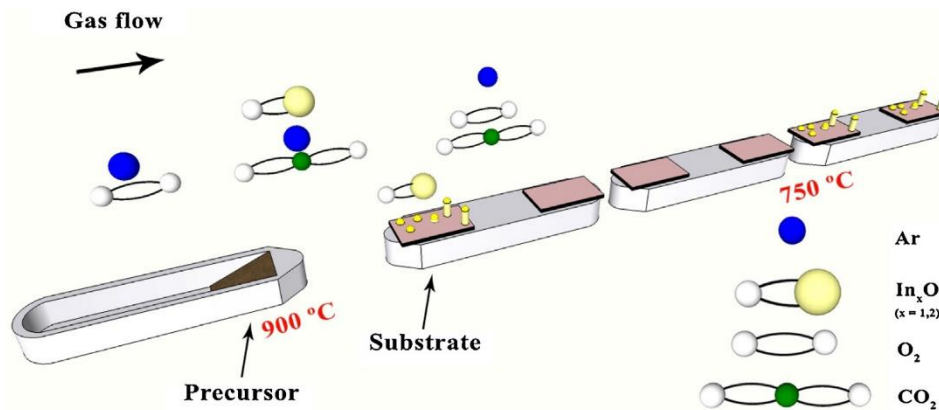


Fig. 1. Scheme of the experimental layout inside the quartz tube furnace used for the growth of indium oxide.

not allow to extract the information of the sensing mechanisms of the individual NWs.

Ethanol limit values for drivers in European countries range between 0.1 and 0.5 mg/l in blood. The conversion of these values into concentration of ethanol in human breath gives values between 30 and 130 ppm. For this reason, ethanol gas sensors would be highly desirable in this established range.

This work focuses on the vapour-liquid-solid (VLS) growth of In_2O_3 nanostructures by CVD in a quartz tube furnace using gold as growth catalyst [21,22]. A comprehensive study will be presented, which includes the growth of different In_2O_3 nanostructures in the deposition chamber, their characterization and the testing of gas sensing properties of devices fabricated on individual In_2O_3 NWs towards different gases, with a special focus in ethanol.

2. Experimental

The synthesis of In_2O_3 nanostructures has been carried out by CVD of In_2O_3 powder reduced by the carbothermal process according to a VLS mechanism, first reported by Wagner et al. [26]. The preparation process started with the precursor material: pure In_2O_3 (99.99%) nanopowder was mixed for 20 min in an agate mortar with graphite powder in a 4:1 wt proportion. For each experiment 0.25 g of precursor material was used. The substrates were $0.5 \times 0.5 \text{ cm}^2$ pieces cut from a 4-inch thermally oxidized Si wafer, with a $0.5 \mu\text{m}$ -thick SiO_2 layer. These substrates were Au sputter-covered for 20 s, which should give rise to a thin and discontinuous Au layer.

The growth was carried out in a 2" diameter quartz tube inserted into a Lindbergh three-zone furnace, allowing the independent control of the different zone temperatures. The configuration of the furnace limits the temperature difference among the adjoining zones to about 150°C , constraining the experimental conditions. The solid source of In_2O_3 requires high evaporation temperatures, around 1300°C , a value that can be lowered by promoting a carbothermal reduction, where the graphite precursor is oxidized to CO_2 by reducing the In_2O_3 to metallic indium, which evaporates at much lower temperatures. A rotatory pump and a gas flow injection system were connected at the end and beginning of the furnace tube, respectively, allowing the mixture of different gases and the control of the internal tube pressure from atmospheric down to 7 mTorr. The CVD gas injection system is formed by 4 MKS Mass-Flow controllers. The indium vapour arising from the reduction of the oxide source material is transported to the collection area by a carrier gas, consisting of pure argon (5 N quality) and very low levels of pure oxygen, with concentrations ranging from 0.003 to 0.1% in volume. The growth experiments have covered a pressure range from 2 to 100 Torr. A sketch of the experimental layout is

depicted in Fig. 1, where the location of the precursor and the set of substrates can be identified.

In our experiments, the NW growth occurs when, locating the precursor in the first furnace zone adjacent to the gas injection system, the temperature was fixed at 900°C . The substrate temperature has been fixed at 750°C in the central portion of the second furnace zone, with a decreasing temperature slope from this point towards the back-end of the quartz tube where the temperature reaches values around 600°C . A gas mixture of oxygen diluted in Ar with a total gas flow rate of 500 ml/min at 100 Torr was used.

The In_2O_3 nanostructures were investigated using a Jeol J7100F Field Emission Scanning Electron Microscope (SEM), a Jeol J2100 Transmission Electron Microscope (TEM) and a Siemens D-500 X-Ray Diffractometer (XRD). Photoluminescence (PL) characterization has been carried out in a home-made setup by exciting the sample with the 325 nm line of a He-Cd laser, with an estimated power density of $10 \text{ W}/\text{cm}^2$.

The grown In_2O_3 NWs were transferred to microhotplates with pre-patterned electrodes by immersing the substrate in a vial with few millilitres of pure (96%) ethanol, sonicating the vial to promote the detachment of the nanostructures from the growth substrate's surface and depositing solution droplets onto the microhotplates. Each microhotplate, fabricated by surface micromachining, contains a buried Pt heater and pre-patterned Ti/Pt microelectrodes, with a thickness of 5/80 nm, respectively. The heating area is located only in the microhotplate, allowing to reach temperatures up to 300°C with a power consumption of 8 mW. In_2O_3 NWs were electrically contacted using a using a FEI Dual-Beam Strata 235 or a FEI Helios Nanolab 650 (FIB) instruments, equipped with a trimethylcyclopentadienyl-platinum ($(\text{CH}_3)_3\text{CH}_2\text{C}_5\text{H}_4\text{Pt}$) injector for Pt deposition. The electron and the Ga^+ ion beams were accelerated to 5 and 30 kV, respectively. The complete procedure for this contact fabrication method is explained in detail elsewhere [27] and is used to prevent any exposure of the NW to Ga ions that would modify the structural and electrical properties of the NW. Finally, the chips containing the microhotplates were glued to a TO-8 support and electrically contacted using a ball bonding machine. The gas sensing measurements are performed inside a self-constructed stainless steel gas chamber, of 8.6 ml volume, connected to a Gometrics MGP2 gas mixer with 4 Bronkhorst Mass-Flow Controllers. Constant flow of 200 ml/min was kept for the gas measurements. A Keithley 2602A dual Source Measure Unit allowed to control simultaneously the sensor's resistance and the voltage for heating the microhotplate. Electrical measurements and flowing gases were controlled by a home-developed Labview software.

Several gas sensors containing, each of them, one single contacted In_2O_3 NW was characterized towards different gases

(ethanol, CO and NO₂) by allowing first 3 h to stabilize the baseline and then exposing the sensor for 1 h to an atmosphere containing the specific gas to be tested for and, afterwards, to synthetic air for 1 h to recover the baseline. This sequence was repeated for the different concentrations for dry characterization.

Due to the reduced diameter of the NWs, the current applied to measure their resistance may easily damage or even destroy the sensor. For this reason, NWs were electrically tested under two and four probe configurations with very low current values, typically between 1 and 100 nA [28]. Most of the NWs showed non-linear symmetric I–V characteristics in two-probe measurements at room temperature. This doubly-rectifying behaviour possibly originates in the Schottky barrier between the In₂O₃ NW and the amorphous C–Pt deposition obtained (by Focused Electron Beam Induced Deposition (FEBID)) in the absence of interface states, as reported for other NWs [27–29]. This barrier accounts for the differences between the work function of the C–Pt group and the electron affinity of In₂O₃. The experimental high resistance values arising from the contacts due to the high carbon content are minimized in the 4-probe measurements because of the much lower contribution of the Schottky barrier. Ohmic behaviour is observed when the NWs are heated above 150 °C, which are the lowest operating temperatures employed in this work, thus completely removing the contribution of the barrier.

The response of metal oxides resistors to changes of the surrounding gas atmosphere is accounted through resistance changes in the sensor. The sensor's response is defined [25] as the relative change of resistance divided by the resistance value in synthetic air, according to:

$$S(\%) = \frac{R_{SA} - R_{gas}}{R_{SA}} \times 100 = \left(1 - \frac{R_{gas}}{R_{SA}}\right) \times 100 \quad (1)$$

In₂O₃ NWs have been tested towards ethanol, CO and NO₂. Different concentrations of ethanol and CO, from 10 to 100 ppm, at

various temperatures, between 100 and 300 °C, were tested. For NO₂ concentrations from 1 to 5 ppm at various temperatures were tested.

3. Results and discussion

3.1. Physical characterization

3.1.1. Morphological characterization

Different morphologies, shown in Fig. 2, were obtained under the here employed growth parameters. Highly anisotropic nanostructures, like NWs, require the presence of a Au catalyst confirming the VLS growth method, while other nanostructures, like octahedral microparticles, form through a non-Au supported mechanism (Fig. 2c). The presence of a mixture of the different structures on the substrates suggests that a competition of the growth mechanisms exists under the given experimental conditions.

The partial pressure of the gas components appears to be the main parameter controlling the morphology of the deposited structures. The process starts with the carbothermal reduction of In₂O₃ to In_xO ($x = 1, 2$) vapour [30,31]. After that, in the octahedral growth case, a nucleation stage is initiated and non-stoichiometric indium oxide nuclei are formed either via gas phase nucleation or at the substrate's surface. The growth can proceed via this metal-free growth mechanism, forming preferentially octahedral structures with (111) facets, which is accompanied by the deactivation of the catalyst layer with an oxygen partial pressure equal or below 0.01%, leading to a non-catalysed growth.

The desired NWs preferentially form at oxygen concentration values between 0.01 and 0.02%. The first step of the formation is, again, a carbothermal reduction, giving rise to a sub-stoichiometric indium oxide vapour. However, in this case, a more oxidizing ambient promotes the formation of In₂O₃ NWs, which is supported by the Au nucleation layer. The indium oxide vapour species are

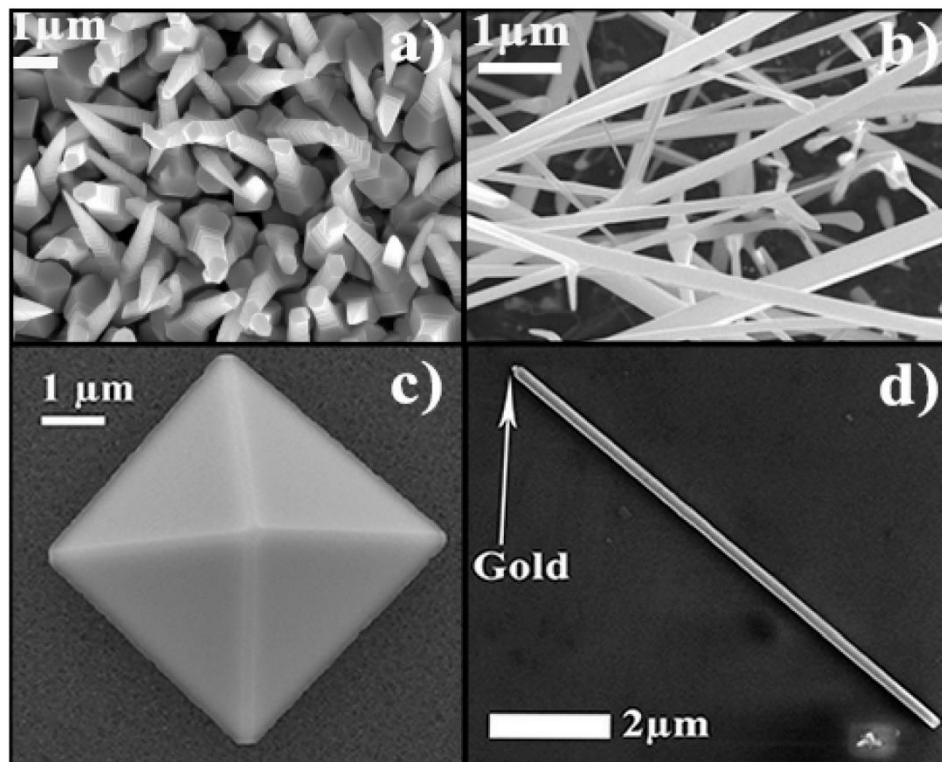


Fig. 2. Scanning electron microscopy images corresponding to (a) grown nanorods, (b) grown nanowires, (c) grown octahedral structure and (d) a single NW with a visible gold tip.

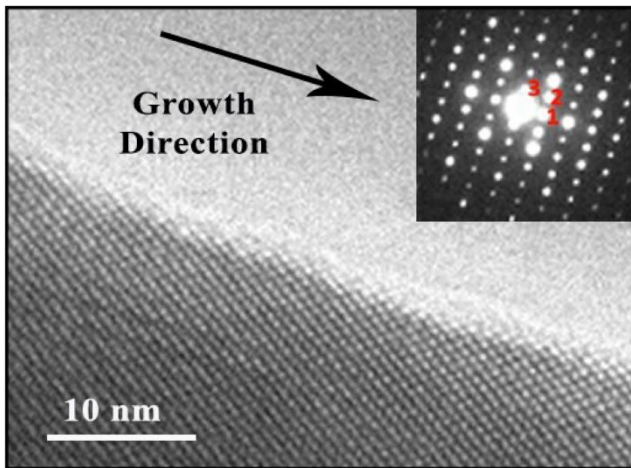


Fig. 3. High resolution transmission electron microscopy image of an indium oxide nanowire and selected area electron diffraction pattern of the nanowire, which corresponds to the [011] zone axis, being the spots labelled 1–3 corresponding to the $\{200\}$, $\{0\bar{1}1\}$ and $\{2\bar{1}1\}$ planes, respectively.

adsorbed preferentially by the gold catalyst and the nucleation of the In_2O_3 NW occurs at the Au/substrate interface in contrast to the heterogeneous nucleation, as described before. With the continuous flow of indium oxide vapour the gold growth promoter supports the growth of anisotropic crystals according to the VLS mechanism, as shown in Fig. 2b and d. In addition, the different oxygen partial pressures can influence the morphology of the deposits, which also have different surface facets as a termination and, therefore, surface energies are influencing the nanostructure morphology [32]. It is also reported [30] that reducing atmospheres promote the growth of nanoarrows (NWs terminated by octahedral structures, see Fig. 2a). For oxygen concentration higher than 0.02% other morphologies are promoted, like nanorods, nanoneedles or dendritic growth.

The NWs growth was found to be promoted at different source distances, which seems to indicate that it is related with variations of the experimental parameters. The grown NWs were observed at two different source distances, namely between 3 and 5 cm and between 16 and 20 cm, the former corresponding to a sample temperature of about 900 °C, while the latter, to about 720 °C.

3.1.2. Structural characterization

Among the several different morphologies, NWs have been further selected for TEM analysis. The morphology and the crystalline structure of the In_2O_3 NWs have been studied by SEM and TEM, as shown in Figs. 2 and 3. The NWs are monocrystalline, with a cubic structure and a lattice parameter of (1.005 ± 0.05) nm, with good agreement to the reported values in literature [32,33]. The growth direction is identified by the selected area electron diffraction (SAED) pattern in Fig. 3. The corresponding diffraction pattern allows to identify the growth direction to be (100), identified by the spot labelled 1 (corresponding to the $\{200\}$ plane). The whole diffraction pattern is in agreement with the [011] zone axis of cubic In_2O_3 .

XRD in Bragg-Brentano and grazing incidence configurations has been also used to study the crystalline properties of the grown structures on the different substrates. Again, the work is focused on the NWs, thus, XRD has been used to confirm their crystalline structure, Fig. 4. The results show a cubic structure corresponding to space group Ia3 with a lattice parameter of 1.0118 nm, perfectly matching the reported value in literature [36–38].

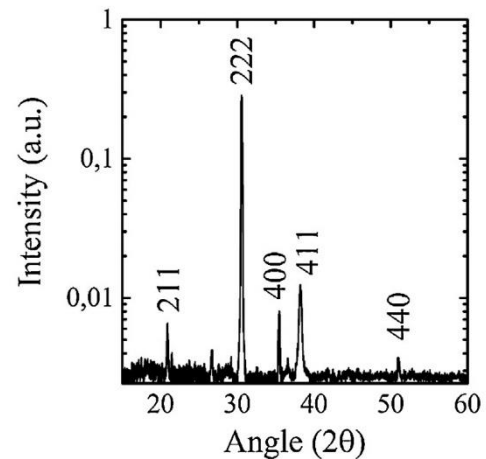


Fig. 4. X-Ray diffraction pattern for indium oxide nanowires with reflections. Matching with the reference for cubic indium oxide (JCPDS 6-416 used to index the XRD). The contribution for the amorphous silicon oxide corresponding to the background has been subtracted.

3.1.3. Photoluminescence characterization

All the nanostructures grown in the studied range give rise to a sizeable PL emission in the visible spectrum (measured range: 370–850 nm). The spectrum is dominated by an intense, wide PL band centred at around 600 nm, while an additional shoulder appears at a lower wavelength in some of the samples. A spectra subtraction has been carried out, revealing a broad additional symmetrical band centred at about 475 nm in the case of NWs.

The assignment of the PL features to specific emitting centres of nanostructured In_2O_3 has been widely discussed in the literature by other groups [33–36]. Their results fairly agree with ours, but some differences exist, due to the large variety of crystalline structures appearing with this material, and further studies are required to clarify the origin of these differences in PL emission [37–40].

The presence of oxygen vacancies that act as recombination centres is a well-established occurrence, and is thought to be the responsible of the main PL band peaked around 600 nm, observed in bulk In_2O_3 materials [31]. When the dimensionality is reduced, additional weaker PL bands can make their appearance. Their attribution is still under debate, and a multifold of cases have been reported: depending on the specific morphology of the grown structures, the new PL bands are located in the UV range, in the blue–green range, or even in the near infrared portion of the spectrum [17].

In our nanostructures, the structural change is followed by a variation of the PL spectrum, as shown in Fig. 5. In the case of bulk-

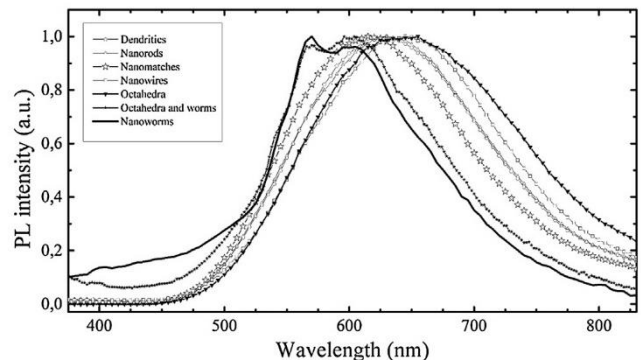


Fig. 5. Photoluminescence spectra of different indium oxide nanostructures, whose scanning electron microscopy images are shown in Fig. 4 at supplemental information.

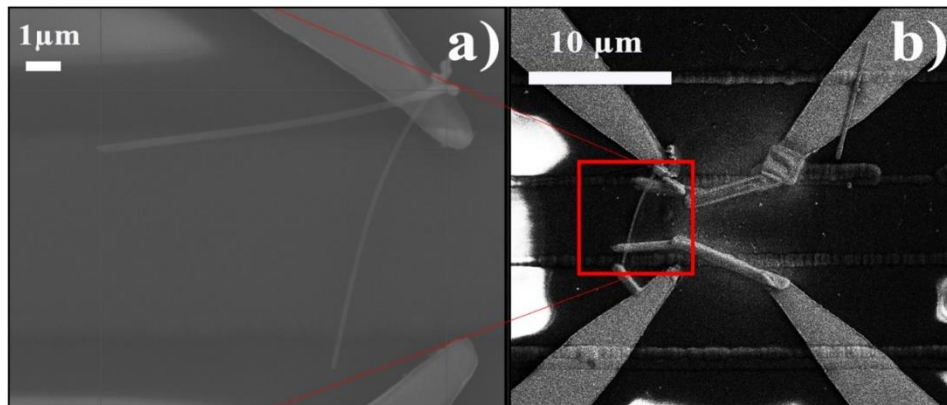


Fig. 6. (a) Indium oxide nanowire over an electrode on top of a suspend microhotplate used to produce a gas sensor. (b) Indium oxide nanowire from image (a) already contacted using focused ion beam techniques.

like material the spectrum is dominated by the above-mentioned wide, well defined band peaked at 600 nm. When very small NW-like morphologies are studied, weaker bands show up (they may appear just as a shoulder of the main band). Their origin can be related to the widening of the electronic band gap in materials with reduced dimensionality. An alternative explanation would take into account the fact that in such small structures, where the surface-to-volume ratio is strongly enhanced, the oxygen vacancy defects are more likely to be modified by impurities, incorporated during the growth or adsorbed at the surface, or by stress from the surrounding media.

Reproducible correlation between structural and optical features of the grown material have been observed, establishing a PL fingerprint for each kind of fabricated nanostructure.

3.2. Gas response of single NW-based sensors

The resistance of In_2O_3 NWs studied at room temperature have values ranging from (2 ± 0.08) to (130 ± 5) M Ω and decreases around a 30% for increasing temperatures up to 300 °C. This large variation in resistance at room temperature is due to the NW-contacting material interface barrier, but that disappears when above 150 °C. The conductivity associated to this resistances and the physical parameters for this NW range from $\rho_0 = 0.3 \Omega \text{ m}$ to $\rho_0 = 0.95 \Omega \text{ m}$. The observed change in resistance with increasing temperature is associated to the excitation of the majority charge carriers. The NWs from the studied sensors have a diameter between 140 and 220 nm and effective lengths between contacts from 3 to 5 μm , as can be seen in Fig. 6b.

The change in resistance against ethanol, NO_2 and CO in synthetic air has been measured for three individual In_2O_3 NW based sensor. For NO_2 and CO the sensors provided a response lower than 10%, even taking into account the high level of these gases, well above the limit safe values. For this reason the study is focused in ethanol sensing and the response of the NWs towards both gases are included in the Supplementary material.

The resistance evolution of one sensor at 200, 250 and 300 °C is represented in Fig. 7, where the decrease in resistance in the presence of ethanol is observed. This decrease is in agreement with the one expected for an n-type semiconductor gas sensor. The same behaviour is observed for the other sensors, with small variations in the response level. An average response of the different sensors at different temperatures is shown in Figs. 8 and 9. The response of the sensor at 100 °C is negligible and increases with the temperature. Due to the very limited variation of the NWs diameter of only a 50%, no clear correlation between this parameter and the sensing behaviour is observed.

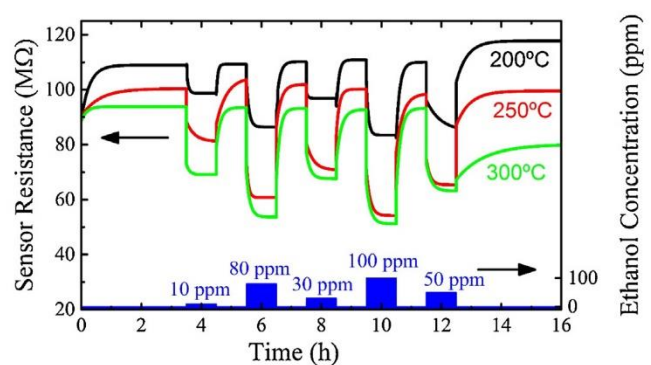


Fig. 7. Resistance evolution of individual indium oxide nanowire based sensor towards 10, 80, 30, 100 and 50 parts per million of ethanol concentration at 200, 250 and 300 °C.

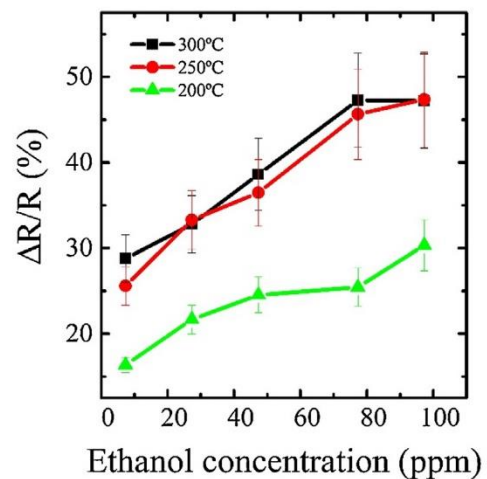


Fig. 8. Response of 3 sensors based on individual indium oxide nanowire towards ethanol in synthetic air at 300 °C.

The optimal sensing behaviour for all the sensors tested was obtained at 300 °C, where the maximum response and lowest response and recovery times were obtained. It is evident that in the measured ethanol concentration ranging from 10 to 100 ppm the sensor response increases with the concentration. The response time is defined as the time to evolve from the 10% to the 90% of the response. The obtained values of In_2O_3 NWs response time at 300 °C range between 4 and 12 min and increases with ethanol con-

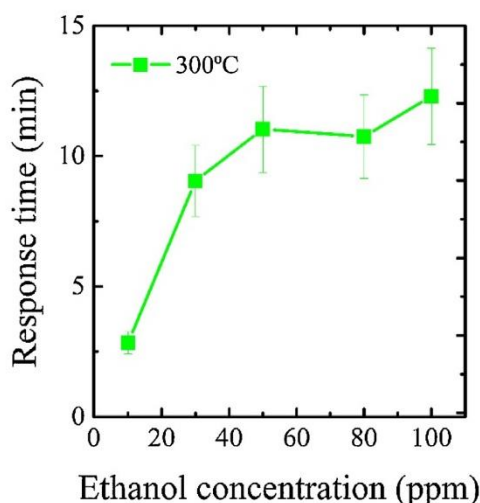


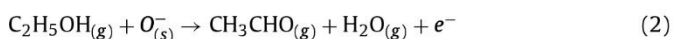
Fig. 9. Response time of individual indium oxide nanowire devices for different ethanol concentrations in synthetic air at 300 °C.

centration values (Fig. 9). The recovery time is found between 35 and 45 min at temperatures between 200 and 300 °C.

The most accepted sensing mechanisms in metal oxide materials consists in the chemisorption of oxidizing gases in adsorption sites and the oxidation of reducing gases by previously chemisorbed oxygen at the surface of the metal oxide, when no additives are present on the surface [41]. The substoichiometric surface of the metal oxide allows the interaction with gas molecules. The molecular or atomic oxygen chemisorption, for instance, captures a free electron from the conduction band giving adsorbed O_2^- or O^- respectively. Thus, the accumulated surface charge leads to a surface depletion layer of majority carriers, since In_2O_3 is n-type wide band gap semiconductor, and to a surface potential barrier that determines the resistance of the nanostructure. Consequently, the conductivity is reduced for In_2O_3 when oxygen is chemisorbed at the surface, due to the depletion layer that reduces the effective channel width through which the current flows [42].

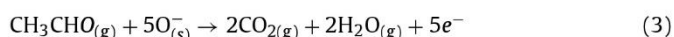
In the case of ethanol, a decrease in the sensor resistance is induced, as can be seen in Fig. 7. Ethanol dehydration and dehydrogenation are two possible mechanisms explaining this sensing behaviour [43–47].

The process is rather complicated and, in addition to adsorbed species, different gaseous intermediates, such as acetaldehyde, acetone, ethylene and carbon monoxide, can be formed [43]. The dehydrogenation of ethanol into acetaldehyde and the dehydration of ethanol into ethylene are initial steps and these gaseous products can be further oxidized by the metal oxide and the associated chemisorbed oxygen species. The dehydrogenation process is more likely in the case of material with basic surfaces. Due to the fact that In_2O_3 is a basic material, the main intermediate product of ethanol is acetaldehyde [44,47] described by the following reaction:



At temperatures above 150 °C ionized atomic oxygen species, O^- , are adsorbed on the surface producing ethoxide moieties and protons. Then, the ethoxide is further dehydrogenated/oxidized to acetaldehyde molecule and the resulting protons are desorbed resulting in hydrogen or water molecules increasing the conductivity. Acetaldehyde reacts with ionized atomic oxygen and produces carbon dioxide and water vapour after complete oxidation (Eq. (3)). The conversion of the initially ionized atomic oxygen to CO_2 and water vapour is accompanied by a reduction of the negative charges

accumulated at the surface, thus increasing the conductance of the metal oxide NW because of the diminishing depletion zone at the surface [44].



The adsorption and desorption of gas species occur continuously until a steady state is reached, where gas sensor obtains the final resistance value. The reactions with the metal oxide surface depends on the temperature and at temperatures higher than 150–200 °C the metal oxide surface promotes catalytic processes against adsorption/desorption ones [47]. Therefore, the response to ethanol is promoted at higher temperatures as observed in these measurements.

For the case of CO and NO_2 , although one could expect a good response, the observed values are below 10%, even in high concentrations up to 100 ppm for CO and 5 ppm for NO_2 . The reason for such behaviour is not well known and further experiments should be carried out to gain more insight in the fundamental processes upon adsorption of three gases.

4. Conclusions

In this work, the growth of In_2O_3 nanostructures via a carbothermal supported CVD process has been carried out. While changing the growth conditions, different nanostructures have been formed, showing that the main growth parameters determining the different morphologies are the oxygen concentration and the substrate's temperature. For NW growth, interesting for gas sensor applications, a 0.01 and 0.02% oxygen concentration range was used. Gas sensors based on individual NWs, using a low power microhotplate as electronic platform, were produced and showed a high response to ethanol, with resistance variations up to 50% at concentration ranges between 10 and 100 ppm. The obtained response and recovery times as low as 4 and 35 min, respectively, were obtained. This gas response could be explained by the ethanol dehydrogenation occurring at the surface of the In_2O_3 NW. The response is considerably higher than for the case of CO and NO_2 , where response values lower than 10% have been observed in all the studied temperature range.

Acknowledgment

The research leading to these results has been partially funded by the Spanish Ministerio de Economía y Competitividad, through project TEC2013-48147-C6.

Appendix A. Supplementary data

Supplementary data associated with this article can be found, in the online version, at <http://dx.doi.org/10.1016/j.snb.2016.07.084>.

References

- [1] C. Li, D. Zhang, S. Han, X. Liu, T. Tang, B. Lei, Synthesis, electronic properties, and applications of indium oxide nanowires, *Ann. N. Y. Acad. Sci.* 121 (2003) 104–121, <http://dx.doi.org/10.1196/annals.1292.007>.
- [2] K.K. Makhija, A. Ray, R.M. Patel, U.B. Trivedi, H.N. Kapse, Indium oxide thin film based ammonia gas and ethanol vapour sensor, *Bull. Mater. Sci.* 28 (2005) 9–17, <http://dx.doi.org/10.1007/BF02711165>.
- [3] G. Korotcenkov, V. Brinzari, J.R. Stetter, I. Blinov, V. Blaja, The nature of processes controlling the kinetics of indium oxide-based thin film gas sensor response, *Sens. Actuators B* 128 (2007) 51–63, <http://dx.doi.org/10.1016/j.snb.2007.05.028>.
- [4] G. Korotcenkov, M. Ivanov, I. Blinov, J.R. Stetter, Kinetics of indium oxide-based thin film gas sensor response: the role of redox and adsorption/desorption processes in gas sensing effects, *Thin Solid Films* 515 (2007) 3987–3996, <http://dx.doi.org/10.1016/j.tsf.2006.09.044>.

- [5] N. Singh, R.K. Gupta, P.S. Lee, Gold-nanoparticle-functionalized In₂O₃ nanowires as CO gas sensors with a significant enhancement in response, *ACS Appl. Mater. Interfaces* (2011) 2246–2252.
- [6] J.D. Prades, S. Barth, A. Cirera, S. Mathur, J.R. Morante, Ultralow power consumption gas sensors based on self-heated individual nanowires, *Appl. Phys. Lett.* (2014) 8–11, <http://dx.doi.org/10.1063/1.2988265>, 123110.
- [7] G. Shen, B. Liang, X. Wang, P. Chen, C. Zhou, Indium oxide nanospirals made of kinked nanowires, *Am. Chem. Soc.* 5 (2011) 2155–2161, <http://dx.doi.org/10.1021/nn103358y>.
- [8] M. Tonezzer, N.V. Hieu, Size-dependent response of single-nanowire gas sensor, *Sens. Actuators B* 163 (2012) 146–152, <http://dx.doi.org/10.1016/j.snb.2012.01.022>.
- [9] C. Hsu, J. Tsai, T. Hsueh, Ethanol gas and humidity sensors of Cu/CuO₂ composite nanowires based on a Cu through-silicon via approach, *Sens. Actuators B* 224 (2016) 95–102, <http://dx.doi.org/10.1016/j.snb.2015.10.018>.
- [10] O. Lupan, V. Cretu, V. Postica, M. Ahmadi, B.R. Cuenya, L. Chow, I. Tiginyanu, B. Viana, T. Pauporté, R. Adelung, Silver-doped zinc oxide single nanowire multifunctional sensor with a significant enhancement in response, *Sens. Actuators B* 223 (2016) 893–903, <http://dx.doi.org/10.1016/j.snb.2015.10.002>.
- [11] N.D. Cuong, Y.W. Park, S.G. Yoon, Chemical Microstructural and electrical properties of Ga₂O₃ nanowires grown at various temperatures by vapor–liquid–solid technique, *Sens. Actuators B* 140 (2009) 240–244, <http://dx.doi.org/10.1016/j.snb.2009.04.020>.
- [12] A. Qurashi, E.M. El-maghraby, T. Yamazaki, T. Kikuta, Catalyst supported growth of In₂O₃ nanostructures and their hydrogen gas sensing properties, *Sens. Actuators B* 147 (2010) 48–54, <http://dx.doi.org/10.1016/j.snb.2010.03.024>.
- [13] M. Meyyappan, M. Sunkara, Inorganic Nanowires Applications, properties and characterization (2009). ISBN: 978-1-4200-6783-5.
- [14] X. Lai, D. Wang, N. Han, J. Du, J. Li, C. Xing, et al., Ordered arrays of bead-chain-like In₂O₃ nanorods and their enhanced sensing performance for formaldehyde, *Chem. Mater.* (2010) 3033–3042, <http://dx.doi.org/10.1021/cm100181c>.
- [15] D. Maestre, H. Dietrich, A. Cremades, J. Wolfgang, J. Piqueras, Nanopipes in In₂O₃ nanorods grown by a thermal treatment, *Cryst. Growth Des.* 11 (2011) 1117–1121, [10.1021/cg101350f](http://dx.doi.org/10.1021/cg101350f).
- [16] J. Du, M. Yang, S.N. Cha, D. Rhen, M. Kang, Microcubes and nanorods: synthesis and optical properties, *Cryst. Growth Des.* 8 (2008) 2312–2317, <http://dx.doi.org/10.1021/cg701058v>.
- [17] D.A. Magdas, A. Cremades, J. Piqueras, Three dimensional nanowire networks and complex nanostructures of indium oxide, *J. Appl. Phys.* 100 (2006), <http://dx.doi.org/10.1063/1.2372435>, 094320–094320-5.
- [18] W. Yang, P. Wan, X. Zhou, J. Hu, Y. Guan, L. Feng, Self-assembled In₂O₃ truncated octahedron string and its sensing properties for formaldehyde, *Sens. Actuators B* 201 (2014) 228–233, <http://dx.doi.org/10.1016/j.snb.2014.05.003>.
- [19] S. Barth, M.S. Seifner, J. Bernardi, Growth of monocrystalline In₂O₃ by a seed orientation dependent vapour–solid–solid mechanism, *J. Mater. Chem. C* 2 (2014) 5747–5751, <http://dx.doi.org/10.1039/C4TC00878B>.
- [20] M.J. Zheng, L.D. Zhang, G.H. Li, X.Y. Zhang, X.F. Wang, Ordered indium-oxide nanowire arrays and their photoluminescence properties, *Appl. Phys. Lett.* 79 (2001) 839–841, <http://dx.doi.org/10.1063/1.1389071>.
- [21] F.I. Lai, S.Y. Kuo, W.T. Lin, W.C. Chen, C.N. Hsiao, Y.K. Liu, J.L. Shen, Photoluminescence studies of indium nitride films grown on oxide buffer by metalorganic molecular-beam epitaxy, *J. Cryst. Growth* 320 (2011) 32–35, <http://dx.doi.org/10.1016/j.jcrysgro.2010.12.020>.
- [22] A.M. Morales, C.M. Lieber, A laser ablation method for the synthesis of crystalline semiconductor nanowires, *Science* 279 (1998) 208–211, <http://dx.doi.org/10.1021/ar00368075>.
- [23] N. Singh, T. Zhang, P.S. Lee, The temperature-controlled growth of In₂O₃ nanowires, nanotowers and ultra-long layered nanorods, *Nanotechnology* 20 (2009), <http://dx.doi.org/10.1088/0957-4484/20/19/195605>, 195605, 7pp.
- [24] S. Barth, R. Jimenez-Díaz, J. Daniel Prades, I. Gracia, J. Santander, C. Cane, et al., Localized growth and *in situ* integration of nanowires for device applications, *Chem. Commun.* 48 (2012) 4734–4736, <http://dx.doi.org/10.1039/c2cc30920c>.
- [25] J. Samà, S. Barth, G. Domènech-Gil, J.D. Prades, A. Romano-Rodríguez, N. López, O. Casals, et al., Localised grown SnO₂ NWs on heated Micromembranes for efficient ammonia sensors in humid conditions, *Sens. Actuators B* (2016), <http://dx.doi.org/10.1016/j.snb.2016.03.091>.
- [26] R.S. Wagner, W.C. Ellis, The vapor–liquid–solid mechanism of crystal growth and its application to Silicon, *Appl. Phys. Lett.* 233 (1965) 1053–1064.
- [27] A. Vilà, F. Hernández-Ramírez, J. Rodríguez, O. Casals, A. Romano-Rodríguez, J.R. Morante, M. Abid, Fabrication of metallic contacts to nanometre-sized materials using a focused ion beam (FIB), *Mater. Sci. Eng.* 26 (2006) 1063–1066, <http://dx.doi.org/10.1016/j.msec.2005.09.092>.
- [28] F.H. Ramírez, Fabrication Strategies and Electrical Characterisation of nanodevices Fabricated with Focused Ion Beam Techniques Tesis (2007).
- [29] S. Mathur, F. Hernández-Ramírez, A. Tarancón, O. Casals, J. Rodríguez, A. Romano-Rodríguez, J.R. Morante, S. Barth, T. Choi, D. Poulikakos, V. Callegari, P.M. Nellen, Fabrication and electrical characterization of circuits based on individual tin oxide nanowires, *Nanotechnology* 17 (2006) 5577–5583, <http://dx.doi.org/10.1088/0957-4484/17/22/009>.
- [30] D. Calestani, M. Zha, A. Zappettini, L. Lazzarini, L. Zanotti, In-catalyzed growth of high-purity indium oxide nanowires, *Chem. Phys. Lett.* 445 (2007) 251–254, <http://dx.doi.org/10.1016/j.cplett.2007.07.089>.
- [31] J.P. Singh, M. Kumar, B.R. Mehta, V.N. Singh, Tunable synthesis of indium oxide octahedra, nanowires and tubular nanoarrow structures under oxidizing and reducing ambients, *Nanotechnology* 20 (2009) 235608, <http://dx.doi.org/10.1088/0957-4484/20/23/235608>.
- [32] P. Agoston, K. Albe, Thermodynamic stability, stoichiometry, and electronic structure of bcc-In₂O₃ surfaces, *Phys. Rev. B* 84 (2011) 043511, <http://dx.doi.org/10.1103/PhysRevB.84.043511>.
- [33] G. Cheng, E. Stern, S. Guthrie, M.A. Reed, R. Klie, Y. Hao, G. Meng, L. Zhang, Indium oxide nanostructures, *Appl. Phys. A* 85 (2006) 233–240, <http://dx.doi.org/10.1007/s00339-006-3706-x>.
- [34] X.S. Peng, Y.W. Wang, J. Zhang, X.F. Wang, L.X. Zhao, G.W. Meng, Large-scale synthesis of In₂O₃ nanowires, *Appl. Phys. A* 74 (2002) 437–439, <http://dx.doi.org/10.1007/s003390101037>.
- [35] H.T. Ng, P. Nguyen, T. Yamada, M.K. Smith, J. Li, J. Han, Direct integration of metal oxide nanowire in vertical field-effect transistor, *Nano Lett.* 4 (2004) 651–657, <http://dx.doi.org/10.1021/nl0498536>.
- [36] X.C. Wu, J.M. Hong, Z.J. Han, Y.R. Tao, Fabrication and photoluminescence characteristics of single crystalline In₂O₃ nanowires, *Chem. Phys. Lett.* 373 (2003) 28–32, [http://dx.doi.org/10.1016/S0009-2614\(03\)00582-7](http://dx.doi.org/10.1016/S0009-2614(03)00582-7).
- [37] N.M. a. Hadia, H. a. Mohamed, Synthesis, structure and optical properties of single-crystalline In₂O₃ nanowires, *J. Alloys Compd.* 547 (2013) 63–67, <http://dx.doi.org/10.1016/j.jallcom.2012.08.116>.
- [38] G. Wang, J. Park, D. Wexler, M.S. Park, Characterization, and optical properties of In₂O₃ semiconductor nanowires, *J. Synth.* 46 (2007) 4778–4780.
- [39] X. Liu, L. Zhou, R. Yi, N. Zhang, R. Shi, G. Gao, Single-crystalline indium hydroxide and indium oxide microcubes: synthesis and characterization, *J. Phys. Chem. C* 112 (2008) 18426–18430, <http://dx.doi.org/10.1021/jp802778p>.
- [40] M. Cao, B. Wei, Vertically well-aligned In₂O₃ cone-like nanowire arrays grown on indium substrates, *Eur. J. Inorg. Chem.* (2011) 1570–1576, <http://dx.doi.org/10.1002/ejic.201001071>.
- [41] P.T. Moseley, Solid state gas sensors, *Meas. Sci. Technol.* 8 (1997) 223–237, <http://dx.doi.org/10.1088/0957-0233/8/3/003>.
- [42] N. Barsan, U. Weimar, Conduction model of metal oxide gas sensors, *J. Electroceram.* 7 (2001) 143–167, <http://dx.doi.org/10.1023/A:1014405811371>.
- [43] S. Sänze, A. Gurlo, C. Hess, Monitoring gas sensors at work: operando raman–FTIR study of ethanol detection by indium oxide, *Angew. Chem. Int. Ed.* (2013) 3607–3610, <http://dx.doi.org/10.1002/anie.201207258>.
- [44] F. Gu, L. Zhang, Z. Wang, D. Han, G. Guo, Fine-tuning the structure of cubic indium oxide and their ethanol-sensing properties, *Sens. Actuators B* 193 (2014) 669–678, <http://dx.doi.org/10.1016/j.snb.2013.12.026>.
- [45] S. Sänze, C. Hess, Ethanol gas sensing by indium oxide: an operando spectroscopic Raman–FTIR study, *J. Phys. Chem. C* 118 (2014) 25603–25613, <http://dx.doi.org/10.1021/jp509068s>.
- [46] N. Yamazoe, G. Sakai, K. Shimano, Oxide semiconductor gas sensors, *Catal. Surv. Asia* 7 (2003) 63–75, <http://dx.doi.org/10.1023/A:1023436725457>.
- [47] O. Lupan, V. Cretu, V. Postica, N. Ababii, O. Polonskyi, V. Kaidas, F. Schütt, Y.K. Mishra, E. Monico, I. Tiginyanu, V. Sontea, T. Strunskus, F. Faupel, R. Adelung, Enhanced ethanol vapour sensing performances of copper oxide nanocrystals with mixed phases, *Sens. Actuators B* 224 (2016) 434–448, <http://dx.doi.org/10.1016/j.snb.2015.10.042>.

Biographies

Guillem Domènech-Gil was born in Barcelona in 1986. He graduated in physics at University of Barcelona in 2009 and obtained a master degree in nanoscience and nanotechnology at the same faculty in 2014. His research activities started with the growth of metal oxide nanowires for their employment as gas sensors main element towards toxic gases and fabricating nanodevices for monitoring environment. Coauthor at a MRS 2014 and in Eurosensors 2015 with poster and oral presentations. His doctoral studies are focused in enhancing the gas sensing technology through the use of nanostructures with a deeper comprehension of the sensing mechanisms occurring.

Sven Barth is a group leader at Vienna University of Technology, where he received the venia docendi for inorganic chemistry in 2015. He graduated in chemistry (2003) and received his Ph.D. (2008) from Saarland University. His core experience is related to the molecule-based synthesis and characterization of nanoscaled metal oxide and group 14 semiconductors. The nanomaterials are prepared in gas and liquid phase processes. He has published over 50 scientific papers, reviews and book chapters.

Jordi Samà was born in Barcelona in 1985. He received the degree in Physics at the University of Barcelona (UB) in 2010. Nowadays he is a predoctoral researcher in MIND group in Electronics Departament at UB. His current research is focused on the development and fabrication of nanostructured metal oxide gas sensors. His works also includes the structural and electrical characterization of the metal oxide nanostructures and the interaction mechanisms with toxic gases.

Paolo Pellegrino received the graduate degree in physics from the University of Pavia, Pavia, Italy, and the Ph.D. degree in electronic engineering from the Royal Institute of Technology, Stockholm, Sweden, in 1996 and 2001, respectively. Since 2002, he has been a Researcher at the Universitat de Barcelona, Barcelona. Since 2009 is associate professor at the same institution. He is coauthor of more than 80 papers in international journals, and other scientific contributions. His current inter-

ests include modeling and characterization of nanostructures, optical properties of semiconductors, as well as advanced photonic devices.

Isabel Gràcia received her Ph.D. degree in physics in 1993 from the Autonomous University of Barcelona, Spain, working on chemical sensors. She joined the National Microelectronics Center (CNM) working on photolithography, currently she is full time senior researcher in the Micro-Nano Systems department of the CNM and her work is focused on gas sensing technologies and MEMS reliability.

Carles Cané is Telecommunications Engineer and he received his Ph.D. in 1989. Since 1990 he is full time senior researcher at CNM and has been working in the development of CMOS technologies and also on mechanical and chemical sensors and microsystems. Since 2012, he is the director of the IMB-CNM in Barcelona. He is member of the technical committee of EURIMUS-EUREKA programme since 1999. Over the years he has been coordinator of several R&D projects, both at national and international level in the MST field.

Albert Romano-Rodríguez received his degree in Physics at the University of Barcelona in 1986. He immediately joined the group of Electronics at the Department of Applied Physics and Electronics (FAE) of the same university. In 1989 he joined the laboratory IMEC (Leuven, Belgium), where he worked out his Ph.D. in Physics, presented at the University of Barcelona (1991), on the application of electron microscopy for the development of ULSI devices. He continued in IMEC as post-doctoral fellow and returned to UB as researcher in 1991 and was appointed in 1993 as Professor Titular in electronics. His research activities are in the fields of structural, chemical and electrical characterization of electronic materials and processes employed in the electronic industries and in the development, characterization and test of chemical sensors. Dr. Romano has co-authored over 70 papers in international journals and over 120 contributions to conferences.

Supporting information

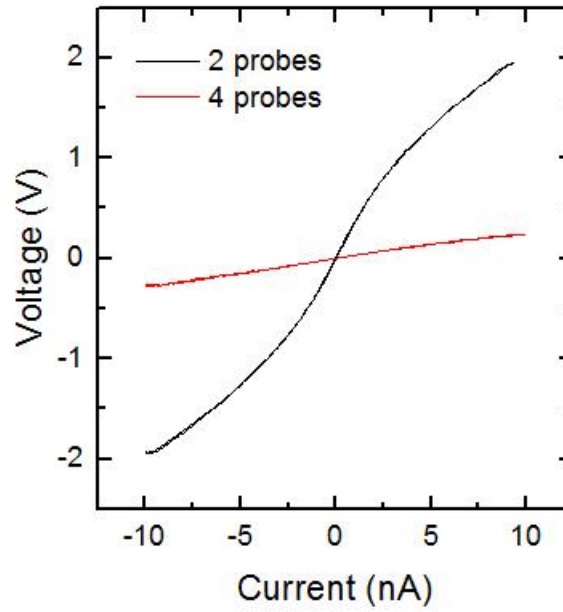


Fig. 1: current versus voltage test for a single indium oxide nanowire based sensor

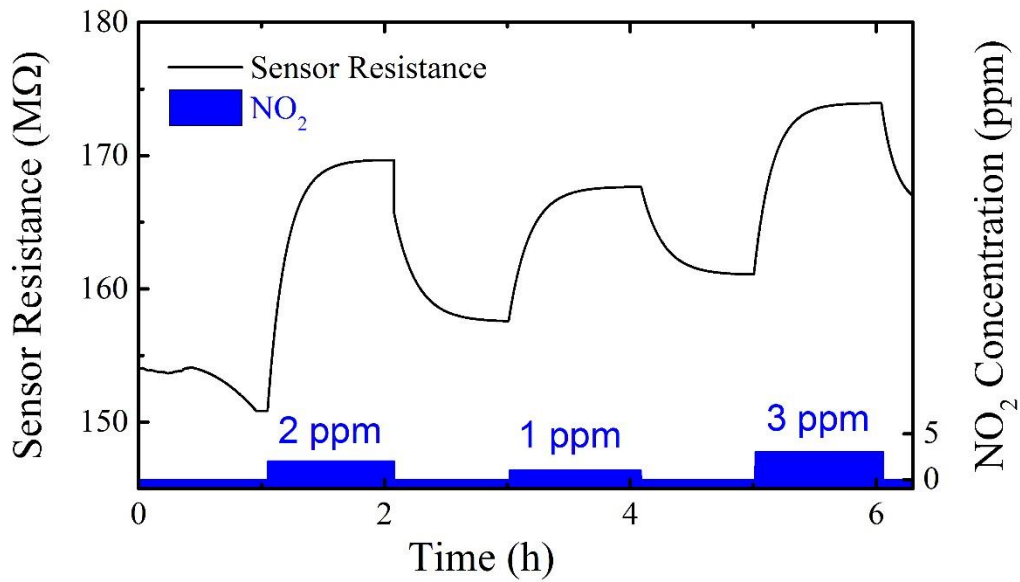


Fig. 2: response of a single indium oxide nanowire based sensor to different pulses of NO₂ at 300°C

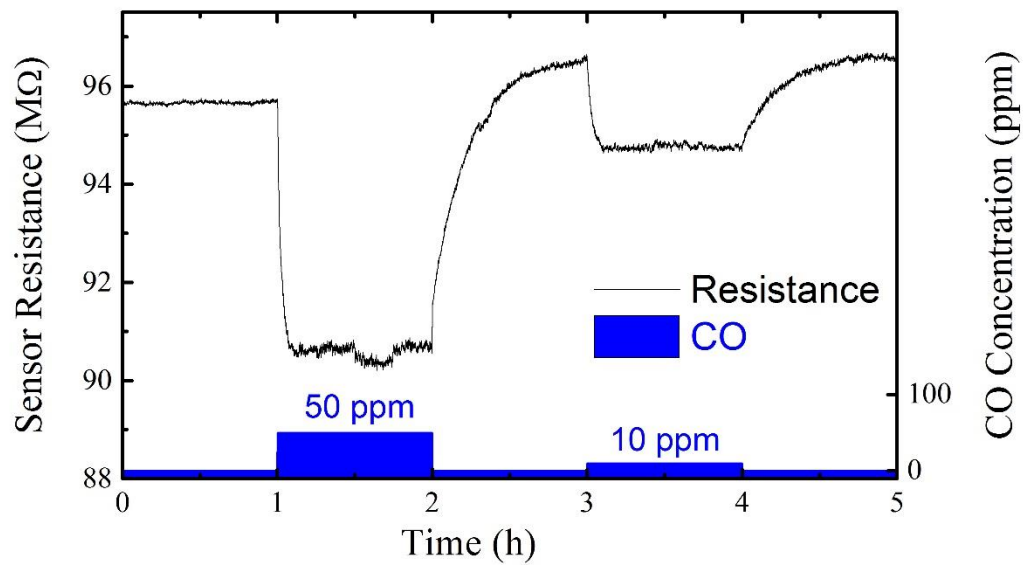


Fig. 3: response of a single indium oxide nanowire based sensor to different pulses of CO at 300°C

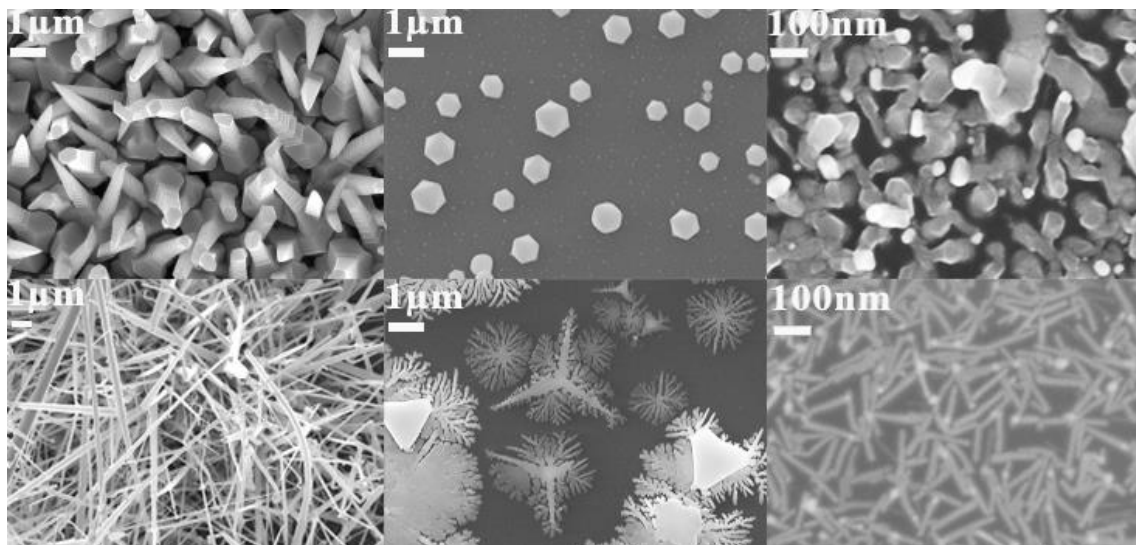


Fig. 4: SEM images corresponding to, from left to right starting for the upper line, nanorods, octahedral structures, nanoworms, nanowires, dendritic growth and nanomatches

3.2 Gas sensor based on individual gallium oxide nanowire

Humidity gas sensors made from individual Ga₂O₃ nanowires: impact of the carbothermal reduction synthesis method on their high selectivity and room temperature operation

*Guillem Domènech-Gil †,‡, Irmina Peiró †, Elena López-Aymerich †,‡, Jan Romano-deGea †,#,
Isabel Gràcia §, Christophe Serre †,‡, Paolo Pellegrino †,‡, Mauricio Moreno †,‡,
Carles Cané §, Sven Barth ||, Albert Romano-Rodríguez †,‡,**

† Institute of Nanoscience and Nanotechnology (IN2UB), Universitat de Barcelona (UB),
c/Martí i Franquès 1, 08028 Barcelona, Spain

‡ Department of Electronic and Biomedical Engineering, Universitat de Barcelona (UB), c/Martí
i Franquès 1, 08028 Barcelona, Spain

Department of Inorganic and Organic Chemistry, Universitat de Barcelona (UB), c/Martí i
Franquès 1, 08028 Barcelona, Spain

§ Centre Nacional de Microelectrònica - Institut de Microelectrònica de Barcelona, Consejo
Superior de Investigaciones Científicas (CSIC), Campus UAB, Carrer dels Til·lers, 08193
Bellaterra, Spain

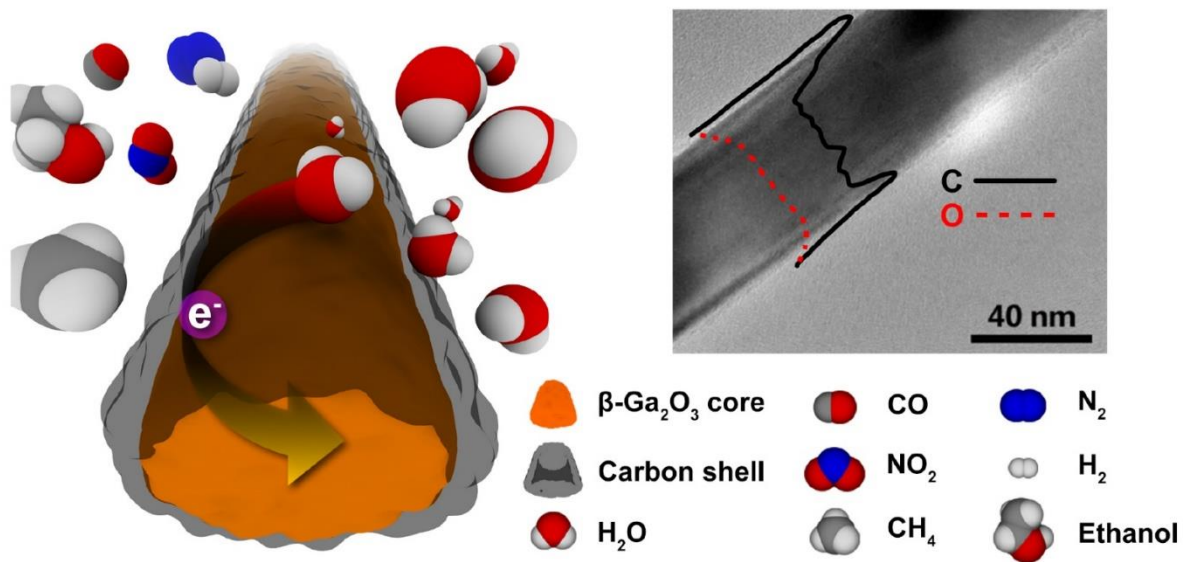
|| Physikalisches Institut, Goethe University Frankfurt, Max-von-Laue-Straße 1, 60438 Frankfurt
am Main, Germany

Abstract

Gallium oxide (Ga_2O_3) is a wide bandgap semiconducting material with application in the fields of high power, high temperature and gas sensing electronic devices. In this work we report the selective and fast detection of relative humidity at room temperature by chemoresistive gas sensors based on individual $\beta\text{-Ga}_2\text{O}_3$ nanowires (NWs), with negligible response to other gases. The synthesis has been carried out by a vapor-liquid-solid (VLS) method from mixtures of Ga_2O_3 powder and graphite, which produces core $\beta\text{-Ga}_2\text{O}_3$ NWs surrounded by a 4-10 nm-thick amorphous carbon shell. The measured room-temperature resistance variation as a function of relative humidity concentration can only be explained by the adsorption-desorption gas-solid reactions taking place at this carbon shell, as the commonly accepted interaction mechanisms for $\beta\text{-Ga}_2\text{O}_3$ occur at temperatures in excess of 150 °C. The interpretation of the NW material's response to changes in humidity can be related to the surface composition on the semiconductor NWs. Similarities to carbon-based sensor performance can be traced back to the carbon enrichment on the surface as a feature of the carbothermal reduction method used. This fact should be considered when reevaluating gas sensing data published in literature from nanostructured materials obtained using the carbothermal reduction.

KEYWORDS. gallium oxide nanowires, carbothermal reduction, carbon shell, fast and selective gas sensors, relative humidity

Abstract Graphic



3. Individual semiconducting metal oxide nanowires for gas sensing

β -Ga₂O₃ is a wide bandgap semiconducting material that is used in electronics for high power and high temperature devices.¹ This material offers the possibility to fabricate large single-crystals substrates at low cost using a melt-growth process, allowing the fabricated devices to surpass their performance in Si. In the gas sensing field, thin films of β -Ga₂O₃ are used as main element of high-temperature gas sensors.^{2,3} These devices have been reported to respond towards varying concentrations of oxygen (O₂), hydrogen (H₂), methane (CH₄) and carbon monoxide (CO) at temperatures above 600 °C, i.e., both to oxidizing and reducing gases. The sensing properties of the material have been largely studied and several improvements for its use as gas sensor have been achieved, either by introducing surface functionalization with metal-particles,⁴ dopants⁵ or by choosing morphologies that give rise to higher surface-to-volume ratios, such as NWs.^{6,7}

When compared to thin film-based gas sensors, the β -Ga₂O₃ nanostructure-based devices exhibit enhanced performances, one of the most important being the possibility to sense at considerably lower temperatures or even at room temperature. For example, pure β -Ga₂O₃ NWs decorated with Pt nanoparticles or covered with GaN nanometer-thick shells have been reported to exhibit high sensitivity towards CO at 50-100 °C,^{8,9} while nitrogen dioxide (NO₂) has been detected using Pd-doped β -Ga₂O₃ NW networks working at room temperature.¹⁰ The sensing of relative humidity using β -Ga₂O₃ NWs, however, has been scarcely reported.^{11,12} When dealing with individual β -Ga₂O₃ NW-based gas sensors, only one work can be found in literature,¹³ which presents the devices as sensors towards ammonia and nitrogen dioxide at room temperature.

In this work, we report very selective water vapor gas sensors based on individual β -Ga₂O₃ NWs operating between room temperature and 100°C, being completely insensitive to other interfering gases, like H₂, CH₄, ethanol (EtOH), CO and NO₂. This behavior^{14,15} is highly unusual for β -Ga₂O₃ and cannot be explained by the known gas-solid reactions occurring in Ga₂O₃ at this temperature

range. The observed response and selectivity, however, can be attributed to the presence of a 4-10 nm thick carbon shell around the NWs, which is the result of the material synthesis method, VLS, which in this experiment uses the carbothermal reduction of microcrystalline Ga₂O₃ mixed with graphite to generate the required vapor.

The NW growth is only observed in two regions of the quartz tube, located at 2-5 cm and at 28-31 cm from the evaporating source. These zones are kept at different temperatures, namely 950 and 820 °C, respectively. The sketch of the gas flow in the furnace tube and identification of these are shown in the supplementary information, Figure S1. The average diameter of the grown NWs is about 50 ± 20 nm, while their length depends on the region of formation, with values of $\sim 2 \pm 0.5$ μm for short and 12 ± 5 μm for the longer distance from the source material. Figure 1a shows a scanning electron microscopy (SEM) image of the NWs grown at the longer distance, while Figure S2 in the supplementary information allows comparing the morphology of the resulting NWs in both regions.

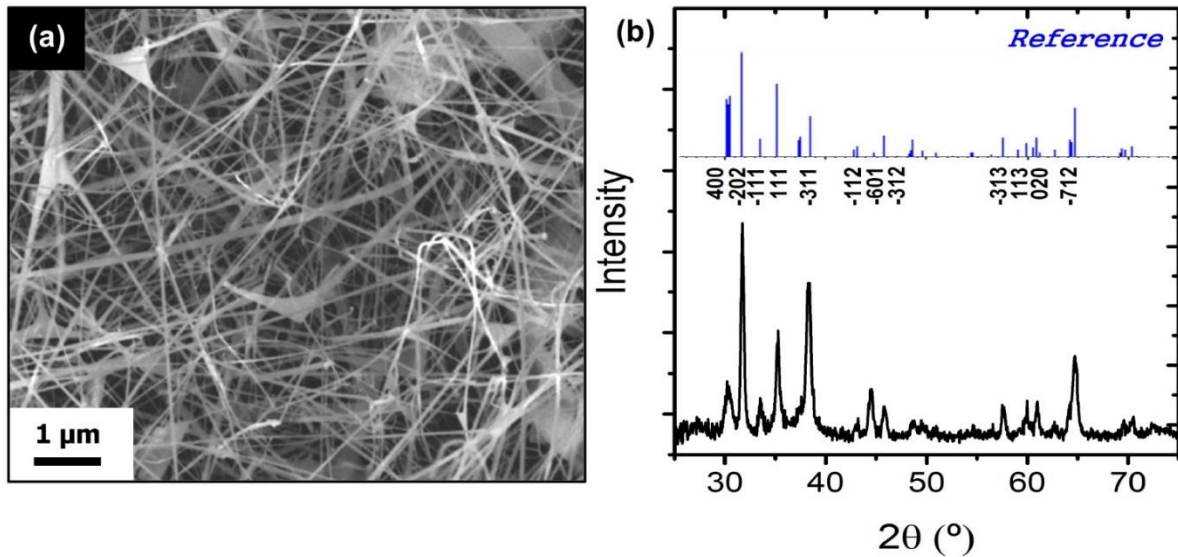


Figure 1. (a) Scanning electron microscope image of gallium oxide nanowires grown at 30 cm from the evaporation source. (b) Grazing incidence X-ray diffraction pattern for gallium oxide nanowires grown at 30 cm from the evaporating source, together with the reference data for monoclinic β -Ga₂O₃ (JCPDS 41-1103).

Under the different studied growth conditions, we can state that the presence of Au is essential to start the β -Ga₂O₃ NW growth, forming a liquid Au-Ga eutectic.^{16,17} However, the Au droplet must have a specific size (< 100 nm) to promote effectively the NW growth.¹⁸ In addition to the appropriate Au droplet size, the limiting factor of the NW's growth is the partial vapor pressure of the precursor material in gas phase, which varies as a function of the furnace geometry, as shown in the supporting information (Figure S1).

The grazing incidence X-ray diffraction (XRD) pattern obtained from the NWs, are presented in Figure 1b, after correction for the contribution of the SiO₂ substrate layer. The observed reflections match perfectly the standard monoclinic β -Ga₂O₃ structure (JCPDS 41-1103)¹⁹. The difference in

the relative intensity between the reflections of the sample and of the reference powder diffraction data can be attributed to preferential growth directions of the NWs.

X-ray photoelectron spectroscopy (XPS) measurements of the samples reveal confirm the presence of signals corresponding to gallium, silicon, oxygen and carbon, as shown in the supplementary information (Figure S3). The presence of carbon signal is a result of the carbothermal reduction growth method and could be due to carbon incorporation into the Ga_2O_3 lattice or to a surface carbon layer. To elucidate this, high-resolution XPS measurements have been carried out in the energy region corresponding to the carbon peak in the as-grown sample, after a 20-minute oxygen plasma treatment and after 3 days keeping the sample in air, as shown in Figure 2a. The results report that the carbon signal almost completely vanishes after the plasma treatment, which undoubtedly confirms that most of this carbon signal comes from a surface layer. The successive exposure to air gives rise to a new carbon-containing layer with a lower count number, suggesting that it is thinner than the as-grown one. The fitting of the carbon XPS signals for the as-grown (Figure 2b) and in air (Figure 2c) samples show that this does not correspond to the same carbon compound. These fitting parameters are listed in table I in the supplementary information. For the as-grown sample, only one peak, located at 285 eV, is required, which corresponds to C-C bonds and suggests the presence of a graphitic surface layer. The fitting of the spectrum of the sample in air, however, requires two peaks, centered at 285 and 286 eV, the latter being associated to C-O-C bonds²¹.

3. Individual semiconducting metal oxide nanowires for gas sensing

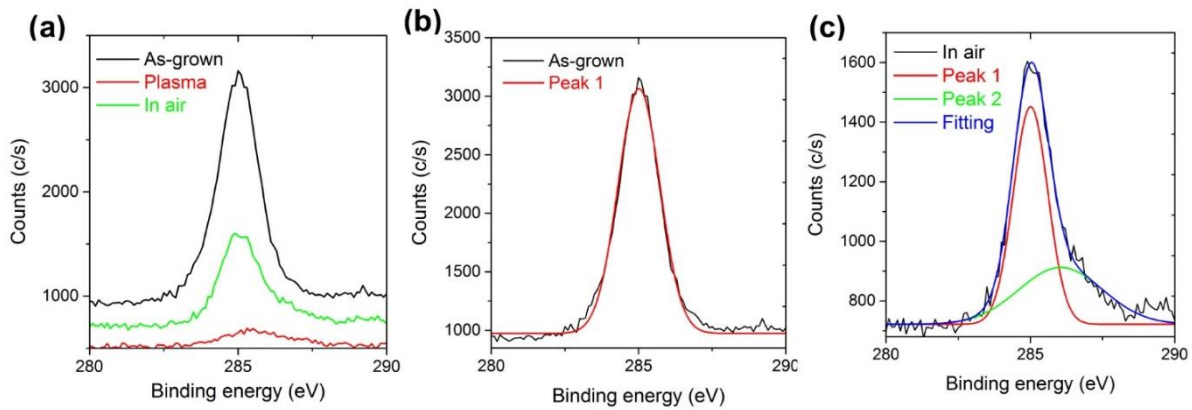


Figure 2. (a) XPS carbon measurements for Ga₂O₃ NWs as-grown, immediately after applying an oxygen plasma and 3 days later, after being exposed to ambient air. XPS carbon spectra of the (b) as-grown and (c) in air, as well as their corresponding fittings.

Transmission Electron Microscopy (TEM) and Electron Energy Loss Spectroscopy (EELS) has been used to study the crystallinity, determine possible preferential growth orientations, and to elucidate the C content and distribution in the NWs. Figure 3a shows a Ga₂O₃ NW with a gold tip, confirming that the growth occurred according to a VLS process. The selected area electron diffraction (SAED) pattern, shown in the inset of Figure 3a, confirms the monocrystalline nature of the NWs through the indexation of several reflections, which are in agreement with the [201] zone axis of monoclinic β -Ga₂O₃. Furthermore, from this figure one can deduce the growth direction, which is [001] for most of the investigated NWs (this crystallographic direction is almost parallel to the direction normal to the plane $(\bar{2}04)$). From these images one can also observe that the NWs present a smooth surface and uniform diameter. TEM further shows that the NWs edges present a thin amorphous layer, whose thickness ranges from 4 to 10 nm around the NW. This has been observed in all the analyzed NWs and can be clearly seen in the TEM image in Figure 3b.

Electron Energy Loss Spectroscopy (EELS) is used to study the distribution of carbon and oxygen signals across the NWs. For this, several NWs positioned on the holes of holey carbon TEM grids, like the one in the dark field scanning transmission electron microscope (STEM) image in Figure 3c, have been analyzed. This allows minimizing the carbon contribution from the supporting carbon film. The Electron Energy Loss spectra have been recorded while moving the electron beam across the section of the NW, indicated by the yellow line in Figure 3c, and from them, the carbon and oxygen signals have been extracted and are represented in Figure 3d. It is clear that the carbon signal has an almost constant value at the central part of the NW, while it is much higher at its edges. Simultaneously, the oxygen signal, which is directly related to the presence of gallium oxide, is also almost constant in the central part of the NW and decreases towards the edges. This clearly points that the central part of the NW is Ga_2O_3 , with probably some carbon incorporation, while the edges are carbon, giving rise to a core-shell structure. This is in agreement with the results obtained from XPS, which show that the carbon signal decreases after the oxygen plasma treatment. This core-shell structure can only be the consequence of the carbothermal reduction of the precursor material.

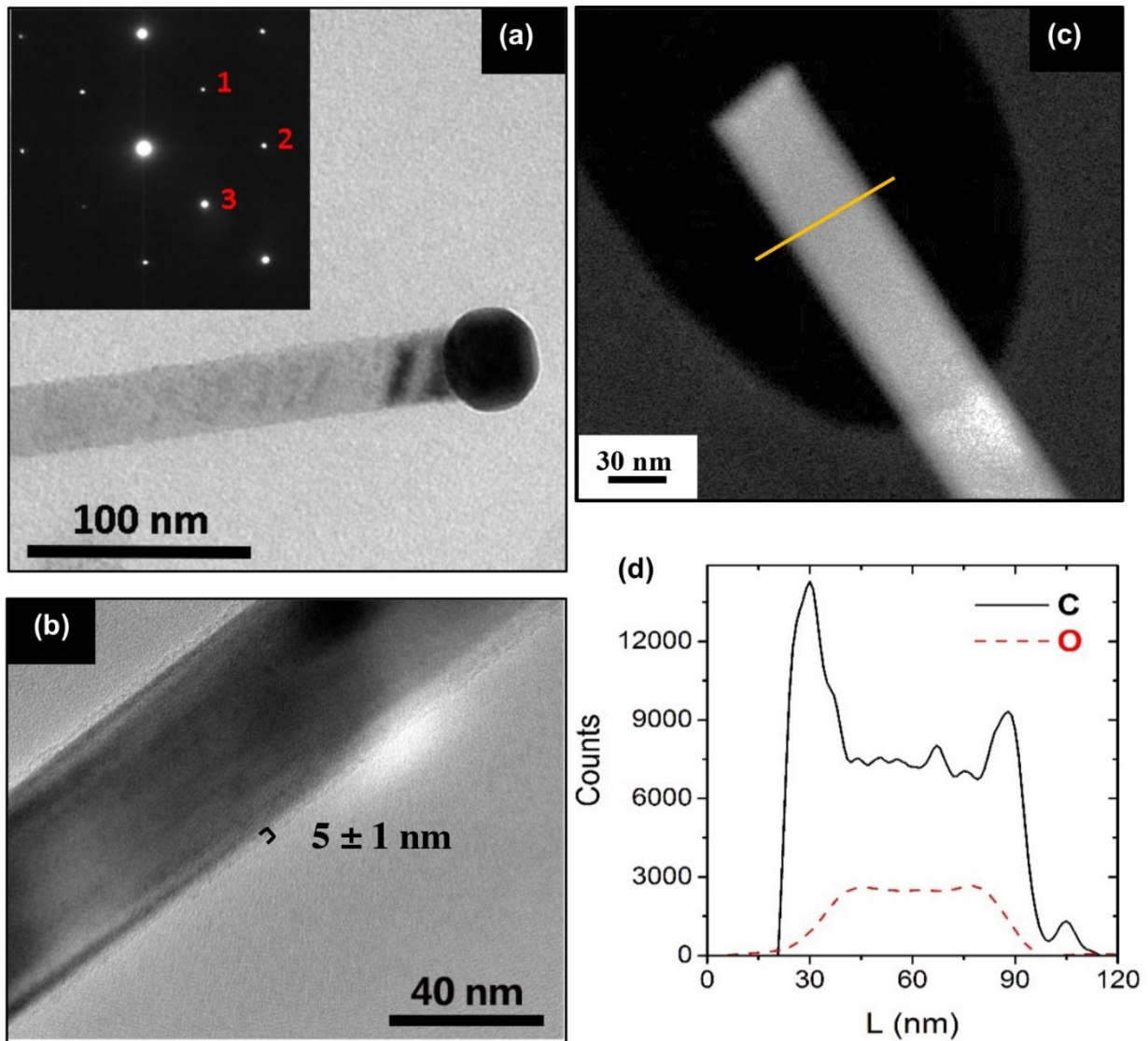


Figure 3. (a) TEM image of a gallium oxide nanowire and (inset) SAED pattern of the nanowire, with spots labeled as 1, 2 and 3 corresponding $(\bar{1}\bar{1}2)$, $(\bar{2}04)$ and $(\bar{1}12)$, respectively. (b) Higher magnification TEM image of one nanowire, showing the presence of an amorphous carbon shell. (c) Dark field STEM image of a β -Ga₂O₃ nanowire on top of the hole of a holey carbon film; (d) EELS signals corresponding to carbon and oxygen, measured along the line shown in (c). The higher carbon and the lower oxygen content at the edges of the nanowire prove the presence of the carbon shell around the β -Ga₂O₃ nanowire.

NWs from Region 2 (average diameters of 50 ± 20 nm) have been used in this work for gas sensor fabrication. The individual β -Ga₂O₃ NW-based gas sensors consist of a single monocrystalline NW electrically contacted using Focused Electron Beam Induced Deposition (FEBID) techniques on top of a microhotplate, with buried Pt heaters and Ti/Pt top electrodes²², as shown in Figures 4a and 4b. This allows the measurement of the resistance evolution of the individual NWs between room temperature (25 °C) and 200 °C, while different concentrations of H₂, CH₄, EtOH, CO, NO₂ and relative humidity flow in the gas test chamber. In this way, twelve single β -Ga₂O₃ NW-based gas sensors have been studied. In gas sensing applications, one of the commonly accepted sensor response definition is the relative change of resistance related to the resistance baseline in synthetic air²³, according to:

$$S (\%) = \frac{|R_{SA} - R_{gas}|}{R_{SA}} \times 100 \quad [1]$$

for both reducing and oxidizing gases, irrespective.

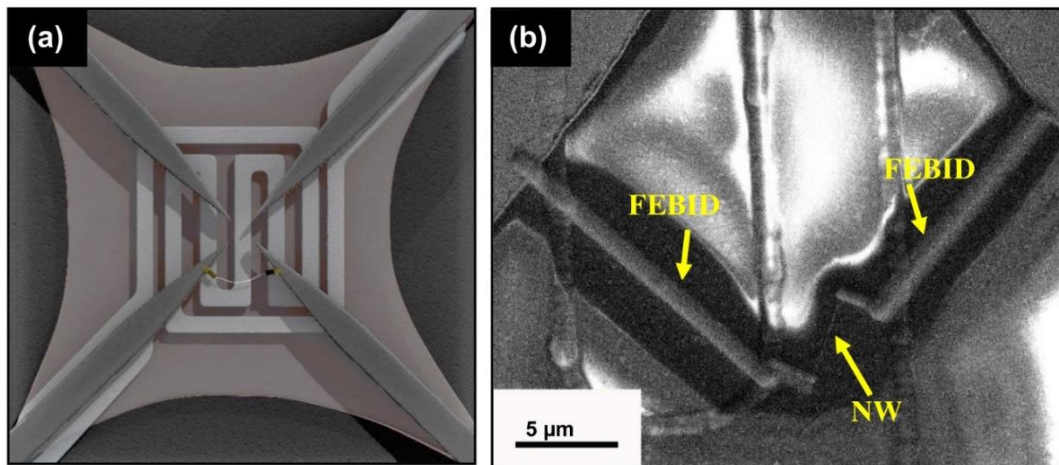


Figure 4. (a) Sketch of a microhotplate with a nanowire electrically contacted. (b) Scanning electron microscope image showing the nanowire contacted by focused electron beam induced deposition techniques on top of the microhotplate.

3. Individual semiconducting metal oxide nanowires for gas sensing

At room temperature and in dry synthetic air, the sensor's resistance baseline ranges between several tens of $M\Omega$ to few $G\Omega$. Figure 5a illustrates the reduction of resistance with increasing temperature, which confirms the expected behavior for a semiconductor as a consequence of charge carrier excitation. At the highest measured temperature, the resistance dropped by $\sim 90\%$, as compared to its initial base resistance at room temperature.

This behavior is different from other metal oxide NWs, like SnO_2 ²⁴, for which already at 150-200 °C adsorption of molecular oxygen (O_2) induces charge transfer²⁵. This causes the resistance to increase with temperature, reversing the tendency when compared to the situation in which only charge carrier excitation occurs.

The sensors showed an important resistance variation when exposed to RH (30 to 80 %) between ambient temperature and 100 °C. However, no variation was observed when H_2 , CH_4 , EtOH, CO or NO_2 were introduced in the gas chamber, as shown in the supplementary information, Figure S5. This demonstrates the high selectivity of these sensors.

The relative humidity tests typically start with 1 h stabilization under synthetic air flow, followed by alternating pulses of water vapor (diluted in dry air) and dry air of 10 and 20 minutes, respectively, as shown in Figure 5b. In metal oxide NW gas sensors, when RH is introduced in the gas test chamber, the oxygen desorption from the NW's surface is promoted, which in the present case occurs with the release of electrons to the $\beta\text{-Ga}_2\text{O}_3$ NW, giving rise to a measured resistance decrease, and which constitutes the sensor's response. In Figure 5c the response to 50 % RH from RT to 100 °C is plotted, clearly indicating a decrease of the resistance change with operating temperature. At 150 °C the response completely vanishes.

In addition to the well-known high-temperature response, metal oxide-based gas sensors present low-temperature (up to about 100 °C) gas adsorption and desorption processes, which can be

described by Langmuir or Brunauer-Emmett-Teller (BET) isotherms²⁷. Langmuir isotherm relates the adsorption sites occupancy on an adsorbent surface at a fixed temperature with the partial pressure of the specific adsorbate. BET model, on the other hand, considers multilayer adsorption with random distributed vacancies on the adsorbent. At temperatures up to 100 °C water adsorbates can be formed at the surface of the NW and the rates of adsorption and desorption of BET water layers depend on the surface morphology. The relation between sensor response and surface coverage is described in the supporting information.

The curve in Figure 5d summarizes the response of the sensor to the exposure to different water vapor concentrations and matches the adsorption isotherm type V from the IUPAC classification^{28,29}. This is in agreement with the curve of adsorbed water vapor as a function of its concentration for several different carbon-based materials at constant temperature. This behavior has been reported for carbon fiber-based monoliths³⁰, single-wall carbon nanotubes²⁷, activated carbon³¹, carbon nanofibers³² and charcoal³³ and is characterized by a very low adsorption at low RH values, a considerable increase between 50 and 60 % of RH, and a final saturation at high water vapor concentrations.

Generally, metal oxide gas sensors operating at room temperature present a completely different behavior. SnO₂ flat and nano-granular layers show an integrator-type performance³⁴, with responses increasing with temperature, not recovering the baseline after the gas has been removed from the testing chamber. Low temperature water vapor response of TiO₂, Fe₂O₃, rare-earth sesquioxides³⁵, Nd₂O₃, La₂O₃, Sm₂O₃ or Y₂O₃ can also be found in literature but the reported adsorption isotherms do not fit to type V^{36,37,38}. All this supports that the carbon shell is key for explaining the observed humidity response and selectivity of these sensors.

3. Individual semiconducting metal oxide nanowires for gas sensing

For a practical gas sensor, in addition to high response and selectivity, the response and recovery times are also very important parameters. At room temperature and under 80 % of RH, the response and recovery times reached values below 2 and 1 minute, respectively, making this type of devices suitable for atmospheric RH measurements.

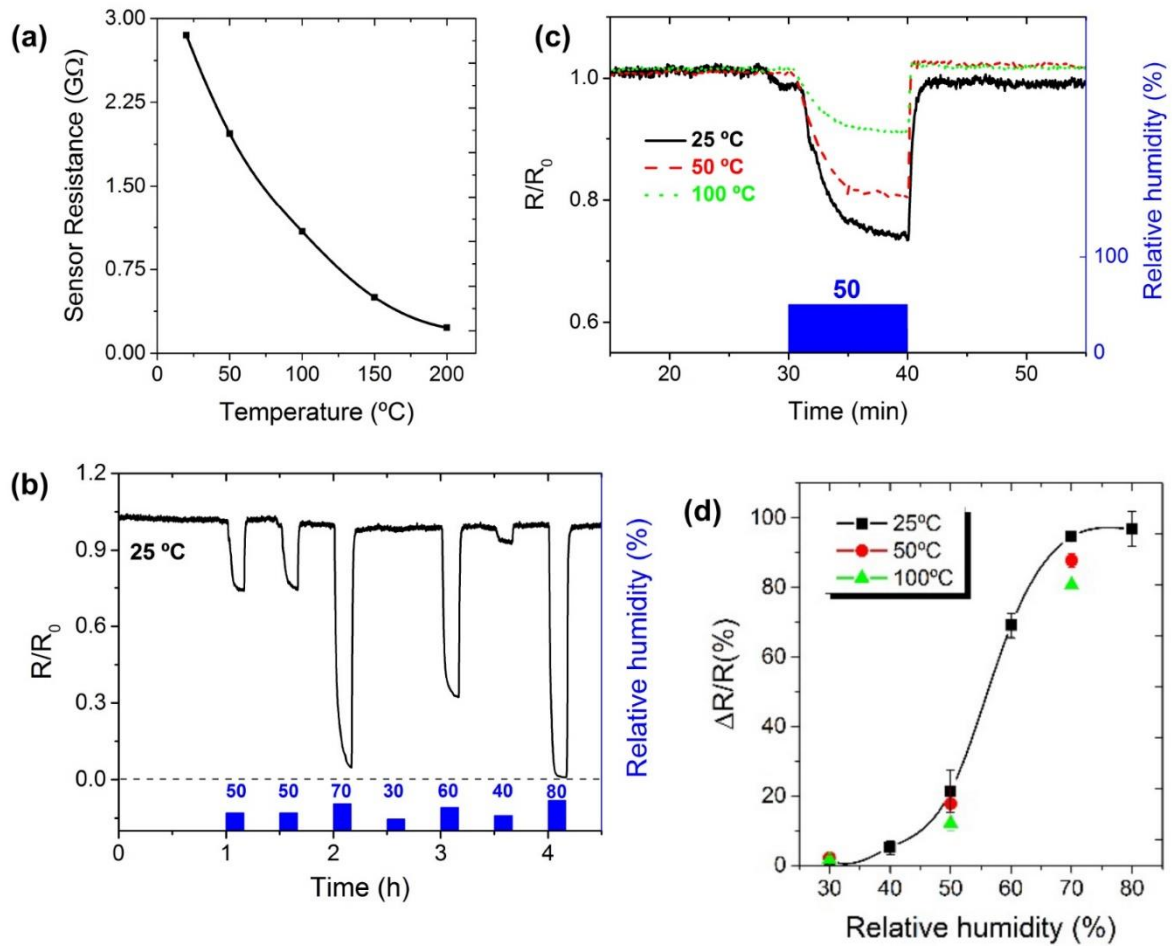


Figure 5. (a) Resistance variation of a single gallium oxide nanowire-based gas sensor as a function of temperature when in synthetic air. (b) Resistance evolution of a single Ga_2O_3 nanowire-based sensors towards different relative humidity concentrations at 25 $^{\circ}C$. (c) Relative resistance changes for pulses of 50 % relative humidity at temperatures of 25, 50 and 100 $^{\circ}C$. (d) Sensor's response as a function of the relative humidity.

In conclusion, monocrystalline β -Ga₂O₃ NWs have been grown via gold-assisted VLS process, employing the carbothermal reduction method to generate the precursor gas flow. The resulting NWs have a core-shell structure, with diameters of 50 ± 20 nm, surrounded by a 4-10 nm carbon shell, as confirmed by XPS and EELS. Several gas sensing devices containing single β -Ga₂O₃ NWs as main element have been fabricated using FEBID techniques and have been tested towards different concentrations of H₂, CH₄, EtOH, CO, NO₂ and water vapor, from room temperature to 200 °C. When operated in the temperature range between room temperature and 100°C, the sensors show high and fast responses to different concentrations of RH, with the maximum response obtained at room temperature, but remain insensitive to the presence of the other gases. This selective behavior can only be explained by the presence of the carbon shell at the NW's surface, as it agrees with the behavior of different types of carbon-based materials. Furthermore, the response time of the sensors can be as low as 2 minutes. This makes the individual β -Ga₂O₃ NW-based gas chemoresistors suitable candidates for room temperature humidity gas sensors. Finally, these results suggest that a critical reevaluation of gas sensing data published in literature from nanostructured materials obtained using the carbothermal reduction might be necessary.

Methods

In the present experiments, β -Ga₂O₃ NWs have been synthesized inside a chemical vapor deposition (CVD) furnace connected to a gas injection system according to a VLS mechanism, first reported by Wagner et al.¹⁶. The precursor material has been pure β -Ga₂O₃ (99.99%) micropowder mixed with graphite in a 2:3 wt proportion for 20 minutes in an agate mortar. The vapor phase generated by the carbothermal reduction of the precursor material was carried to the substrates by a 100 ml/min flow of pure argon (5N) at ambient pressure. The substrates were 0.5

3. Individual semiconducting metal oxide nanowires for gas sensing

$\times 0.5 \text{ cm}^2$ slabs cut from a 4-inch thermally oxidized Si wafer, with a $0.5 \mu\text{m}$ thick SiO_2 layer. A non-continuous thin Au layer, of nominal thickness of 2 nm, was sputtered-deposited on top of them, giving rise to Au nanoparticles when the substrates were heated up. The substrates were placed from 2 to 31 cm from the evaporating source. The precursor and the nearest substrates were heated up to $950 \text{ }^\circ\text{C}$ and a decreasing temperature gradient was maintained from this point towards the back-end of the quartz tube, where the temperature was kept at $820 \text{ }^\circ\text{C}$. The system and the sample distribution are explained in detail elsewhere³⁹.

The $\beta\text{-Ga}_2\text{O}_3$ nanostructures were investigated using a Jeol J7100F scanning electron microscope, a Jeol J2010F transmission electron microscope equipped with a Gatan Electron Energy Loss Spectrometer, a Siemens D-500 X-Ray Diffractometer and a PHI ESCA-5500 X-Ray Photoelectron Spectrometer.

In order to fabricate the sensors, $\beta\text{-Ga}_2\text{O}_3$ NWs were transferred to microhotplates with buried Pt heaters and pre-patterned Ti/Pt electrodes. These microhotplates allow to rise the temperatures up to 350°C with a power consumption of 8 mW. A FEI Helios Nanolab 650 Dual Beam instrument, equipped with a trimethylcyclopentadienyl–platinum-filled ($(\text{CH}_3)_3\text{CH}_3\text{C}_5\text{H}_4\text{Pt}$) injector for Pt deposition, was used to electrically contact the individual $\beta\text{-Ga}_2\text{O}_3$ NWs²² using FEBID with an electron beam accelerated to 5 kV. Finally, the chips containing the individual $\beta\text{-Ga}_2\text{O}_3$ contacted NWs were fixed and electrically bonded to a TO-8 support. Electrical and gas measurements were carried out plugging the TO-8 support to a gas sensing measurements station equipped with a home-made stainless-steel gas chamber of 8.6 ml volume, a home-developed Labview software that allows the control of 4 Bronkhorst Mass-Flow Controllers, a Keithley 2602A dual Source Measure Unit and a Keithley 2400 SourceMeter. The resistance measurements were carried out at low current, 5 nA, to avoid NW heating. The different gases, CO (up to 25

ppm), NO₂ (up to 2.5 ppm), CH₄ (up to 500 ppm), EtOH (100 ppm), H₂ (up to 1.25 %) or RH (up to 80%) were diluted in dry synthetic air and a constant gas flow of 200 ml/min into the measuring chamber was kept, alternating pulses of diluted gas and clean dry synthetic air.

ASSOCIATED CONTENT

Supporting Information.

Sketch of the placement of precursor powder and substrates in the furnace and the modelling of the gas flow; SEM images of the NW grown close and far to the evaporation source; XPS survey spectrum of the as-grown sample; table showing the fitting parameters of the XPS spectra; expressions to obtain the relation between sensors' response and analyte surface coverage; gas measurement towards one of the interfering gases (NO₂) and maximum response measured for all the different gases.

AUTHOR INFORMATION

Corresponding Author

*E-mail: albert.romano@ub.edu

Acknowledgment

This work has been partially supported by the Spanish Ministerio de Economía y Competitividad, through projects TEC2013-48147-C6 and TEC2016-79898-C6 (AEI/FEDER, EU). J. Pardo is acknowledged for the microhotplate sketch of Figure 4a.

REFERENCES

- (1) Higashiwaki, M.; Sasaki, K.; Kuramata, A.; Masui, T.; Yamakoshi, S. Development of gallium oxide power devices. *Phys. Status Solidi A* **2014**, 211, 21-26.
- (2) Fleischer, M.; Meixner, H. Gallium oxide thin films: a new material for high-temperature oxygen sensors. *Sens. Actuators, B* **1991**, 4, 437-441.
- (3) Fleischer, M.; Meixner, H. Sensing reducing gases at high temperatures using long-term stable Ga₂O₃ thin films; *Sens. Actuators, B* **1992**, 6, 257-261.
- (4) Schwebel, T.; Fleischer, M.; Meixner, H. A selective, temperature compensated O₂ sensor based on Ga₂O₃ thin films. *Sens. Actuators, B* **2000**, 65, 176–180.
- (5) Lia, Y.; Trinchib, A.; Wlodarskib, W.; Galatsisb, K.; Kalantar-zadeh, K. Investigation of the oxygen gas sensing performance of Ga₂O₃ thin films with different dopants. *Sens. Actuators, B* **2003**, 93, 431–434.
- (6) Liu, Z.; Yamazaki, T.; Shen, Y.; Kikuta, T.; Nakatani, N.; Li, Y. O₂ and CO sensing of Ga₂O₃ multiple nanowire gas sensors. *Sens. Actuators, B* **2008**, 129, 666–670;

- (7) Barth, S.; Hernández-Ramírez, F.; Holmes, J.D.; Romano-Rodríguez, A. Synthesis and applications of one-dimensional semiconductors. *Prog. Mater. Sci.* **2010**, *55*, 567-623.
- (8) Kim, H.; Jin, C.; An, S.; Lee, C. Fabrication and CO gas-sensing properties of Pt-functionalized Ga₂O₃ nanowires. *Ceram. Int.* **2012**, *38*, 3563–3567.
- (9) Park, S. H.; Kim, S. H.; Park, S. Y.; Lee, C. Synthesis and CO gas sensing properties of surface nitridated Ga₂O₃ nanowires. *RSC Adv.* **2014**, *4*, 63402.
- (10) Park, S.; Kim, H.; Jin, C.; Lee, C. Synthesis, structure, and room-temperature gas sensing of multiple-networked Pd-doped Ga₂O₃ nanowires. *J. Kor. Phys. Soc.* **2012**, *60*, No. 10, 1560-1564.
- (11) Juan, Y.M.; Chang, S.J.; Hsueh, H.T.; Wang, S.H.; Weng, W.Y.; Cheng, T.C.; Wu, C.L. Effects of humidity and ultraviolet characteristics on β -Ga₂O₃ nanowire sensor. *RSC Adv.* **2015**, *5*, 84776–84781.
- (12) Tsai, T.-Y.; Chang, S.-J.; Weng, W.-Y.; Liu, S.; Hsu, C.-L.; Hsueh, H.-T.; Hsueh, T.-J. β -Ga₂O₃ Nanowires-Based Humidity Sensors Prepared on GaN/Sapphire Substrate. *IEEE Sens. J.* **2013**, *13*, 4891-4896.
- (13) Huang, Y.; Yue, S.; Wang, Z.; Wang, Q.; Shi, C.; Xu, Z.; Bai, X.D.; Tang, C.; Gu, C. Preparation and electrical properties of ultrafine Ga₂O₃ nanowires. *J. Phys. Chem. B* **2006**, *110*, 796-800.
- (14) Domènech-Gil, G.; Peiró, I.; López-Aymerich, E.; Pellegrino, P.; Barth, S.; Gràcia, I.; Cané, C.; Prades, J.D.; Moreno-Sereno, M.; Romano-Rodríguez, A. Individual gallium oxide nanowires for humidity sensing at low temperature. *Proceedings* **2017**, *1*, 468.

3. Individual semiconducting metal oxide nanowires for gas sensing

(15) Domènech-Gil, G.; Peiró, I.; López-Aymerich, E.; Moreno, M.; Pellegrino, P.; Gràcia, I.; Cané, C.; Barth, S.; Romano-Rodríguez, A. Room temperature humidity sensor based on single β - Ga_2O_3 nanowires. *Proceedings* **2018**, *2*, 958.

(16) Wagner, R.S.; Ellis, W.C. The vapor–liquid–solid mechanism of crystal growth and its application to Silicon. *Appl. Phys. Lett.* **1965**, *233*, 1053–1064.

(17) Wu, Y.; Yang, P. Direct observation of vapor-liquid-solid nanowire growth. *J. Am. Chem. Soc.* **2001**, *123*, 3165-3166.

(18) Haruta, M. When gold is not noble: catalysis by nanoparticles. *Chem. Rec.* **2003**, *3*, 75–87.

(19) Grant-in-Aid; ICDD: Fargo, North Dakota, 1989; PDF#41-1103_Ga2O3(m).df (Accessed May 10th, 2019).

(20) Cuong, N.D.; Park, Y.W.; Yoon, S.G. Microstructural and electrical properties of Ga_2O_3 nanowires grown at various temperatures by vapor–liquid–solid technique. *Sens. Actuators, B* **2009**, *140*, 240-244.

(21) Moulder, J.F.; Stickle, W.F.; Sobol, P.E.; Bomben, K.D. Handbook of X-ray photoelectron spectroscopy. Perkin-Elmer Corporation **1992**, 40-41.

(22) Hernández-Ramírez, F.; Tarancón, A.; Casals, O.; Rodríguez, J.; Romano-Rodríguez, A.; Morante, J.R.; Barth, S.; Mathur, S.; Choi, T.Y.; Poulidakos, D.; Callegari, V.; Nellen, P.M. Fabrication and electrical characterization of circuits based on individual tin oxide nanowires. *Nanotechnology* **2006**, *17*, 5577–5583.

- (23) Samà, J.; Seifner, M.S.; Domènech-Gil, G.; Santander, J.; Calaza, C.; Moreno, M.; Gràcia, I.; Cané, C.; Barth, S.; Romano-Rodríguez, A. low temperature humidity sensor based on Ge nanowires selectively grown on suspended microhotplates. *Sens. Actuators, B* **2017**, 243, 669-677
- (24) Chang, S. Oxygen chemisorption on tin oxide: Correlation between electrical conductivity and EPR measurements. *J. Vac. Sci. Technol.* **1980**, 17, 366.
- (25) Samà, J.; Barth, S.; Domènech-Gil, G.; Prades, J.D.; López, N.; Casals, O.; Gràcia, I.; Cané, C.; Romano-Rodríguez, A. Site-selectively grown SnO₂ NWs networks on micromembranes for efficient ammonia sensing in humid conditions. *Sens. Actuators, B* **2016**, 232, 402-409.
- (26) Feng, P.; Xue, X.Y.; Liu, Y.G.; Wan, Q.; Wang, T.H. Achieving fast oxygen response in individual β -Ga₂O₃ nanowires by ultraviolet illumination. *App. Phys. Lett.* **2006**, 89, 112114.
- (27) Kim, P.; Agnihotri, S. Application of water-activated carbon isotherm models to water adsorption isotherms of single-walled carbon nanotubes. *J. Coll. Interf. Sci.* **2008**, 325, 64–73.
- (28) Sing, K.S.W.; Everett, D.H.; Haul, R.A.W.; Moscou, L.; Pirotti, R.A.; Rouquerol, J.; Siemieniowska, T. Reporting physisorption data for gas/solid systems with special reference to the determination of surface area and porosity. *Pure App. Chem.* **1985**, 57, 4, 603-619.
- (29) Mahle, J.J. An adsorption equilibrium model for Type 5 isotherms. *Carbon* **2002**, 40, 2753–2759.
- (30) Marbán, G.; Fuertes, A.B. Co-adsorption of n-butane/water vapour mixtures on activated carbon fibre-based monoliths. *Carbon* **2004**, 42, 71–81.

3. Individual semiconducting metal oxide nanowires for gas sensing

(31) Yao, X.; Li, L.; Li, H.; He, S.; Liu, Z.; Maa, W. A new model for calculating the adsorption equilibrium constant of water vapor in micropores of activated carbon. *Comp. Mat. Sci.* **2014**, *89*, 137–141.

(32) Monereo, O.; Casals, O.; Prades, J.D.; Cirera, A. Self-heating in pulsed mode for signal quality improvements: Application to carbon nanostructured-based sensors. *Sens. Actuators, B* **2016**, *226*, 254-265.

(33) Wiig, E.O.; Juhola, A.J. The adsorption of water vapor on activated charcoal. *J. Am. Chem. Soc.* **1949**, *71*, 2, 561–568.

(34) Maier, K.; Helwig, A.; Müller, G.; Hille, P.; Eickhoff, M. Effect of water vapor and surface morphology on the low temperature response of metal oxide semiconductor gas sensors. *Materials* **2015**, *8*, 6570-6588.

(35) Nagao, M.; Hamano, H.; Hirata, K.; Kumashiro, R.; Kuroda, Y. Hydration process of rare-earth sesquioxides having different crystal structures. *Langmuir* **2003**, *19*, 9201-9209.

(36) Bârsan, N.; Weimar, U. Conduction model of metal oxide gas sensors. *J. Electroceram.* **2001**, *7*, 143–167.

(37) Koziej, D.; Bârsan, N.; Weimar, U.; Szuber, J.; Shimanoe, K.; Yamazoe, N. Water-oxygen interplay on tin dioxide surface: Implication on gas sensing. *Chem. Phys. Lett.* **2005**, *410*, 321-323.

(38) Morimoto, T.; Nagao, M.; Tokuda, F. The relation between the amounts of chemisorbed and physisorbed water on metal oxides. *J. Phys. Chem.* **1969**, *73*, 1, 243-248.

(39) Domènech-Gil, G.; Barth, S.; Samà, J.; Pellegrino, P.; Gràcia, I.; Cané, C.; Romano-Rodriguez, A. Gas sensors based on individual indium oxide nanowire. *Sens. Actuators, B* **2017**, *238*, 447-454.

Supporting Information

Humidity gas sensors made from individual Ga₂O₃ nanowires: impact of the carbothermal reduction synthesis method on their high selectivity and room temperature operation

Guillem Domènech-Gil †,‡, Irmina Peiró †, Elena López-Aymerich †,‡, Jan Romano-deGea †,#,

Isabel Gràcia §, Christophe Serre †,‡, Paolo Pellegrino †,‡, Mauricio Moreno †,‡,

Carles Cané §, Sven Barth ||, Albert Romano-Rodríguez †,‡,*

† Department of Electronic and Biomedical Engineering, Universitat de Barcelona (UB), c/Martí i Franquès 1, 08028 Barcelona, Spain

‡ Institute of Nanoscience and Nanotechnology (IN2UB), Universitat de Barcelona (UB), c/Martí i Franquès 1, 08028 Barcelona, Spain

Department of Inorganic and Organic Chemistry, Faculty of Chemistry, Universitat de Barcelona (UB), c/Martí i Franquès 1, 08028 Barcelona, Spain

§ Centre Nacional de Microelectrònica - Institut de Microelectrònica de Barcelona, Consejo Superior de Investigaciones Científicas (CSIC), Campus UAB, Carrer dels Til·lers, 08193 Bellaterra, Spain

|| Physikalisches Institut, Goethe University Frankfurt, Max-von-Laue-Straße 1, 60438 Frankfurt am Main, Germany

Corresponding Author

*E-mail: albert.romano@ub.edu

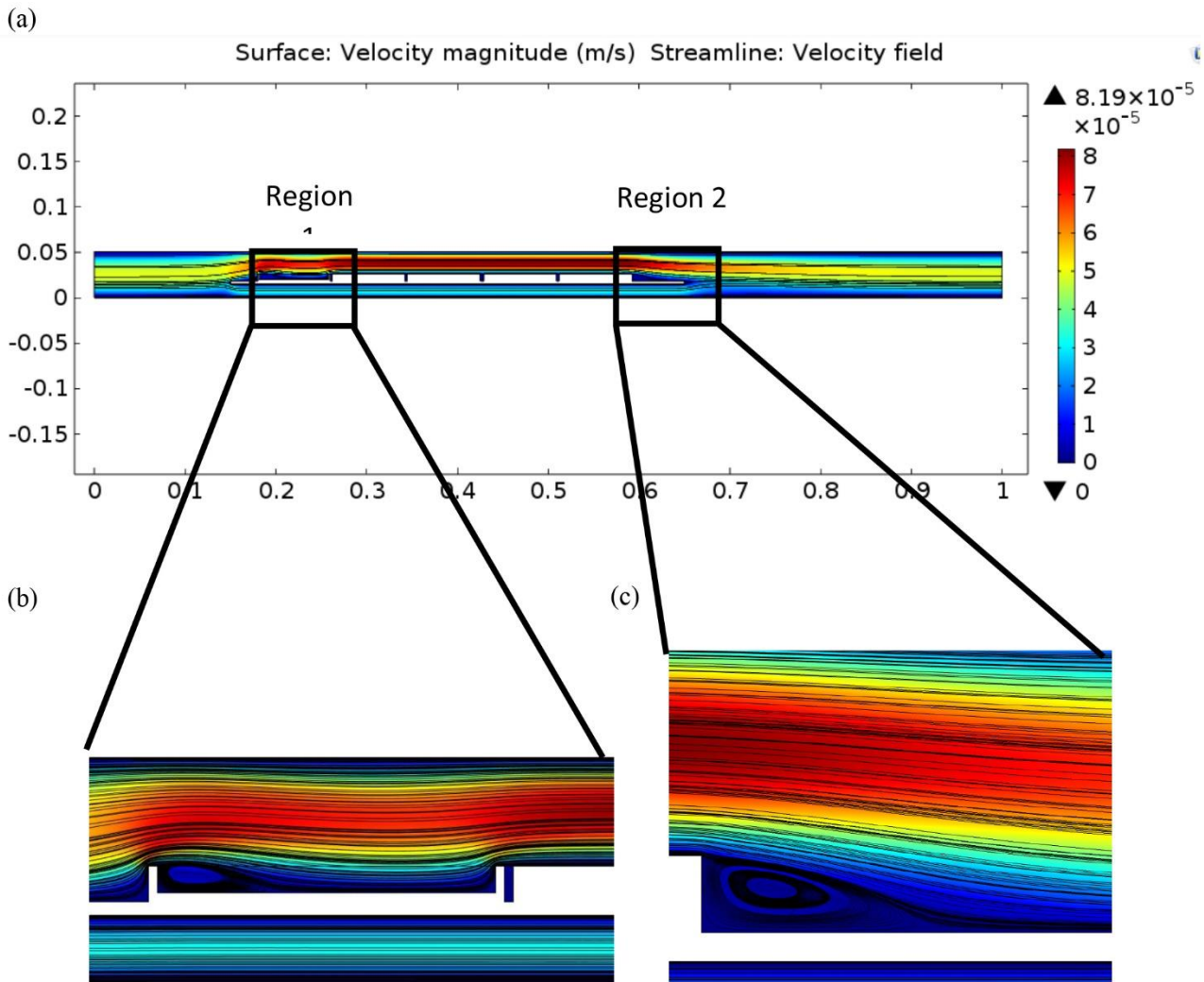


Figure S1: (a) COMSOL simulation of the gas flow velocity profile inside the quartz tube of the chemical vapor deposition furnace used to perform the experiments presented in this work; (b) detail of the regions close (Region 1) and (c) far (Region 2) from the precursor source, where the nanowire growth occurs and which correspond to closed flow lines. In between these zones, absence of nanowire growth is attributed to the absence of closed flow lines

3. Individual semiconducting metal oxide nanowires for gas sensing

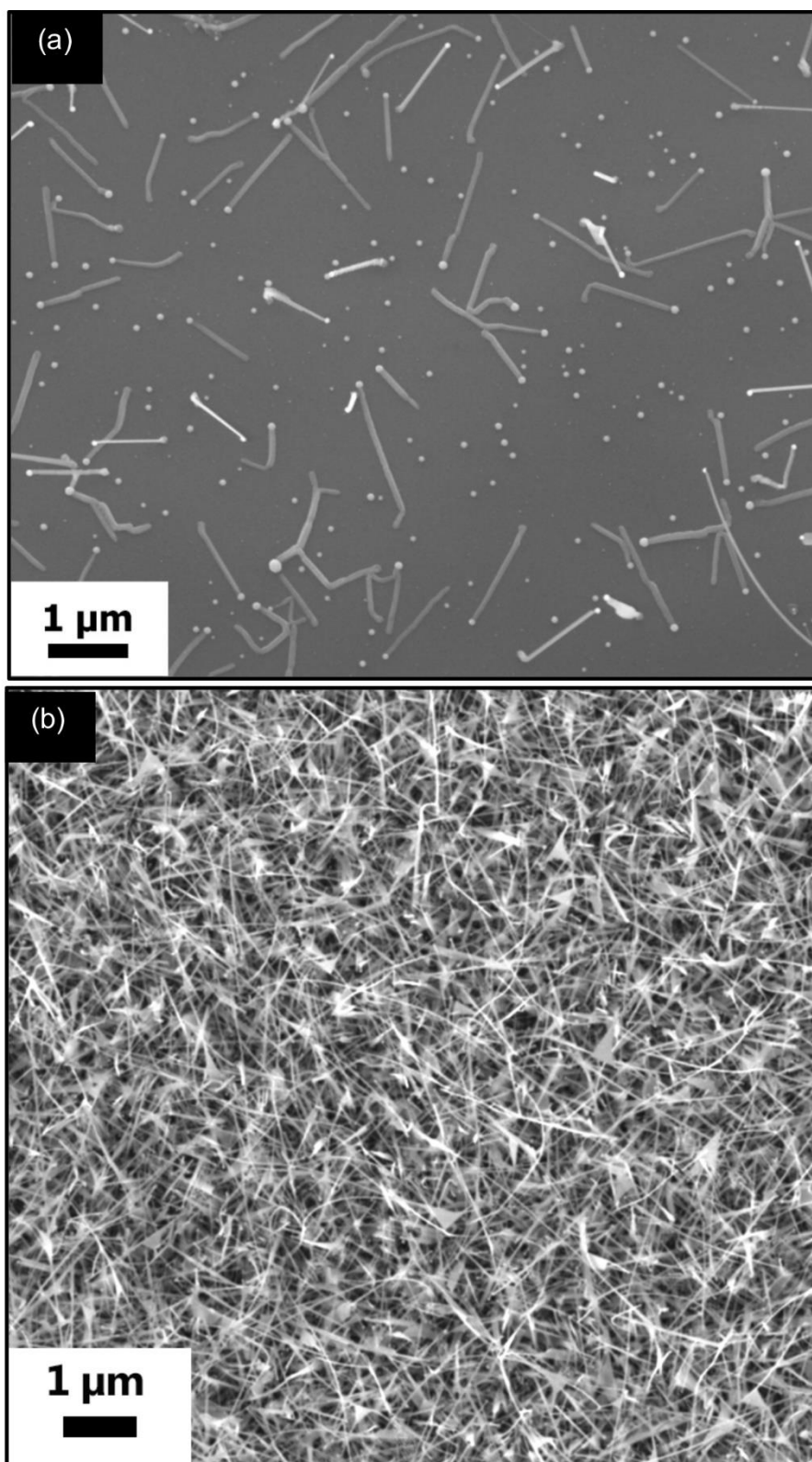


Figure S2: Scanning electron microscopy images of gallium oxide nanowires grown at (a) 2 cm and (b) 30 cm from the evaporation source, corresponding to regions 1 and 2 in Figure S1, respectively. The difference in nanowire density is clearly visible.

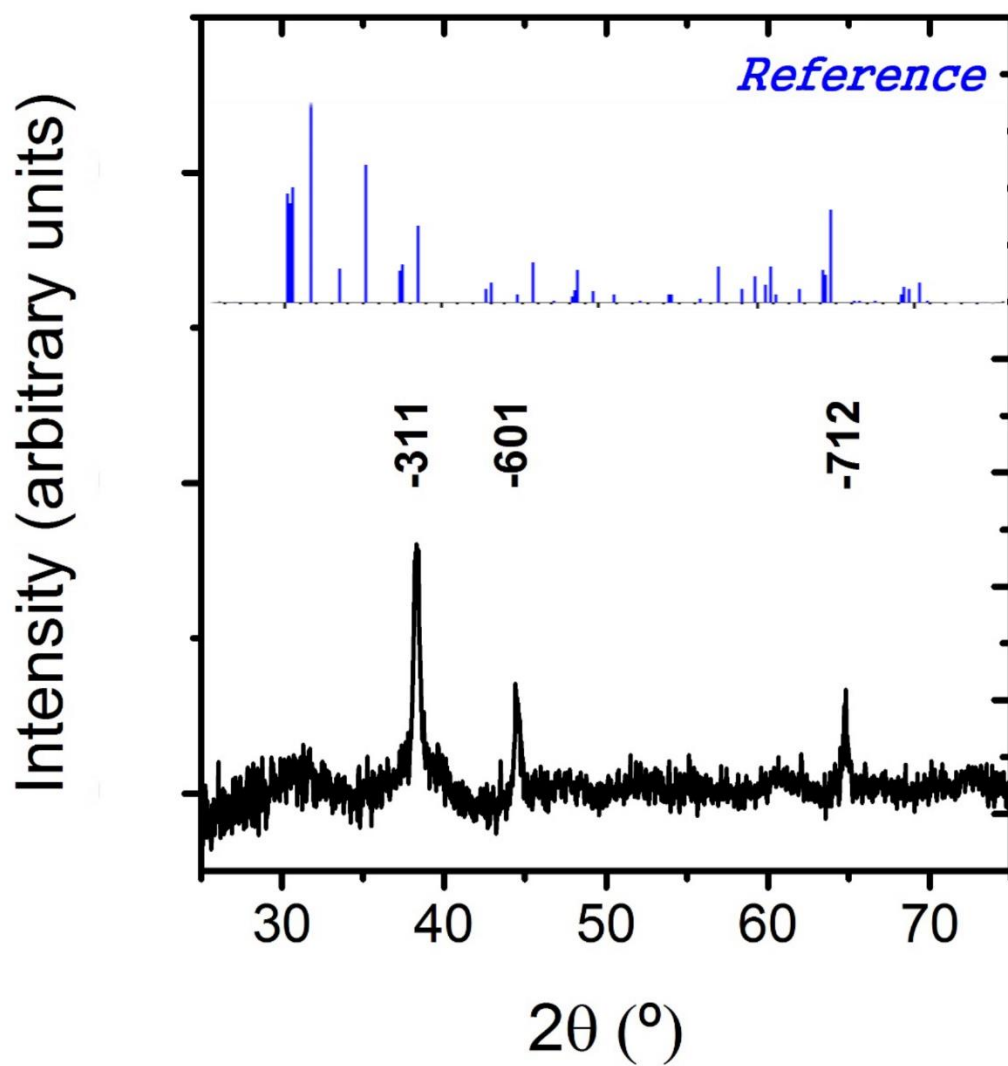


Figure S3: X-ray diffraction spectrum for gallium oxide nanowires grown at 2 cm from the evaporating source. The reflections are in agreement with reference data for monoclinic β - Ga_2O_3 (JCPDS 41-1103), whose diffraction angles are also indicated.

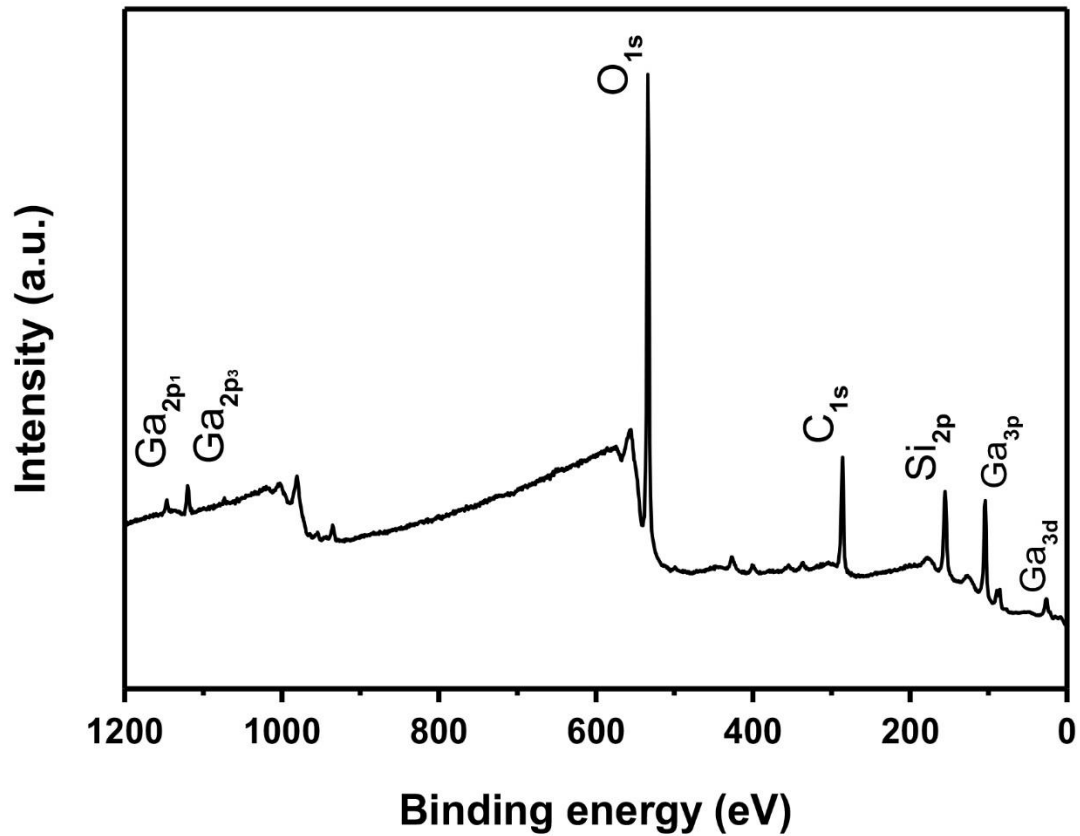


Figure S4: XPS survey spectrum of a sample grown at 30 cm from the evaporating source, f peaks corresponding to gallium, oxygen, carbon and silicon have been identified. The silicon signal comes from the Si/SiO₂ substrate.

Table I: Fitting parameters of the XPS spectra from Figures 3b and 3c. For Figure 3b, only one peak is used, while for Figure 3c two peaks are required.

| | As-grown | In air | |
|---------------|-------------|-------------|-------------|
| | | Peak 1 | Peak 2 |
| Amplitude | 2870±23 | 1255±60 | 328±30 |
| Position (eV) | 285.01±0.01 | 285.01±0.01 | 286.05±0.13 |
| FWHM (eV) | 1.65±0.01 | 1.41±0.03 | 3.42±0.17 |

BET model multilayer adsorption relation with sensor response

The BET isotherms relate the RH concentration to the water surface coverage, θ , defined as the fraction of the active sites with adsorbed species. Coverage is also related to the sensor response¹, determining the following relation:

$$S \propto \theta(RH, T) = \frac{RH}{1-RH} \frac{b_{BET}(T)}{[1+RH(b_{BET}(T)-1)]} \quad [1]$$

where $b_{BET}(T)$ stands for the BET constant:

$$b_{BET}(T) = \exp \left[\frac{\varepsilon_1 - \varepsilon_{lf}}{k_B T} \right] \quad [2]$$

and where ε_1 and ε_{lf} are two energy parameters that measure the strength of adsorption of the first monolayer on the surface and in each following monolayer of water molecules, respectively (multilayer water adsorption can occur when $\varepsilon_1 > \varepsilon_{lf}$), k_B is the Boltzmann constant, and T , the temperature.

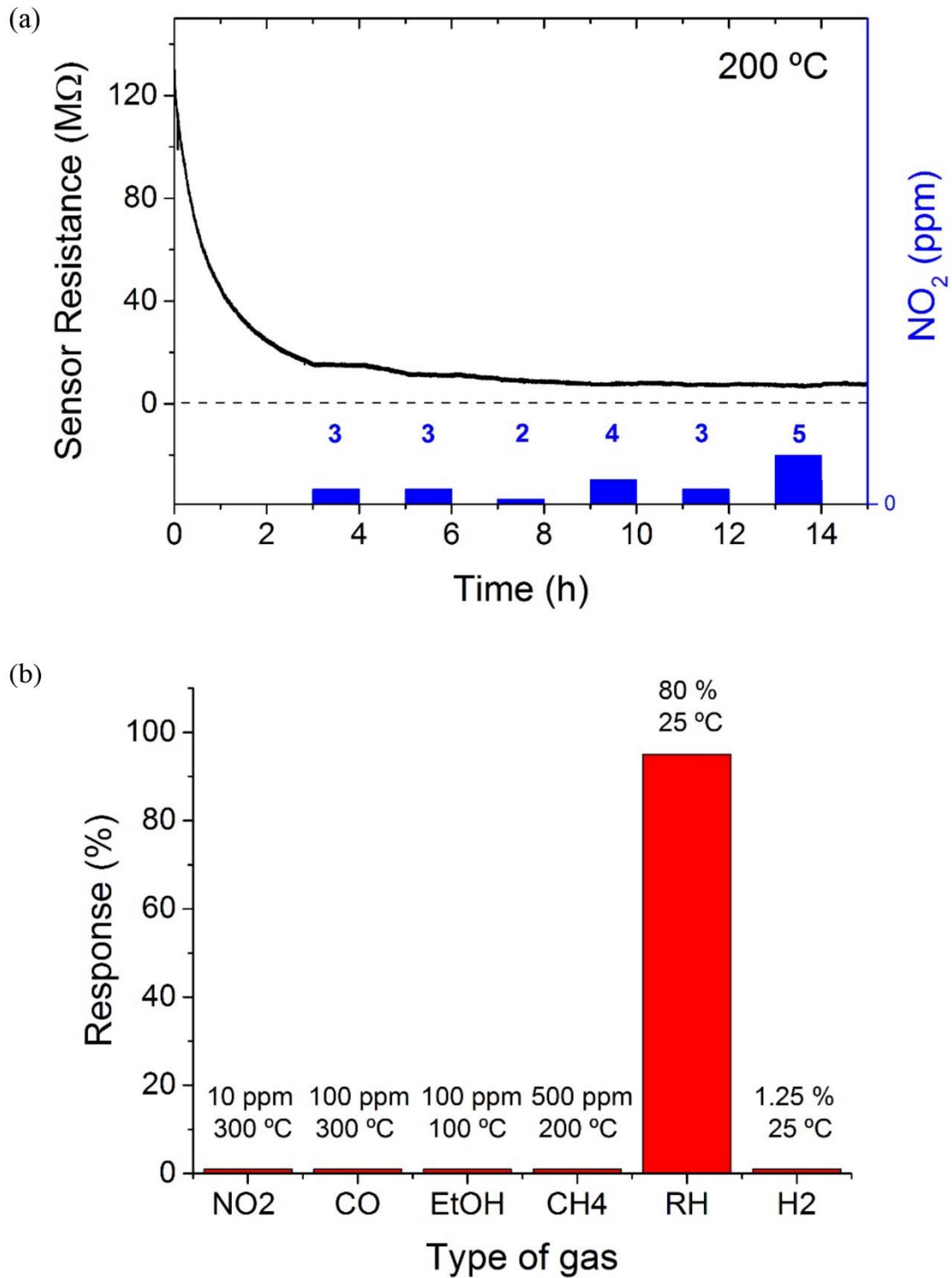


Figure S5: (a) Resistance evolution of an individual gallium oxide NW-based gas sensor towards different pulses of nitrogen dioxide diluted in dry synthetic air at 200 °C; (b) Summary of the response to the different gases tested in this work, all diluted in dry synthetic air or nitrogen.

References:

1. Monereo, O.; Prades, J.D.; Cirera, A. Self-heating effects in large arrangements of randomly oriented carbon nanofibers: Applications to gas sensors. *Sens. Act. B Chem.* **2015**, 211, 489-497.



*“I never think of the future,
it comes soon enough”
Albert Einstein*

4. Advanced integration methodologies for nanowire-based gas sensors

The integration of NWs onto MHP and MM and their testing as gas sensors is another objective of this thesis. With this aim, two studies devoted to fabricating gas nanosensors based on MOX NWs using different contacting approaches are presented.

In section 4.1, the dielectrophoretic alignment of NWs is used to fabricate chemoresistors. WO_3 NWs, either pristine or surface-functionalized with *Pt*-nanoparticles to enhance their sensibility, were used. Arrays of single WO_3 NWs, suspended in water, were successfully aligned via dielectrophoresis between plane electrodes. The optimal conditions employed for the alignment were the use of square wave, with amplitude of 5 V peak-to-peak and a frequency of 9.5 MHz, keeping the applied field for 20 s. After this, the water was allowed to dry by heating the samples to 80°C. This fixed the NWs between the contacts.

The fabricated gas sensors were characterized at 250 °C towards NO_2 and EtOH, diluted in dry synthetic air. The chemoresistors responded differently depending on their surface functionalization. Pristine WO_3 NWs showed a maximum response value of 87 % towards 5 ppm of NO_2 and of 32 % towards 100 ppm of EtOH, while for *Pt*-functionalized WO_3 NWs, the maximum response was 43 % for 5 ppm of NO_2 and 86 % for 100 ppm of EtOH. This opposite behavior between both types of NWs was attributed to a higher amount of pre-adsorbed oxygen species at the NW surface, inducing additional chemical and electronic interactions. This proves the feasibility of dielectrophoresis for gas sensor fabrication.

In section 4.2, EBL is used to fabricate metallic contacts to individual SnO₂ NWs on top of MHP or MM, replacing the more common FEBID method, employed routinely in our research group. The difficulty of this fabrication process is that the substrate presents an important bending, caused by the stresses of the different layers from which it is made. To achieve this, both the photoresist spinning speed and time and the required electron dose to introduce changes in the photoresist had to be fine tune. Additionally, a special holder to fix the chip in the spinner had to be designed and machined with the aim of avoiding border effect in the photoresist. This holder showed to be key in achieving the correct spinning. After exposing the photoresist, which required a dose of 600 $\mu\text{C}/\text{cm}^2$ and which is about 4 time larger than the usual dose employed in the used EBL machine, the photoresist was developed. After the photoresist development, the lift-off process was used to make the Ti/Pt deposits in the exposed areas. The method allows fabricating several devices sequentially but without breaking the vacuum of the EBL system.

The chemoresistors were characterized between 150 and 400 °C towards ammonia (NH₃) diluted in dry synthetic air. The maximum resistance variation was 70 % at 200°C and towards 20 ppm of NH₃ and is larger than that obtained for the reference fabrication technique, FEBID, which showed a response of 30 % for 25ppm at 250 °C. This superior behavior can be the result of the better electrical characteristics of the Ti/Pt contacts in front of the FEBID Pt-deposition. This demonstrates the potentiality of this techniques for contacting individual NWs on top of suspended MHP and MM for gas sensing applications. The technique can be easily tuned to contact other NWs, other nanostructures (such as nanotubes or nanorods) and, even, to other substrates with different thickness, surface structure, roughness and shape.

4.1 Dielectrophoretic alignment of individual tungsten oxide nanowires for gas sensing

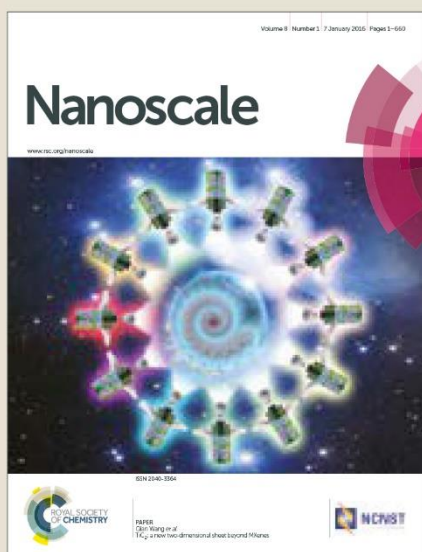


View Article Online
View Journal

Nanoscale

Accepted Manuscript

This article can be cited before page numbers have been issued, to do this please use: O. Chmela, J. Sadílek, G. Domènech-Gil, J. Samà, J. Somer, R. Mohan, A. Romano-Rodríguez, J. Hubalek and S. Vallejos, *Nanoscale*, 2018, DOI: 10.1039/C8NR01588K.



This is an Accepted Manuscript, which has been through the Royal Society of Chemistry peer review process and has been accepted for publication.

Accepted Manuscripts are published online shortly after acceptance, before technical editing, formatting and proof reading. Using this free service, authors can make their results available to the community, in citable form, before we publish the edited article. We will replace this Accepted Manuscript with the edited and formatted Advance Article as soon as it is available.

You can find more information about Accepted Manuscripts in the [author guidelines](#).

Please note that technical editing may introduce minor changes to the text and/or graphics, which may alter content. The journal's standard [Terms & Conditions](#) and the ethical guidelines, outlined in our [author and reviewer resource centre](#), still apply. In no event shall the Royal Society of Chemistry be held responsible for any errors or omissions in this Accepted Manuscript or any consequences arising from the use of any information it contains.



rsc.li/nanoscale



Nanoscale

ARTICLE

Selectively arranged single-wire based nanosensor array systems for gas monitoring

O. Chmela,^{a,b} J. Sadílek,^a G. Domènech-Gil,^{c,d} J. Samà,^{c,d} J. Somer,^{a,b} R. Mohan,^a A. Romano-Rodríguez,^{c,d} J. Hubálek,^{a,b} S. Vallejos^{a,e,*}

Received 00th January 20xx,
Accepted 00th January 20xx

DOI: 10.1039/x0xx00000x

www.rsc.org/

Gas nanosensors, comprised of arrays of nanoelectrodes with finger-widths of ~100 nm developed by electron beam lithography and aerosol assisted chemical vapor deposited non-functionalized and Pt-functionalized tungsten oxide nanowires (<100 nm) subsequently integrated across the pairs of electrodes via dielectrophoresis method, are developed in this work. The functionality of these devices is validated towards various concentrations of NO₂ and C₂H₅OH. Results demonstrate reproducible and consistent responses with better sensitivity and partial selectivity for the non-functionalized systems to NO₂, as opposed to the Pt-functionalized systems, which display better sensing properties towards C₂H₅OH with a loss of response to NO₂, that, in turn, increases the cross-sensitivity between these gases. These results are explained on the basis of the additional chemical and electronic interactions at the Pt/tungsten oxide interface, which increase the pre-adsorption of oxygen species and make the functionalized surface rather more sensitive to C₂H₅OH than to NO₂, in contrast to the non-functionalized surface.

Introduction

One-dimensional (1D) metal oxide (MOX) nanostructures in the form of nanowires (NWs), nanotubes, nanorods or nanobelts have demonstrated to play a significant role in the functional properties of different components (e.g., solar cells, supercapacitors, smart windows, photodetectors, biosensors, and gas sensors),^{1,2} improving typically their performance, as opposed to bulk MOXs. The high aspect ratios of 1D nanostructures, with nanometric widths or diameters (between 1 and 100 nm) and micrometric lengths that allow for their connection with the macroscopic world, make these structures attractive for device miniaturization enabling low power consumption, as demonstrated previously in single-NW-based devices, including gas sensors.⁴

1D MOX nanostructures are attractive in gas sensors because they have proved to enhance the functionality of these devices, providing better sensitivity, stability, and to some extent better selectivity not only due to their higher surface area to volume ratio, as opposed to bulk materials, but also

due to the presence of specific crystal facets that provide a particular electronic structure to the surface.^{5,6} Further enhancements on the gas sensing properties of MOXs have also been achieved by the functionalization (or surface modification) of the MOX with second-phase materials (particularly noble metal nanoparticles (NPs) with sizes less than 10 nm),⁷ providing chemical sensitization via the promotion of gas-solid interactions with spillover of active species from the second-phase material to the MOX surface and/or electronic sensitization of the MOX via the regulation of charge carrier concentration at the interface of the MOX and the second-phase material.⁸

Gas sensors based on functionalized 1D MOX nanostructures (e.g., tungsten oxide NWs functionalized with Pt NPs) have been used previously for monitoring various toxic and hazardous gases. In particular tungsten oxide has attracted much attention due to its sensitivity to nitrogen oxides or ozone,^{9,10} whereas functionalized structures with dispersed Pt NPs have demonstrated better sensitivity to hydrogen, ethanol or toluene.^{2,3,11} Tungsten oxide has been synthesized previously in a variety of forms (particles, wires, rods, etc) using wet- or vapor-chemical routes, and recently we have achieved the formation of tungsten oxide NWs and their functionalization with Pt NPs in a single-step process via a vapor-solid (VS) mechanism enabled by the Aerosol-Assisted Chemical Vapor Deposition (AACVD) of tungsten hexacarbonyl [W(CO)₆] and an inorganic platinum precursor (H₂PtCl₆·xH₂O).³

^a CEITEC - Central European Institute of Technology, Brno University of Technology, Brno, Czech Republic.

^b Department of Microelectronics, Faculty of Electrical Engineering and Communication, Brno University of Technology, Brno, Czech Republic.

^c Institute of Nanoscience and Nanotechnology (IN2UB), Universitat de Barcelona (UB), Barcelona, Spain

^d MIND - Department of Electronics, Universitat de Barcelona (UB), Barcelona, Spain

^e Instituto de Microelectrónica de Barcelona (IMB-CNM, CSIC), Barcelona, Spain

Electronic Supplementary Information (ESI) available: [details of any supplementary information available should be included here]. See DOI: 10.1039/x0xx00000x



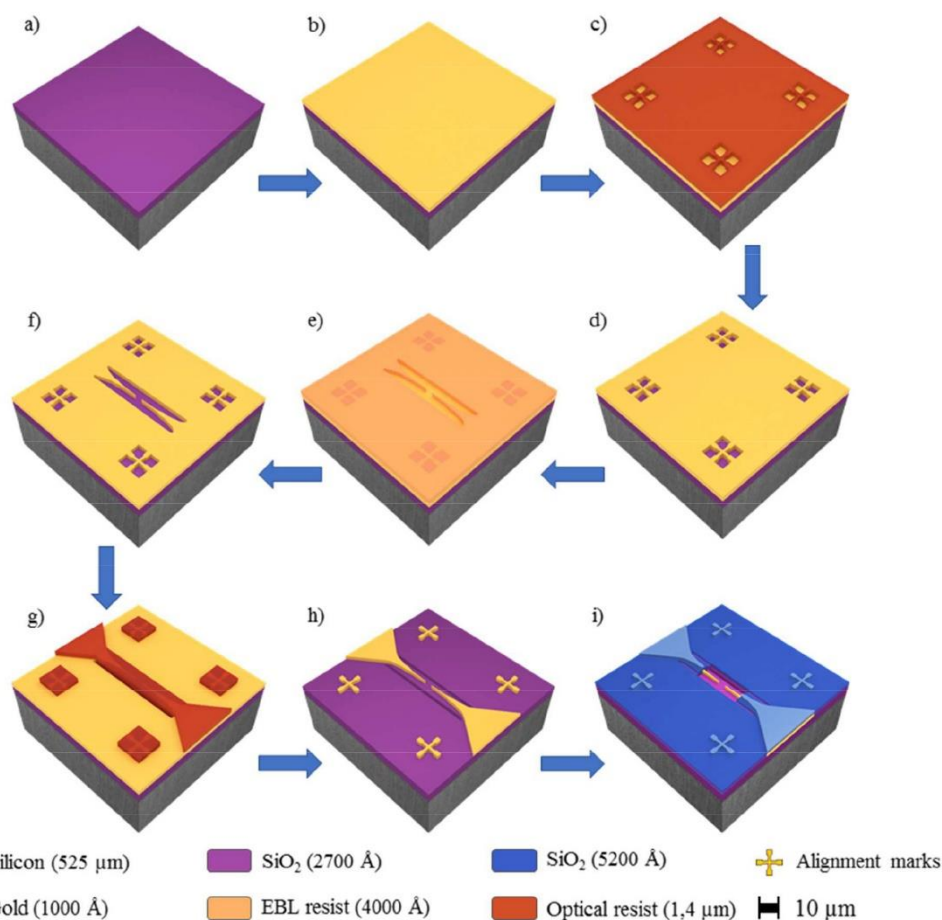


Figure 1. Simplified schematic view of the steps used to fabricate the array of nanoelectrodes (not to scale). SiO₂/Si wafer (a), sputtered gold on SiO₂/Si wafer (b), patterned of alignment marks (10 μm) for stitching fields – alignment procedure (c), gold structures after IBE (d), EBL resist layer for the nanoelectrode patterning (e), gold structures after IBE (f), DWL resist for the microelectrode patterning (g), final gold structure after IBE (h), SiO₂ insulation layer patterned (i).

Previous studies demonstrated that gas sensors based on a single (or few) -wire structures connected in parallel are the ideal architecture to achieve well-defined conduction channel easy to modulate by external stimuli (e.g., gaseous molecules) and with better gas detection efficiency compared to bulk materials or multiple wire systems. This improved efficiency, in single-wire systems, is attributed to the lack of grain boundaries and thus more efficient transfer of charge with a lower probability of recombination.^{5,12,13} Nevertheless, yet current gas sensor devices based on wires still depend on the wire-wire interfaces, despite the loss of efficiency that this architecture introduces, due to the relatively easier technological steps to integrate multiple-wire based films with

devices, as opposed to single-wires.² Focus ion beam (FIB) has demonstrated to be a useful tool to connect and fabricate single-wire devices, particularly in academic research, however, this technique restricts the scalability of the process and increase the cost and time of fabrication.^{14,15} In contrast, dielectrophoresis (DEP) method has become an attractive and robust manufacturing technique for positioning wires across contacts, often in microscale systems with single¹⁶ or multiple wires (e.g., in interdigitated electrodes),¹⁷ however, its use on nanoscale systems and in particular on arrays for gas sensing (without the need of a contact step with FIB) is still rarely found in the literature.



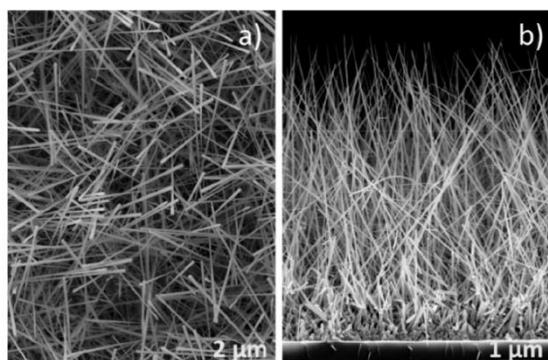


Figure 2. Top view and cross-sectional SEM images of the NW based films. Non-functionalized and Pt-functionalized tungsten oxide nanowires showed similar characteristics at microscale.

In this context, recently, we have advanced on the development of nanoelectrode array systems for the integration of single-NWs connected in parallel.¹⁸ These systems indicated suitability for the selective integration of single-NWs connected across arrays of electrodes using dielectrophoresis (DEP) method, and here we describe their fabrication in detail, their functionality and the sensing mechanism of these systems based on non-functionalized or Pt-functionalized tungsten oxide NWs synthesized via AACVD.

Sensor fabrication and characterization methods

The fabrication of the nanosensors involved three processing steps that included, (1) development of nanoelectrode arrays, (2) AACVD of non-functionalized or Pt-functionalized tungsten oxide NWs and (3) integration of both systems (i.e., nanoelectrodes and NWs) via DEP method. These processing steps are described in detail below.

Nanoelectrode arrays

Nanoelectrode arrays with 15, 30, 45 or 60 electrodes connected in parallel were produced at wafer-level employing various fabrication steps, including electron-beam lithography (EBL, Raith, E-beam writer Raith150 Two), direct writing laser lithography (DWL, Heidelberg Instruments, DWL 66-fs), metallization (Ion Beam Sputtering, Kaufman & Robinson—KRI®), passivation (RF Magnetron Sputtering, Bestec), ion beam etching (IBE, SCIA system, SCIA coat 200), reactive ion etching (RIE, Oxford Instruments, Plasma NGP 80) and dicing (Oxford Lasers, A-series). Overall, in this work, the resists were used following the standard conditions recommended by Allresist GmbH general product information. **Figure 1** displays a schematic view of the main processing steps carried out for the fabrication of the array of nanoelectrodes. Initially, a SiO₂/Si wafer (**Figure 1a**) was covered with gold (100 nm thick) (**Figure 1b**). Subsequently, the calibration marks were developed by DWL using positive tone resist (Allresist GmbH, AR-P 3540) (**Figure 1c, 1d**) in order to facilitate the next step,

i.e., the EBL process employed to define the nanoelectrodes with finger-widths of 100 nm. Thus EBL was performed at 20 kV using stitching strategy by 100 μm area on a positive tone electron beam resist (Allresist GmbH, AR-P 6200-13) with 400 nm thickness (**Figure 1e**), afterwards IBE was used to etch the gold and pattern the fine electrodes (**Figure 1f**). The microelectrodes and contact PADs were achieved by DWL; this process was carried out using a negative-tone optical-active resist (Allresist GmbH, AR-N 4340) with 1.4 μm thickness (**Figure 1g**) which also served as a temporary protective mask for the gold layer and the prior formed EBL structures. After development, IBE was repeated to establish the contact between the micro and nanoelectrodes (**Figure 1h**). Next, we use a double-stack bilayer of negative tone optical resist (Allresist GmbH, AR-N 4340 on top) mixed with a non-optical transparent resist layer (Allresist GmbH, AR-BR 5460 on bottom). Then, the electrically active areas were covered previously the RF magnetron sputtering (Bestec, Magnetron sputtering system) of a SiO₂ layer (250 μm thick), subsequently removed by lift-off (**Figure 1i**). Finally, the dicing procedure (5 × 5 mm) was performed using compact laser micromachining system (Oxford Lasers, A-series), followed by cleaning (Microchem, PG Remover) to remove the residual resist and other organic compounds from the surface.

Synthesis of functionalized tungsten oxide NWs

Pt-functionalized tungsten oxide NWs were co-deposited via AACVD from a methanolic solution (5 ml, Penta, ≥99.8%) of W(CO)₆ (20 mg, Sigma-Aldrich, ≥97%) and H₂PtCl₆·xH₂O (4 mg, Sigma-Aldrich, 99.9%), whereas non-functionalized tungsten oxide NWs were deposited from a methanolic solution (5 ml, Penta, ≥99.8%) containing only W(CO)₆ (20 mg, Sigma-Aldrich, ≥97%). Both processes were carried out on bare silicon tiles (2 × 2 mm) at 390 °C employing the AACVD system described previously.² The aerosol droplets of this solution were transported to the heated substrate using a constant nitrogen gas flow (200 sscm) that needed 45 min to transport the entire volume of solution (i.e., 5 ml). Overall, the AACVD of W(CO)₆ or W(CO)₆ co-reacted with H₂PtCl₆·xH₂O resulted in the formation of relatively weakly adhered (easily abraded or removed by sonication) uniform NW-based films, with diameters and lengths of approximately 100 nm and 10 μm, respectively. The characteristic top view and cross-sectional SEM images of the as-grown films are displayed in **Figure 2**. Prior to integrating the NWs into the nanoelectrode array, the NWs were removed from the silicon tiles by sonication (10 s) in water (the suspended NWs in water remained stable for several weeks showing unchanged properties).

On-chip integration

NWs, suspended in water, were integrated into the nanoelectrode array via DEP process using an alternating voltage (5V_{pp}, 9.5 MHz, Agilent 33220A) for 20 s, as illustrated in (**Figure 3**). To this end, a contact angle measurement station (SEO, Phoenix 300) provided of two CCD cameras to control the volume of the drop (0.7 μl) and facilitate the alignment of



the syringe with the electrode system was also employed. Prior to the integration of NWs, the array of nanoelectrodes was cleaned with oxygen plasma to remove unwanted organic impurities and activate the localized hydrophilic surface patterned around the electrodes. Electrical measurements were also performed to prove open circuit between the electrodes before the integration of nanowires.

source, 1486.74 eV). Gas sensing tests of the gas sensor devices were carried out towards ethanol (C_2H_5OH) and nitrogen dioxide (NO_2) by monitoring the electrical resistance changes of the NWs while applying different currents in the order of nanoamperes (Keithley 2400 SourceMeter®). The sensors were exposed to various concentrations of C_2H_5OH or NO_2 for five minutes in a continuous flow test chamber

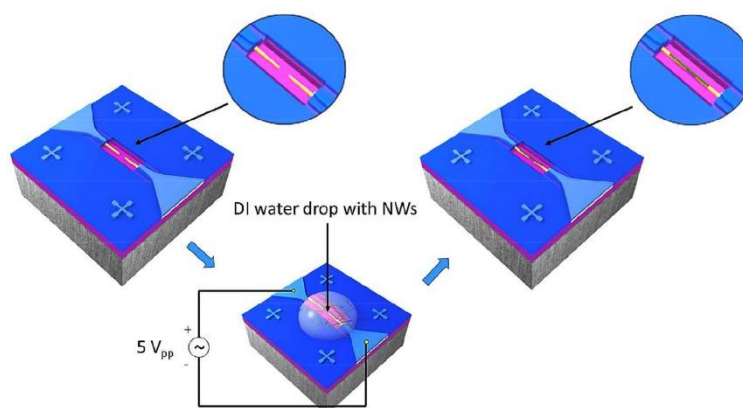


Figure 3. On-chip integration steps showing a pair of electrodes connected to the AC voltage source, the droplet with the suspended nanowires for DEP process and a single-nanowire connected across the electrodes after DEP. (not to scale)

Additionally, a resistive heating element was also developed to control the temperature of the Si-based chip during the gas sensing tests. This element was attached to the bottom of the nanosensor array system using silver glue (RS Pro, type 186-3593), and then mounted on a TO-8 package interconnected by gold wires (Wire bonder TPT, HB16) to the pins, as shown in **Figure 4**. The heating element consists of a multilayer thick film coated on the top of an alumina substrate (99 % Al_2O_3 , 250 μm thick).¹⁹ The multilayer thick film comprises a conductive layer for electrical connection, ruthenium resistive layer for heating and glass cover layer for electrical insulation.

Characterization methods

Samples were examined using scanning and transmission electron microscopy (SEM; Tescan FE Mira II LMU and TEM; FEI Tecnai F20, 200 kV) equipped with Energy Dispersive X-ray detection system (EDX), X-ray diffraction (XRD; Rigaku SmartLab 3 kW, Cu $K\alpha$ radiation) and X-ray photoelectron spectroscopy (XPS — Phoibos 150 analyzer — SPECS GmbH, Berlin, Germany - in ultrahigh vacuum conditions (base pressure 1×10^{-10} mbar) and a monochromatic $K\alpha$ X-ray

(200 sccm) provided of mass-flow controllers, and subsequently, the test chamber was purged with synthetic air for five minutes until the initial baseline resistance was recovered. The sensor response was defined as $(\Delta R/R_{air})$, i.e., $(R_{air}-R_{gas}/R_{air})$ for ethanol (reductive gas) and $(R_{gas}-R_{air}/R_{air})$ for nitrogen dioxide (oxidative gas), where R_{air} is the sensor resistance in air at the stationary state and R_{gas} the sensor resistance after five minutes of analyte exposure.

Results and discussions

Single-wire based nanosensor array systems

The processing steps described above led to the fabrication of gas sensing systems consisting of various parallel-connected pairs of nanoelectrodes with a single-NW interconnected across each pair. Generally, the integration of single-NWs into the nanoelectrode arrays (15 pairs) proved a success rate of approximately 33 %, thus each nanosensor employed in this work consisted of arrays of 5 single-NWs (non-functionalized or Pt-functionalized). The SEM images of the nanoelectrode array and a single-NW interconnected across a pair of electrodes after DEP process are displayed in **Figure 5**.

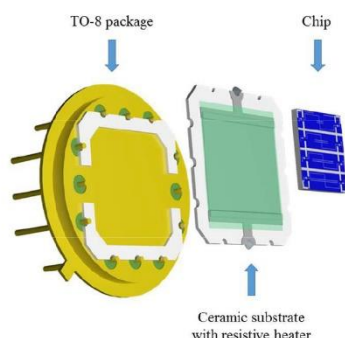


Figure 4. Schematic view of the elements comprising the gas-sensing device



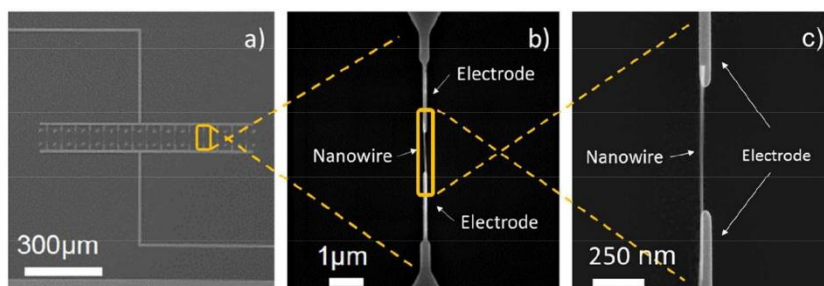


Figure 5. View of the nanoelectrodes connected in parallel (a) and detail view of a pair of electrodes with a NW interconnected across them (b)(c).

Analysis of the NWs (non-functionalized and Pt-functionalized) using XRD, TEM and XPS indicated the formation of monoclinic tungsten oxide NWs with monoclinic phase (P21/n space group, $a = 7.306 \text{ \AA}$, $b = 7.540 \text{ \AA}$, $c = 7.692 \text{ \AA}$, and $\beta = 90.88^\circ$; ICDD card no. 72-0677) and preferred orientation in the [010] direction, inferred by the intense diffraction peaks at $23.5^\circ 2\theta$ ($d = 3.7 \text{ \AA}$) and $48.2^\circ 2\theta$ ($d = 1.8 \text{ \AA}$), corresponding the (020) and (040) reflections of the tungsten oxide monoclinic phase, as well as by the marked planar spacing ($3.5 \pm 0.2 \text{ \AA}$) observed by HRTEM (Figure 6).

TEM of the NWs removed from the substrate by sonication and re-deposited on Cu grids confirmed the wire-like morphology with diameters between 50 and 100 nm. Non-functionalized NWs displayed a clean surface (Figure 7a),

whereas Pt-functionalized NWs displayed a surface covered with quasi-spherical nanoparticles of 1 to 5 nm dispersed along the NW surface (Figure 7b). Localized EDX of these structures confirmed the presence of W on the non-functionalized NWs, and W and Pt on the functionalized NWs. Moreover, analysis of the W 4f core level spectrum recorded on the non-functionalized (inset Figure 7a) and Pt-functionalized (inset Figure 7b) tungsten oxide NWs showed similar peak positions than those obtained in a tungsten oxide powder standard, with the peaks broadening in the NW-based films likely due to the presence of higher surface defects at the NWs, as noticed in previous studies.²⁰ The XPS spectrum recorded on the Pt-functionalized NWs (inset Figure 7b) also demonstrated the presence of Pt 4f core level peaks (found for Pt:W 3.7%), thus corroborating the incorporation of Pt at the tungsten oxide surface.

Functional properties

Gas sensing tests of the non-functionalized and Pt-functionalized tungsten oxide nanosensor array systems were carried out at different temperatures (from RT to 250 °C) and currents (from 10 to 100 nA), finding the maximum sensor responses to C₂H₅OH and NO₂ at 250 °C and better signal-to-noise ratio when using a constant current of 50 nA. For these conditions, the nanosensors showed consistently an increase or decrease of the electrical resistance after exposure to NO₂ (Figure 8) or C₂H₅OH (Figure 9), respectively, as noticed previously for other n-type MOX (including tungsten oxide) when exposed to oxidative or reductive species.¹⁰ These electrical resistance changes were proportional to the gas concentration (Figure 10) and reproducible, displaying similar characteristics (e.g., magnitude of the electrical resistance change and time of response and recovery) for the same gas concentration, as shown in Figure 8, Figure 9 and the supplementary information (Figure S1-S4). The recovery of the nanosensor (based on non-functionalized or Pt-functionalized NWs) proved slower towards NO₂, as opposed to C₂H₅OH, particularly at the high NO₂ concentration tested (i.e., 2.5 and 5 ppm). This is likely related to the need of higher thermal energy for desorption of NO₂ at the surface, however, due to the bonding and packaging characteristics, designed not to exceed a temperature of 300 °C, gas sensing test of the device at higher temperature were not performed in this work.

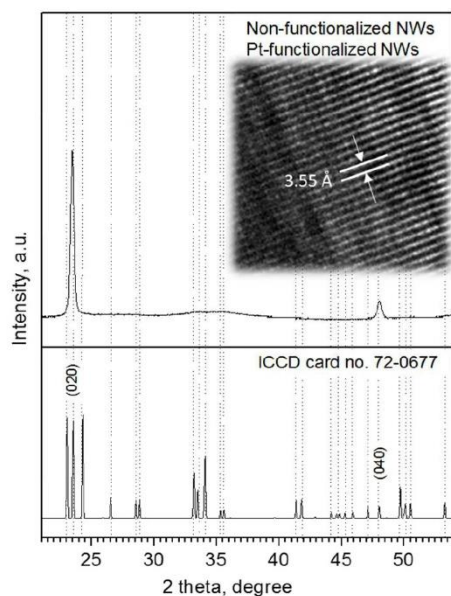


Figure 6. Typical XRD pattern and HRTEM (in set image) of the non-functionalized and Pt-functionalized tungsten oxide NWs. Overall, XRD patterns indicated a monoclinic phase (P21/n) with the peaks of high intensity (preferred orientation) specifically indexed to the ICDD card no. 72-0677, consistent with previous reports.³



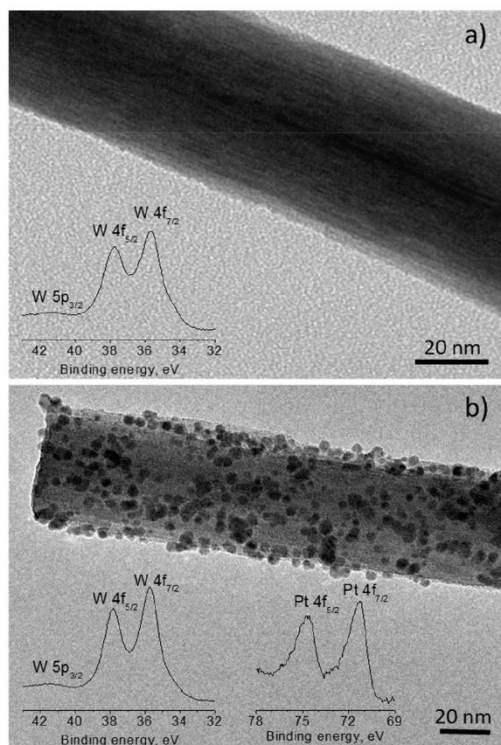


Figure 7. TEM of the non-functionalized (a) and Pt-functionalized (b) tungsten oxide NWs. The insets display the W 4f and Pt 4f XPS core-level spectrum for each type of wires.

Overall, the electrical resistance recorded on the non-functionalized nanosensors showed larger changes towards NO_2 , as opposed to the Pt-functionalized nanosensors, which showed larger changes towards $\text{C}_2\text{H}_5\text{OH}$. For instance the sensor response towards 2.5 ppm NO_2 registered a value of approximately 68% for the non-functionalized nanosensors and 30% for those functionalized with Pt NPs, whereas the sensor response towards 100 ppm of $\text{C}_2\text{H}_5\text{OH}$, registered a value of approximately 32% and 86% for the non-functionalized and Pt-functionalized nanosensors, respectively (Figure 10). These results indicate a better sensitivity to NO_2 for the non-functionalized nanosensors, in contrast to the Pt-functionalized nanosensors, showing consistency with the literature, which previously demonstrated that non-modified tungsten oxide in various forms (e.g., thin films,²¹ nanoparticles, nanolamellas,²² or nanofibers²³) is more sensitive to oxidative species than reductive species,¹⁰ even at low concentrations (e.g., 1 ppm²⁴) and in the range of operating temperatures studied in this work. Similarly, these results show better sensitivity to $\text{C}_2\text{H}_5\text{OH}$ for the Pt-functionalized nanosensors compared to those without functionalization, which is also consistent with previous reports in the literature that demonstrated the enhancement

of sensitivity in n-type MOX modified with Pt NPs (e.g., Pt@ WO_3 ,^{25,26} Pt@ ZnO ,²⁵ or Pt@ TiO_2 ²⁷) towards reductive species, including $\text{C}_2\text{H}_5\text{OH}$.

A comparative table showing the sensor responses recorded in this work and the literature for other single-wire and multiple randomly connected wire systems towards NO_2 and $\text{C}_2\text{H}_5\text{OH}$ is displayed in Table 1. We consider Table 1 is meant to provide a general idea of the properties of our sensors, despite the complexity behind the comparison of the sensor outputs, which depend strongly on the fabrication and test set-up employed in each work. It is worth noting that Table 1 takes into account only the optimum condition reported in each work towards NO_2 or $\text{C}_2\text{H}_5\text{OH}$. Also, that the use of tungsten oxide for single-wire sensors is not frequent in literature, which has been found to be particularly focused on other MOX wires such as SnO_2 ,²⁸ In_2O_3 ^{15,29} or ZnO .³⁰ Based on this literature search, we have noticed that our sensors show better or similar responses than other single-NW systems reported previously (considering the gas concentrations tested). We also noticed lower magnitudes of response for the single-wire based sensors compared to those based on multiple wires. This is attributed to the broader exposed surface area in multiple wires (as opposed to a single or few NWs), which allows for a greater number of gas molecules to impinge the surface, in turn, amplifying the electrical output signal, as demonstrated previously when comparing the gas sensing performance of thin films and single-NW systems.¹²

Table 1. Summary of the responses recorded in this work and the literature for sensors based on single and multiple wires towards NO_2 and $\text{C}_2\text{H}_5\text{OH}$.

| Type | Material | Features, nm | R, % | Gas | ppm | Ref |
|------|------------------------------|--|------|---------------------------------|------|-----------|
| S-WA | WO_3 | 100^{D} 10000^{L} | 55 | NO_2 | 1 | This work |
| S-W | SnO_2 | 90^{D} 15000^{L} | 25 | NO_2 | 0.5 | 28 |
| S-W | SnO_2 | 78^{D} | 100 | NO_2 | 100 | 31 |
| M-Ws | WO_{3-x} | 50^{D} | 1560 | NO_2 | 1 | 32 |
| M-Ws | $\text{W}_{15}\text{O}_{49}$ | 90^{D} 1000^{L} | 1304 | NO_2 | 1 | 33 |
| M-Ws | $\text{W}_{15}\text{O}_{49}$ | 1000^{D} | 335 | NO_2 | 1 | 34 |
| M-Ws | WO_{3-x} | --- | 500 | NO_2 | 5 | 35 |
| S-WA | Pt@ WO_{3-x} | 5^{DNP} 100^{D} 10000^{L} | 88 | $\text{C}_2\text{H}_5\text{OH}$ | 100 | This work |
| S-W | In_2O_3 | 220^{D} 5000^{L} | 47 | $\text{C}_2\text{H}_5\text{OH}$ | 100 | 15 |
| S-W | CP | 220^{D} 6000^{L} | 0.15 | $\text{C}_2\text{H}_5\text{OH}$ | 2000 | 36 |
| M-Ws | WO_{3-x} | 100^{D} 10000^{L} | 300 | $\text{C}_2\text{H}_5\text{OH}$ | 10 | 37 |
| M-Ws | Pt@ WO_{3-x} | 5^{DNP} 100^{D} 10000^{L} | 450 | $\text{C}_2\text{H}_5\text{OH}$ | 10 | 37 |
| M-Ws | Au@ WO_{3-x} | 30^{DNP} 200^{D} 2000^{L} | 98 | $\text{C}_2\text{H}_5\text{OH}$ | 4 | 38 |

S-WA: single-NW array, S-W: single-NW, M-Ws: multiple wires (wire based films), ^D: wire diameter, ^L: wire length, R: response ($\Delta R/R_{\text{air}}$)

Further tests of the sensors towards other analytes including carbon monoxide (CO) and ammonia (NH_3) showed typical n-type semiconducting behaviour during gas exposure (Figure S1 and S5). Overall, the responses to CO were negligible, whereas the response to NH_3 registered higher values for the non-functionalized nanosensors than for the Pt-functionalized nanosensors. A global view of the results (Figure S6) suggests good selectivity for the non-functionalized nanosensors to NO_2 respect to $\text{C}_2\text{H}_5\text{OH}$, NH_3 and CO, and a moderate cross-response among the reductive gases (i.e., $\text{C}_2\text{H}_5\text{OH}$, NH_3 and CO). In contrast, Pt-functionalized nanosensors suggest better selectivity among reductive gases compared to the non-functionalized nanosensors, although with a higher probability of interference from NO_2 (oxidative gas) to $\text{C}_2\text{H}_5\text{OH}$.



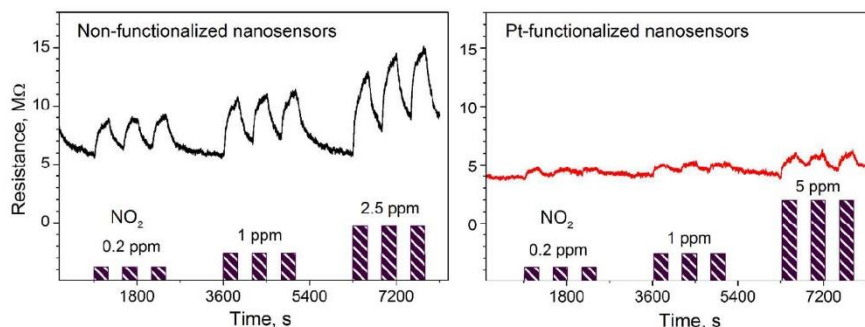


Figure 8. Electrical resistance changes of the non-functionalized and Pt-functionalized nanosensors at 250 °C and 50 nA to various concentrations of NO_2 . Purple color bars represent the concentrations and exposure time to NO_2 in each test.

Pt-functionalized nanosensors also displayed sensitivity to humidity (Figure S7). However, and despite this property is undesired in gas sensors, strong humidity interferences have also been noticed in previous reports on tungsten oxide and its modification with Pt,^{2,39} in agreement with our results.

Gas sensing mechanism

The sensing results can be understood on the basis of the mechanism of chemical sensing on MOX surfaces, in which the pre-adsorbed oxygen species at the MOX react with gaseous analytes producing electrical changes in the MOX. Thus, when non-functionalized NWs are exposed to air, they adsorb oxygen molecules at their surface leading to the formation of different chemisorbed oxygen species (O_2^- at temperatures lower than 130 °C, O^- at temperatures between 130 – 300 °C and O^{2-} at temperatures higher than 300 °C)⁴⁰ by capturing electrons from the conduction band (Equations 1-3), which in turn produces a depletion layer and an increase in the resistance of the tungsten oxide NWs, as illustrated in Figure 11a and 11b. This mechanism is similar for the Pt-functionalized NWs (Figure 11c), although, due to the large difference in the work function of Pt (5.12 – 5.93 eV)⁴¹ and band gap of tungsten oxide (2.5-3.5 eV),⁴² nano-Schottky barriers are formed at the interface of the Pt NPs and the tungsten oxide NW. This induces to an accumulation of electrons on the Pt NPs and the formation of holes on the

tungsten oxide NWs,²⁷ thus resulting in an enlargement of the tungsten oxide depletion layer at the surroundings of the Pt NPs. Simultaneously, the catalytic Pt NPs also activate the dissociation of molecular oxygen and their distribution onto the surface of the NW. This effect, known as “spillover”, strongly increases the quantity of adsorbed oxygen species on the tungsten oxide surface (Figure 11d).



After the exposure of the sensors to ethanol at 250 °C, the following reaction paths are likely to occur at the surface dominated by pre-adsorbed O^- :^{43,44}

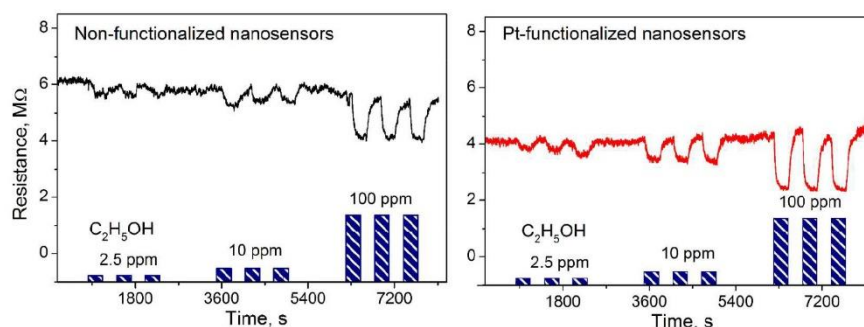
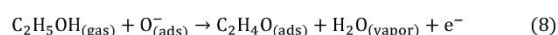
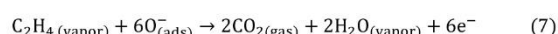
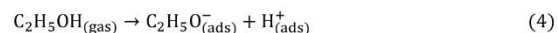


Figure 9. Electrical resistance changes of the non-functionalized and Pt-functionalized nanosensors at 250 °C and 50 nA to various concentrations of $\text{C}_2\text{H}_5\text{OH}$. Blue color bars represent the concentrations and exposure time to $\text{C}_2\text{H}_5\text{OH}$ in each test.



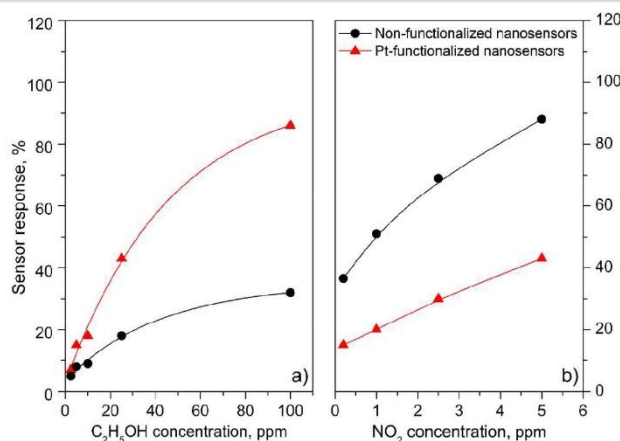


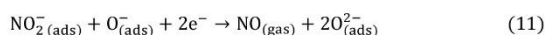
Figure 10. Sensor response Vs. concentration curves of the non-functionalized and Pt-functionalized nanosensors towards C_2H_5OH (a) and NO_2 (b).



Generally, C_2H_5OH molecules are adsorbed on the surface of tungsten oxide via the oxygen atoms of the hydroxyl groups (Equation 4), and the resultant H^+ ions react with O^- ions (Equation 5) to form water molecules, which are then desorbed. At elevated temperatures ($>200^\circ C$), the adsorbed ethoxy groups can also be decomposed into ethylene and water that later are desorbed from the surface (Equations 6 and 7). C_2H_5OH can also be decomposed to acetaldehyde by reaction with the lattice oxygen with subsequent desorption of vapor of acetic acid and the release of electrons towards tungsten oxide due to the formation of oxygen vacancies (V_O) (Equations 8 and 9).⁴³ To sum up, the C_2H_5OH molecules adsorb at the non-functionalized tungsten oxide surface, providing electrons to reduce the adsorbed ionic oxygen and release the free electrons back to the tungsten oxide conduction band. This process reduces the width of the depletion region and increases the conduction of the tungsten oxide NWs.

A similar mechanism occurs for Pt-functionalized tungsten oxide during C_2H_5OH sensing, however with significant improvements in the response to C_2H_5OH , first, due to the increment of pre-adsorbed oxygen as a result of the trap and accumulation of oxygen species at the Pt NPs and/or spill of these species over the NW surface, and second, due to the promotion and acceleration of the reactions described above at the Pt NPs, unlike the mechanism occurring at the non-functionalized tungsten oxide surface.⁴⁵ Hence, in contrast to the non-functionalized NWs, the Pt-functionalized surface (that is covered with a higher amount of pre-adsorbed oxygen species) promotes the release of more electrons into the tungsten oxide conduction band during C_2H_5OH adsorption, and in turn, the record of larger resistance changes in the Pt-functionalized nanosensors towards C_2H_5OH .

On the other hand, when the NWs are exposed to NO_2 , the NO_2 molecules are adsorbed as NO_2^- (Equation 10) capturing electrons from the tungsten oxide conduction band and reacting further with the adsorbed ionic oxygen (Equation 11) to form nitric oxide and O^{2-} .⁴⁶



These reactions take electrons from the conduction band of the tungsten oxide NW producing a wider depletion layer than that formed during the pre-adsorption of oxygen, which results in a further increase of the resistance along the non-functionalized wire. As for the Pt-functionalized NWs, due to these structures are more depleted of electrons after the pre-adsorption of oxygen, the NO_2 molecules exposed to this surface find less electrons in the tungsten oxide conduction band to be accepted and to form NO_2^- adsorbents, making the Pt-functionalized NW less sensitive to NO_2 than to C_2H_5OH , as noticed in the functional tests of these systems.

In summary, these results demonstrate a reliable operation of the nanosensors, with consistent functional properties that validate the fabrication of the sensing device. The fabrication method reported here, which includes the selective integration of functional single-NWs (<100 nm) into an array of EBL developed electrodes with nanoscale finger-widths of ~ 100 nm, is an attractive route for developing the next generation of single-wire based nanosensors without using non-scalable and time-consuming techniques, such as FIB, and circumventing the electrical percolation issues of conventional chemoresistive sensors based on sensitive films with multiple NWs.



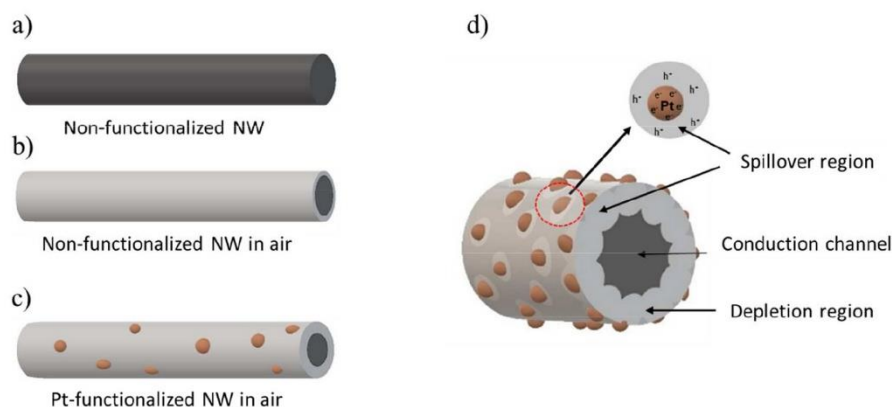


Figure 11. A schematic illustration of the sensing mechanism of the non-functionalized and Pt-functionalized nanosensor. Fully conducting tungsten oxide NW (a). Formation of depletion region around the NW when exposed to air (b) and increase of the depletion region on modification with Pt nanoparticles (c). Formation of Schottky barriers at the Pt NPs and tungsten oxide NW interface contributing to the spillover effect and the enlargement of the depletion region in air (d).

Conclusions

Single-NW gas nanosensor array systems based on non-functionalized or Pt-functionalized tungsten oxide were fabricated using various processing steps that include electron beam lithography to define the parallel-connected nanoelectrodes, AACVD to grow the NWs and DEP to align single-NWs across each pair of nanoelectrodes. Results demonstrated the selective integration of single-NWs into the array of nanoelectrodes, and the gas sensing tests of these systems validated the functionality of the device. Overall, the sensor performance proved a reproducible behavior with the Pt-functionalized NWs, showing a better response to C_2H_5OH , compared to the non-functionalized NWs systems, which responded better to NO_2 ; in agreement with similar systems reported previously in the literature. These results were attributed to the additional chemical and electronic interactions at the interface of the Pt NPs and tungsten oxide NWs, which increase the pre-adsorption of oxygen species at the functionalized NW surface and, in turn, the sensitivity to C_2H_5OH rather than NO_2 ; as opposed to the non-functionalized tungsten oxide surface.

Acknowledgements

This work has been supported by the Czech Science Foundation (GAČR) via Grant no. 17-16531S, and in part by the Czech Ministry of Education, Youth and Sports of Czech Republic under grant LO141 and CEITEC Nano Research (ID LM2015041, MEYS CR, 2016–2019). This research made use of the SIX Research Centre. O. Ch. acknowledges the Grant no. FEKT-S-17-3934. The support from the Spanish Ministry of Economy and Competitiveness, via projects TEC2016-79898-C6 (AEI/FEDER, EU) and TEC2015-74329-JIN-(AEI/FEDER, EU), is also acknowledged.

Conflicts of interest

There are no conflicts to declare.

Notes and references

- M. Anish Kumar, S. Jung and T. Ji. *Sensors*, 2011, **11**, 5087-5111; K.-Y. Choi, J.-S. Park, K.-B. Park, H. J. Kim, H.-D. Park and S.-D. Kim. *Sens. Actuators B*, 2010, **150**, 65-72; L. Chih-Hao, H. Min Hsiung, K. Chi-Yun and L. Ing-Chi. *Jpn. J. Appl. Phys.*, 2014, **53**, 06JG08; D. K. Roh, R. Patel, S. H. Ahn, D. J. Kim and J. H. Kim. *Nanoscale*, 2011, **3**, 4162-4169; K. Joondong, Y. Ju-Hyung, K. Chang Hyun, P. Yun Chang, W. Ju Yeon, P. Jeunghee, L. Jung-Ho, Y. Junsin and H. Chang-Soo. *Nanotechnology*, 2010, **21**, 115205.
- S. Vallejos, I. Gràcia, O. Chmela, E. Figueras, J. Hubálek and C. Cané. *Sens. Actuators B*, 2016, **235**, 525-534.
- S. Vallejos, I. Gràcia, E. Figueras and C. Cané. *ACS Appl. Mater. Interfaces*, 2015, **7**, 18638-18649.
- H. Huang, B. Liang, Z. Liu, X. Wang, D. Chen and G. Shen. *J. Mater. Chem.*, 2012, **22**, 13428-13445.
- D. R. Miller, S. A. Akbar and P. A. Morris. *Sens. Actuators B*, 2014, **204**, 250-272.
- A. Gurlo. *Nanoscale*, 2011, **3**, 154-165.
- J. F. Mcaleer, P. T. Moseley, J. O. W. Norris, D. E. Williams and B. C. Tofield. *J. Chem. Soc., Faraday Trans. 1*, 1988, **84**, 441-457.
- A. Kolmakov, D. O. Klenov, Y. Lilach, S. Stemmer and M. Moskovits. *Nano Lett.*, 2005, **5**, 667-673.
- H. G. Moon, S. D. Han, M.-G. Kang, W.-S. Jung, B. Kwon, C. Kim, T. Lee, S. Lee, S.-H. Baek, J.-S. Kim, H.-H. Park and C.-Y. Kang. *Sens. Actuators B*, 2016, **229**, 92-99; Y. Qin, X. Zhang, Y. Wang and Y. Liu. *Sens. Actuators B*, 2017, **240**, 477-486.
- S. Vallejos, V. Khatko, J. Calderer, I. Gracia, C. Cané, E. Llobet and X. Correig. *Sens. Actuators B*, 2008, **132**, 209-215.
- J. Zhang, X. H. Liu, M. J. Xu, X. Z. Guo, S. H. Wu, S. M. Zhang and S. R. Wang. *Sens. Actuators B*, 2010, **147**, 185-190; I. Lee, S.-J. Choi, K.-M. Park, S. S. Lee, S. Choi, I.-D. Kim and C. O. Park. *Sens. Actuators B*, 2014, **197**, 300-307.
- E. Brunet, T. Maier, G. C. Mutinati, S. Steinhauer, A. Köck, C. Gspan and W. Grogger. *Sens. Actuators B*, 2012, **165**, 110-118.
- X. Chen, C. K. Y. Wong, C. A. Yuan and G. Zhang. *Sens. Actuators B*, 2013, **177**, 178-195; R. M. Penner. *Annu. Rev. Anal. Chem.*, 2012, **5**, 461-485; N. S. Ramgir, Y. Yang and M. Zacharias. *Small*, 2010, **6**, 1705-1722.

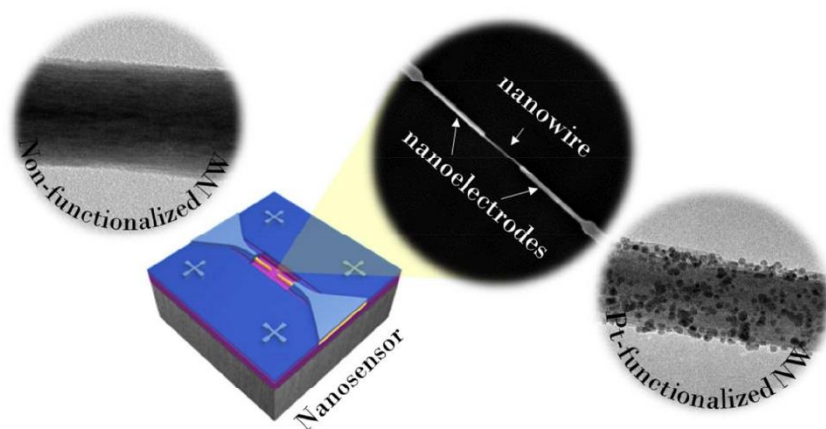


ARTICLE

Nanoscale

- 14 F. Hernandez-Ramirez, A. Tarancon, O. Casals, J. Rodriguez, A. Romano-Rodriguez, J. R. Morante, S. Barth, S. Mathur, T. Y. Choi, D. Poulidakos, V. Callegari and P. M. Nellen. *Nanotechnology*, 2006, **17**, 5577-5583.
- 15 G. Domènech-Gil, S. Barth, J. Samà, P. Pellegrino, I. Gràcia, C. Cané and A. Romano-Rodriguez. *Sens. Actuators B*, 2017, **238**, 447-454.
- 16 E. M. Freer, O. Grachev, X. Duan, S. Martin and D. P. Stumbo. *Nat. Nanotechnol.*, 2010, **5**, 525; S. Junya, N. Nobutaka, H. Shin-ichiro, U. Makoto, I. Kiminobu, H. Mitsuhiro, O. Tatsuo and H. Masanori. *Nanotechnology*, 2006, **17**, 2567.
- 17 J. Guiler, C. Fàbrega, O. Casals, F. Hernández-Ramírez, S. Wang, S. Mathur, F. Udrea, A. De Luca, S. Z. Ali, A. Romano-Rodríguez, J. D. Prades and J. R. Morante. *Sens. Actuators B*, 2015, **221**, 104-112.
- 18 O. Chmela, J. Sadílek, J. Samà, A. Romano-Rodríguez, J. Hubálek and S. Vallejos. in *Proceedings of SPIE - The International Society for Optical Engineering*. 102480F.
- 19 G. Radosavljevic and W. Smetana. in *Printed Films 429-468* (Woodhead Publishing, 2012).
- 20 C. Navío, S. Vallejos, T. Stoycheva, E. Llobet, X. Correig, R. Snyders, C. Blackman, P. Umek, X. Ke, G. Van Tendeloo and C. Bittencourt. *Mater. Chem. Phys.*, 2012, **134**, 809-813.
- 21 A. Maity and S. B. Majumder. *Sens. Actuators B*, 2015, **206**, 423-429.
- 22 T. Liu, J. Liu, Q. Hao, Q. Liu, X. Jing, H. Zhang, G. Huang and J. Wang. *CrystEngComm*, 2016, **18**, 8411-8418.
- 23 L. Giancaterini, S. M. Emamjomeh, A. De Marcellis, E. Palange, A. Resmini, U. Anselmi-Tamburini and C. Cantalini. *Sens. Actuators B*, 2016, **229**, 387-395.
- 24 A. J. T. Naik, M. E. A. Warwick, S. J. A. Moniz, C. S. Blackman, I. P. Parkin and R. Binions. *J. Mater. Chem. A*, 2013, **1**, 1827-1833.
- 25 Y. A. Zhang, J. Q. Xu, P. C. Xu, Y. H. Zhu, X. D. Chen and W. J. Yu. *Nanotechnology*, 2010, **21**.
- 26 J. Y. Luo, X. X. Chen, W. Da Li, W. Y. Deng, W. Li, H. Y. Wu, L. F. Zhu and Q. G. Zeng. *Appl. Phys. Lett.*, 2013, **102**; R. J. Bose, N. Illyaskutty, K. S. Tan, R. S. Rawat, M. V. Matham, H. Kohler and V. P. M. Pillai. *Europhys. Lett.*, 2016, **114**.
- 27 H. Chen, S. Chen, X. Quan, H. T. Yu, H. M. Zhao and Y. B. Zhang. *J. Phys. Chem. C*, 2008, **112**, 9285-9290.
- 28 J. D. Prades, R. Jimenez-Diaz, F. Hernandez-Ramirez, S. Barth, A. Cirera, A. Romano-Rodriguez, S. Mathur and J. R. Morante. *Appl. Phys. Lett.*, 2008, **93**, 123110; J. D. Prades, R. Jimenez-Diaz, F. Hernandez-Ramirez, J. Pan, A. Romano-Rodríguez, S. Mathur and J. R. Morante. *Appl. Phys. Lett.*, 2009, **95**, 053101.
- 29 X. Zou, J. Wang, X. Liu, C. Wang, Y. Jiang, Y. Wang, X. Xiao, J. C. Ho, J. Li, C. Jiang, Y. Fang, W. Liu and L. Liao. *Nano Letters*, 2013, **13**, 3287-3292.
- 30 M. Cardoza-Contreras, J. Romo-Herrera, L. Ríos, R. García-Gutiérrez, T. Zepeda and O. Contreras. *Sensors*, 2015, **15**, 29816.
- 31 M. Toneyzer and N. V. Hieu. *Sens. Actuators B*, 2012, **163**, 146-152.
- 32 T. Stoycheva, F. E. Annanouch, I. Gràcia, E. Llobet, C. Blackman, X. Correig and S. Vallejos. *Sens. Actuators B*, 2014, **198**, 210-218.
- 33 Y. Qin, M. Hu and J. Zhang. *Sens. Actuators B*, 2010, **150**, 339-345.
- 34 N. Van Hieu, H. Van Vuong, N. Van Duy and N. D. Hoa. *Sens. Actuators B*, 2012, **171-172**, 760-768.
- 35 A. Ponzoni, E. Comini, G. Sberveglieri, J. Zhou, S. Z. Deng, N. S. Xu, Y. Ding and Z. L. Wang. *Appl. Phys. Lett.*, 2006, **88**, 203101.
- 36 D. Yaping, C. Yanyan, E. M. Tom, E. Stephane and A. T. C. Johnson. *Nanotechnology*, 2009, **20**, 434014.
- 37 S. Vallejos, P. Umek, T. Stoycheva, F. Annanouch, E. Llobet, X. Correig, P. De Marco, C. Bittencourt and C. Blackman. *Adv. Funct. Mater.*, 2013, **23**, 1313-1322.
- 38 F. Di Maggio, M. Ling, A. Tsang, J. Covington, J. Saffell and C. Blackman. *J. Sens. Sens. Syst.*, 2014, **3**, 325-330.
- 39 C. Zhang, A.-F. Kanta, H. Yin, A. Boudiba, J. D'Haen, M.-G. Olivier and M. Debliquy. *Int. J. Hydrogen Energy*, 2013, **38**, 2929-2935; W.-T. Koo, S.-J. Choi, N.-H. Kim, J.-S. Jang and I.-D. Kim. *Sens. Actuators B*, 2016, **223**, 301-310.
- 40 S. Lenaerts, J. Roggen and G. Maes. *Spectrochim. Acta, Part A*, 1995, **51**, 883-894; M. Sinha, R. Mahapatra, B. Mondal, T. Maruyama and R. Ghosh. *J. Phys. Chem. C*, 2016, **120**, 3019-3025; J. C. Belmonte, J. Manzano, J. Arbiol, A. Cirera, J. Puigcorbe, A. Vila, N. Sabate, I. Gracia, C. Cane and J. R. Morante. *Sens. Actuators B*, 2006, **114**, 881-892; N. Barsan and U. Weimar. *J. Electroceram.*, 2001, **7**, 143-167.
- 41 M. H. Luo, W. F. Yao, C. P. Huang, Q. Wu and Q. J. Xu. *J. Mater. Chem. A*, 2015, **3**, 13884-13891.
- 42 Y. Baek and K. Yong. *J. Phys. Chem. C*, 2007, **111**, 1213-1218.
- 43 D. L. Chen, X. X. Hou, H. J. Wen, Y. Wang, H. L. Wang, X. J. Li, R. Zhang, H. X. Lu, H. L. Xu, S. K. Guan, J. Sun and L. Gao. *Nanotechnology*, 2010, **21**.
- 44 K. Mirabbaszadeh and M. Mehrabian. *Phys. Scr.*, 2012, **85**; F. Hellegouarc'h, F. Arefi-Khonsari, R. Planade and J. Amouroux. *Sens. Actuator B*, 2001, **73**, 27-34; A. Labidi, E. Gillet, R. Delamare, M. Maaref and K. Aguir. *Sens. Actuator B*, 2006, **120**, 338-345.
- 45 L. M. Petkovic, S. N. Rashkeev and D. M. Ginosar. *Catal. Today*, 2009, **147**, 107-114.
- 46 E. Oh, H. Y. Choi, S. H. Jung, S. Cho, J. C. Kim, K. H. Lee, S. W. Kang, J. Kim, J. Y. Yun and S. H. Jeong. *Sens. Actuators B*, 2009, **141**, 239-243.





Arrays of gas nanosensors comprised of electrodes with finger-widths of ~ 100 nm and nanowires (< 100 nm) are fabricated and validated.



Supplementary Information

Selectively arranged single-wire based nanosensor array systems for gas monitoring

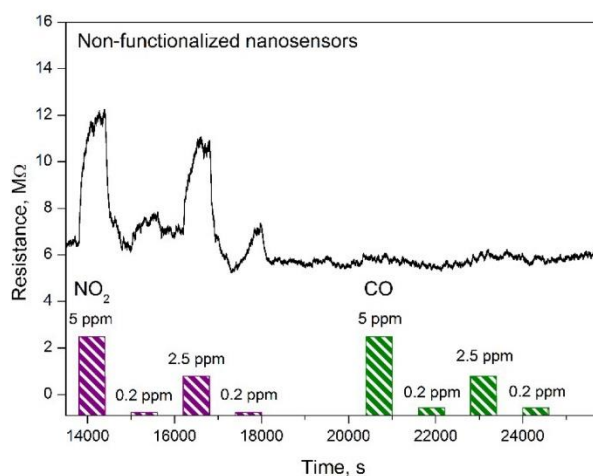
O. Chmela,^{a,b} J. Sadílek,^a G. Domènech-Gil,^{c,d} J. Samà,^{c,d} J. Somer,^b R. Mohan,^a A. Romano-Rodriguez,^{c,d}
J. Hubálek,^{a,b} S. Vallejos^{a,e*}

Figure S1. Electrical resistance changes (black color line) of the non-functionalized nanosensors towards various concentrations of NO₂ and CO in air, showing negligible resistance changes (i.e., response) during the exposure of the sensors to CO. Purple and green color bars represent the concentration and exposure time to NO₂ and CO, respectively.

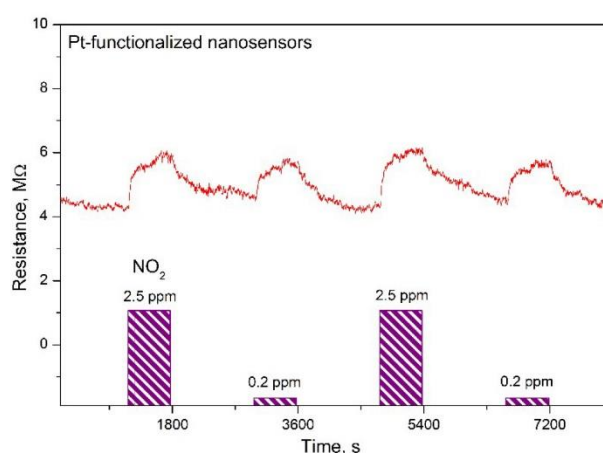


Figure S2. Electrical resistance changes (red color line) of the non-functionalized nanosensors towards various concentrations of NO₂. Purple color bars represent the concentration and exposure time to NO₂.

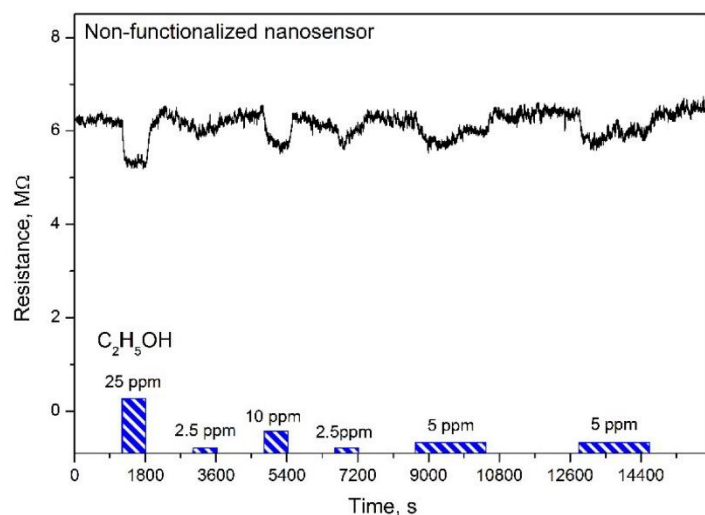


Figure S3. Electrical resistance changes (black color line) of the non-functionalized nanosensors towards various concentrations of C₂H₅OH. Blue color bars represent the concentration and exposure time to C₂H₅OH.

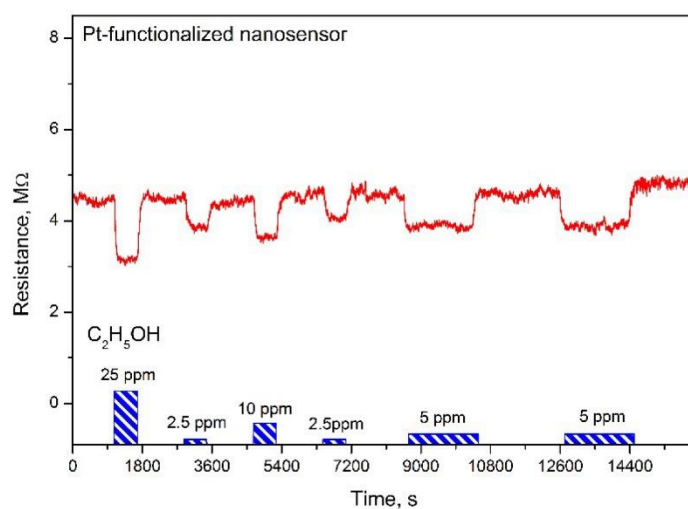


Figure S4. Electrical resistance changes (red color line) of the non-functionalized nanosensors towards various concentrations of C₂H₅OH. Blue color bars represent the concentration and exposure time to C₂H₅OH.

4. Integration methodologies for nanowire-based gas sensors

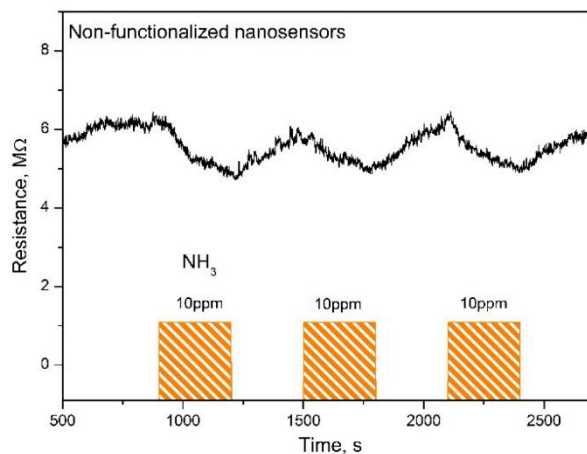


Figure S5. Electrical resistance changes of the non-functionalized (black color line) nanosensors towards 10 ppm of NH₃. Orange color bars represent the concentration and exposure time to NH₃. Generally, the response to NH₃ using both the non-functionalized and Pt-functionalized nanosensors displayed large response and recovery times as noticed in the figure.

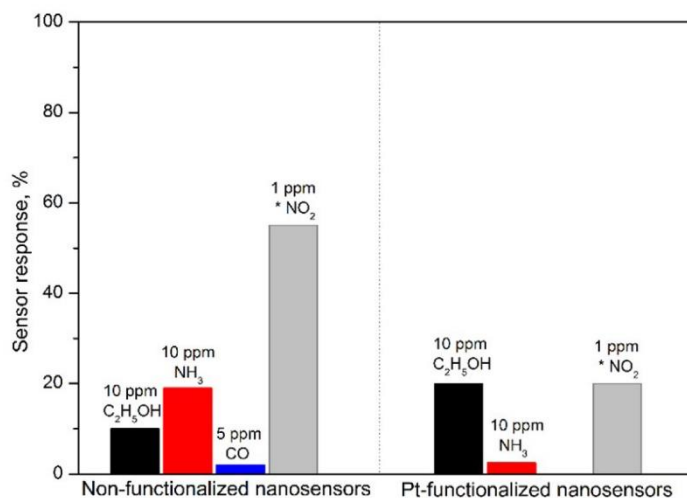


Figure S6. Summary of the sensor response towards various analytes including C₂H₅OH, NH₃, CO and NO₂ (*oxidative gas) showing the possible cross-responses among them.

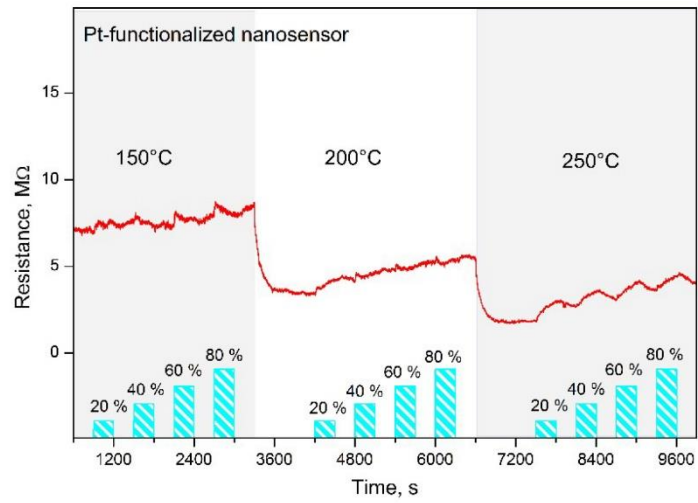


Figure S7. Electrical resistance changes of the Pt-functionalized nanosensors (red color line) towards various RH (relative humidity, cyan color bars) at different sensor operating temperatures.

4.2 Gas sensor based on individual tin oxide nanowire contacted by Electron Beam Lithography



Contents lists available at ScienceDirect

Sensors and Actuators B: Chemical

journal homepage: www.elsevier.com/locate/snb

Electron beam lithography for contacting single nanowires on non-flat suspended substrates

Jordi Samà^{a,b}, Guillem Domènech-Gil^{a,b}, Isabel Gràcia^c, Xavier Borrís^c, Carles Cané^c,
Sven Barth^d, Frederik Steib^e, Andreas Waag^e, Juan Daniel Prades^{a,b},
Albert Romano-Rodríguez^{a,b,*}

^a Institute of Nanoscience and Nanotechnology (IN2UB), Universitat de Barcelona (UB), c/Martí i Franquès 1, 08028 Barcelona, Spain

^b MIND-Department of Electronic and Biomedical Engineering, Universitat de Barcelona (UB), c/Martí i Franquès 1, 08028 Barcelona, Spain

^c Institut de Microelectrònica de Barcelona, Centre Nacional de Microelectrònica, Consejo Superior de Investigaciones Científicas, (IMB-CNM-CSIC), Campus UAB, 08193 Bellaterra, Spain

^d Institute of Materials Science, University of Stuttgart, Heisenbergstrasse 3, 70569 Stuttgart, Germany

^e Institut für Halbleitertechnik and Laboratory for Emerging Nanometrology, Technische Universität Braunschweig, 38092 Braunschweig, Germany

ARTICLE INFO

Keywords:

Gas sensor
Individual nanowire
Metal oxide
EBL fabrication
Microhotplates

ABSTRACT

A methodology based on the use of Electron Beam Lithography for contacting individual nanowires on top of non-flat micromembranes and microhotplates has been implemented, and the practical details have been exhaustively described. The different fabrication steps have been adapted to the substrate's topology, requiring specific holders and conditions. The methodology is demonstrated on individual SnO₂ nanowires, which, after fabrication, have been characterized as functional resistive gas nanosensors towards NH₃ and benchmarked against similar devices fabricated using more conventional Dual Beam Focused Ion Beam techniques, demonstrating the superior properties of the here presented methodology, which can be further extended to other non-conventional suspended substrates and nanomaterials.

1. Introduction

Engineered nanomaterials, like nanotubes, nanowires, nanorods, etc. can be tailored to meet the needs of many applications in chemistry, physics, biology, and electronics [1–3]. As a result, they are nowadays becoming key elements in the design and production of advanced microsystems and devices [4]. In electronic engineering, these nanomaterials are being integrated using existing microfabrication technologies to develop the prototypes of tomorrow's electronic devices. The development of such prototypes is still an open challenge with a number of unsolved fabrication issues [5,6].

Among them, and specifically when dealing with individual nanostructures, the fabrication of electrical contacts are widely performed by the most advanced direct writing nanofabrication techniques to provide high spatial resolution and flexibility to operate on a wide range of device layouts, nanomaterial shapes and sizes, and substrate properties, in order to ensure the electrical conduction through a reliable contact [7].

Concerning the use of individual nanostructures, and specifically nanowires, one of the most deeply explored application is sensing, and

among these, resistive nanowire-based gas sensors are of significant interest due to their high surface-to-volume ratio, which enhances the interaction between the nanostructure and the surrounding gas atmosphere, but also due to their relatively simple measurement and operation mechanisms [8].

The construction of such gas sensing devices starts with the transfer of the nanowires from the initial growth substrate to a microelectronic platform, containing electrodes and signal conditioning elements, like heaters, temperature sensors, etc. To date, this removal and transfer is mostly performed manually. There have been reported successful attempts to grow directly the nanowires on top of the sensing platforms [9,10], but it has only be possible to grow bundles and not individual nanowires; although, there are also initiatives in this direction [11].

Once the nanowires lay on the final substrate, they need to be accessed electrically. This issue has been mostly addressed for flat substrates. In the most advanced devices, however, the substrates consist of complex suspended microstructures designed to optimize other operation properties, like the power needed to reach the optimum working temperature. These patterned substrates present a non-negligible surface roughness and can be strongly bent. In these conditions, electrode

* Corresponding author.

E-mail addresses: aromano@el.ub.edu, albert.romano@ub.edu (A. Romano-Rodríguez).

<https://doi.org/10.1016/j.snb.2019.01.040>

Received 5 April 2018; Received in revised form 4 January 2019; Accepted 8 January 2019

Available online 09 January 2019

0925-4005/ © 2019 Elsevier B.V. All rights reserved.

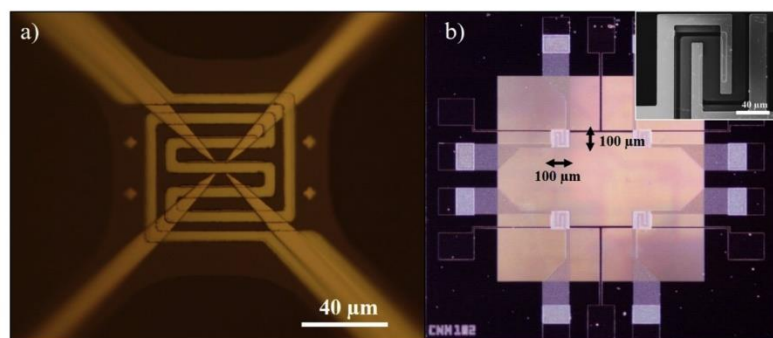


Fig. 1. a) Optical image of a suspended microhotplate, in which the central part has a size of $100 \times 100 \mu\text{m}^2$. The 4 arms supporting the hotplate contain electrodes accessing the centre of the microhotplate and 2 of them allow the access to the buried heater, seen as a meander in the image. Note that the 4 alignment marks (crosses) used in EBL can be clearly seen. b) Optical image of a micromembrane of $1.15 \times 1.15 \text{ mm}^2$. In the membrane (light pink), 4 heaters have been fabricated below the interdigitated electrodes, located on the front side. The inset is an SEM image, showing the active area ($100 \times 100 \mu\text{m}^2$) with the interdigitated electrodes and where the heater can be identified as a meander. Both structures have been fabricated using bulk micromachining techniques.

fabrication was only possible to date with dual-beam focused ion beam systems, employing the electron- and/or ion-sources to decompose a metal-organic gas precursors, like $\text{PtC}_9\text{H}_{16}$, to locally deposit a metal-like platinum/carbon composite, with high spatial resolution [12,13]. This process allowed for the fabrication of nano-contacts to the individual nanowires through a direct and mask-less process [14], and could cope with the surface variations of rough, non-flat substrates, like the aforementioned microhotplates or micromembranes, with an embedded heater [15].

However, the technique is time consuming, requiring few hours to fabricate the contacts to one single nanowire, and most of the metal-organic precursors employed for this purpose gave rise to important amounts of carbon in the deposit, which were responsible for high resistance and limited thermal stability, as the deposited contact material started to evaporate and degrade at about 400°C [16].

As an alternative, electron beam lithography (EBL) is a resist patterning technique which can achieve very high resolution (down to few nanometres) and which can be used on large area substrates (up to $8''$ wafers). Its combination with thermal evaporation or magnetron sputtering of metals, followed by a lift-off process, also allows for the fabrication of nano-contacts. In this way, individual nanowires were successfully contacted [17–19], resulting e.g. in field effect transistors that use the nanowires as the channel [20]. Few works are found, however, reporting resistive gas sensors based on individual nanowires fabricated with EBL. Instead, nano-trenches defined by EBL were etched on previously deposited films of TiO_2 [21] or SnO_2 [22] to fabricate nanostrip-like metal oxide gas sensors. These strips are, in contrast to the desired bottom-up synthesized nanowires, polycrystalline and their width is usually much larger, giving rise to a smaller effective surface-to-volume ratio. However, all these works were carried out on flat substrates that contained no efficient means to heat up the sensor material [23–26]. If rough, bent, and non-flat substrates come into play, standard EBL processing fails to provide the required fabrication capabilities. In this context, a thorough study, analysing how the EBL process can be adapted and optimized to operate well on non-flat substrates, is much sought after.

On the other hand, some papers can be found in literature in which the authors report that contacts for the individual nanowires are fabricated without a direct writing method on top of the nanostructure. The techniques are based, among others, on locating the nanowires on pre-patterned electrodes, applying an external electric field using dielectrophoretic alignment [27], using lithographically patterned nanowire electrodeposition [28] or laser ablation combined with photolithography [29].

In this work, we present a methodology to fabricate electrical contacts on individual nanowires laying on top of strongly bent and rough microhotplates and micromembranes by means of EBL. This is, to the best of our knowledge, the first time such a study is carried out. To illustrate the validity of the here-presented approach, single SnO_2 nanowires have been contacted on top of non-flat substrates and their gas sensing properties have been studied and compared [30] with another,

more well-established, contacting method like dual beam focused ion beam lithography. The here-presented methodology can be adapted to contact different nanostructures on top of other unconventional substrates.

2. Experimental

Monocrystalline defect-free tin dioxide nanowires were grown by a chemical vapor deposition (CVD) process in a cold-wall quartz reactor, using Au as catalyst, as explained in detail elsewhere [31]. The precursor used is $\text{Sn}(\text{OtBu})_4$, which is introduced into the chamber in the gas phase. Previously, a Au layer of 3–5 nm thickness is sputter-deposited, which forms nanoclusters when the temperature is raised. The NWs are grown on oxidised Si or Al_2O_3 substrates, at a temperature around 700°C .

After the growth, the nanowires were removed from the substrate by sonicating them while immersed in a solvent, either ethanol, isopropanol (IPA), ethylene glycol or toluene. Next, a drop of the solvent, of about $20 \mu\text{l}$, containing the removed NWs, was deposited on top of the suspended substrates and the solvent was allowed to dry. The NWs remained, thus, randomly oriented on the surface of the substrate and the electrical contacts could be fabricated ad hoc for each nanowire subsequently.

The substrates employed for this work were micromembranes and microhotplates (micro-sized thin structures that contain a buried heater and surface electrodes) both fabricated employing bulk micromachining of Si substrates (see Fig. 1a) and b)). They are widely used as substrates for gas sensing purposes thanks to their reduced dimensions that allow them to provide locally temperatures of several hundreds of $^\circ\text{C}$ on the membrane with a low power consumption (in the range of mW), while keeping the rest of the substrate cold. Microhotplates, shown in Fig. 1a), are free-standing structures, only supported by thin arms that thermally isolate them from the bulk, while micromembranes are thin closed structures (i.e. the entire perimeter of the membrane is attached to the thicker substrate, Fig. 1b)). In this work, the thickness of both structures was about $1.1 \mu\text{m}$. For their fabrication, first, a layer of $0.3 \mu\text{m}$ of Si_3N_4 was used as a dielectric layer, in which the heater was embedded. The heater was made either from doped polysilicon for the micromembranes or from Pt for the microhotplates. On top, 800 nm of SiO_2 , with electrical isolation purposes and which covers the heater, was deposited, while the upper contacts consisted of deposited Ti/Pt interdigitated electrodes, with $25/150 \text{ nm}$ nominal thickness in the case of micromembranes, and $25/250 \text{ nm}$ thickness for the microhotplates, defined by a lift-off process. These electrodes were used to provide the electrical contact to the nanostructures to be measured. The active area was $100 \times 100 \mu\text{m}^2$ for both the microhotplates and micromembranes. The microhotplate required a power supply of 6 mW to reach a temperature of 350°C , while the value is 8 mW for each heater of the micromembrane.

The photoresist employed in this work was 7% poly(methyl methacrylate) (PMMA) diluted in anisole (950k A7, purchased from

MicroChem), which is a positive tone resist. Following the spin-coating process, the resist was soft baked at 180 °C for 1 min. The exposure of the photoresist was performed in a Raith150 Two machine, operated at 20 kV, and with a current ranging from 100 to 600 pA. The scanned area was kept constant in the experiments, being $100 \times 100 \mu\text{m}^2$. This was large enough to avoid the need of stitching because the whole exposed pattern was kept within this writing field. After the exposure, the photoresist was developed using a mixture of methyl isobutyl ketone (MIBK) and isopropyl alcohol (1:3) for 30 s. The developer was stopped in isopropyl alcohol for additional 30 s.

The metal layers deposited on the developed substrate were a stack of Ti (20 nm) and Pt (80 nm), deposited either by e-beam evaporation or magnetron sputtering. This value was selected in this work to assure that the NWs would be completely covered by the metal, assuring an optimal contact. The dimensions of the fabricated contacts range from 10 to 50 μm in length, and 1–10 μm in width, since the contacts are designed *ad hoc* to each device.

Subsequently, the lift-off process was performed by immersing the samples in acetone for several minutes at room temperature, which assured the complete dissolution of the photoresist. It is important to mention that no ultrasounds were used during the lift-off process to avoid damaging the suspended microstructures. Finally, samples were submerged again in IPA to clean the devices from potential remaining resist impurities, followed by a soft nitrogen blow-dry.

To inspect the photoresist on the surface of the suspended substrate, confocal microscopy images of the microstructures were obtained on a Leica DCM 3D system. To measure the electrical characteristics of the devices, a Keithley 2602-A instrument equipped with two source-measurement units (SMU) was used, forcing a constant current of 1 nA. The upper limit of measurable resistance values by the mentioned equipment under those conditions is approximately 15 G Ω . High impedance measurements have been corrected considering the input impedance of the instrument. To test their functionality as sensors, the devices were bonded to a TO8 holder and then mounted in a homemade stainless steel chamber of 8.6 ml, in which a gas mixture was injected at a flow rate of 200 ml/min, using a gas mixer Gometrics MGP2. Electrical measurements and flowing gases were controlled by a home-developed Labview software. To perform the cross-section analysis of the photoresist shape and thickness on the suspended structures, a FEI Dual-Beam Strata 235 Focused Ion Beam, equipped with a Ga ion source, was used.

3. Results and discussion

3.1. Resist profile on microhotplates and micromembranes

A crucial aspect for a successful exposure in EBL is the uniformity and flatness of the spin-coated resist. Thickness and resist height differences throughout the sample may lead to an incomplete exposure of the thicker resist regions and to an uncontrolled electron dose due to a defocused electron spot, both giving rise to non-reliable and non-reproducible lithography patterns. These effects are stronger when working with small chips due to the added edge effects during the resist spinning, which give rise to accumulation of photoresist at the edges of the spun substrates. In our case, the chips containing the microhotplates and the micromembranes had sizes of $1.2 \times 3.4 \text{ mm}^2$ and $4 \times 4 \text{ mm}^2$, respectively. In order to reduce the edge effect during spin-coating, a stainless steel holder for the chips was fabricated (Fig. 2c). As shown in the figure, the upper surfaces of the chip and of the holder were at the same height. Thus, the resist could easily be extended over the whole surface of the holder in a manner that the edge effect would mostly appear at the edges of the stainless steel holder. This simple solution significantly reduced the problem of spinning on non-flat substrates, related to the edge effect.

As explained above, since both the micromembranes and the microhotplates contained embedded heaters and top electrodes,

irregularities at their surface were expected, which would affect the uniformity of the spin-coated resist. For this reason, prior to any resist spinning study, the topography of the active area of the microhotplates was analysed by confocal microscopy, as shown in Fig. 2a). For this, the whole chip was sputter-covered with a very thin Au layer of about 10 nm to enhance the reflection of the upper transparent SiO₂ surface, which was required in confocal profilometry. The topography of the four upper electrodes and the meanders of the heater can be clearly observed in the image, in which the suspended membrane presented a significant curvature, forming an upwards bow, with a maximum height difference in the central part, compared to the wafer's surface, of around 12 μm . This was attributed to the residual mechanical stresses remaining in the structure after the bulk micromachining fabrication process, consequence of the internal stresses of the different layers, and which lead the spun resist to accumulate at the edges of the suspended membrane, giving rise to a thinner layer in the central part of the devices.

The line profile along the black line depicted in Fig. 2a) is shown in Fig. 2b), which gives additional local information about the topography resulting from the underlying heater. The 7 protrusions created by this heater, that extended throughout the central part of the suspended membrane, followed the shape of the heater, and protruded, approximately, 220 nm each. These protrusions, together with the curvature of the membrane, compromised the uniformity of PMMA when spin-coated, which was a critical issue that had to be examined. Additionally, but not shown in Fig. 2b), one must take into account the height of the surface electrodes, about 175 nm (indicated by an "E" in Fig. 2a), which gave a maximum local height difference of about 400 nm.

To sum up, the microsubstrates presented (1) internal edges arising from the open structures, (2) surface bending as a result of residual mechanical stresses of the membrane/hotplates and (3) surface roughness due to the heater and surface electrodes.

To analyse in depth the profile of the spun PMMA layer and the variations in its thickness, a cross-section of the spin-coated resist was performed inside a Focused Ion Beam machine, using the Ga ion beam. Three different spin processes, employing steady velocities between 3000 and 4500 rpm for 1 min, were studied. PMMA was always soft-baked for 1 min at 180 °C, followed by the sputtering of a thin Au layer to facilitate the observation of the PMMA layer under a confocal microscope. The measured thicknesses as a function of the spin speed are summarized in Table 1. As described in the table, thickness changed along the surface of the micromembrane.

It is important to notice that, according to the technical notes of the supplier, the expected resist thickness for the selected spinning speed is about 600 nm [32]. The most important contribution to the varying thickness of the PMMA layer was caused, as shown in Fig. 3, by the heater, and to a smaller extent, by the electrodes. The height differences of about 220 nm at the microhotplate's surface prior to the deposition was reduced to about 100 nm after spinning the PMMA coating. This effect was taken into account in the fabrication of the contacts: to minimize the variations if the PMMA thickness, it was more convenient to fabricate the EBL contacts along the heater meander than across that.

Furthermore, SEM cross-section images taken in the outer part of the membranes show that, within the experimental uncertainty, the PMMA layer had the same thickness as in the central part. In addition, measurements carried out on other membranes from the same chip and from other chips showed no appreciable changes in thickness, confirming that the use of the stainless-steel holder strongly reduced the edge effect in the chip and proved the repeatability of the method.

3.2. Optimization of the fabrication parameters

In addition to the surface topography, the thickness of the NWs played also a very important role in the feasibility of the here-presented

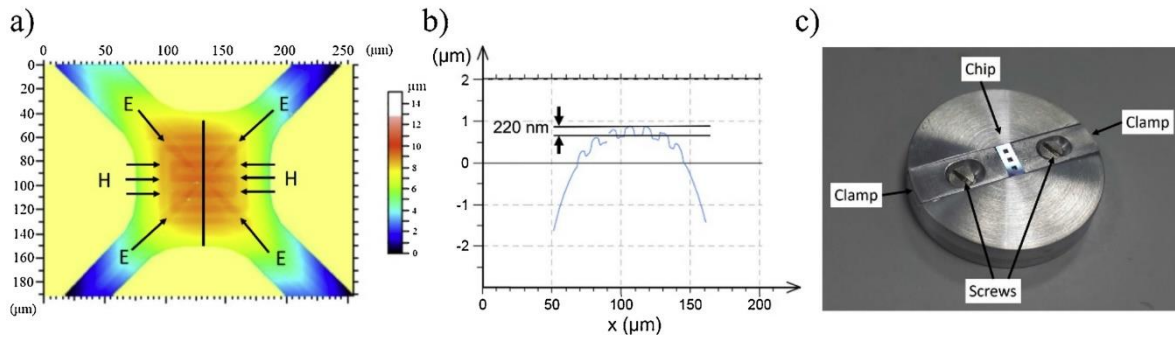


Fig. 2. a) Topographic image from the central part of the membrane obtained by confocal microscopy. The membrane is curved upwards, in which the heater (H) and electrodes (E) are visible due to the distinct height at which they are found. b) Surface profile along the line indicated in a). The 7 tracks of the heater, crossed by the drawn line, present each a height difference of about 220 nm. Note that the x- and y-axes are represented in a different scale than the z-axis. c) Image of the holder used to extend the effective area at which the resist is deposited during the spin-coating process. Diameter: 2 cm.

Table 1
Thickness of the PMMA resist obtained on top of microhotplates at different spin speeds.

| Spin speed (rpm) | Thickness on top of heater (nm) | Thickness with no underlying heater (nm) |
|------------------|---------------------------------|--|
| 3000 | 400–450 | 550–600 |
| 4000 | 270–320 | 370–440 |
| 4500 | 230–290 | 330–400 |

approach. In our case, the diameter of the NWs ranged between 50 and 80 nm. Consequently, in order to ensure the full coverage of the nanowires by the metal deposition, this had to be thicker than the nanowire's diameter. Thus, in this experiment we selected a metal thickness of 100 nm. To ensure a successful lift-off process, a rule of thumb tells that the resist thickness should be, at least, a factor 3 larger than the metal thickness. This brought the required resist thickness to, at least, 300 nm.

The appropriate spin coating conditions of the PMMA photoresist were studied by varying the spinning speed between 3000 and 4500 rpm for 1 min, followed by a soft bake at 180 °C for 1 min. Next, the samples were mounted in the EBL machine, the designed patterns were exposed and the resist was developed. Subsequently, a 20 nm thick Ti adhesion layer, followed by a 80 nm thick Pt layer, were sputter-deposited on the samples. A lift-off process, consisting in the immersion of the sample in acetone, finalized the fabrication procedure.

Regarding the PMMA spinning result, it was observed that at speeds

below or equal to 3000 rpm the PMMA was too thick, which resulted in an incomplete exposure of the photoresist. This caused that most part of the fabricated contacts were removed during the lift-off step. Further increasing the electron dose was not effective in circumventing this problem. When spinning at 4500 rpm, lift-off was non-reproducible, since it failed to completely remove the metal everywhere in the sample, possibly due to thin resist residues. The most appropriate conditions for the PMMA deposition, in terms of a successful exposure and lift-off, were found to be 4000 rpm for 1 min, which lead to a PMMA thickness around 300 nm on top of the meanders and 400 nm, elsewhere.

Under these optimal conditions, the effect of the electron dose was also studied. According to the data sheet [32], the range of doses was set according to the recommendations of the supplier from 50 to 500 $\mu\text{C}/\text{cm}^2$ (the usual values employed in our laboratory for bulk Si substrates being 100 $\mu\text{C}/\text{cm}^2$). Our results showed that for doses up to 300 $\mu\text{C}/\text{cm}^2$, bad adhesion of the metal layers on top of the PMMA occurred, and that the PMMA is further removed (or partially peeled off) during the lift-off process. Most probably this is because the bottom PMMA resist layer was not sufficiently exposed, as shown in Fig. 4a) and b), corresponding to a microhotplate and a micromembrane, respectively, exposed at 100 $\mu\text{C}/\text{cm}^2$. Similar results were obtained at 300 $\mu\text{C}/\text{cm}^2$. For the optimised PMMA photoresist thickness, a complete exposure of the resist and thus, a good adhesion of the metal layers, was achieved using an electron dose of 600 $\mu\text{C}/\text{cm}^2$ or above. The images of the fabricated contacts using this dose are presented in Fig. 4 c) and d), corresponding to the same type of substrates shown in Fig. 4a) and b), respectively. The most likely reason for the need of this higher electron

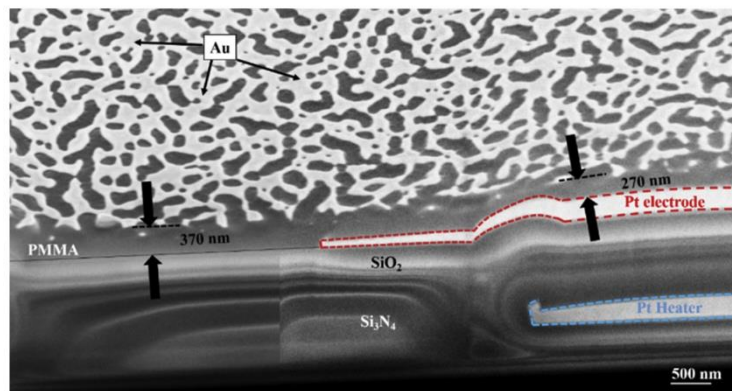


Fig. 3. Cross-section SEM image of the central area of a suspended microhotplate with spin-coated PMMA on the top. The heater gives rise to a thinner resist on top of it, and the area between the heater lines involves a thicker PMMA layer. The scale and the thickness are compensated for the tilt of the sample, which is 52°.

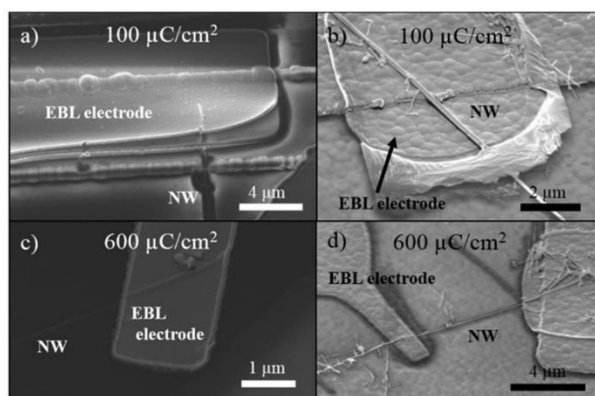


Fig. 4. SEM images of the Ti/Pt contacts fabricated by EBL. a) c) on a suspended microhotplate, and b) d) on a micromembrane. A bad adherence due to the remaining resist, which is caused by an incomplete exposure, is shown in a) and b), exposed with an electron dose of $100 \mu\text{C}/\text{cm}^2$. For a complete exposure, as shown in c) and d), a much higher electron dose has been required ($600 \mu\text{C}/\text{cm}^2$).

dose to define a pattern in our micromachined platforms, in comparison with bulk Si substrates, was the reduced thickness of the former, which resulted in a much lower number of back scattered electrons due to the absence of underlying silicon substrate [33]. This is an important result to be considered when extending this methodology to other suspended substrates with different thickness as the ones employed here, which might require an even higher dose for thinner substrates.

The electrical characterization of the titanium and platinum deposits in correctly spun and exposed samples was performed by defining linear patterns connecting two of the top electrodes. The measured resistance values were below 300Ω and the exact value depended on the length and width of the contacts. The average metal resistivity measured in these samples was of $25 \pm 6 \mu\Omega\text{-cm}$, which is between the bulk resistivity of Pt ($9.76 \mu\Omega\text{-cm}$) and of Ti ($41.8 \mu\Omega\text{-cm}$) [34]. For practical applications, it is important that the resistance of the EBL-fabricated metal contacts is orders of magnitude lower than the resistance of the material to be contacted. In our case, the resistance of individual SnO_2 nanowires ranges usually between hundreds of $\text{k}\Omega$ and hundreds of $\text{M}\Omega$ [16]. This assures that the contribution of the contacts on the overall measured resistance of the gas sensors is negligible.

3.3. Fabrication and characterization of devices based on individual nanowires

The gas nanosensors were fabricated starting by drop casting the NWs onto the suspended platforms. Next, the samples were introduced in the EBL system and the NWs were localized with the electron microscope, employing prepatterned alignment marks which were introduced during the fabrication processes of the micromembrane and microhotplate. The contacts were designed *ad-hoc* for each nanowire. The samples were then removed from the EBL chamber, the photoresist was spun on and the samples were transferred back into the EBL chamber, where the alignment marks were localized and the designed patterns were exposed onto the photoresist.

SEM pictures of two different SnO_2 NWs with EBL-fabricated contacts are shown in Fig. 5. A single NW, contacted on top of a microhotplate (with a diameter of $50 \pm 3 \text{ nm}$) is shown in Fig. 5a) and b). The NW on Fig. 5c) (with a diameter of $55 \pm 4 \text{ nm}$) was contacted on top of a micromembrane, which is shown in higher magnification images in Fig. 5d) and e). The magnified images in Fig. 5b), d) and e) show the fabricated contacts, which prove the full coverage of the NW contact region that could later be used to carry out electrical measurements.

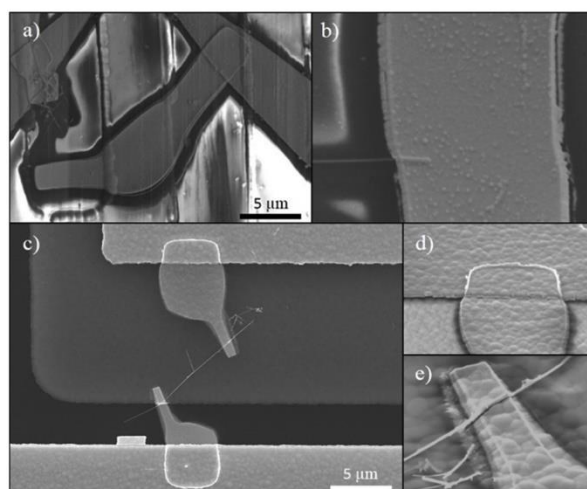


Fig. 5. SEM pictures of the individual SnO_2 NWs contacted on top of a) a microhotplate and c) a micromembranes. b) Zoom into the lower contact of a). d) and e) are zoomed into the upper and lower contacts, respectively. The metal patterns defined by EBL clearly cover the NW and the slope caused by the electrode from the microplatform, suggesting a good electrical contact.

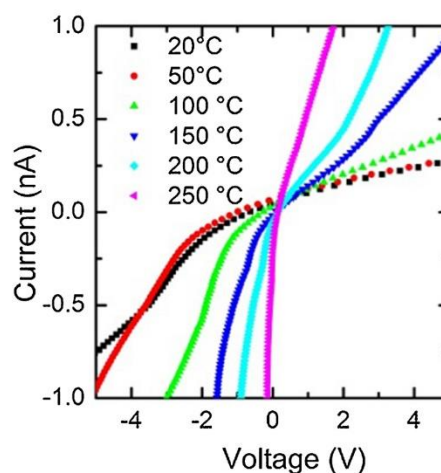


Fig. 6. I-V curves at different temperatures from a SnO_2 NW contacted by EBL on top of a microhotplate.

3.3.1. Electrical characterization of the contacted nanowires

The contacted nanowires were electrically characterized at different temperatures to determine the type of contact formed between the metals and the NW (Fig. 6). The experimental curves clearly showed a non-linear behaviour for the Pt/Ti/ SnO_2 /Ti/Pt structures, for which an ohmic behaviour would be preferred (i.e. a linear current-voltage curve).

In this sense, the contact between a metal and a semiconductor can introduce a Schottky barrier for the charge carriers crossing that junction, giving rise to an exponential current-voltage dependence like the one observed in Fig. 6. In this case, the effective barrier height, the so-called built-in potential eV_{bi} at a metal/n-type semiconductor junction (which is the case of SnO_2 nanowires), is defined as the difference between the work function of the metal (ϕ_m) and electron affinity of the semiconductor (χ_s):

$$eV_{bi} = \phi_m - \chi_s \quad (1)$$

Since titanium has a low work function (3.84 eV), and the electron affinity of SnO_2 is around 4.74 eV [35], no barrier would be expected,

which is estimated to result in an ohmic behaviour. The observed non-Ohmic behaviour might be attributed either to the oxidation of the Ti layer at the interface, or to chemical residues at the semiconductor/metal interface originated from the organic solvents used during the spin-coating of PMMA and the lift-off process. Both phenomena would create surface states that would modulate the junction barrier, likely promoting the high resistance observed on the experimental measurements.

As expected theoretically, the rectifying behaviour was reduced with increasing temperature and approached the Ohmic characteristics (see measurements at 250 °C in Fig. 6). In order to improve the quality of the contacts and achieve low resistance Ohmic contacts, an oxygen plasma cleaning process could be considered after the development of the resist and before the deposition of the metals [36], but has not been employed in this work.

3.3.2. Chemical sensing response towards NH₃

The gas response of the individual, EBL-contacted SnO₂ NWs was studied towards different concentrations of ammonia diluted in air. For this, the NWs were exposed to alternating pulses of different concentrations of ammonia diluted in dry air at different temperatures, as shown in Fig. 7a). While the n-type metal oxide nanowire is in contact with dry air, oxygen molecules are adsorbed at its surface and are dissociated into atomic oxygen, which occurs with the capture of electrons from the semiconductor. When this surface is next exposed to ammonia, its adsorption occurs together with its oxidation with the preadsorbed oxygen species, leading to oxygen desorption from the SnO₂ and releasing the electrons back to the metal oxide. As a consequence, the resistance of the semiconductor is reduced, which is clearly observed in Fig. 7a). All this is in agreement with data published in literature [37]. This reduction is larger the higher the ammonia concentration, as observed in the same figure, which proves the sensing behaviour of the device. For practical applications, it is important that the NW recovers its original resistance baseline after removing ammonia from the ambience and this is also clearly seen in Fig. 7.

In gas sensing applications, a common way to define the gas response is as follows:

$$\text{Response}(\%) = (R_{\text{air}} - R_{\text{NH}_3})/R_{\text{air}} \quad (2)$$

where R_{air} is the resistance in the presence of dry synthetic air and R_{NH_3} , in presence of a certain amount of ammonia diluted in air. The steady state response of the nanowire as a function of ammonia concentration is represented in Fig. 7b), and as a function of the temperature for 20 ppm of NH₃ is represented in Fig. 7c). In metal-oxide sensors, this response depends on the temperature, showing the typical bell shape [30]. According to well established models, this behaviour is attributed to the opposite temperature dependence of the adsorption, diffusion and desorption of oxygen, ammonia and other gas species. In

this case, these effects are balanced (i.e. the response is maximized) at approximately 200 °C, reaching a response value of 75% at 20 ppm of NH₃.

The response time of the sensor, defined as the time to evolve from the 10% to the 90% of the steady state response value (Fig. 7c), decreased exponentially with temperature, following an Arrhenius-type trend. Response times under 2 min at 300 °C were measured in the experiments with ammonia.

The nanowire's resistance at 400 °C dropped immediately after ammonia entered into the measuring chamber, followed by a slow rise, which almost cancelled the response of the NW. Such behaviour was also observed, to a lower extent, at 300 °C. For this reason, the result at 400 °C was not included in the figure of the sensor's response, Fig. 7c). The same trend was observed in other resistive gas sensors based on nano-WO₃ powders [38] or meshes of SnO₂ NWs [10]. Compared to these works, the effect is more pronounced in the EBL-contacted NW. In the here-presented results, the response is not only reduced but almost suppressed. According to previous works [10], this effect is caused by the promotion of nitric oxide as a byproduct of the ammonia oxidation by the chemisorbed oxygen at the surface of the nanowire, which occurs at high temperatures.

The results obtained in this work were compared with those from sensors based on individual SnO₂ NWs, contacted using a FIB-based technique, which showed a maximum response at 250 °C of about 40% for 100 ppm [37] and about 30% for 25 ppm has been reported [39]. The results obtained in the present work with the EBL-fabricated sensors show a significantly higher response, namely 70% of resistance variation at 20 ppm of NH₃ at 200 °C, as already stated.

Regarding the response times, previous works reported values from 50 s [37] to 15 min [39] for 100 ppm of NH₃. Our device presented times around 5 min for 20 ppm of NH₃ at 200 °C. Although this value is higher than the one reported above [37], it is important to note that for concentrations of 100 ppm of ammonia, shorter response times are expected, due to a quicker response of sensors with rising gas concentration [40].

3.4. Comparison with other methods and further applications

Comparing the EBL approach to the FIB-related one, the here presented method offers important reduction in the fabrication time, due to the higher throughput of EBL. Also, the better conductivity of the EBL-fabricated contacts leads to more robust and stable devices (e.g. less Joule heating at the contacts). Furthermore, unlike FIB deposition-assisted contacts, the EBL contacts are carbon-free, which provides better chemical stability when operating at 400 °C or above, allowing an extension of the operating temperature when compared to FIB deposition.

The detailed fabrication process described was demonstrated for nanowires with a diameter up to 80 nm. Thicker nanowires will require

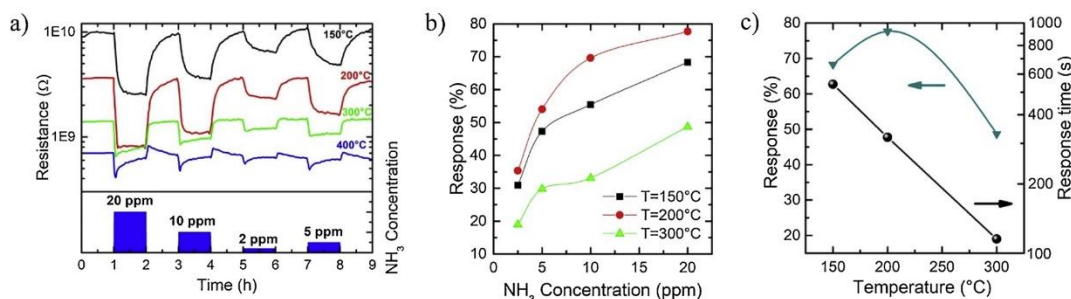


Fig. 7. a) Resistance change of individual NWs towards different ammonia concentration exposures for 1 h, at temperatures between 150 and 400 °C; b) Measured ammonia gas sensing response represented as a function of the concentration. The response obtained at 400 °C is not shown due to the abnormal behaviour caused by side reactions interfering the measurement; c) Plot of the response (left axis) and Arrhenius plot of the response time (right axis) as a function of temperature for 20 ppm of NH₃.

thicker metal layers and will, thus, demand thicker PMMA layers, which might not be completely exposed unless higher acceleration voltages are used (> 30 kV). The parameter optimization procedure presented in this paper can be tailored to attain the optimal conditions for experiments with other EBL equipment and substrate features.

4. Conclusions

In this work, a methodology for the fabrication of contacts by electron beam lithography to individual SnO₂ nanowires on top of suspended microhotplates and micromembranes has been presented. The difficulties originating from a significant buckling of suspended structures and strong surface roughness caused by the buried heater and surface electrodes have been addressed. The photoresist spinning conditions and the electron doses required to expose the photoresist correctly have been optimized to obtain adequate electrical contact to the nanowires.

The devices have been tested against the presence of ammonia and the measured resistance variations followed the expected dependence reported for other SnO₂ devices, with an optimal response at a temperature of about 200 °C. Compared with similar nanowire integration techniques (e.g. Focused Electron Beam technologies), the nanosensors described herein show an improved response and a shorter response time.

The here-presented fabrication methodology can be easily adapted to other nanostructures, like nanotubes or nanorods, and to unconventional substrates with different thicknesses, structuring, roughness and shapes.

Acknowledgements

This work has been partially supported by the Spanish Ministerio de Economía y Competitividad, through projects TEC2013-48147-C6 and TEC2016-79898-C6 (AEI/FEDER, EU) and by the European Research Council, under the European Union's Seventh Framework Program (FP/2007-2013) / ERC Grant Agreement n. 336917. J.D. Prades acknowledges the support of the Serra Hünter Program and the DFG Project GRK NanoMet. Part of this work has been carried out through a STSM within the COST project TD1105.

References

- [1] P. Yang, R. Yan, M. Fardy, Semiconductor Nanowire: What's Next? *Nano Lett.* 10 (2010) 1529–1536, <https://doi.org/10.1021/nl100665r>.
- [2] Q. Cao, J.A. Rogers, Ultrathin films of single-walled carbon nanotubes for electronics and sensors: a review of fundamental and applied aspects, *Adv. Mater.* 21 (2009) 29–53, <https://doi.org/10.1002/adma.200801995>.
- [3] S. Barth, F. Hernández-Ramírez, J.D. Holmes, A. Romano-Rodríguez, Synthesis and applications of one-dimensional semiconductors, *Prog. Mater. Sci.* 55 (2010) 563–627, <https://doi.org/10.1016/j.pmatsci.2010.02.001>.
- [4] UNESCO Global Science Report: Towards 2030, UNESCO Publishing, Paris, 2015.
- [5] C.M. Hung, D.T.T. Le, N. Van Hieu, On-chip growth of semiconductor metal oxide nanowires for gas sensors: a review, *J. Sci. Adv. Mater. Devices* 2 (2017) 263–285, <https://doi.org/10.1016/j.jsamd.2017.07.009>.
- [6] L. Chen, W. Lu, C.M. Lieber, Semiconductor nanowire growth and integration, Chapter 1, *Semicond. Nanowires From Next-Generation Electron. to Sustain. Energy*, The Royal Society of Chemistry, 2015, pp. 1–53, <https://doi.org/10.1039/9781782625209-00001>.
- [7] Y. Chen, Nanofabrication by electron beam lithography and its applications: a review, *Microelectron. Eng.* 135 (2015) 57–72, <https://doi.org/10.1016/j.mee.2015.02.042>.
- [8] H.Y. Tuan, D.C. Lee, T. Hanrath, B.A. Korgel, Catalytic solid-phase seeding of silicon nanowires by nickel nanocrystals in organic solvents, *Nano Lett.* 5 (2005) 681–684, <https://doi.org/10.1021/nl050099d>.
- [9] S. Barth, R. Jimenez-Diaz, J. Samà, J. Daniel Prades, I. Gracia, J. Santander, C. Cane, A. Romano-Rodríguez, Localized growth and in situ integration of nanowires for device applications, *Chem. Commun.* 48 (2012) 4734–4736, <https://doi.org/10.1039/c2cc30920c>.
- [10] J. Samà, S. Barth, G. Domènech-Gil, J.-D. Prades, N. López, O. Casals, I. Gràcia, C. Cané, A. Romano-Rodríguez, Site-selectively grown SnO₂ NWs networks on micromembranes for efficient ammonia sensing in humid conditions, *Sens. Actuators B Chem.* 232 (2016) 402–409, <https://doi.org/10.1016/j.snb.2016.03.091>.
- [11] K. Chikkadi, M. Muoth, V. Maiwald, C. Roman, C. Hierold, Ultra-low power operation of self-heated, suspended carbon nanotube gas sensors, *Appl. Phys. Lett.* 103 (2013) 223109, <https://doi.org/10.1063/1.4836415>.
- [12] M.N. Cardoza-Contreras, J.M. Romo-Herrera, L.A. Ríos, R. García-Gutiérrez, T.A. Zepeda, O.E. Contreras, Single ZnO nanowire-based gas sensors to detect low concentrations of hydrogen, *Sensors* 15 (2015) 30539–30544, <https://doi.org/10.3390/s151229816>.
- [13] O. Lupan, V. Postica, F. Labat, I. Ciofini, T. Pauporté, R. Adelung, Ultra-sensitive and selective hydrogen nanosensor with fast response at room temperature based on a single Pd/ZnO nanowire, *Sens. Actuators B Chem.* 254 (2018) 1259–1270, <https://doi.org/10.1016/j.snb.2017.07.200>.
- [14] F. Hernández-Ramírez, J.D. Prades, A. Tarancon, S. Barth, O. Casals, R. Jimenez-Diaz, E. Pellicer, J. Rodríguez, J.R. Morante, M.A. Juli, S. Mathur, A. Romano-Rodríguez, Insight into the role of oxygen diffusion in the sensing mechanisms of SnO₂ nanowires, *Adv. Funct. Mater.* 18 (2008) 2990–2994, <https://doi.org/10.1002/adfm.200701191>.
- [15] G. Domènech-Gil, S. Barth, J. Samà, P. Pellegrino, I. Gràcia, C. Cané, A. Romano-Rodríguez, Gas sensors based on individual indium oxide nanowire, *Sens. Actuators B Chem.* 238 (2017) 447–454, <https://doi.org/10.1016/j.snb.2016.07.084>.
- [16] F. Hernández-Ramírez, A. Tarancon, O. Casals, J. Rodríguez, A. Romano-Rodríguez, J.R. Morante, S. Barth, S. Mathur, T.Y. Choi, D. Poulikakos, V. Callegari, P.M. Nellen, Fabrication and electrical characterization of circuits based on individual tin oxide nanowires, *Nanotechnology* 17 (2006) 5577–5583, <https://doi.org/10.1088/0957-4484/17/22/009>.
- [17] M.S. Arnol, P. Avouris, Z. Wei Pan, Z.L. Wang, Field-effect transistors based on single semiconducting oxide nanobelts, *J. Phys. Chem. B* 107 (2003) 659–663, <https://doi.org/10.1021/jp0271054>.
- [18] D. Kälblein, R.T. Weitz, H.J. Böttcher, F. Ante, U. Zschieschang, K. Kern, H. Klauk, Top-Gate ZnO nanowire transistors and integrated circuits with ultrathin self-assembled monolayer gate dielectric, *Nano Lett.* 11 (2011) 5309–5315, <https://doi.org/10.1021/nl202767h>.
- [19] X. Jiang, Q. Xiong, S. Nam, F. Qian, Y. Li, C.M. Lieber, InAs/InP radial nanowire heterostructures as high electron mobility devices, *Nano Lett.* 7 (2007) 3214–3218, <https://doi.org/10.1021/nl072024a>.
- [20] P. Feng, F. Shao, Y. Shi, Q. Wan, Gas sensors based on semiconducting nanowire field-effect transistors, *Sensors (Basel)* 14 (2014) 17406–17429, <https://doi.org/10.3390/s140917406>.
- [21] P. Durina, A. Bencurova, A. Konecnikova, I. Kostic, K. Vutova, E. Koleva, G. Mladenov, P. Kus, A. Plecenik, Patterning of structures by e-beam lithography and ion etching for gas sensor applications, *J. Phys. Conf. Ser.* 514 (2014) 12037.
- [22] P. Candeloro, A. Carpentiero, S. Cabrini, E. Di Fabrizio, E. Comini, C. Baratto, G. Faglia, G. Sberveglieri, A. Gerardino, SnO₂ sub-micron wires for gas sensors, *Microelectron. Eng.* 78–79 (2005) 178–184, <https://doi.org/10.1016/j.mee.2004.12.024>.
- [23] S.N. Das, J.P. Kar, J.-H. Choi, T. Il Lee, K.-J. Moon, J.-M. Myoung, Fabrication and Characterization of ZnO Single Nanowire-Based Hydrogen Sensor, *J. Phys. Chem. C* 114 (2010) 1689–1693, <https://doi.org/10.1021/jp910515b>.
- [24] A. Köck, L. Chitu, S. Defregger, E. Kraker, G. Maier, S. Steinhauer, R. Wimmer-Teubenbacher, Metal oxide nanowires for gas sensor applications, *BHM Berg- Und Hüttenmännische Monatshefte* 159 (2014) 385–389, <https://doi.org/10.1007/s00501-014-0286-5>.
- [25] L. Liao, Z. Zheng, B. Yan, J.X. Zhang, H. Gong, J.C. Li, C. Liu, Z.X. Shen, T. Yu, Morphology controllable synthesis of α -Fe₂O₃1D nanostructures: growth mechanism and nanodevice based on single nanowire, *J. Phys. Chem. C* 112 (2008) 10784–10788, <https://doi.org/10.1021/jp802968a>.
- [26] A. Varea, S. Pane, S. Gerstl, M.A. Zeeshan, B. Ozkale, B.J. Nelson, S. Surinach, M.D. Baro, J. Nogues, J. Sort, E. Pellicer, Ordered arrays of ferromagnetic, compositionally graded Cu_{1-x}Ni_x alloy nanopillars prepared by template-assisted electrodeposition, *J. Mater. Chem. C* 1 (2013) 7215–7221, <https://doi.org/10.1039/C3TC31310G>.
- [27] O. Chmela, J. Sadilek, G. Domenech-Gil, J. Sama, J. Somer, R. Mohan, A. Romano-Rodríguez, J. Hubalek, S. Vallejos, Selectively arranged single-wire based nanosensor array systems for gas monitoring, *Nanoscale* 10 (2018) 9087–9096, <https://doi.org/10.1039/C8NR01588K>.
- [28] F. Yang, S.-C. Kung, M. Cheng, J.C. Hemminger, R.M. Penner, Smaller is faster and more sensitive: the effect of wire size on the detection of hydrogen by single palladium nanowires, *ACS Nano* 4 (2010) 5233–5244, <https://doi.org/10.1021/nl101475c>.
- [29] M. Afshar, E.M. Preiß, T. Sauerwald, M. Rodner, D. Feili, M. Straub, K. König, A. Schütze, H. Seidel, Indium-tin-oxide single-nanowire gas sensor fabricated via laser writing and subsequent etching, *Sens. Actuators B Chem.* 215 (2015) 525–535, <https://doi.org/10.1016/j.snb.2015.03.067>.
- [30] P.T. Moseley, Solid state gas sensors, *Meas. Sci. Technol.* 8 (1997) 223–237, <https://doi.org/10.1088/0957-0233/8/3/003>.
- [31] S. Mathur, S. Barth, H. Shen, J.-C. Pyun, U. Werner, Size-dependent photo-conductance in SnO₂ nanowires, *Small* 1 (2005) 713–717, <https://doi.org/10.1002/sml.200400168>.
- [32] MicroChem, PMMA Data Sheet, (2001).
- [33] A.N. Broers, Resolution limits of PMMA resist for exposure with 50 kV electrons, *J. Electrochem. Soc.* 128 (1981) 166–170, <https://doi.org/10.1149/1.2127360>.
- [34] J. Bass, 1.2.1 Pure metal resistivities at T = 273.2 K: Datasheet from Landolt-Börnstein - Group III Condensed Matter - Volume 15A: Electrical Resistivity, Kondo and Spin Fluctuation Systems, Spin Glasses and Thermopower, (n.d.). doi:https://doi.org/10.1007/10307022_3.
- [35] J.F. Geiger, K.D. Schierbaum, W. Göpel, Surface spectroscopic studies on Pd-doped SnO₂, *Vacuum* 41 (1990) 1629–1632, [https://doi.org/10.1016/0042-207X\(90\)94037-Q](https://doi.org/10.1016/0042-207X(90)94037-Q).

- [36] Y. Cheng, R. Yang, J.P. Zheng, Z.L. Wang, P. Xiong, Characterizing individual SnO₂ nanobelt field-effect transistors and their intrinsic responses to hydrogen and ambient gases, *Mater. Chem. Phys.* 137 (2012) 372–380, <https://doi.org/10.1016/j.matchemphys.2012.09.037>.
- [37] D.C. Meier, S. Semancik, B. Button, E. Strelcov, A. Kolmakov, Coupling nanowire chemiresistors with MEMS microhotplate gas sensing platforms, *Appl. Phys. Lett.* 91 (2007), <https://doi.org/10.1063/1.2768861>.
- [38] I. Jiménez, Ma. Centeno, R. Scotti, F. Morazzoni, A. Cornet, J.R. Morante, NH₃ interaction with catalytically modified nano-WO₃ powders for gas sensing applications, *J. Electrochem. Soc.* 150 (2003) H72–H80, <https://doi.org/10.1149/1.1556055>.
- [39] F. Shao, M.W.G. Hoffmann, J.D. Prades, J.R. Morante, N. López, F. Hernández-Ramírez, Interaction mechanisms of ammonia and Tin oxide: a combined analysis using single nanowire devices and DFT calculations, *J. Phys. Chem. C* 117 (2013) 3520–3526, <https://doi.org/10.1021/jp3085342>.
- [40] J.W. Gardner, A non-linear diffusion-reaction model of electrical conduction in semiconductor gas sensors, *Sens. Actuators B Chem.* 1 (1990) 166–170, [https://doi.org/10.1016/0925-4005\(90\)80194-5](https://doi.org/10.1016/0925-4005(90)80194-5).

5

*“All my life through, the new sights of nature
made me rejoice like a child”
Maria Salomea Skłodowska-Curie*

5. Electronic-nose based on semiconducting nanowires

In section 5.1 a study devoted to achieving the fabrication and characterization of an e-nose based on devices made from semiconducting NWs is presented. This corresponds to the last objective addressed in this thesis work. In this case, three semiconducting NWs, namely SnO₂, WO₃ and Ge NWs, have been grown on well-defined and pre-specified regions of one single chip, so that they are directly integrated into the final chip, which contains 4 MM. For the growth of SnO₂ and Ge, a modification of the VLS methodology, employed in chapter 3, is used, consisting in using a gaseous precursor and replacing the furnace-heated substrates by the local heating achieved by the integrated heater of the micromembranes. For each process, only one MM was electrically biased and the growth of NW meshes took place on their heated part, while the rest of the chip remained cold and no growth was observed. This was true also for the successive growths, which did not affect the electrical and gas sensing properties of the previously grown NWs. WO₃, on the contrary, has been grown using the Atmospheric Aerosol CVD (AACVD) technique, introducing the precursor in aerosol form, but still using the local heating of the MM for the gas decomposition and NW growth.

The three sensors, made of three different materials and operating simultaneously, constitute an electronic nose, which has been tested towards NO₂, CO and relative humidity (RH), always diluted in dry synthetic air. The calibration of each individual sensor has been carried out exposing the whole chip to the individual gases but with only this particular sensor heated and biased, while the others were unheated and unbiased. This has allowed determining the optimal operation conditions for each sensor. Next, at these optimal temperatures, all the sensors have been tested, simultaneously, towards each

gas specie alone. The similar response of these gas sensors to those reported for devices containing exclusively one type of NW material demonstrates that there exist no cross-effects when one or several devices operate at the same time. This is valid even in the presence of different levels of RH. Finally, tests of the three sensors, operating simultaneously, towards mixtures of the three gases were performed. The data from all the mentioned measurements have been treated according to the Principal Component Analysis (PCA) methodology and the results demonstrate that the fabricated e-nose can discriminate between the three different studied analytes (NO₂, CO and RH) and can even quantify the amount of each gas.

The methodology here developed is envisaged to be compatible, as postprocess, with the fabrication technology of complementary metal-oxide-semiconductor (CMOS) devices and is, therefore, expected to allow the integration of gas sensors onto chips for electronic control and signal treatment.

5.1 Site-selective growth and In-situ integration of different nanowire material for Electronic-nose applications


Site-Specific Growth and in Situ Integration of Different Nanowire Material Networks on a Single Chip: Toward a Nanowire-Based Electronic Nose for Gas Detection

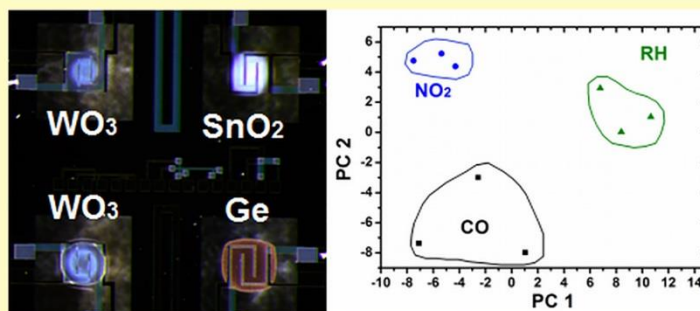
Lukas Hrachowina,^{#,||} Guillem Domènech-Gil,^{§,†,||} Antonio Pardo,[§] Michael S. Seifner,^{#,||} Isabel Gràcia,[‡] Carles Cané,[‡] Albert Romano-Rodríguez,^{*,§,†,||} and Sven Barth^{*,#}

[#]Institute of Materials Chemistry, TU Wien, 1060 Vienna, Austria

[§]Department of Electronic and Biomedical Engineering and [†]Institute of Nanoscience and Nanotechnology (IN2UB), Universitat de Barcelona (UB), 08028 Barcelona, Spain

[‡]Institut de Microelectrònica de Barcelona, Centre Nacional de Microelectrònica, Consejo Superior de Investigaciones Científicas (CSIC), 08193 Bellaterra, Spain

 Supporting Information



ABSTRACT: A new method for the site-selective synthesis of nanowires has been developed to enable material growth with defined morphology and, at the same time, different composition on the same chip surface. The chemical vapor deposition approach for the growth of these nanowire-based resistive devices using micromembranes can be easily modified and represents a simple, adjustable fabrication process for the direct integration of nanowire meshes in multifunctional devices. This proof-of-concept study includes the deposition of SnO₂, WO₃, and Ge nanowires on the same chip. The individual resistors exhibit adequate gas sensing responses toward changing gas concentrations of CO, NO₂, and humidity diluted in synthetic air. The data have been processed by principal component analysis with cluster responses that can be easily separated, and thus, the devices described herein are in principle suitable for environmental monitoring.

KEYWORDS: nanowires, electronic nose, tin oxide, tungsten oxide, germanium, CVD

In this day and age, there is an important societal concern about the presence of toxic and potentially harmful gases in the atmosphere, which is valid both for industrial as well as for outdoor and indoor environments. To carry out this monitoring, gas sensors or gas sensor systems are required, among which solid state gas sensors are an excellent choice due to their low cost and relatively high sensitivity; however, these metal oxides usually lack in selectivity due to their simultaneous response to the presence of several gases.

In general, semiconducting nanowires (NWs) have emerged as suitable components for several applications, including gas and liquid sensing, energy harvesting, and generation, as well as electronics and optoelectronics.¹ Remarkable performances can be obtained with NW-based gas sensors in terms of sensitivity and response time.² There are several ways for recording the actual response of a sensor device including simple optical and

electronic readout. One of the most simple and robust ways to detect a sensor's response is the monitoring of the device's resistance values changing upon surface reactions with gaseous analytes, which are called chemiresistors.³ There have been tremendous improvements on device performances related to actual crystal size and additives used to facilitate the surface reactions more effectively.^{4,5} The high surface-to-volume ratio as well as the typically high crystallinity of NWs are beneficial for the use in chemiresistors. In this regard, the most impressive results have typically been reported for single NW-based devices, including surface decoration with inorganic particles for sensitivity enhancement,⁶ self-heating for ultralow power

Received: January 22, 2018

Accepted: February 27, 2018

Published: February 27, 2018

devices,⁷ etc. However, the fabrication of single NW-based devices requires time-consuming contacting procedures via nanolithography^{8–10} or the use of dielectrophoresis to assemble NWs in specific locations.¹¹ These processes are usually quite time-consuming, and therefore, configurations using NW networks are of particular interest. Several groups have reported the fabrication of NW-based devices using networks.^{12,13} Typically, these NWs are either transferred to the sensor's surface via dry transfer,¹² drop casting,¹⁴ or the complete substrate is heated, and the growth of NWs and other deposits covers the whole substrate.^{15,16} As mentioned above, the remarkable performance obtained with NW devices is normally obtained on single prototypes and optimized using a trial-and-error approach. The important issue of NW-based sensor integration on multifunctional chips for their commercialization is usually not addressed and requires good control over their growth behavior. The site-selective growth on actual sensing platforms would be a viable approach for the large scale integration of these nanostructures, but literature on NW growth without contamination of the whole growth substrate is limited to a few reports using microhotplates and micromembranes as heating elements for thermally induced growth processes.^{17–20}

On the other hand, the well-known lack of selectivity toward gaseous species adsorbing on the surface for metal-oxide-based resistors as gas sensors is an issue that has to be addressed. A solution to this problem is pattern recognition across sensor arrays of different materials or temperature gradients with preferred reactions at a given temperature and surface, giving rise to a so-called e-nose configuration.^{21,22} There are also optoelectronic e-noses or combinations of different sensor types to achieve sufficient analyte recognition.²³ NW-based electronic noses using arrays of individual NWs have been described in the literature for a single material such as SnO₂,²⁴ surface modified SnO₂ NWs,²⁵ or different NW materials.²⁶ Reproducibility, reliability, and stability of NW-based sensing devices have been investigated; however, the influence on the performances of electrical contacts and their design and in situ integration during their growth has been rarely studied.

This paper demonstrates for the first time that site-selective growth of different NW materials for sensing applications is possible on a single chip using chemical vapor deposition (CVD) techniques. Since all the growth stages are thermally initiated, the deposition of the NWs can be performed on previously contaminated surfaces, and the process should be compatible with complementary metal-oxide-semiconductor technology (CMOS) processing. This proof of concept study will pave the way for site-selective NW growth and, thus, a potential integration in actual multifunctional devices.

EXPERIMENTAL SECTION

Chemicals and Precursors. All solvents have been purchased from Sigma-Aldrich. Solvents for the synthesis of Sn(O^tBu)₄ have been dried over sodium, and the alkoxide precursor has been prepared as described in literature.²⁷ Diphenylgermane (DPG) and W(CO)₆ (99%) have been purchased from ABCR and have been used as received.

Nanowire Growth. Bulk micromachined substrates were used as a platform for the growth of NWs. The substrate chips contain four electrically separated Si₃N₄/SiO₂ micromembranes with a thickness of 1.1 μm and a resistive poly-Si heater embedded within.²⁸ Pt interdigitated electrodes deposited on top of the membrane are used to electrically access the active sensing layer. The micromembranes are mounted onto a TO-8 holder and wire-bonded to them. The

temperature has been controlled through the voltage applied to the poly-Si heater in the respective membranes. Two of the membranes have been sputter-coated with an ~1 nm Au layer to allow a seed mediated VLS-type growth, while the other two have been shadow-masked to avoid Au deposition. Ge NWs have been grown using 15 mg of DPG in a low-pressure micro-CVD reactor via VLS using gold as growth seed in a manner similar to that of the published procedure for the growth on microhotplates at pressures of approximately 2 × 10⁻² mbar for 10 min.¹⁹ SnO₂ NWs have been grown on a gold-coated membrane using the same procedures described in literature, employing 15 mg of Sn(O^tBu)₄ as a precursor at pressures of 9 × 10⁻² mbar for 20 min.¹⁷ The tungsten oxide NWs have been grown in home-built aerosol assisted CVD (AACVD) reactors using 15 mL of methanol as solvent for W(CO)₆ with a concentration of 7.58 mmol/L and carrier gas flow rates of 50–200 sccm using welding argon, while keeping the substrate temperatures at ~360 °C. The temperature was determined by comparing the morphology evolution of tungsten oxides with those grown on large substrates, where the substrate temperature was monitored by a thermocouple, and all other parameters were held constant. For the deposition, 10 sccm of argon are passed through the flask where the aerosol is generated, and the rest of the argon is added to this stream above the aerosol chamber to contribute to the overall flux. This procedure was chosen to generate a sufficient vapor transport to the substrate while controlling the precursor concentration by dilution of the generated aerosol. The deposition was carried out for 1 h on micromembranes without Au coating. After the growth, the complete device was soaked three times in ethanol for 2 min to remove potential contamination due to the AACVD process. The vapor transport of the aerosol can also lead to a surface coverage with undecomposed precursor on the nonheated parts of the device. Since the precursor can easily be removed by an alcohol, this procedure was used to ensure potential remains of this carbonyl precursor. Finally, the material was heated in air for 2 h at 400 °C to oxidize the NWs to WO₃, using the resistive heater for this purpose. Reference samples have been prepared in a cold-wall CVD reactor as described in literature with a modification to allow the AACVD growth. The deposition parameters have been used as benchmarks to facilitate the growth on the microhotplates.

Structural Characterization. The NWs were analyzed using a FEI Inspect F50 scanning electron microscope (SEM). The Ge NWs were deposited on lacey carbon copper grids for transmission electron microscope (TEM) characterization (Plano). In this study, a FEI TECNAI F20 operated at 200 kV and equipped with a high-angle annular dark field (HAADF) STEM and EDX detector was used. The images were recorded and treated using Digital Micrograph software. X-ray diffraction (XRD) patterns have been recorded on a PANalytical X-Pert PRO PW 3050/60 in Bragg–Brentano geometry with Cu K α radiation.

Sensor Characterization. The response of the NW containing devices toward different gases has been recorded using a homemade stainless steel chamber of 8.6 mL volume connected to a Gometrics MGP2 gas mixer with four Bronkhorst Mass-Flow Controllers. Electrical measurements and flowing gas concentrations were controlled using self-developed Labview software. For all the gas measurements, a constant flow of 200 mL/min was kept. Water vapor was added by deviating a part of the synthetic air flow through a bubbler. The air flow corresponding to each relative humidity (RH) concentration was calibrated before testing the sensors using a commercial humidity sensor at 20 °C. Keithley 2602A dual source measure units and various Keithley 2280S-32-6 source measurement DC supply units allowed simultaneous measurement of the resistance of the sensors and control of the voltage for heating the micromembranes for the gas sensing measurements.

The three NW-based gas sensors were characterized toward carbon monoxide (CO), nitrogen dioxide (NO₂), and RH with very similar conditions of stabilization, gas exposure, and recovery times but with every step adapting to the particularities of each type of sensor. The gas measurements include allowing the device to stabilize the baseline at the operation temperature for 6 or 8 h, between 0.25 and 1 h of exposition toward the studied gases, and between 0.5 and 4 h in dry

synthetic ambient air to recover the baseline after the exposition. This procedure was repeated for the different concentrations of every studied gas using one, two, or three types of sensors simultaneously. The measurements were repeated at different temperatures to optimize the working temperature, except for the case of the Ge-NW-based sensors. Ge NWs were maintained at 100 °C to ensure a constant thickness of the GeO_x layer, important to ensure a stable behavior as a gas sensor.

RESULTS AND DISCUSSION

The different NW materials have been successfully grown on micromembranes that can be individually addressed on a single chip. Each chip consists of four isolated micromembranes with low thermal mass that provides fast thermal response. Each micromembrane contains a doped polysilicon heater embedded in an Si₃N₄ membrane with an isolating layer of SiO₂ encapsulating the structure and Pt interdigitates for electrical readout at the top surface. The details of this sensing platform are described elsewhere.²⁸

In a first step, the tungsten oxide NWs are grown taking advantage of preferential nucleation of elongated substoichiometric NW-type crystals under the appropriate experimental conditions without the use of a metal growth promoter. The large number of reports on tungsten oxide NW growth for their use as sensors relies on experimental conditions that are not favorable for site-selective growth of NWs. Typically, the processes rely on the heating of the entire device to temperatures >400 °C in a hotwall CVD reactor, leading to “parasitic” nucleation of the oxide on the entire substrate.^{29–31} While shadow masking can be used to channel some of the precursor flux toward preferential growth areas, it cannot fully prevent the diffusion of gaseous species, and thus, surface contamination on the devices and also the reactor walls will occur. An exception in literature depending on a local heating approach resulted in a large number of tubular structures in combination with other nanostructures and the resulting coating did not resemble the products obtained in the hotwall reactor CVD, where the whole device was exposed to heat.³² We achieved site-selective growth of tungsten oxide NWs exclusively in the heated area of a micromembrane by aerosol assisted CVD using a methanol solution of tungsten hexacarbonyl. The best results were obtained when the solution was stirred for 1 h prior to deposition, which leads to a partial CO ligand exchange to coordinated methanol triggered by UV light.³³ The SEM image in Figure 1a clearly illustrates the formation of tungsten oxide NWs in the process and shows that these NWs can be grown on site-selectively heated areas in a cold-wall reactor. Fine-tuning of the deposition temperature allows the exclusive formation of NWs, without a particle codeposit on the membranes and NWs (Figure S1). The substoichiometric WO_{3-x} NWs are highly crystalline and display a well-known growth direction along the (010) axis in TEM images and the corresponding fast Fourier transformations (FFT) that are consistent with monoclinic W₁₈O₄₉ (Figure S2). A high number of stacking faults perpendicular to the growth axis are a well-known phenomenon in tungsten oxide and tungsten suboxide NWs.^{34,35} The presence of stacking faults is visible in the FFT pattern showing a streaking of the spots perpendicular to the growth direction (Figure S2). The initially blue NW deposits can be oxidized by a short heat treatment for 2 h at 400 °C in air leading to visually white deposits. The overall morphology does not change by this oxidation procedure, while the conversion

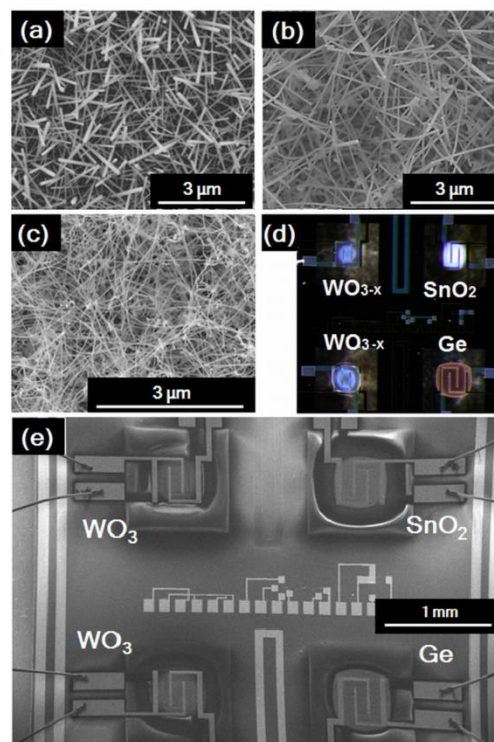


Figure 1. SEM images of (a) W₁₈O₄₉ NWs, (b) Ge NWs, and (c) SnO₂ NWs site-selectively grown on micromembranes. (d) The optical image shows the blue color of the substoichiometric tungsten oxide WO_{3-x} NWs, the white SnO₂ NW deposit, and a typical brown coating of Ge. The SEM image in (e) shows all deposits bridging the visible interdigitates on top of the membranes and the corresponding scale bar allows a comparison with the optical image, which is missing a reference. The tungsten oxide is already oxidized to WO₃ in the SEM images.

can be followed by XRD showing a shift in the dominating reflection toward lower 2θ values (Figure S3). The high crystallinity of the tungsten oxide NWs remains, as shown in XRD, and is also illustrated by HRTEM images of single NWs and their corresponding FFT images (Figure S2b).

Growth procedures of Ge and SnO₂ NWs on micromembranes and microhotplates have been previously described.^{17,19} Ge NW growth has been achieved on micromembranes, as shown in the SEM image in Figure 1b, using Au as growth seed and DPG as precursor and keeping the substrate at ~400 °C.¹⁹ Lower temperatures lead to curly and defect-rich NWs, while temperatures that are too high result in a larger number of NWs growing in the plane of the substrate. Both regimes have been mapped out and have been avoided, because in particular, the surface migrating NWs will lead to conduction paths with small surface area and, therefore, are less suitable for sensor operation. The as-grown Ge NWs are single crystalline, as shown in Figure S4a. The DPG precursor does not react with hydroxyl groups on the surface, and therefore, contamination issues can be neglected, even when tungsten oxide NWs have been deposited prior on a different membrane of the same chip. Finally, tin oxide NWs have been grown on the remaining micromembrane using Au as growth promoter and Sn(O^tBu)₄ as precursor. The HRTEM image in Figure S4b

shows the single crystalline nature of the SnO₂ NWs.¹⁷ In a previous study, we mentioned the absence of a surface bound SnO₂ particle layer for SnO₂ NW growth,¹⁸ but further investigation is required to understand the low tendency of thin film formation even though in this temperature regime non-catalyzed precursor decomposition occurs.³⁶ An expected SnO₂ particle film forms at lower temperatures by heating a membrane without the gold growth seed (Figure S5). Increasing the deposition temperature reveals a clean silicon oxide surface of the membrane in the center, which is generally slightly higher in temperature than the outer heated part of the membrane that remains with a SnO₂ particle layer. At the SnO₂ NW growth temperatures, the whole inner part is so hot that desorption dominates under the given experimental conditions including a low precursor concentration. Therefore, this absence of a particle film can be attributed to a thermal desorption process at elevated temperatures, which is in accordance with the generally accepted dependence of growth rates on the temperature for a given precursor flux.³⁷ The Au-supported NW nucleation leads to a quick formation of single crystalline material, which will not easily desorb and the NW product remains on the membrane. Figure 1d,e shows optical and SEM images of one chip with the four membranes, on top of which the different NWs have been grown. Cross-section SEM images in Figure S6 show the length of the NWs grown on the micromembranes, which can be used for the calculation of the surface area being in the range of ~5–20 m²/g (WO₃ ≈ 5.6 m²/g; Ge ≈ 9.4 m²/g; SnO₂ ≈ 19.5 m²/g).

The response of the sensors toward the different adsorbing species can be defined as the relative change in the sensor's resistance, which is expressed in general terms as illustrated in eq 1, irrespective from oxidizing or reducing gases or p- or n-type semiconductors

$$\text{response}(\%) = \frac{|R_{\text{air}} - R_{\text{gas}}|}{R_{\text{air}}} \quad (1)$$

The sensor's response time is defined as the time required to reach 90% of the steady state resistance under a given gaseous concentration, while the recovery time is the time between the gas flow stops, and the resistance varies for 90% of the interval between the steady state and the base resistance. The sensors response toward the different gas species was tested either individually or with two or three sensors working simultaneously. Comparisons between individual and simultaneous measurements reveal no differences, proving that the proximity between operating sensors has no influence on the actual readout of the individual devices. SnO₂ and WO₃ are typically n-type semiconductors, and therefore, surface reactions with the same gas will show similar trends in respect to resistance changes.^{38–43} The response of Ge NWs is typically reversed when compared to the aforementioned oxides due to the fact that this material behaves like a p-type semiconductor.¹⁹ All the measurements in this study are carried out in synthetic air, because the absence of oxygen alters the sensors' response dramatically, and base resistance values are highly dependent on the chemisorption of oxygen at their surface, resulting in an altered space charge region at the surface.⁴⁴

The change in resistance of the locally grown SnO₂ NWs meshes against varying CO concentration in synthetic air was investigated in the range of 10 to 50 ppm, which is very close to the legal limit for an 8 h exposure time-weighted average (TWA) of 8.6 ppm of CO.⁴⁵ The evolution of the SnO₂

sensor's resistance at different temperatures is represented in Figure 2a. The decrease in resistance upon CO exposure is

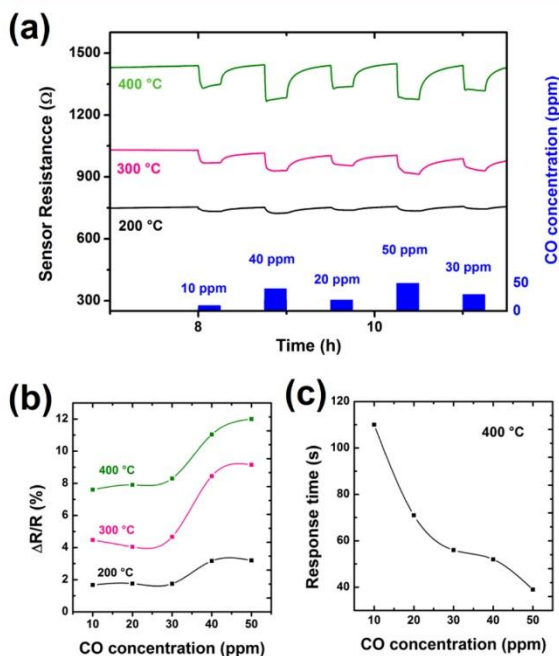


Figure 2. (a) Evolution of SnO₂ NW device resistance for different concentrations of CO in synthetic air. The response of the results from (a) are shown in (b) as a function of concentration at different temperatures and in (c) as the CO concentration dependence of response time at 400 °C.

expected for an n-type semiconductor gas sensor such as SnO₂. The shift in baseline can be attributed to different chemisorbed oxygen species on the SnO₂ surface. In the temperature range of 200–400°, the dissociation of initially molecular (O₂⁻) to atomic (O⁻) chemisorbed oxygen species leads to an increased number of charges captured from the semiconductor and, thus, an increase in the resistance.^{19,46,47} Response of the SnO₂ NW device toward CO up to 50 ppm in concentration as a function of temperature is illustrated in Figure 2b. The site-selectively grown SnO₂ NW sensors show a response of up to 12% for 50 ppm of CO at 400 °C, accompanied by a response time as low as 40 s. At these temperatures, the sensor's response is at a maximum, and also, the response time is lowest. A plot of the response time as a function of concentration is represented in Figure 2c, and its decrease with increasing CO concentration is observed. Nonlinear responses are well-known for semiconductor gas sensors and can be typically represented by a power law.⁴⁸ The response of this sensor toward NO₂ shows the well-known increase in resistance upon exposure, typical of an n-type semiconductor toward an oxidizing atmosphere in dry synthetic air at 300 °C (Figure S7). This range is slightly higher than the upper time-weighted average exposure limit in the EU (0.1 ppm) for air quality standards in urban areas and 1 day exposure times;⁴⁹ however, in specific areas such as underground parking garages⁵⁰ or ice arenas,⁵¹ the values can be higher. However, responses of 56% toward 0.2 ppm of NO₂, as illustrated in Figure S7b, demonstrate that these values can be easily detected with the devices presented here. Figure S8

shows the response of the SnO₂ NW meshes toward relative humidity. The interaction with the oxide surface leads to a reduction of resistance in the SnO₂ NW-based devices, which is in agreement with reports on single NW resistors⁵² as well as NW meshes.¹⁶

We recently demonstrated that Ge-NW-based resistors based on microhotplates can be successfully used as humidity sensors.¹⁹ The Ge NW containing micromembranes, as shown in Figure 1, have been used as humidity sensors revealing a linear response toward different humidity levels (Figure 3). The dynamic response is rather slow but reliable

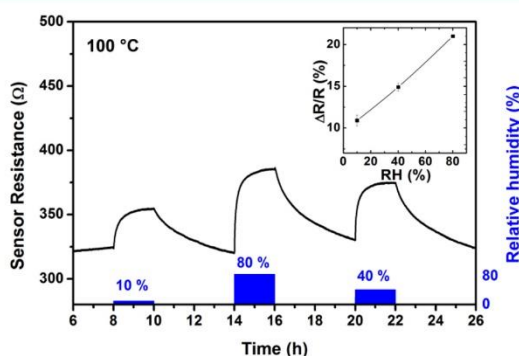


Figure 3. Response of Ge NWs toward changes in the humidity levels in synthetic air at 100 °C. The resistance changes are linear as shown in the inset.

and reproducible. A noticeable difference from our previous study on microhotplates is the increased cross-sensitivity against other gases such as CO (response 0.8% for 50 ppm of CO; previously 0.8% for 150 ppm of CO) and NO₂ (11% for 1 ppm of NO₂, which was merely 1.7% observed before), as shown in Figures S9 and S10. This is most likely due to a slight surface modification of the Ge NWs by SnO₂ residues that were deposited due to the previously mentioned thermally activated desorption of SnO₂ during the growth. According to these results and in order to optimize the NW-based devices, the fabrication process could be changed slightly to avoid the obvious modification of the material on the surface. In future experiments, a short plasma treatment will be applied after the tin oxide deposition to remove any unwanted contamination.

Tungsten oxides are well-known for their electrical response toward different gaseous species.^{53,54} The response of tungsten oxide NW meshes toward NO₂ is highly temperature dependent, as demonstrated in Figure 4. The measured responses are in the range of more than 300% for NO₂ concentrations of ≥ 3 ppm in synthetic air at a temperature of 350 °C. However, the response toward CO is moderate (<10%) as illustrated in Figure S11. The reduction of resistance in WO₃ NW devices during the interaction with water molecules is up to 69% for a relative humidity of 70%, keeping the sensor at 250 °C (Figure S12).

However, at real ambient conditions, the sensors are not exposed to single gases but to complex gas mixtures, where it is difficult to deduce the contribution of the individual species. This scenario is illustrated in Figure 5a, showing the response of an NW-based SnO₂ gas sensor toward mixtures of CO, NO₂, and humidity in the same concentrations as described before. It is clear that the responses obtained are not simply the sum of

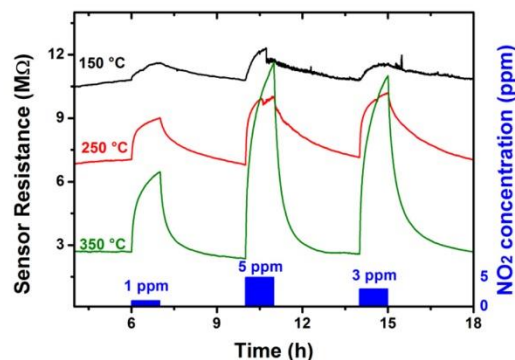


Figure 4. Response of WO₃ NWs toward different concentrations of NO₂ at temperatures of 150, 250, and 350 °C.

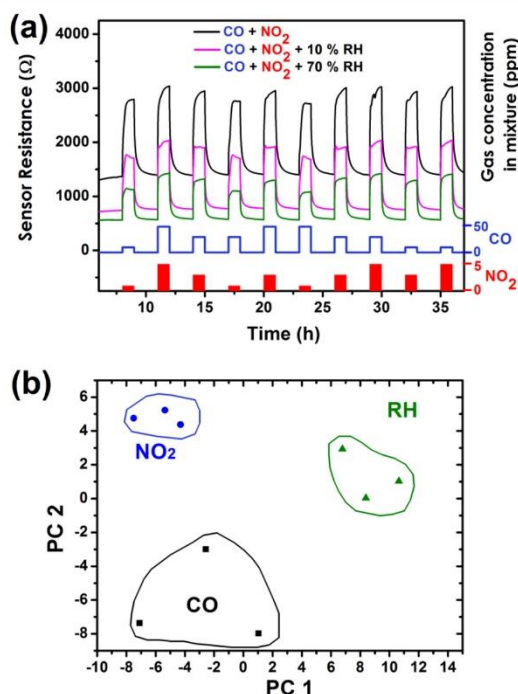


Figure 5. (a) Resistance of a SnO₂-NW-based device in a changing environment of gas mixtures composed of CO, NO₂, and relative humidity with variable concentrations in synthetic air at 250 °C. (b) Principal component analysis for SnO₂, WO₃, and Ge NW-based gas sensor toward carbon monoxide, nitrogen dioxide, and relative humidity clearly showing the different clustering of the measured data. The actual area illustrated is for included guidance of the eyes only.

the response to the individual gases but that these gases can compete for the same adsorption sites and, consequently, react differently as for one single gas. This makes the sensing of gas mixtures using metal oxides quite complicated, and electronic noses are required for their discrimination.

For this reason, it is necessary that the observed response of the chemiresistors is monitored using more complex analysis to determine the concentrations of different analytes in gas mixtures. Principal component analysis (PCA) is mathemati-

cally defined as an orthogonal linear transformation. This transformation changes the data to a new coordinate system such that the greatest variances are projected to lie in the first and second axes.^{55,56} The PCA method helps classifying different gas species using clustering and helps, visually, to easily identify the ability of the sensor array to distinguish between the analyzed gases. The main objective of this type of work is to determine the cluster in which a studied gas resides and to quantify its presence. In our principal component analysis (PCA) study, the results from SnO₂, WO₃, and Ge NW-based gas sensors, working at 300, 250, and 100 °C, respectively, toward CO (10 to 50 ppm), NO₂ (1 to 5 ppm), and RH (from 0 to 80%) reveal three different clusters corresponding to each gas species, as shown in Figure 5b. The existence of different clusters and their obvious separation in the PCA representation proves the capacity of the three-sensor system to distinguish between these three gases in the measured concentration range, which can be harmful for human health. The next generation of such NW devices is expected to be even more efficient in discriminating between different gases, when the processes will be further optimized, and potentially, a fourth NW material incorporated. The NW-based devices do also respond to gases such as ethanol or ammonia as shown in Figures S13 and S14, and thus, their field of application can be much broader. A detailed study of the gas sensor response, the PCA analysis in the presence of several gases in the atmosphere, and the corresponding discrimination properties of this system is under preparation and will be published elsewhere.

CONCLUSION

The proof-of-concept study presented here related to the in situ preparation of a NW-based sensor system by different CVD approaches shows clearly that the methodology can be successfully applied. Three different materials are demonstrated to be grown on one single chip in a defined morphology with little interference on the growth parameters caused by the prior deposition of other NW material. The use of CVD techniques is compatible with CMOS processing, and therefore, the impact of preparing gas sensors on any kind of chip for multifunctional devices is intriguing. The sensors herein show responses similar to those of individual devices prepared exclusively on single micromembranes when exposed to atmospheres containing known harmful gases, such as CO and NO₂, and at different levels of relative humidity. Some improvements to the sensors can be already imagined including an additional site-selective surface decoration with metal or metal-oxide particles for a well-known sensitivity improvement^{5,30} by thermal CVD using appropriate precursors. However, even at this stage, the discrimination between all the three analytes in the environment is obtained by the well-known PCA representation, and the cluster responses can be easily distinguished.

ASSOCIATED CONTENT

Supporting Information

The Supporting Information is available free of charge on the ACS Publications website at DOI: 10.1021/acssens.8b00073.

Supporting TEM, SEM, and XRD images are provided to illustrate the quality of the NWs prepared by CVD and used in this study as gas sensor material. Moreover,

additional information on gas responses of the different materials described herein is provided. (PDF)

AUTHOR INFORMATION

Corresponding Authors

*E-mail: sven.barth@tuwien.ac.at (S.B.)

*E-mail: aromano@el.ub.edu (A.R.R.)

ORCID

Michael S. Seifner: 0000-0001-9101-5520

Albert Romano-Rodríguez: 0000-0002-4999-6588

Sven Barth: 0000-0003-3900-2487

Author Contributions

[†]L.H. and G.D.-G. contributed equally to this paper.

Notes

The authors declare no competing financial interest.

ACKNOWLEDGMENTS

We would like to thank the University Service Center for TEM (USTEM) for access to the electron microscopes at TU Wien. Financial support of TU Wien is gratefully acknowledged. We thank the X-ray center (XRC) at TU Wien for access to the powder diffraction facilities. This work has been partially supported by the Spanish Ministerio de Economía y Competitividad, through projects TEC2013-48147-C6-1-R and TEC2016-79898-C6-2-R (AEI/FEDER, EU).

REFERENCES

- (1) Barth, S.; Hernandez-Ramirez, F.; Holmes, J. D.; Romano-Rodríguez, A. Synthesis and Applications of One-Dimensional Semiconductors. *Prog. Mater. Sci.* **2010**, *55*, 563–627.
- (2) Comini, E.; Baratto, C.; Faglia, G.; Ferroni, M.; Vomiero, A.; Sberveglieri, G. Quasi-One Dimensional Metal Oxide Semiconductors: Preparation, Characterization and Application as Chemical Sensors. *Prog. Mater. Sci.* **2009**, *54*, 1–67.
- (3) Seiyama, T.; Kato, A.; Fujiishi, K.; Nagatani, M. A New Detector for Gaseous Components Using Semiconductive Thin Films. *Anal. Chem.* **1962**, *34*, 1502–1503.
- (4) Yamazoe, N. New Approaches for Improving Semiconductor Gas Sensors. *Sens. Actuators, B* **1991**, *5*, 7–19.
- (5) Degler, D.; Rank, S.; Müller, S.; Pereira de Carvalho, H. W.; Grunwaldt, J.-D.; Weimar, U.; Barsan, N. Gold-Loaded Tin Dioxide Gas Sensing Materials: Mechanistic Insights and the Role of Gold Dispersion. *ACS Sensors* **2016**, *1*, 1322–1329.
- (6) Kolmakov, A.; Klenov, D. O.; Lilach, Y.; Stemmer, S.; Moskovits, M. Enhanced Gas Sensing by Individual SnO₂ Nanowires and Nanobelts Functionalized with Pd Catalyst Particles. *Nano Lett.* **2005**, *5*, 667–673.
- (7) Prades, J. D.; Jimenez-Diaz, R.; Hernandez-Ramirez, F.; Barth, S.; Cirera, A.; Romano-Rodríguez, A.; Mathur, S.; Morante, J. R. Ultralow Power Consumption Gas Sensors based on Self-Heated Individual Nanowires. *Appl. Phys. Lett.* **2008**, *93*, 123110.
- (8) Kolmakov, A.; Zhang, Y.; Cheng, G.; Moskovits, M. Detection of CO and O₂ Using Tin Oxide Nanowire Sensors. *Adv. Mater.* **2003**, *15*, 997–1000.
- (9) Hernández-Ramírez, F.; Tarancón, A.; Casals, O.; Rodríguez, J.; Romano-Rodríguez, A.; Morante, J. R.; Barth, S.; Mathur, S.; Choi, T. Y.; Poulidakos, D.; Callegari, V.; Nellen, P. M. Fabrication and Electrical Characterization of Circuits Based on Individual Tin Oxide Nanowires. *Nanotechnology* **2006**, *17*, 5577.
- (10) Domènech-Gil, G.; Barth, S.; Samà, J.; Pellegrino, P.; Gràcia, I.; Cané, C.; Romano-Rodríguez, A. Gas sensors based on individual indium oxide nanowire. *Sens. Actuators, B* **2017**, *238*, 447–454.
- (11) Freer, E. M.; Grachev, O.; Duan, X.; Martin, S.; Stumbo, D. P. High-Yield Self-Limiting Single-Nanowire Assembly with Dielectrophoresis. *Nat. Nanotechnol.* **2010**, *5*, 525–530.

- (12) Sysoev, V. V.; Schneider, T.; Goschnick, J.; Kiselev, I.; Habicht, W.; Hahn, H.; Strelcov, E.; Kolmakov, A. Percolating SnO₂ Nanowire Network as a Stable Gas Sensor: Direct Comparison of Long-Term Performance Versus SnO₂ Nanoparticle Films. *Sens. Actuators, B* **2009**, *139*, 699–703.
- (13) Ponzoni, A.; Comini, E.; Sberveglieri, G.; Zhou, J.; Deng, S. Z.; Xu, N. S.; Ding, Y.; Wang, Z. L. Ultrasensitive and Highly Selective Gas Sensors using Three-Dimensional Tungsten Oxide Nanowire Networks. *Appl. Phys. Lett.* **2006**, *88*, 203101.
- (14) Chávez, F.; Pérez-Sánchez, G. F.; Goiz, O.; Zaca-Morán, P.; Peña-Sierra, R.; Morales-Acevedo, A.; Felipe, C.; Soledad-Priego, M. Sensing Performance of Palladium-Functionalized WO₃ Nanowires by a Drop-Casting Method. *Appl. Surf. Sci.* **2013**, *275*, 28–35.
- (15) Vomiero, A.; Ponzoni, A.; Comini, E.; Ferroni, M.; Faglia, G.; Sberveglieri, G. Direct Integration of Metal Oxide Nanowires into an Effective Gas Sensing Device. *Nanotechnology* **2010**, *21*, 145502.
- (16) Choi, Y.-J.; Hwang, I.-S.; Park, J.-G.; Choi, K. J.; Park, J.-H.; Lee, J.-H. Novel Fabrication of an SnO₂ Nanowire Gas Sensor with High Sensitivity. *Nanotechnology* **2008**, *19*, 095508.
- (17) Barth, S.; Jimenez-Diaz, R.; Sama, J.; Daniel Prades, J.; Gracia, I.; Santander, J.; Cane, C.; Romano-Rodríguez, A. Localized Growth and *in situ* Integration of Nanowires for Device Applications. *Chem. Commun.* **2012**, *48*, 4734–4736.
- (18) Samà, J.; Barth, S.; Domènech-Gil, G.; Prades, J.-D.; López, N.; Casals, O.; Gràcia, I.; Cané, C.; Romano-Rodríguez, A. Site-Selectively Grown SnO₂ NWs Networks on Micromembranes for Efficient Ammonia Sensing in Humid Conditions. *Sens. Actuators, B* **2016**, *232*, 402–409.
- (19) Samà, J.; Seifner, M. S.; Domènech-Gil, G.; Santander, J.; Calaza, C.; Moreno, M.; Gràcia, I.; Barth, S.; Romano-Rodríguez, A. Low Temperature Humidity Sensor Based on Ge Nanowires Selectively Grown on Suspended Microhotplates. *Sens. Actuators, B* **2017**, *243*, 669–677.
- (20) Steinhauer, S.; Brunet, E.; Maier, T.; Mutinati, G. C.; Köck, A. On-Chip Synthesis of CuO Nanowires for Direct Gas Sensor Integration, Proceedings of the 2012 12th IEEE International Conference on Nanotechnology (IEEE-NANO), Aug. 20–23, 2012; pp 1–4.
- (21) Persaud, K.; Dodd, G. Analysis of Discrimination Mechanisms in the Mammalian Olfactory System using a Model Nose. *Nature* **1982**, *299*, 352.
- (22) Wilson, A.; Baietto, M. Applications and Advances in Electronic-Nose Technologies. *Sensors* **2009**, *9*, 5099.
- (23) Li, Z.; Suslick, K. S. Portable Optoelectronic Nose for Monitoring Meat Freshness. *ACS Sensors* **2016**, *1*, 1330–1335.
- (24) Sysoev, V. V.; Goschnick, J.; Schneider, T.; Strelcov, E.; Kolmakov, A. A Gradient Microarray Electronic Nose Based on Percolating SnO₂ Nanowire Sensing Elements. *Nano Lett.* **2007**, *7*, 3182–3188.
- (25) Baik, J. M.; Zielke, M.; Kim, M. H.; Turner, K. L.; Wodtke, A. M.; Moskovits, M. Tin-Oxide-Nanowire-Based Electronic Nose Using Heterogeneous Catalysis as a Functionalization Strategy. *ACS Nano* **2010**, *4*, 3117–3122.
- (26) Sysoev, V. V.; Button, B. K.; Wepsiec, K.; Dmitriev, S.; Kolmakov, A. Toward the Nanoscopic “Electronic Nose”: Hydrogen vs Carbon Monoxide Discrimination with an Array of Individual Metal Oxide Nano- and Mesowire Sensors. *Nano Lett.* **2006**, *6*, 1584–1588.
- (27) Hampden-Smith, M. J.; Wark, T. A.; Rheingold, A.; Huffman, J. C. Solid State and Solution Structural Investigation of Homoleptic Tin(IV) Alkoxide Compounds. Part I. Sn(O—t-Bu)₄ and [Sn(O—i-Pr)₄•HO—i-Pr]₂. *Can. J. Chem.* **1991**, *69*, 121–129.
- (28) Puigcorbè, J.; Vogel, D.; Michel, B.; Vilà, A.; Gràcia, I.; Cané, C.; Morante, J. R. Thermal and Mechanical Analysis of Micromachined Gas Sensors. *J. Microchem. Microeng.* **2003**, *13*, 548.
- (29) Molkenova, A.; Sarip, R.; Sathasivam, S.; Umek, P.; Vallejos, S.; Blackman, C.; Hogarth, G.; Sankar, G. Single-Step Co-Deposition of Nanostructured Tungsten Oxide Supported Gold Nanoparticles using a Gold–Phosphine Cluster Complex as the Gold Precursor. *Sci. Technol. Adv. Mater.* **2014**, *15*, 065004.
- (30) Vallejos, S.; Umek, P.; Stoycheva, T.; Annanouch, F.; Llobet, E.; Correig, X.; De Marco, P.; Bittencourt, C.; Blackman, C. Single-Step Deposition of Au- and Pt-Nanoparticle-Functionalized Tungsten Oxide Nanoneedles Synthesized Via Aerosol-Assisted CVD, and Used for Fabrication of Selective Gas Microsensor Arrays. *Adv. Funct. Mater.* **2013**, *23*, 1313–1322.
- (31) Stoycheva, T.; Annanouch, F. E.; Gràcia, I.; Llobet, E.; Blackman, C.; Correig, X.; Vallejos, S. Micromachined Gas Sensors Based on Tungsten Oxide Nanoneedles Directly Integrated Via Aerosol Assisted CVD. *Sens. Actuators, B* **2014**, *198*, 210–218.
- (32) Annanouch, F. E.; Gràcia, I.; Figueras, E.; Llobet, E.; Cané, C.; Vallejos, S. Localized Aerosol-Assisted CVD of Nanomaterials for the Fabrication of Monolithic Gas Sensor Microarrays. *Sens. Actuators, B* **2015**, *216*, 374–383.
- (33) Zhu, L.; Saha, S.; Wang, Y.; Keszler, D. A.; Fang, C. Monitoring Photochemical Reaction Pathways of Tungsten Hexacarbonyl in Solution from Femtoseconds to Minutes. *J. Phys. Chem. B* **2016**, *120*, 13161–13168.
- (34) Klinke, C.; Hannon, J. B.; Gignac, L.; Reuter, K.; Avouris, P. Tungsten Oxide Nanowire Growth by Chemically Induced Strain. *J. Phys. Chem. B* **2005**, *109*, 17787–17790.
- (35) Rao, P. M.; Zheng, X. Flame Synthesis of Tungsten Oxide Nanostructures on Diverse Substrates. *Proc. Combust. Inst.* **2011**, *33*, 1891–1898.
- (36) Mathur, S.; Barth, S. Molecule-Based Chemical Vapor Growth of Aligned SnO₂ Nanowires and Branched SnO₂/V₂O₅ Heterostructures. *Small* **2007**, *3*, 2070–2075.
- (37) Choy, K. L. Chemical Vapor Deposition of Coatings. *Prog. Mater. Sci.* **2003**, *48*, 57–170.
- (38) Gaggiotti, G.; Galdikas, A.; Kaciulis, S.; Mattogno, G.; Šetkus, A. Surface Chemistry of Tin Oxide Based Gas Sensors. *J. Appl. Phys.* **1994**, *76*, 4467–4471.
- (39) Weimar, U.; Göpel, W. A.C. Measurements on Tin Oxide Sensors to Improve Selectivities and Sensitivities. *Sens. Actuators, B* **1995**, *26*, 13–18.
- (40) Polleux, J.; Gurlo, A.; Barsan, N.; Weimar, U.; Antonietti, M.; Niederberger, M. Template-Free Synthesis and Assembly of Single-Crystalline Tungsten Oxide Nanowires and their Gas-Sensing Properties. *Angew. Chem.* **2006**, *118*, 267–271.
- (41) Vallejos, S.; Di Maggio, F.; Shujah, T.; Blackman, C. Chemical Vapour Deposition of Gas Sensitive Metal Oxides. *Chemosensors* **2016**, *4*, 4.
- (42) Bãrsan, N.; Weimar, U. Understanding the Fundamental Principles of Metal Oxide Based Gas Sensors; the Example of CO Sensing with SnO₂ Sensors in the Presence of Humidity. *J. Phys.: Condens. Matter* **2003**, *15*, R813.
- (43) Zou, Y.; Chen, S.; Sun, J.; Liu, J.; Che, Y.; Liu, X.; Zhang, J.; Yang, D. Highly Efficient Gas Sensor Using a Hollow SnO₂ Microfiber for Triethylamine Detection. *ACS Sensors* **2017**, *2*, 897–902.
- (44) Yamazoe, N.; Sakai, G.; Shimanoe, K. Oxide Semiconductor Gas Sensors. *Catal. Surv. Asia* **2003**, *7*, 63–75.
- (45) World Health Organization. *Air Quality Guidelines for Europe*, 2nd ed.; World Health Organization: Copenhagen, Denmark, 2000.
- (46) Ahlers, S.; Becker, T.; Hellmich, W.; Braunmühl, C. B.-v.; Müller, G., Temperature- and Field-Effect-Modulation Techniques for Thin-Film Metal Oxide Gas Sensors. In *Advanced Gas Sensing: The Electroadsorptive Effect and Related Techniques*, Doll, T., Ed. Springer US: Boston, MA, 2003; pp 123–159.
- (47) Chang, S. C. Oxygen chemisorption on tin oxide: Correlation between electrical conductivity and EPR measurements. *J. Vac. Sci. Technol.* **1980**, *17*, 366–369.
- (48) Yamazoe, N.; Shimanoe, K. Theory of Power Laws for Semiconductor Gas Sensors. *Sens. Actuators, B* **2008**, *128*, 566–573.
- (49) European Environment Agency. Air Quality Standards. <https://www.eea.europa.eu/themes/air/air-quality-standards> (accessed January 21, 2018).
- (50) Glorennec, P.; Bonvallot, N.; Mandin, C.; Goupil, G.; Pernelet-Joly, V.; Millet, M.; Filleul, L.; Le Moulec, Y.; Alary, R. Is a

Quantitative Risk Assessment of Air Quality in Underground Parking Garages Possible? *Indoor Air* **2008**, *18*, 283–292.

(51) Levy, J. I.; Lee, K.; Yanagisawa, Y.; Hutchinson, P.; Spengler, J. D. Determinants of Nitrogen Dioxide Concentrations in Indoor Ice Skating Rinks. *Am. J. Public Health* **1998**, *88*, 1781–1786.

(52) Hernández-Ramírez, F.; Tarancón, A.; Casals, O.; Arbiol, J.; Romano-Rodríguez, A.; Morante, J. R. High Response and Stability in CO and Humidity Measures Using a Single SnO₂ Nanowire. *Sens. Actuators, B* **2007**, *121*, 3–17.

(53) Kim, Y. S.; Ha, S.-C.; Kim, K.; Yang, H.; Choi, S.-Y.; Kim, Y. T.; Park, J. T.; Lee, C. H.; Choi, J.; Paek, J.; Lee, K. Room-Temperature Semiconductor Gas Sensor Based on Nonstoichiometric Tungsten Oxide Nanorod Film. *Appl. Phys. Lett.* **2005**, *86*, 213105.

(54) Penza, M.; Tagliente, M. A.; Mirengi, L.; Gerardi, C.; Martucci, C.; Cassano, G. Tungsten Trioxide (WO₃) Sputtered Thin Films for a NO_x Gas Sensor. *Sens. Actuators, B* **1998**, *50*, 9–18.

(55) Jolliffe, I. T. Principal Component Analysis and Factor Analysis. In *Principal Component Analysis*; Springer: New York, NY, 1986; pp 115–128.

(56) Jolliffe, I. T. *Principal Component Analysis*, 2nd ed.; Springer: New York, 2002.

Supporting information

Site-specific growth and in situ integration of different nanowire material networks on a single chip: towards a nanowire-based electronic nose for gas detection

Lukas Hrachowina,^{#,||} Guillem Domènech-Gil,^{§,†,||} Antonio Pardo,[§] Michael S. Seifner,[#] Isabel Gràcia,[¥] Carles Cané,[¥] Albert Romano-Rodríguez,^{§,†,*} Sven Barth^{#,*}

[#] Institute of Materials Chemistry, TU Wien, 1060 Vienna, Austria; [§] Departament of Electronic and Biomedical Engineering, Universitat de Barcelona (UB), 08028 Barcelona, Spain; [†] Institut of Nanoscience and Nanotechnology (IN2UB), Universitat de Barcelona (UB), 08028 Barcelona, Spain; [¥] Centre Nacional de Microelectrònica-Institut de Microelectrònica de Barcelona, Consejo Superior de Investigaciones Científicas (CSIC), 08193 Bellaterra, Spain.

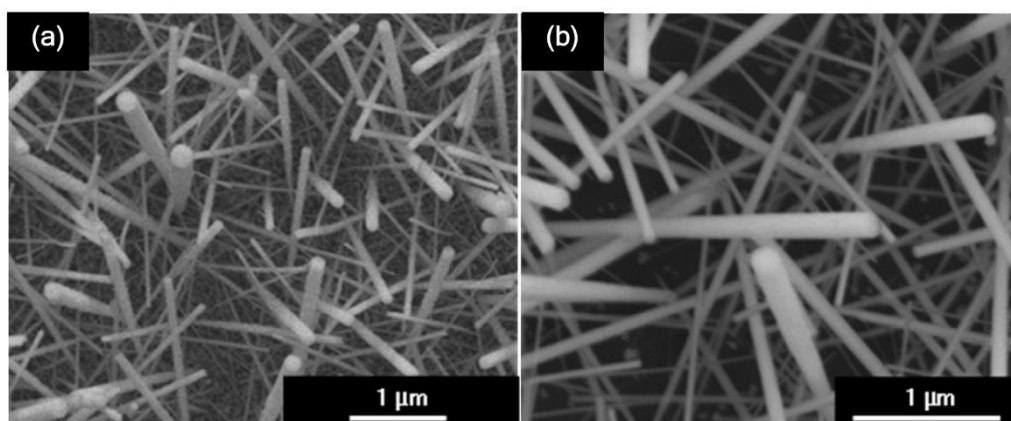


Figure S1: SEM images of WO_{3-x} NWs with (a) additional nucleation of particles leading to a film on the micromembranes at higher temperatures that can also lead to nucleation on the WO_{3-x} NWs. (b) Optimised growth conditions prevent the film formation and a pure NW WO_{3-x} NW mesh can be obtained.

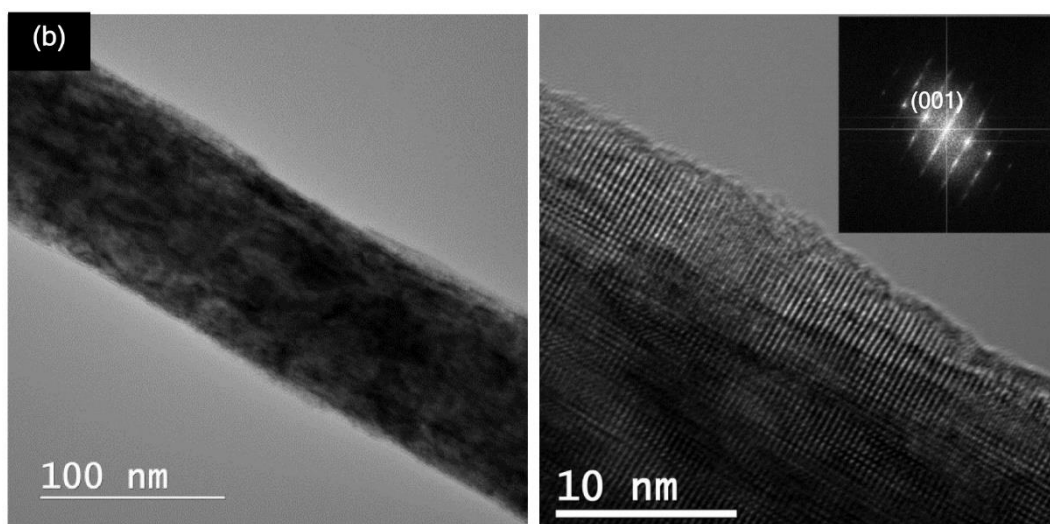
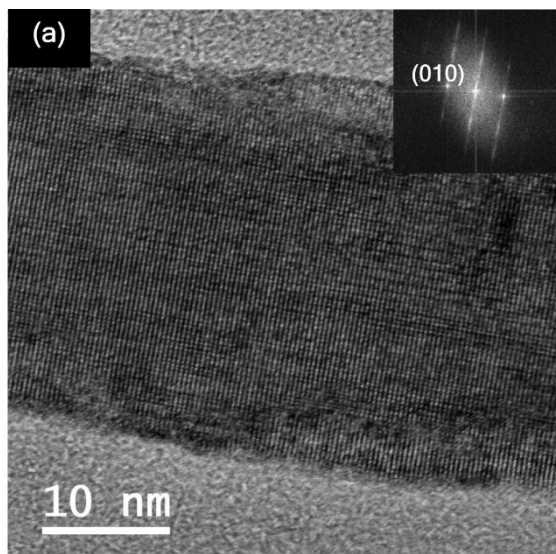


Figure S2: (a) TEM images before annealing showing the highly crystalline $W_{18}O_{49}$ NWs grown along the $\langle 010 \rangle$ axis and (b) after the annealing in air for 2h at $400\text{ }^{\circ}\text{C}$ show highly crystalline tungsten oxide NWs. The FFT images show excellent orientation along the $\langle 001 \rangle$ WO_3 NW growth axis and well-known stacking faults perpendicular to it, which is well known for these tungsten oxide NWs with a layer-type crystal structure.

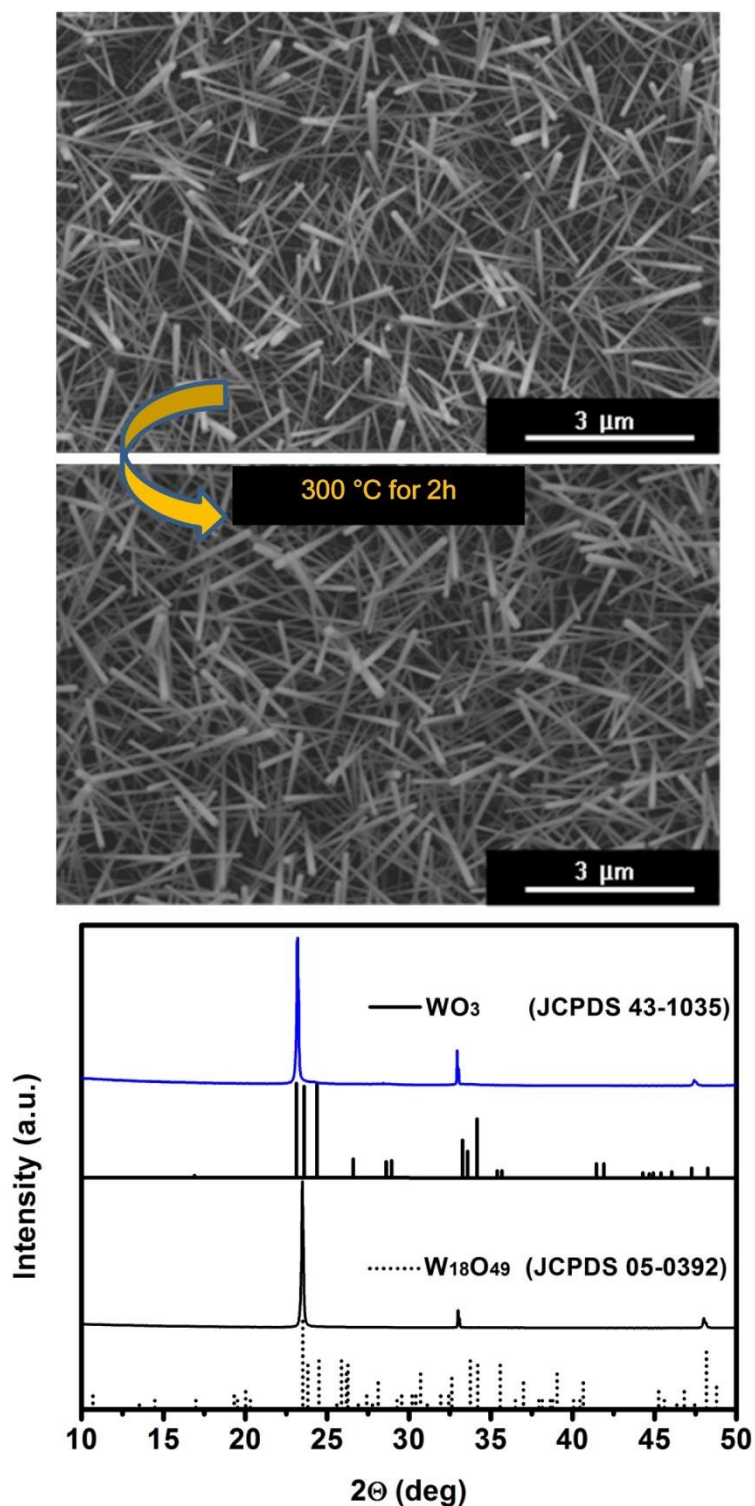


Figure S3: SEM images of as-grown $W_{18}O_{49}$ NWs before and after annealing in air for 2h at 300 °C and corresponding XRD shows a small shift toward smaller angles and therefore a bigger unit cell as expected upon oxidation to WO_3 . The absence of most of the reflections is indicative for the highly anisotropic crystal growth and therefore a preferred orientation in the XRD pattern.

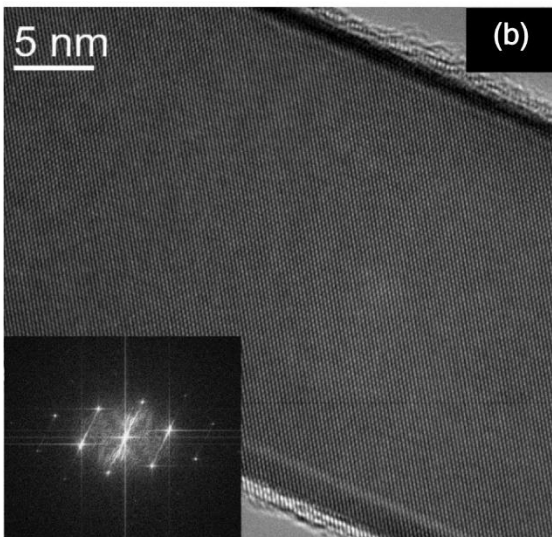
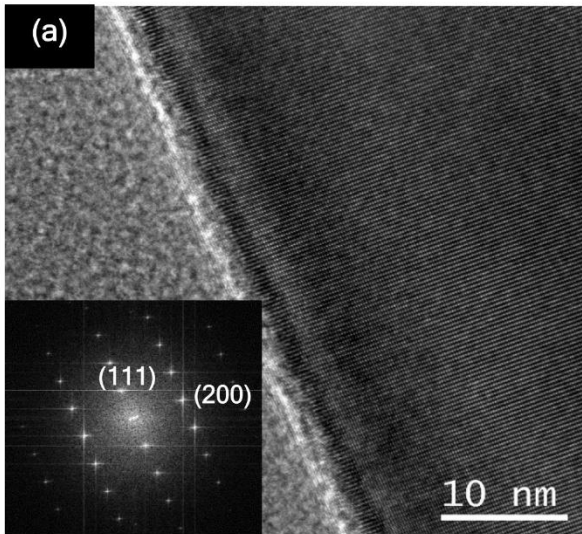


Figure S4: TEM images of (a) a Ge NW and (b) a SnO₂ NW prepared by CVD on micromembranes.

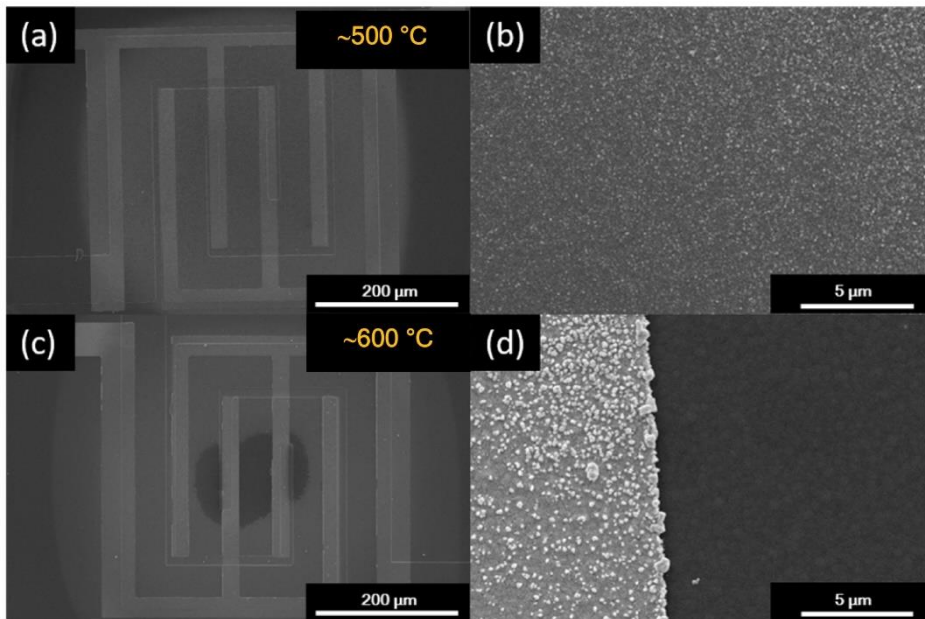


Figure S5: Evolution of thin film layer for SnO₂ nanoparticle formation using micromembranes as substrate and increasing temperature. The experimental parameters are the same as for the SnO₂ NW growth but without Au seed layer to induce NW growth. (a) and (b) are grown at 500 °C and (b) is a SEM of the middle of the membrane surface, while (c) and (d) are grown at 600 °C and the middle part of the SiO₂ membrane does not contain any SnO₂ particle layer.

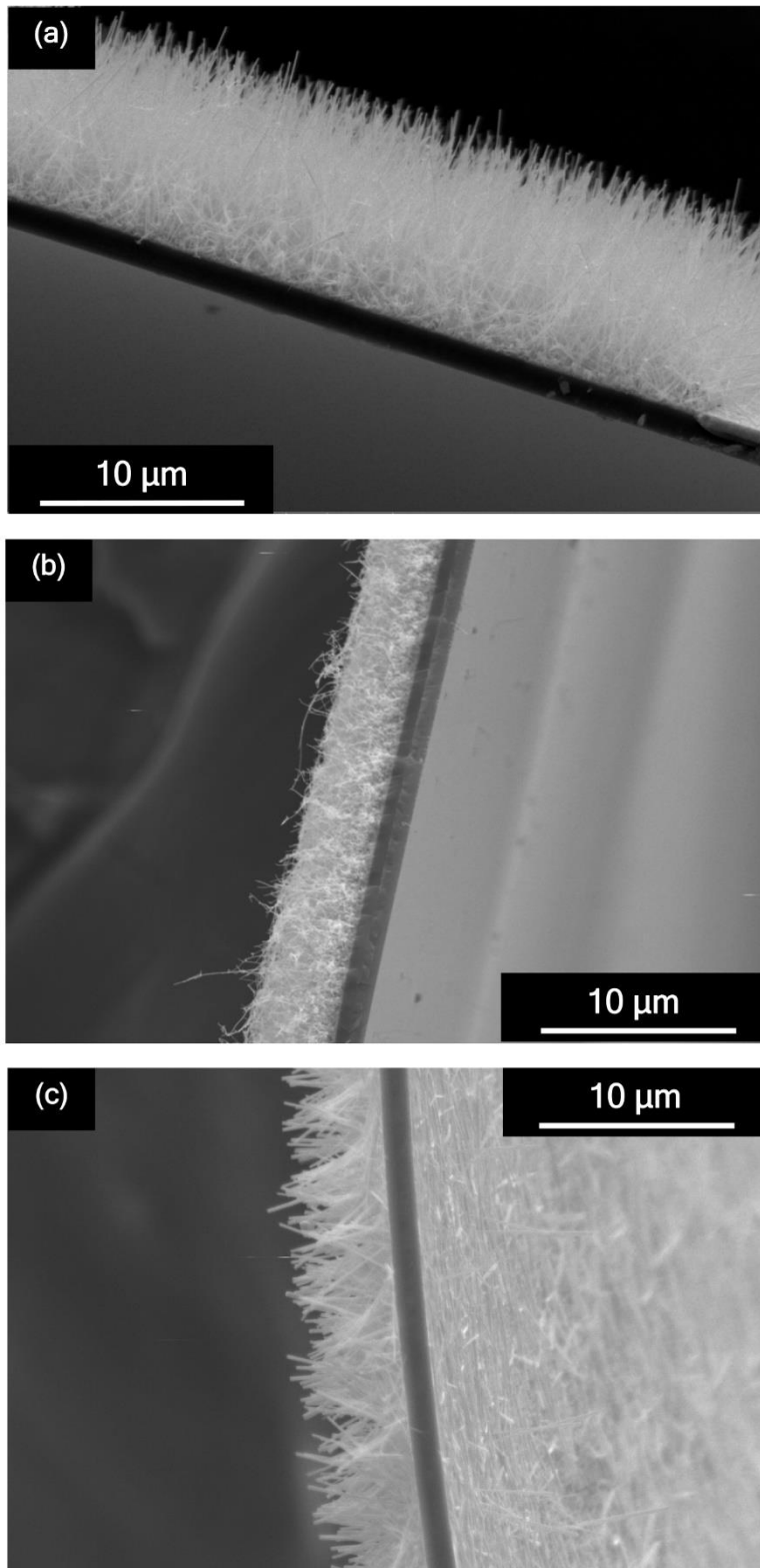


Figure S6: Cross sections of micromembranes containing (a) Ge NWs with length of $\sim 10 \mu\text{m}$ ($\varnothing = \sim 80 \text{ nm}$), (b) SnO₂ NWs with length of $> 5 \mu\text{m}$ ($\varnothing = \sim 30 \text{ nm}$) and (c) WO₃ NWs with length of $\sim 6 \mu\text{m}$ ($\varnothing = \sim 100 \text{ nm}$).

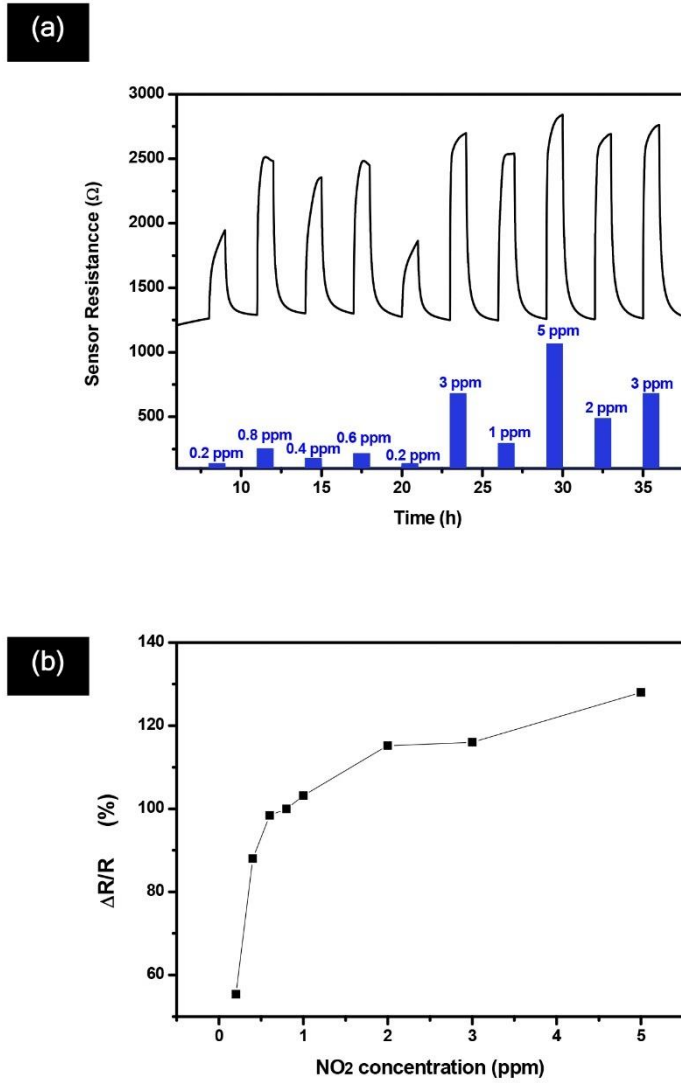


Figure S7: (a) Response of SnO₂ NW device towards changes in NO₂ concentrations at 300°C and (b) another representation of the data from (a) showing 130% response for 5 ppm NO₂.

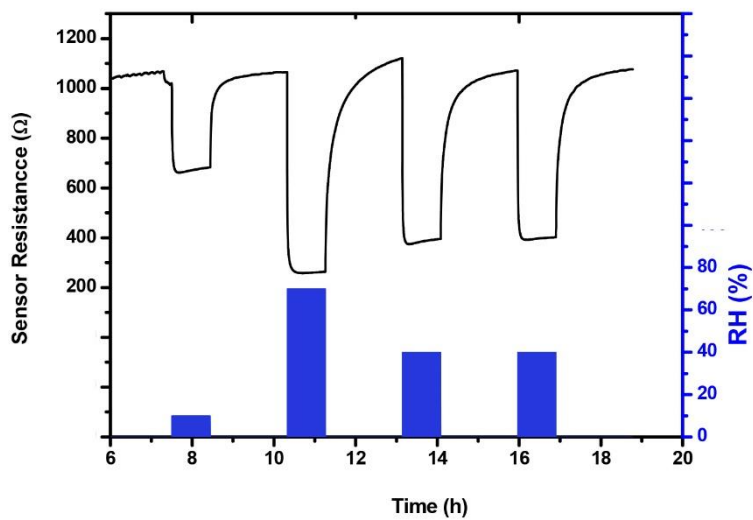


Figure S8: Response of SnO₂ NW device towards changes in humidity levels from 10-70 % at 300 °C.

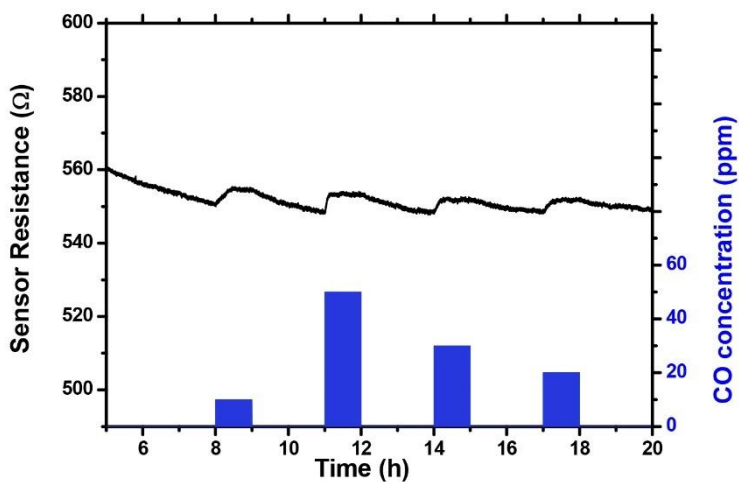


Figure S9: Response of Ge NW meshes towards changes in CO concentrations (10-50 ppm) at 100 °C with max. changes of 1.7 % for 50 ppm CO.

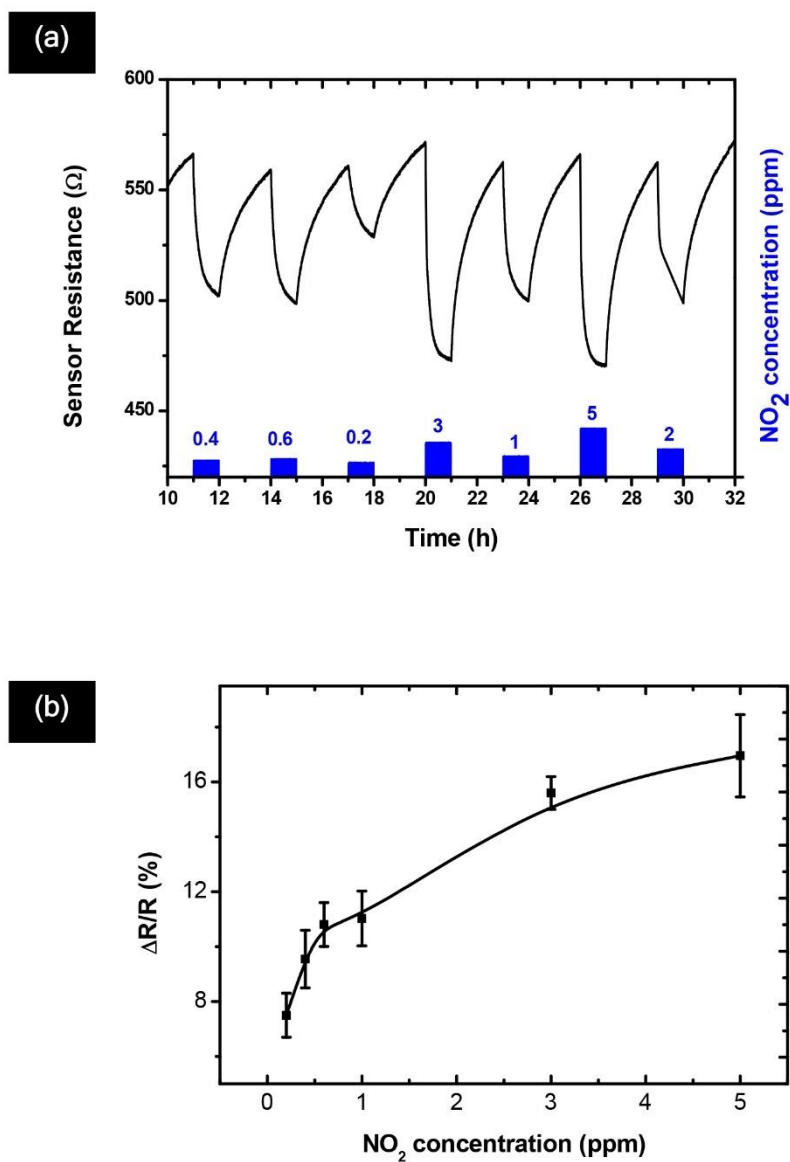


Figure S10: (a) Response of Ge NW meshes towards changes in NO₂ concentrations at 100 °C and (b) another representation of the data from (a) showing 11 % response for 1 ppm NO₂ in contrast to data on Ge NWs derived before.

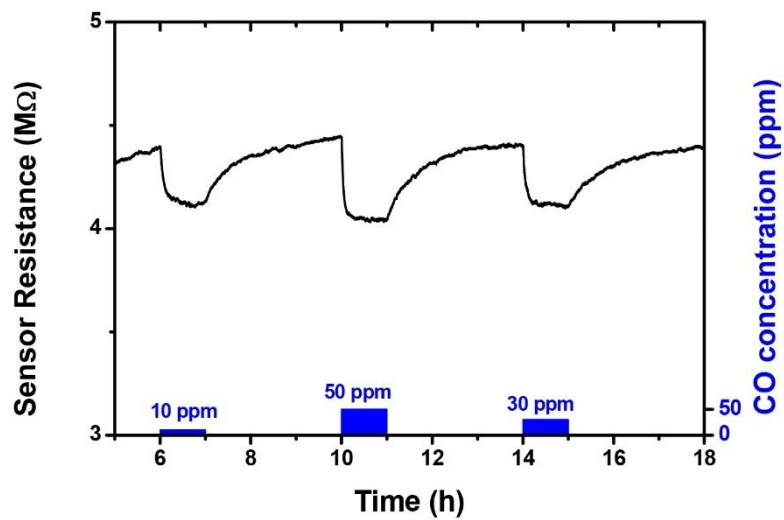


Figure S11: Response of WO_3 NW meshes towards changes in CO concentrations (10-50 ppm) at 250 °C with max. responses of <10 % for 50 ppm CO.

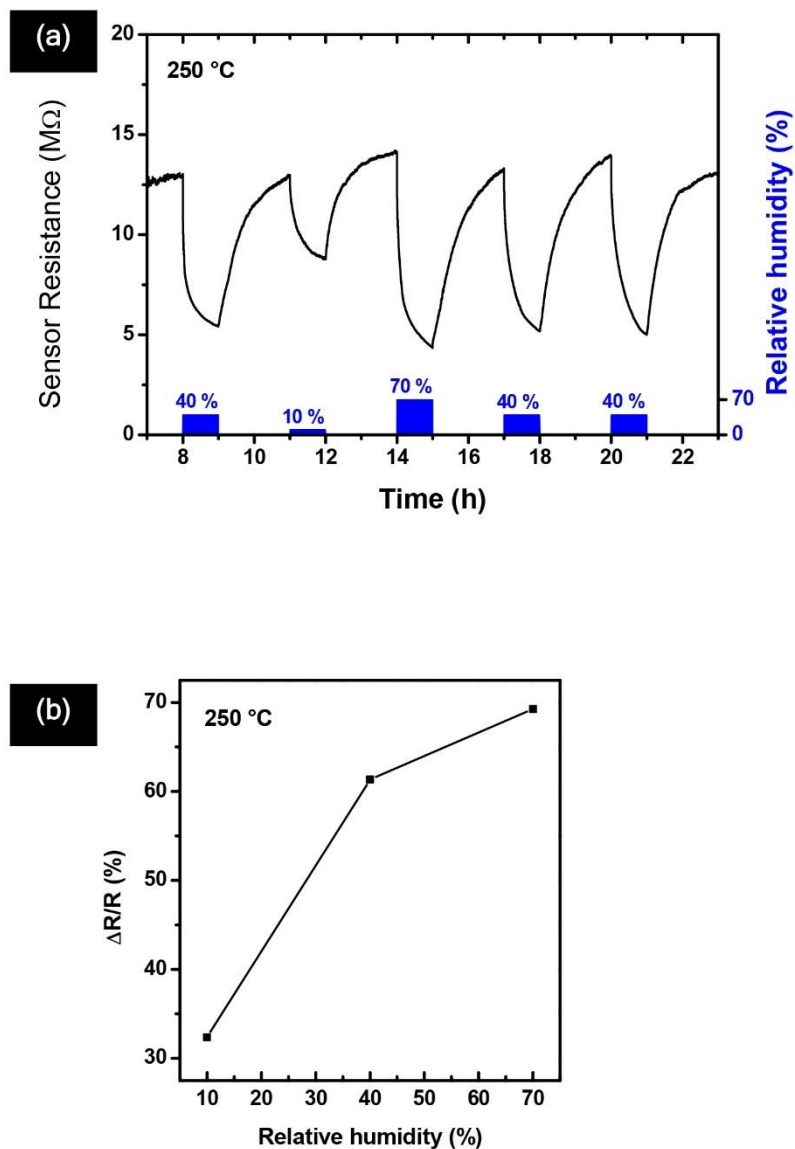


Figure S12: (a) Response of WO₃ NW meshes towards changes in humidity levels in the range between 10-70% at 250 °C with max. response of 69%, which is displayed in (b).

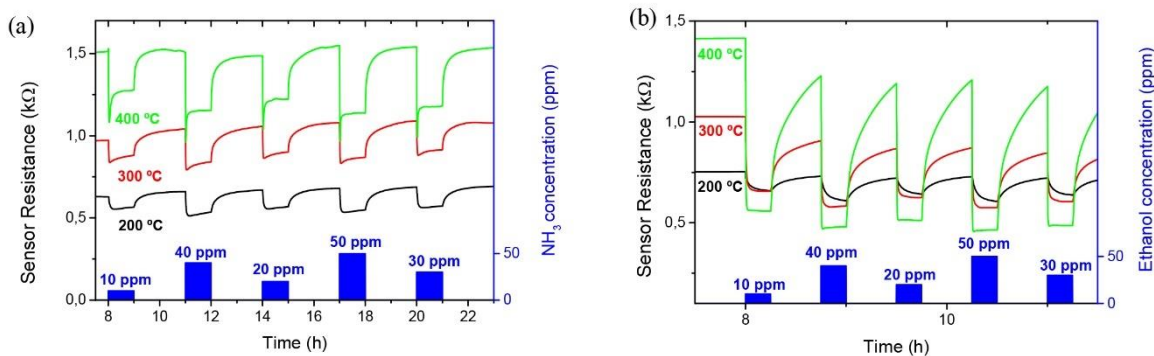


Figure S13: (a) Resistance evolution of tin oxide nanowire-based sensor towards different concentrations of ammonia working at 200, 300 and 400 °C in dry synthetic air; (b) Resistance evolution of tin oxide nanowire-based sensor towards different concentrations of ethanol working at 200, 300 and 400 °C in dry synthetic air.

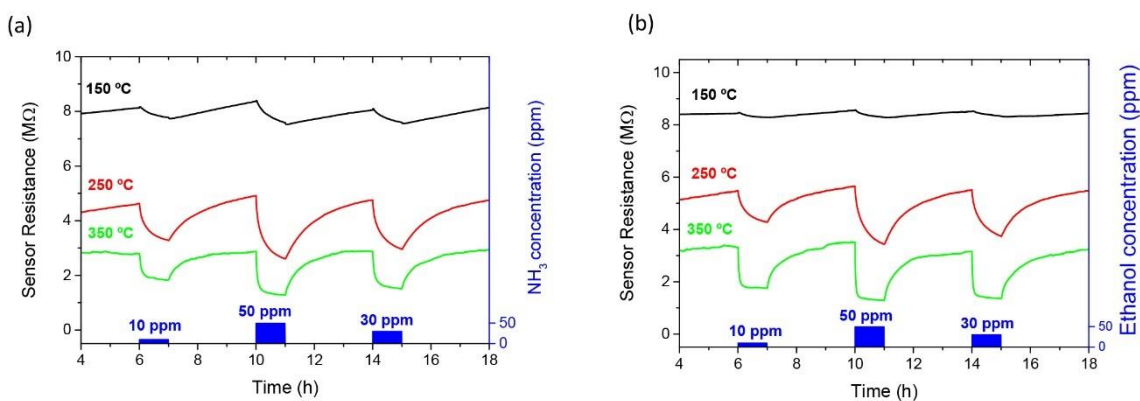


Figure 14: (a) Resistance evolution of tungsten oxide nanowire-based sensor towards different concentrations of ammonia working at 150, 250 and 350 °C in dry synthetic air; (b) Resistance evolution of tungsten oxide nanowire-based sensor towards different concentrations of ethanol working at 150, 250 and 350 °C in dry synthetic air.



6. Conclusions and future work

6.1 General conclusions

The general objectives proposed at the beginning of this thesis were the synthesis of metal oxide nanowires, the fabrication of gas sensors based on them and the development of their integration into devices and, finally, the development and test of an e-nose based on semiconducting NWs. All of them have been fulfilled.

- The successful growth of In_2O_3 and Ga_2O_3 nanowires, based on the vapor-liquid-solid mechanism, using a chemical vapor deposition system and employing metal oxide precursors combined with carbon, has been achieved. The different experimental conditions required for growing both materials have been established, allowing the nanowires to be the unique or the majority nanostructure formed.
- Devices based on individual In_2O_3 and Ga_2O_3 nanowires, contacted on top of microhotplates, have been fabricated and their gas sensing properties have been studied. Their operation conditions, response and selectivity towards the different gases tested is strongly dependent on the experimental growth conditions. Extremely relative humidity selectivity has been achieved with Ga_2O_3 nanowires.
- Two different methodologies for the integration of nanowires into devices to fabricate single nanowire-based gas sensors, overcoming the limitation of the reference contact fabrication route, focused electron beam induced deposition, have been demonstrated. Dielectrophoresis has been used to align individual WO_3 nanowires, for which the experimental conditions, especially solvent and the applied electrical field properties,

have been established. Electron beam lithography, combined with lift-off, has been successfully used to contact SnO₂ on top of suspended microhotplates and micromembranes. This has required setting up the conditions for the electron beam lithography process. In both approaches, the gas sensing properties of these devices have been studied and the results are as good as those from devices fabricated using reference processes.

- The site-selective growth of nanowires was used to grow different nanowire meshes on top of the micromembranes of a chip. The gas sensing behavior of all micromembranes operating simultaneously has been measured and the different response of these micromembranes allow the gas discrimination in a mixture. As a consequence, these systems can be considered a nano-electronic-nose on a single chip.

6.2 Specific conclusions

On the growth of metal oxide semiconducting nanowires for gas sensing

In₂O₃ nanowires

- The growth conditions of In₂O₃ nanowires are strongly dependent on the oxygen concentration in the carrier gas during the experiments, restricted to values between 0.01 and 0.02 % diluted in pure argon, as well as on the precursor and substrate temperatures, which were established to be 900 and 750°C, respectively. In this way, monocrystalline In₂O₃, 5 μm long and 150 nm in diameter have been produced.
- With parameters diverging from the optimal conditions, the formation of non-nanowire like structures, like nanorods and octahedra, is promoted. The nanorods were synthesized for lower oxygen concentration, while the octahedra, formed via a vapor-solid mechanism, were formed at higher oxygen concentration.
- The individual In₂O₃ NWs-based gas sensors present maximum response at 300 °C with values of 47 % and towards 100 ppm of EtOH, and response as fast as 4 minutes. At the

same time, the response to CO is lower than 10 %, proving the selectivity of the fabricated gas sensors towards EtOH.

Ga₂O₃ nanowires

- The growth conditions of Ga₂O₃ NWs are mainly determined by the temperature, the optimal conditions being a precursor temperature of 950 °C and a substrate temperature of 820 °C. The higher temperature, when compared to In₂O₃, is attributed to the use of the carbothermal reduction to evaporate the precursor powder materials. These conditions lead to monocrystalline NWs of average length and radius of 12 μm and 100 nm, respectively.
- The Ga₂O₃ NWs are surrounded by a C shell of 4 to 10 nm. This shell arises from the use of the carbothermal reduction for the evaporation of the precursor material, which generates large amounts of carbon byproducts.
- The gas sensing devices based on individual Ga₂O₃ NWs only respond to relative humidity, with no resistance variation for the other gases like NO₂, CO, EtOH and hydrogen. The maximum response is above 90%, obtained at room temperature, with a response time of 2 minutes. This makes these devices extremely selective and low power consuming.
- This selectivity is due to the carbon shell around the NWs, as the response behavior towards relative humidity is very similar to that of carbon-based materials.

On the development of advanced integration methodologies

Dielectrophoretic alignment

- For the alignment of individual WO₃ NWs, a square wave of 5V_{pp} and 9.5 MHz, using water as solvent, have been found to provide the best results for the used electrode geometry.

- The maximum gas response of the fabricated gas sensors based on arrays of individual NWs has been towards 5 ppm of NO₂ for the pristine and towards 100 ppm of EtOH for the Pt-functionalized WO₃ NWs, respectively. This higher response of the Pt-functionalized WO₃ NWs-based gas sensors is related to the surface decoration of these NWs, which increases the amount of oxygen adsorbed species at their surface, allowing EtOH molecules to be more easily adsorbed than on pristine NWs.

Electron beam lithography

- For the correct contact fabrication on microhotplates and micromembranes, the spinning and exposure processes need to be fine-tuned. A special holder has been developed to fix the chip and avoid photoresist accumulation in its borders during the spinning. The optimized spinning parameters, 4500 rpm for 1 minute, are the best choice for obtaining the most uniform photoresist given the topography and bending of the microhotplates. Furthermore, the required electron dose is increased to 600 $\mu\text{C}/\text{cm}^2$ to achieve the optimal resist exposure.
- The gas sensors based on individual EBL-contacted SnO₂ NWs present maximum response at 200 °C, with values of 70 % towards 20 ppm of ammonia, which is more sensitive than the reference fabrication method.
- The EBL contact fabrication method presents the advantage, compared to the reference method, that the fabricated metallic contacts present much lower resistance values and that several NWs can be contacted in one single EBL session.

On the fabrication and characterization of an electronic-nose based on semiconducting nanowires

- The localized growth method based on a modification of the VLS procedure, employing the micromembranes as heat sources for the decomposition of the precursor gas, have been optimized, allowing one NW material to be grown on each different micromembrane of the same chip. This optimization resulted in minimal impact between the different growth processes. In this way, SnO₂ and Ge NWs have been grown on different micromembranes by VLS, while WO₃ has been grown in a third one employing AACVD.
- The similar response of these gas sensors to those reported for devices containing exclusively one type of NW material demonstrates that there exist no cross-effects when one or several devices operate at the same time.
- The analysis of the simultaneous gas responses of Ge, SnO₂ and WO₃ NWs when exposed towards NO₂, CO and RH diluted in dry synthetic air has been performed for the first time. The data obtained from the tests have been analyzed using the principal component analysis (PCA) and have demonstrated the capacity to discriminate between the different gases, constituting e-nose based on semiconducting NWs. We call this system a nano-electronic-nose.

6.3 Future work

Based on the results reported in this thesis, some open questions which still remain to be solved and some initial activities carried out on lateral topics can constitute the basis for a further development. In the following, a few investigation directions are given, which should further help advancing in the gas sensing field.

- To grow crystalline $\text{In}_2\text{O}_3\text{-Ga}_2\text{O}_3$ core-shell or heterostructured NWs via the VLS mechanism using a CVD furnace and solid precursors, fabricate devices based on individual $\text{In}_2\text{O}_3\text{-Ga}_2\text{O}_3$ NWs and characterize their gas sensing properties.
- To fabricate nanosized patterns using EBL combined with the site-selective growth of semiconducting NWs, develop gas sensors based on meshes of NWs with reduced dimensions or, even, individual NWs and characterize their gas sensing properties.
- To fabricate e-nose based on a single chip containing 4 different site-selective grown NWs and study their gas discrimination capabilities towards combinations of 3 gases or more.



7. Resum en català

Aquesta tesi doctoral, realitzada en el grup MIND del Departament d'Enginyeries Electrònica i Biomèdica, està enfocada al desenvolupament de dispositius i sistemes sensors de gas basats en nanofils semiconductors monocristal·lins i es pot considerar un pas endavant en la recerca que, durant més de 15 anys, s'ha dut a terme en el grup. Abans de començar aquest treball, els nanofils d'òxids metàl·lics, que són components essencials per al desenvolupament dels dispositius i sistemes sensors de gas d'estat sòlid, eren crescuts i subministrats per laboratoris amb qui es col·labora. A la vegada, el departament disposava d'un forn pel dipòsit Químic en fase vapor (CVD), que permet dur a terme el creixement de nanofils i al qual es va tenir accés a començaments de 2015. Per tant, com a primer objectiu i punt de partida d'aquesta tesi, es va plantejar la sintetització de nanofils d'òxids metàl·lics utilitzant el forn CVD per, després, poder fabricar sensors de gas. Això s'ha aconseguit, fabricant nanofils d'òxid d'indi (In_2O_3) i d'òxid de gal·li (Ga_2O_3) seguint el procés vapor-líquid-sòlid (VLS), utilitzant or com a agent catalític i fent ús de la reducció carbotermal. Aquest procés permet disminuir la temperatura emprada per evaporar els precursors d'aquests òxids (primer pas del procés VLS) i l'or promou la formació de nanofils, proporcionant punts predominants d'absorció als vapors dels precursors. En el cas dels nanofils d' In_2O_3 , s'ha determinat que les condicions que promouen el creixement de nanofils en el forn CVD, utilitzant com a precursor 0.25 g d'una mescla de pols d' In_2O_3 i grafit en una proporció de 4:1 en pes i amb un flux de gas portador de 100 sccm d'argó pur, són: una concentració d'entre 0.01 i 0.02 % d'oxigen en el gas portador, el precursor a 900 °C, els substrats a 720 °C, i la pressió residual entre 2 i 100 Torr. S'ha observat que utilitzant d'altres concentracions d'oxigen es promou la formació d'estructures diferents, com ara "nanorods" o

microoctaedres. Els nanofils d' In_2O_3 obtinguts amb les condicions òptimes eren monocristal·lins, amb longituds i diàmetres mitjanes de 5 μm i 150 nm, respectivament. Els nanofils fabricats s'han transferit a xips amb microplataformes calefactores suspeses, que contenen un calefactor integrat i uns elèctrodes a la superfície, per a poder ser utilitzats com a sensors de gas i s'han contactat amb pistes que contenen platí, emprant el dipòsit assistit per feixos d'electrons (FEBID, per el seu acrònim en anglès). Això permet mesurar la resistència dels nanofils individuals, que s'ha utilitzat per a mesurar la presència de gasos a través de la variació d'aquesta resistència. Pels sensors de gas basats en nanofils individuals d' In_2O_3 , les mesures s'han realitzat a temperatures d'entre 200 i 300 °C, assolida mitjançant la resistència integrada, i enfront de monòxid de carboni (CO), diòxid de nitrogen (NO_2) i etanol (EtOH), diluïts en aire sintètic sec. Per a aquests sensors, la màxima variació de la resistència va ser del 47% per a 100 ppm d'EtOH i a 300 °C i la resposta més ràpida va ser de 4 minuts. Per contra, la resposta sempre va ser inferior al 10 % enfront dels altres dos gasos.

Emprant el mateix forn i condicions experimentals semblants, ha estat possible créixer nanofils de Ga_2O_3 . Amb aquest material s'ha observat que no hi ha una dependència amb la concentració d'oxigen i, a més, a cada experiment s'han crescut molts més nanofils, de més longitud (de mitjana, 12 μm) i de menor diàmetre (de 50 nm, de mitjana) que en el cas d' In_2O_3 . Les altres diferències en les condicions de creixement han estat: 0.45 g de precursor format per una mescla de pols de Ga_2O_3 i grafit en una proporció de 2:3 en pes, així com temperatures de 950 °C pel precursor i 820 °C pels substrats. Aquests nanofils monocristal·lins estaven envoltats d'una capa d'entre uns 4 i 10 nm de carboni amorf. Els sensors s'han fabricat de la mateixa manera que en el cas de l' In_2O_3 i s'ha estudiat el seu comportament entre temperatura ambient (25 °C) i 300 °C enfront dels mateixos gasos que els nanofils individuals d' In_2O_3 i, a més, enfront d'humitat relativa (RH). Aquests sensors, treballant a temperatura ambient, són molt selectius a la RH i no modifiquen la seva resistència en presència dels altres gasos. La resposta màxima és superior al 90 % per a una RH del 80% i el temps de resposta és de 2 minuts. Aquest comportament s'ha atribuït al recobriment de carboni i és resultat d'utilitzar el grafit com a material precursor. Aquesta interpretació està en consonància amb el comportament similar que presenten els materials basats en carboni.

Un segon objectiu d'aquesta tesi ha estat explorar diversos mètodes d'integració de nanofils individuals en el sensor amb l'objectiu de substituir FEBID, tècnica molt lenta i costosa. S'han provat de forma satisfactòria dues metodologies: emprar la dielectroforesi, consistent en el moviment de partícules dielèctriques suspeses en un dissolvent com a resultat de l'aplicació de camps elèctrics alterns, i la litografia per feixos d'electrons.

Per als experiments de dielectroforesi s'han fet servir nanofils d'òxid de tungstè (WO_3), sense dopar o decorats amb nanopartícules de platí. Les condicions experimentals per aconseguir satisfactòriament l'alineament i contacte dels nanofils entre els elèctrodes del xip dissenyat per a aquesta tasca han estat emprar aigua com a dissolvent, un senyal periòdic quadrat de 5 V pic a pic i una freqüència de 9.5 MHz i aplicar el camp durant 20 segon. Els sensors fabricats s'han caracteritzat enfront de NO_2 i d'EtOH, diluïts en aire sintètic sec. Els resultats mostren que els nanofils decorats són més sensibles a l'EtOH que els no dopats, mentre que aquest comportament s'inverteix quan se'ls exposa a NO_2 . Aquesta diferència ha estat atribuïda a una major quantitat d'oxigen pre-adsorbit en les superfícies dels nanofils de WO_3 decorats, que donen lloc a unes majors interaccions químiques i electròniques. D'aquesta forma s'ha demostrat la viabilitat de contactar nanofils individuals mitjançant dielectroforesi.

El segon mètode alternatiu ha consistit en emprar la litografia per feixos d'electrons (EBL) en combinació amb la tècnica de lift-off sobre xips amb micromembranes calefactores, dotades d'elèctrodes a la superfície. Per a això, s'han utilitzat nanofils d'òxid d'estany (SnO_2) i ha calgut modificar els procediments habituals d'aquesta tècnica per a substrats de silici. Per començar, s'ha hagut de dissenyar i fabricar un portamostres especial que permetés muntar al seu interior el xip de manera que tots dos estiguessin a la mateixa alçada per tal evitar l'acumulació de fotoresina en els extrems dels xips. A més, a causa de les tensions mecàniques de les capes del substrat, les membranes estaven molt fortament corbades cap amunt, cosa que dificultava la distribució de la fotoresina i que ha requerit un ajustament de les condicions de centrifugació. Les condicions òptimes de fabricació són emprar poli (metil metacrilat) (PMMA 950k A7), centrifugada a 4500 rpm, seguida d'un tractament tèrmic a 180 °C durant 1 minut i exposada el feix de 20 kV amb una dosi de 600 $\mu\text{C}/\text{cm}^2$. Aquesta dosi

és 6 vegades superior a la dosi habitual per a aquesta fotoresina. Després del revelat amb metil-isobutil-cetona i isopropanol (1:3) durant 30 segons, es procedeix a realitzar el lift-off, consistent en dipositar una bicapa Ti/Pt de 20/80 nm i dissoldre la fotoresina amb acetona, de forma que només restarà sobre el substrat el metall on s'ha eliminat la fotoresina restant. Aquesta metodologia permet contactar diversos nanofils a diferents elèctrodes en un sol procés. Aquests sensors amb nanofils individuals de SnO₂, han estat caracteritzats a temperatures entre 150 i 400 °C enfront d'amoníac diluït en aire sintètic sec. La variació màxima de la resistència, que es va mesurar a 200 °C, és d'un 70 % enfront de 20 ppm d'amoníac. Aquests sensors són més sensibles que els fabricats amb la tècnica de referència, FEBID, que és de 30 % per a 25ppm d'amoníac i mesurat a 250 °C valor. Això demostra que el mètode de litografia per feixos d'electrons es pot emprar satisfactòriament per contactar nanofils individuals sobre xips amb membranes calefactores.

L'últim objectiu d'aquesta tesi doctoral és la fabricació i caracterització d'un nas electrònic basat en diverses xarxes de nanofils semiconductors integrats en un mateix xip. És, a més, una ampliació d'un mètode alternatiu per integrar xarxes de nanofils en micromembranes calefactores, desenvolupat en el grup el 2012. En aquest cas s'han crescut nanofils de tres materials semiconductors, SnO₂, WO₃ i germani (Ge), en regions localitzades i predefinides d'un sol xip, de manera que s'integrin directament en ell. Pel creixement de SnO₂ i Ge, s'ha utilitzat una modificació de la metodologia VLS emprada per créixer els nanofils de In₂O₃ i Ga₂O₃. La modificació ha consistit en utilitzar un precursor gasós i substituir els substrats escalfats per l'escalfament local donat pel calefactor integrat de les micromembranes. Per a cada procés només es va polaritzar elèctricament una micromembrana, mantenint les altres fredes i sense polaritzar, i es va aconseguir el creixement de la xarxa de nanofils només a la seva part escalfada. Això també va succeir per als successius creixements, que no van afectar les propietats de detecció elèctrica i de gas dels nanofils prèviament crescuts. El WO₃, per contra, va ser crescut mitjançant la tècnica CVD amb aerosol atmosfèric, introduint el precursor en forma d'aerosol, però, igual que abans, utilitzant l'escalfament local de la micromembrana per a la descomposició dels gasos.

Els tres sensors, formats pels tres materials diferents i funcionant simultàniament, constitueixen un nas electrònic, que s'ha caracteritzat enfront de NO₂, CO i de RH, sempre diluïts en aire sintètic sec. Primer s'ha realitzat el calibratge de cada sensor individual enfront dels tres gasos de forma individual, després enfront dels tres gasos simultàniament i, finalment, es van fer els tests dels tres sensors funcionant simultàniament enfront dels tres gasos. Les dades de totes les mesures s'han tractat segons la metodologia d'anàlisi de components principals (Principal Component Analysis, PCA) i els resultats demostren que el nas electrònic és capaç de discriminar entre diverses mescules amb concentracions en el rang de ppm de NO₂ i CO diluïts en aire sintètic sota diferents nivells de RH.



8. List of publications and conference contributions

Publications

1. “Gas nanosensors based on individual indium oxide nanostructures”

G. Domènech-Gil, J. Samà, P. Pellegrino, S. Barth, I. Gràcia, C. Cané, A. Romano-Rodríguez; *Procedia Engineering* 120 (2015) 795 – 798. DOI: 10.1016/j.proeng.2015.08.826.

2. “Low-cost fabrication of zero-power metal oxide nanowire gas sensors: trends and challenges”

J. Samà, J.D. Prades, O. Casals, S. Barth, I. Gràcia, C. Cané, G. Domènech-Gil, F. Hernández-Ramírez, A. Romano-Rodríguez; *Procedia Engineering* 120 (2015) 488 – 491. DOI: 10.1016/j.proeng.2015.08.678.

3. “Site-selectively grown SnO₂ nanowires networks on micromembranes for efficient ammonia sensing in humid conditions”

J. Samà, S. Barth, G. Domènech-Gil, J.D. Prades, N. López, O. Casals, I. Gràcia, C. Cané, A. Romano-Rodríguez; *Sensors and Actuators B: Chemical* 232 (2016) 402-409; DOI: 10.1016/j.snb.2016.03.091.

4. “Gas sensors based on individual indium oxide nanowire”

G. Domènech-Gil, S. Barth, J. Samà, P. Pellegrino, I. Gràcia, C. Cané, A. Romano-Rodríguez; *Sensors and Actuators B: Chemical* 238 (2017) 447-454. DOI: 10.1016/j.snb.2016.07.084.

5. "Individual gallium oxide nanowires for humidity sensing at low temperature"
G. Domènech-Gil, I. Peiró-Riera, E. López-Aymerich, P. Pellegrino, S. Barth, I. Gràcia, C. Cané, J.D. Prades, M. Moreno-Sereno, A. Romano-Rodríguez; *Proceedings 1* (2017) 468. DOI: 10.3390/proceedings1040468.

6. "Laser Interferometry for broad area SPR-grating couplers in chemical applications"
M. Moreno-Sereno, N. Pérez, G. Domènech-Gil, L. Parellada-Monreal, M. Martínez-Calderon, M. Gomez-Aranzadi, N. Darwish, G. García-Mandayo, A. romano-Rodríguez; *Proceedings 1* (2017) 323. DOI: 10.3390/proceedings1040323.

7. "Gas sensors based on individual (Ga, In)₂O₃ nanowires"
E. López-Aymerich, G. Domènech-Gil, M. Moreno-Sereno, J. D. Prades, P. Pellegrino, S. Barth, A. Romano-Rodríguez; *Proceedings 1* (2017) 321. DOI: 10.3390/proceedings1040458.

8. "Gas sensing characterization of single-nanowire sensor array systems based on non-functionalized and Pt-functionalized tungsten oxide"
O. Chmela, J. Sadílek, J. Somer, J. Samà, G. Domènech-Gil, A. Romano-Rodríguez, J. Hubalek, S. Vallejos; *Proceedings 1* (2017) 437. DOI: 10.3390/proceedings1040458.

9. "Low temperature humidity sensor based on Ge nanowires selectively grown on suspended microhotplates"
J. Samà, M.S. Seifner, G. Domènech-Gil, J. Santander, C. Calaza, M. Moreno-Sereno, I. Gràcia, C. Cané, S. Barth, A. Romano-Rodríguez; *Sensors and Actuators B: Chemical* 243 (2017) 669-677. DOI: 10.1016/j.snb.2016.12.042.

10. "Room temperature humidity sensor based on single β -Ga₂O₃ nanowires"
G. Domènech-Gil, I. Peiró-Riera, E. López-Aymerich, M. Moreno-Sereno, P. Pellegrino, I. Gràcia, C. Cané, S. Barth, A. Romano-Rodríguez; *Proceedings 2* (2018) 958. DOI: 10.3390/proceedings2130958.

11. "Site-specific growth and in situ integration of different nanowire material networks on a single chip: towards a nanowire-based electronic nose for gas detection"
L. Hrachowina, G. Domènech-Gil, A. Pardo, M.S. Seifner, I. Gràcia, C. Cané, A. Romano-Rodríguez, S. Barth; *ACS Sensors* 3 (2018) 727-734; DOI: 10.1021/acssensors.8b00073.

12. “Comparative studies of chemoresistive gas sensors based on multiple randomly connected wires and arrays of single-wires”

O. Chmela, J. Sadílek, G. Domènech-Gil, I. Gràcia, A. Romano-Rodríguez, J. Hubalek, S. Vallejos; *Proceedings 2* (2018) 823. DOI: 10.3390/proceedings2130823.

13. “Localized and in-situ integration of different nanowire materials for electronic nose applications”

G. Domènech-Gil, L. Hrachowina, A. Pardo, M.S. Seifner, I. Gràcia, C. Cané, S. Barth, A. Romano-Rodríguez; *Proceedings 2* (2018) 957. DOI: 10.3390/proceedings2130957.

14. “Selectively arranged single-wire based nanosensor array systems for gas monitoring”

O. Chmela, J. Sadílek, G. Domènech-Gil, J. Samà, J. Somer, R. Mohan, A. Romano-Rodríguez, J. Hubalek, S. Vallejos; *Nanoscale* 10 (2018) 9087-9096. DOI: 10.1039/C8NR01588K.

15. “Different nanowire materials localized growth and in-situ integration for electronic nose applications”

G. Domènech-Gil, L. Hrachowina, A. Pardo, M.S. Seifner, I. Gràcia, C. Cané, S. Barth, A. Romano-Rodríguez; *IEEE* (2018). DOI: 10.1109/CDE.2018.8597020.

16. “Electron Beam Lithography for contacting single nanowires on non-flat suspended substrates”

J. Samà, G. Domènech-Gil, I. Gràcia, X. Borrisé, C. Cané, S. Barth, F. Steib, A. Waag, J.D. Prades, A. Romano-Rodríguez; *Sensors and Actuators B Chemical* 286 (2019) 616-623. DOI: 10.1016/j.snb.2019.01.040.

17. “Humidity gas sensors made from individual Ga₂O₃ nanowires: impact of the carbothermal reduction synthesis: impact of the carbothermal reduction synthesis method on their high selectivity and room temperature operation”

G.Domènech-Gil, I. Peiró, E. López-Aymerich, J. Romano-deGea, I. Gràcia, C. Serre, P. Pellegrino, M. Moreno, C. Cané, S. Barth, A. Romano-Rodríguez; (Submitted to *Nano Letters*)

Conference contributions

MATERIAL RESEARCH SOCIETY FALL MEETING 2014 – BOSTON (USA)

Presentation: “VLS growth of In_2O_3 nanowires via carbothermal reduction: growth conditions, structural characterization and gas sensing properties”

S. Barth, J. Sama, G. Domènech-Gil, A. Romano-Rodríguez;

Presentation: “Gas sensing properties of In_2O_3 nanowires grown via carbothermal reduction”

J. Sama, S. Barth, G. Domènech-Gil, A. Romano-Rodríguez;

EUROSENSORS XXIX 2015 – FREIBURG (GERMANY)

Poster: “Gas nanosensors based on individual indium oxide nanostructures”

G. Domènech-Gil, J. Samà, P. Pellegrino, S. Barth, A. Romano-Rodríguez;

MATERIAL RESEARCH SOCIETY FALL MEETING 2015 – BOSTON (USA)

Poster: “Dependence of the gas nanosensing response and the structural properties of different Indium oxide nanostructures”

G. Domènech-Gil, J. Samà, P. Pellegrino, S. Barth, A. Romano-Rodríguez, I. Gracia;

EUROPEAN MATERIAL RESEARCH SOCIETY SPRING MEETING 2015 – LILLE (FRANCE)

Presentation: “Gas sensors based on individual gallium oxide nanowires”

G. Domènech-Gil, I. Peiró-Riera, J. Samà, P. Pellegrino, S. Barth, A. Romano-Rodríguez;

Poster: “Gas nanosensors based on individual gallium oxide nanowires”

G. Domènech-Gil, I. Peiró-Riera, J. Samà, P. Pellegrino, S. Barth, A. Romano-Rodríguez;

EUROPEAN MATERIAL RESEARCH SOCIETY FALL MEETING 2015 – WARSAW (POLAND)

Presentation: “Gas nanosensors based on individual metal oxide nanowires”

G. Domènech-Gil, J. Samà, P. Pellegrino, S. Barth, A. Romano-Rodríguez;

Presentation: “Localized growth of germanium nanowires for low power gas sensing”

J. Samà, G. Domènech-Gil, S. Barth, M. Seifner, P. Pellegrino, I. Gracia, C. Calaza, A. Romano-Rodríguez;

MATERIAL RESEARCH SOCIETY FALL MEETING 2016 – BOSTON (USA)

Presentation: “Synthesis, characterization and air quality monitoring applications for individual gallium oxide nanowires”

G. Domènech-Gil, I. Peiró-Riera, J. Samà, P. Pellegrino, S. Barth, A. Romano-Rodríguez;

Presentation: “Gas Nanosensors Based on Individual $(\text{In}_{1-x}\text{Ga}_x)\text{}_2\text{O}_3$ Nanowires”

G. Domènech-Gil, E. Lopez-Aymerich, J. Samà, P. Pellegrino, S. Barth, A. Romano-Rodríguez;

EUROSENSORS XXXI 2017 – PARIS (FRANCE)

Preentation: “Gas sensors based on individual $(\text{Ga,In})_2\text{O}_3$ nanowires”

E. López-Aymerich, G. Domènech-Gil, M. Moreno-Sereno, J. D. Prades, P. Pellegrino, S. Barth, A. Romano-Rodríguez;

Poster: “Individual gallium oxide nanowires for humidity sensing at low temperature”

G. Domènech-Gil, I. Peiró-Riera, E. López-Aymerich, P. Pellegrino, S. Barth, I. Gràcia; C. Cané, J.D. Prades, M. Moreno-Sereno, A. Romano-Rodríguez;

Poster: “Indium oxide octahedral structures-based sensor”

G. Domènech-Gil, S. Barth, I. Gràcia, C. Cané, J.D. Prades, M. Moreno-Sereno, A. Romano-Rodríguez;

Poster: “Gas sensing characterization of single-nanowire sensor array systems based on non-functionalized and Pt-functionalized tungsten oxide”

O. Chmela, J. Sadílek, J. Somer, J. Samà, G. Domènech-Gil, A. Romano-Rodríguez, J. Hubálek, S. Vallejos;

Poster: “Laser Interferometry for broad area SPR-grating couplers in chemical applications”

M. Moreno-Sereno, N. Perez, G. Domènech-Gil, L. Parellada, M. Martínez-Calderon, M. Gómez-Aranzadi, N. Darwish-Miranda, G. García-Mandayo, A. Roamano-Rodríguez;

MICRO AND NANO ENGINEERING 2017 – BRAGA (PORTUGAL)

Poster: “Localized growth of germanium nanowires for low power gas sensing”

G. Domènech-Gil, J. Samà, M. Seifner, I. Gràcia, C. Calaza, C. Cané, P. Pellegrino, M. Moreno-Sereno, S. Barth, A. Romano-Rodríguez;

Poster: “Localized-growth of tungsten oxide nanowires for gas sensing applications”

G. Domènech-Gil, L. Hrachowina, I. Gràcia, C. Cané, P. Pellegrino, M. Moreno-Sereno, S. Barth, A. Romano-Rodríguez;

MATERIAL RESEARCH SOCIETY FALL MEETING 2017 –BOSTON (USA)

Presentation: “Humidity sensors from individual gallium oxide nanowires synthesis, characterization and sensing properties”

G. Domènech-Gil, I. Peiró-Riera, P. Pellegrino, S. Hernández, M. Moreno-Sereno, S. Barth, A. Romano-Rodríguez;

Poster: “Individual $(\text{In}_{1-x}\text{Ga}_x)_2\text{O}_3$ nanowire-based gas sensor”

G. Domènech-Gil, E. López-Aymerich, P. Pellegrino, M. Moreno-Sereno, S. Barth, A. Romano-Rodríguez;

EUROSENSORS XXXII 2017 – GRAZ (AUSTRIA)

Presentation: “Localized and in-situ integration of different nanowire materials for electronic nose applications”

G. Domènech-Gil, L. Hrachowina, A. Pardo, M.S. Seifner, I. Gràcia, C. Cané, S. Barth, A. Romano-Rodríguez;

Presentation: “Room temperature humidity sensor based on single Ga_2O_3 nanowires”

G. Domènech-Gil, I. Peiró-Riera, E. López-Aymerich, M. Moreno-Sereno, P. Pellegrino, I. Gràcia, C. Cané, S. Barth, A. Romano-Rodríguez;

Poster:” Comparative studies of chemoresistive gas sensors based on multiple randomly connected wires and arrays of single-wires”

O. Chmela, J. Sadílek, G. Domènech-Gil, I. Gràcia, A. Romano-Rodríguez, J. Hubálek, S. Vallejos;

MATERIAL RESEARCH SOCIETY FALL MEETING 2018 – BOSTON (USA)

Presentation: “Site-specific growth and in-situ integration of different nanowire materials on a single chip for electronic nose applications”

G. Domènech-Gil, L. Hrachowina, A. Pardo, M.S. Seifner, I. Gràcia, C. Cané, S. Barth, A. Romano-Rodríguez;

Presentation: “Fabrication and testing of a nanoelectronic nose employing site-specific growth and integration of nanowire material networks on a single chip”

G. Domènech-Gil, L. Hrachowina, A. Pardo, M.S. Seifner, I. Gràcia, C. Cané, S. Barth, A. Romano-Rodríguez;

Presentation: “Gallium oxide nanowires for gas sensing applications: growth, device fabrication and gas response”

G. Domènech-Gil, I. Peiró-Riera, J. Samà, P. Pellegrino, S. Hernández, M. Moreno-Sereno, J.D. Prades, S. Barth, A. Romano-Rodríguez;

NANOLITO 2017 – MADRID

Poster: “Focused ion and electron beam electrical contacts on individual metal oxide nanowires for gas sensing”

G. Domènech-Gil, I. Gràcia, C. Cané, P. Pellegrino, M. Moreno-Sereno, A. Romano-Rodríguez;

IN2UB 2017 – BARCELONA

Presentation: “Individual gallium oxide nanowire as low power humidity sensor”

G. Domènech-Gil, I. Peiró-Riera, I. Gràcia, C. Cané, P. Pellegrino, S. Barth, A. Romano-Rodríguez;

CDE 2018 – SALAMANCA

Presentation (Best student presentation award): “Different nanowire materials localized in-situ integration for electronic nose applications”

G. Domènech-Gil, L Hrachowina, A. Pardo, M.S. Seifner, I. Gràcia, C. Cané, S. Barth, A. Romano-Rodríguez;

Presentation: “Fabrication, characterization and gas response of individual $(\text{Ga}_{1-x}\text{In}_x)_2\text{O}_3$ nanowire-based chemoresistors”

G. Domènech-Gil, E. López-Aymerich, I. Peiró-Riera, M.S. Seifner, I. Gràcia, C. Cané, S. Barth, A. Romano-Rodríguez;

IN2UB 2018 – BARCELONA

Poster: “Gas sensors based on nanostructured metal oxides”

G. Domènech-Gil, L Hrachowina, E. López-Aymerich, I. Peiró-Riera, A. Pardo, M.S. Seifner, I. Gràcia, C. Cané, M. Moreno-Sereno, S. Barth, A. Romano-Rodríguez;

JUPI 2019 – BARCELONA

Presentation and workshop: “Explaining Stranger Things workshop”

G. Domènech-Gil

IN2UB 2019 – BARCELONA

Poster: “Room temperature humidity sensors based on individual Ga_2O_3 nanowires grown via carbothermal reduction”

G. Domènech-Gil, I. Peiró-Riera, E. López-Aymerich, M. Moreno-Sereno, P. Pellegrino, S. Barth, I. Gràcia, C. Cané, A. Romano-Rodríguez;

